ARGON BUBBLE BEHAVIOR IN SLIDE-GATE TUNDISH NOZZLES DURING CONTINUOUS CASTING OF STEEL SLABS

BY

HUA BAI

B.S., Beijing Institute of Aeronautics and Astronautics, 1983
M.S., Beijing Institute of Aeronautics and Astronautics, 1986

THESIS

Submitted in partial fulfillment of the requirements
for the degree of Doctor of Philosophy in Mechanical Engineering
in the Graduate College of the
University of Illinois at Urbana-Champaign, 2000

Urbana, Illinois

UNIVERSITY OF ILLINOIS AT URBANA-CHAMPAIGN

THE GRADUATE COLLEGE

APRIL 2000
(date)

WE HEREBY RECOMMEND THAT THE THESIS BY

HUA BAI

ENTITLED ARGON BUBBLE BEHAVIOR IN SLIDE-GATE TUNDISH NOZZLES DURING CONTINUOUS CASTING OF STEEL SLABS

BE ACCEPTED IN PARTIAL FULFILLMENT OF THE REQUIREMENTS FOR THE DEGREE OF DOCTOR OF PHILOSOPHY

Brian G. Thomas
Director of Thesis Research

Richard O Buckius
Head of Department

Committee on Final Examination†

Brian G. Thomas
Chairperson

S.P. Vanka

S. Balachandar

† Required for doctor's degree but not for master's.

O-517

ABSTRACT

Argon injection into a tundish nozzle is an efficient and widely employed method to reduce nozzle clogging in the continuous casting process. It also affects casting operation and product quality by changing the flow pattern in the nozzle and mold. The current work combines mathematical modeling and experiments to investigate the argon bubble behavior in slide-gate nozzles and to analyze phenomena related to product defects and operational problems during the continuous casting of steel slabs. Water model experiments are performed to study bubble formation behavior, including bubble size, frequency, mode and effects of variables such as liquid velocity, gas injection flow rate, gas injection hole size and gas density. An analytical model is developed to predict the average bubble size. Argon gas bubbles are predicted to be 1~5mm. This is larger than air bubbles in water, especially at low speed. Typical sizes are 1 ~3mm. A three-dimensional finite difference model is developed to study the turbulent flow of liquid steel and argon bubble in the slide-gate nozzles. Experiments are performed on a 0.4-scale "water caster" to verify the model by comparing the model prediction with the measurements using PIV (Particle Image Velocimetry) technology. A weighted average scheme for the overall outflow is developed to quantify jet characteristics such as jet angle, jet speed, back flow zone fraction, turbulence and biased mass flow. Swirl is generated at nozzle ports. The validated model is employed to perform extensive parametric studies to investigate the effects of casting operation conditions such as gas injection, slide-gate orientation, casting speed, gate opening and bubble size and nozzle port design including port angle and port shape. The interrelated effects of nozzle clogging, argon injection, tundish bath depth, slide gate opening and nozzle bore diameter on the flow rate and pressure in tundish nozzles are quantified using an inverse model, based on interpolation of the numerical simulation results. The results are validated with measurements on operating steel continuous slab-casting machines, and presented for practical conditions. Suggestions to improve argon injection practice are proposed based on the modeling results. During ladle transitions and at other times when either casting speed or tundish level is low, argon flow should be turned off or at least severely reduced. The optimum argon flow rate required to avoid air aspiration in the nozzle is derived from the model.

ACKNOWLEDGEMENTS

I would like to express my sincere gratitude to my advisor, Professor Brian G. Thomas for his guidance, support and encouragement through the course of this work. I am very grateful for the opportunity to work with him, and have learned a great deal from him, which is far more than any course or textbook could ever teach me. I would also like to thank Professor Jonathan Dantzig, Professor S. Pratap Vanka, Professor S. Balachandar for their consent to serve on my dissertation committee. Additionally, I am indebted to them for their advice and many helpful suggestions for this thesis.

I would like to thank the National Science Foundation (Grant #DMI-98-00274) and the Continuous Casting Consortium at UIUC, including Allegheny Ludlum, (Brackenridge, PA), Armco Inc. (Middletown, OH), Columbus Stainless (South Africa), Inland Steel Corp. (East Chicago, IN), LTV Steel (Cleveland, OH), and Stollberg, Inc., (Niagara Falls, NY) for their continued support of our research, Professor J. Mazumder for use of the high speed video camera, AEA Technology for technical support on using CFX4.2 package and the National Center for Supercomputing Applications (NCSA) at the UIUC for computing time on Origin 2000 supercomputers. Additional thanks are extended to technicians at LTV Steel for help with the PIV measurements.

I would like to extend my thanks to my officemates and fellow students, both past and present, Guowei Li, Keith Rackers, David Stone, David Creech, Jon Parkman, Alex Danissov, Yuji Miki, Jie Min, Chensheng Li, Lan Yu, Ya Meng, Tiebiao Shi, Melody Langeneckert and Sivaraj Sivaramakrishnan. Their company, geniality, helpfulness and friendship helped to make these years an enjoyable, memorable and rewarding experience.

I would like to express my deepest appreciation to my wife Snow and my daughter Carrie for their love, counsel, encouragement and understanding throughout this endeavor. I am also very grateful to my parents, whose confidence in me has been a great source of energy and inspiration for me.

TABLE OF CONTENTS

Page

LIST OF TABLES

LIST OF FIGURES

NOMENCLATURE

$a_{i,}\ b_{i,}\ c_{i,}\ d_i$	curve fitting constant in Chapter 4 (i=1, 2, 3….)
C_P	specific heat (J/kg-K)
c_{lg}	inter-phase momentum exchange coefficient
C_D	drag coefficient for bubble
D	instantaneous equivalent bubble diameter (mm)
D_b	equivalent bubble diameter at detachment (mm)
D_N	diameter of nozzle bore (mm)
d	gas injection hole diameter (mm)
E	log-layer constant for velocity, 9.7930
e	elongation factor
e_d	elongation factor at instant of bubble detachment
	from gas injection hole(=L/D_b)
F_A	slide-gate opening, area fraction opening of the slide-gate
F_L	slide-gate opening, linear fraction of the opening distance
F_P	slide-gate opening, linear fraction of plant definition
F_B	buoyancy force for a bubble (N)
F_D	drag force acting on a bubble, due to the flowing liquid (N)
Fr	Froude number
F_S	surface tension force on a bubble (N)
F_{Sz}	vertical component of surface tension force on a bubble (N)
f	frequency of bubble formation from a gas injection hole (s^{-1})
f_l	volume fraction for the liquid phase
f_g	volume fraction for the gas phase (“hot” for argon in steel)

f_θ	contact angle function, $f_\theta = sin\theta_O(cos\theta_r - cos\theta_a)$
g	gravitational acceleration ($9.81 m/s^2$)
H_T	tundish bath depth (m)
H_{SEN}	SEN submerged depth (m)
h	heat transfer coefficient ($W/K\text{-}m^2$)
K	turbulence energy (m^2/s^2)
$\overline{K}$	weighted average turbulent energy on nozzle port (m^2/s^2)
k	heat conductivity (W/m-K)
L	$(=e_d D_b)$ elongation length at instant of bubble detachment (mm)
n	distance normal to the wall, wall law (m)
N	the number of measuring points (PIV) or computational cells (CFX) on the laser light sheet on the nozzle port exit, Equation 3.26
P_L	lowest pressure in nozzle (kPa)
p	pressure (kPa)
p_l	pressure for the liquid phase (kPa)
p_g	pressure for the gas phase (kPa)
Q_G	"cold" argon gas flow rate, measured at standard conditions (STP of 25˚C and 1 atmosphere pressure) (SLPM)
Q_g	gas injection flow rate per hole (ml/s)
Q_{Fe}	steel throughput (tonne/min)
r	horizontal radius of the ellipsoidal bubble (mm)
r_e	horizontal radius of the ellipsoidal bubble at the end of the expansion stage (mm)

r_d	horizontal radius of the ellipsoidal bubble at the instant of bubble detachment from the gas injection hole (mm)
$r_{x,}\ r_{y,}\ r_{z,}$	radii of the ellipsoidal bubble ($r_x = r_y = r$ *and* , $r_z = eD$) (mm)
r_{zd}	vertical radius of the ellipsoidal bubble at detachment (mm)
Re_{bub}	Reynolds number for bubble Re_{bub}=uD/υ
Re_n	Reynolds number for casting nozzle $Re_n = UD_N/\upsilon$
T	temperature (K)
T_W	wall temperature (K)
T_O	argon gas temperature at outer surface of the nozzle wall (K)
t_e	time at the end of the expansion stage (s)
t_d	time at the end of the detachment stage (s)
U	average liquid velocity in nozzle (m/s)
U_B	average velocity at the top inlet of the nozzle (m/s)
U_C	average jet velocity at the nozzle port (m/s)
U_i	liquid speed at cell i of the nozzle port (m/s)
U_{jet}	jet speed (m/s)
u	=u(y), liquid velocity profile across the nozzle bore (m/s)
$\overline{u}$	average liquid speed over the forming bubble (m/s)
$\overline{u_l}$	weighted average liquid velocity at nozzle port in x-direction (m/s)
V_b	bubble volume (=$\pi D^3/6$) (ml)
V_e	bubble volume at the end of the expansion stage (ml)
V_C	casting speed for 8”x52” slab (m/min)
V_t	velocity tangential to the wall, wall law (m/s)
v_{gi}	$=\{u_g, v_g, w_g\}$, velocity components for gas phase (m/s)

v_{li}	$=\{u_l, v_l, w_l\}$, velocity components for liquid phase (m/s)
$\overline{v_l}$	weighted average liquid velocity at nozzle port in y-direction (m/s)
$\overline{w_l}$	weighted average liquid velocity at nozzle port in z-direction (m/s)
We	Weber number
x,y,z	Cartesian coordinates (m)
y^+	non-dimensional distance normal to the wall
y_0^+	crossover point between the laminar sub-layer and the logarithmic region, 11.23
β	gas volume expansion coefficient
Δp	overall pressure-drop across the nozzle (kPa)
Δy	length of the cell sides in the y direction (m)
Δz	length of the cell sides in the z direction (m)
ε	turbulent dissipation (m^2/s^3)
$\bar{\varepsilon}$	weighted average turbulent dissipation at nozzle port (m^2/s^3)
η	back-flow zone fraction at nozzle port (m^2/s^3)
κ	Von-Karman constant, 0.419
μ_g	molecule viscosity of the gas (kg/m-s)
μ_l	molecule viscosity of the liquid (kg/m-s)
μ_t	turbulent viscosity of the liquid (kg/m-s)
μ_{eff}	effect kinetic viscosity of the liquid (kg/m-s)
θ	contact angle (°)
θ_o	static contact angle (°)

θ_a	advancing contact angle of a forming bubble (°)
θ_r	receding contact angle of a forming bubble (°)
θ_{zx}	vertical jet angle (°)
$\theta_{zx\text{-}slice}$	slice jet angle (°)
θ_{yx}	horizontal jet angle (°)
ρ_g	density of the gas (kg/m^3)
ρ_l	density of the liquid (kg/m^3)
σ	surface tension coefficient of the liquid (N/m)
υ	kinematic viscosity of the liquid =(μ_l/ρ_l) (m^2/s)

CHAPTER 1. INTRODUCTION

Continuous casting has been in industrial use for over thirty years and is the predominant way by which steel is produced today in the world. A schematic of part of the typical continuous slab-casting process is depicted in Figure 1.1 [1], showing the tundish, tundish nozzle and mold regions. In a typical slab casting operation, the liquid steel flows from the tundish, through the ceramic tundish nozzle, and exits through bifurcated ports into the liquid pool in the mold. The tundish nozzle consists of the upper tundish nozzle (UTN), the slide-gate plates and the submerged entry nozzle (SEN). Between these two nozzle segments, the flow rate is regulated by moving a" slide gate", which restricts the opening. Argon bubbles are injected through holes or pores in the nozzle wall to mix into the flowing liquid steel. The nozzle outlet ports are submerged below the surface of the molten steel in the mold to avoid interference with the interface between the steel and the slag layers which float on top. The liquid steel in the mold solidifies against the wall of the water-cooled, copper mold. The solidified steel shell acts as a container for the molten steel as it is continuous withdrawn from the mold at a "casting speed" and grows in thickness as it travels down below the mold. The completely solidified slab is then cut into desired lengths by torches.

The quality of the continuous cast steel slab is greatly affected by the flow pattern in the mold, which depends mainly on the flow pattern in the tundish nozzle, specifically the jets from the nozzle port outlets. The flow pattern not only has a great influence on heat transfer to the solidifying shell, but also governs the motion of inclusion particles and surface waves at the meniscus, which affects the internal cleanness and quality of the steel. The tundish nozzle should deliver steel uniformly into the mold while preventing problems such as surface waves, meniscus freezing and crack formation. Impingement of hot liquid metal with high momentum against the solidifying shell can contribute to shell thinning and even costly "breakouts", where liquid steel bursts from the shell [2]. In addition, the nozzle should be designed to deliver steel with the optimum level of superheat to the meniscus while preventing both detrimental surface turbulence and shell erosion or thinning due to excessive impingement of the hot molten steel jets. In some operations, it is also important for the flow pattern to aid in the flotation of detrimental alumina inclusions into the protective molten slag layer. Plant observations have found that many serious quality problems are directly associated with nozzle operation and the flow pattern in the mold [3]. For example, surface waves and turbulence near the top free surface can entrain some of the slag into the steel flow, causing dangerous large inclusions and surface slivers [4]. The high "standing wave" or large variation in the free surface level at the mold can prevent the liquid mold flux from filling and lubricating the gap between the steel shell and the mold. This can cause cracks in the steel shell due to thermal stresses and mold friction [5].

Nozzle clogging is one of the most disruptive phenomena on the operation of the tundish-mold system. During the casting process, a buildup (clog) containing steel impurities may form and deposit on the nozzle wall. This clog adversely affects product quality by changing the flow pattern which is usually carefully designed, based on no-clogging condition, and by degrading the internal quality of the final product when large chunks of it break off and enter the flow stream. Also, as the buildup progresses, the slide gate opening must be increased to maintain the desired flow rate. Once the slide-gate reaches its maximum position, production must stop and the nozzle must be replaced.

Argon injection through the nozzle wall into the steel stream is an efficient and widely employed method to reduce nozzle clogging, even though the real working mechanism is still not fully understood [6]. However, the injected argon bubbles will also affect the flow pattern in the nozzle, and subsequently in the mold. The argon bubbles might attach with small inclusions and become entrapped in the solidifying shell, resulting in “pencil pipe” and blister defects on the surface of the final product [7-10]. Other possible disadvantages of argon injection observed in operation include increased quality defects and nozzle slag line erosion due to the increased meniscus fluctuation [8, 11], exposure of the steel surface and subsequent reoxidation [12], entrapment of the mold power [13]. Large gas injection flow rates might create a boiling action in the mold [14, 15], which can greatly intensify those adverse effects. The boiling action at the mold meniscus was experimentally found [16] related to a flow pattern change inside the tundish nozzle, specifically, the regular “bubbly flow” changes to “annular flow” at high gas flow rate.

There is a great incentive to understand and predict the flow through the tundish nozzle since tundish nozzle geometry is one of the few variables that is both very influential on the continuous casting process and relatively inexpensive to change. Designing an effective nozzle requires quantitative knowledge of the relationship between nozzle geometry and other process variables on the flow pattern and the influential characteristics of the jet flow exiting the nozzle. A well-designed nozzle with optimized argon injection implementation should meet the required clogging-resistance capability, prevent the entrapment of those argon bubbles in solidified shell, as well as provide desired flow patterns in both nozzle and mold, which hence help to achieve a high quality cast slab.

The effect of gas injection on flow in the nozzle is relatively unstudied, especially through mathematical modeling. Most previous works on modeling fluid flow in the nozzle have focused on single-phase flow [1, 17-19]. A better understanding of fluid flow in the nozzle should consider the effect of gas injection. Argon bubble motion and its effect on flow depends greatly on the size of the bubbles which is determined during the initial stage of gas injection. Bubble size is also an essential parameter for other advanced studies such as argon bubble motion [10], inclusion attachment [10, 20], argon bubble and inclusion entrapment [9], in addition to modeling liquid steel-argon bubble two-phase fluid flow in nozzle and mold [21-23].

This work investigates argon bubble behavior in slide-gate tundish nozzles during continuous casting of steel slabs in three parts. First, water model experiments are performed to study bubble formation behavior in flow conditions approximating those in a slide-gate tundish nozzle of continuous casting process. The effects of liquid velocity, gas injection flow rate, gas injection hole diameter, and gas density on bubble formation behavior such as bubble size, injected gas mode are investigated. An analytical model is developed to predict the bubble size. Secondly, a three-dimensional finite difference model is developed to study the liquid steel-argon bubble two-phase turbulent flow in continuous casting tundish nozzles. Experiments are performed on a 0.4-scale water model to verify the computational model by comparing its prediction with velocity measurements using PIV (Particle Image Velocimetry) technology. A weighted average scheme for the overall outflow is developed to quantify the characteristics of the jets exiting the nozzle ports. Thirdly, the validated model is employed to perform extensive parametric studies to investigate the effects of casting operation conditions and nozzle port design. The interrelated effects of nozzle clogging, argon injection, tundish bath depth, slide gate opening and nozzle bore diameter on the flow rate and pressure in tundish nozzles are quantified using a inverse model, based on interpolation of the numerical simulation results. The results are validated with measurements on operating steel continuous slab-casting machines, and presented for practical conditions. Practical insights to optimize argon injection for various casting conditions are presented.

This work is part of a larger project to develop and apply mathematical models to understand and solve problems arising in the continuous casting process.

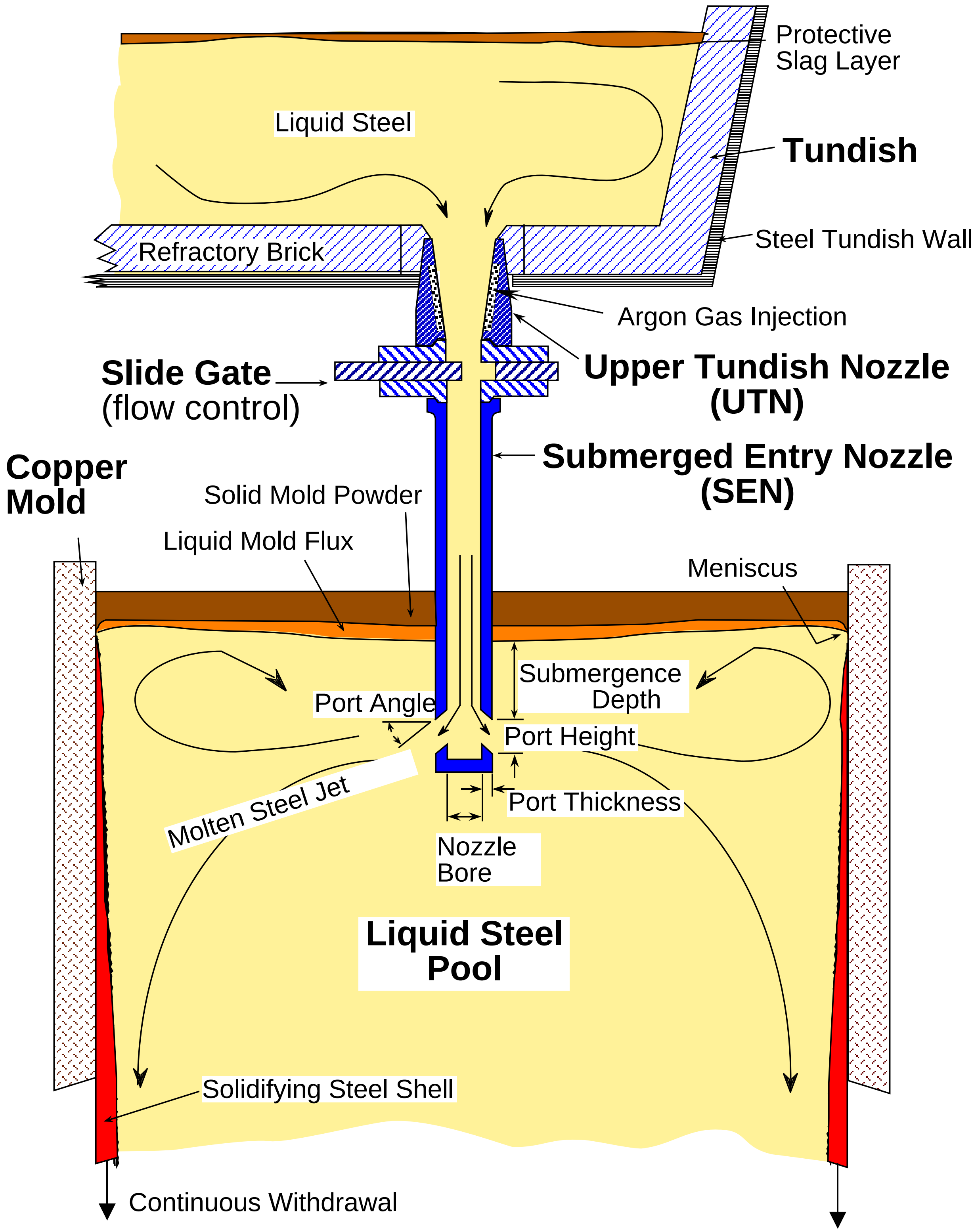

Figure 1.1 Schematic of continuous casting tundish, slide-gate nozzle, and mold [1]

CHAPTER 2. BUBBLE FORMATION STUDY

2.1 Introduction

Argon gas is injected through the walls of the ceramic nozzle into the liquid steel flow to reduce clogging in a slide-gate nozzle. The injected argon bubbles affect the flow pattern in the nozzle, and subsequently in the mold, thereby influencing the steel quality. Thomas et al. [22, 23], modeled the liquid steel-argon bubble two-phase flow in mold, and found that argon bubble size has an important effect that acts in addition to injection rate. Larger bubbles are found to leave the mold faster and, therefore, have less influence on the liquid flow pattern in the mold. Small bubbles travel with the jet further across the mold. Furthermore, small bubbles are more likely penetrate deep into the liquid pool and become entrapped by the solidified shell, causing quality problems, such as “pencil pipe” blister defects [10]. Creech [24] found that smaller bubbles buoyed the jet and encouraged the transition from the classic ”double-roll” flow pattern in the mold to “single-roll” for a given gas fraction. Wang et al. [20] found the optimal bubble size for inclusion removal. Tabata et al. [25] performed water model tests of gas injection into the slide-gate nozzle, and found that large bubbles tended to move to the center of the flow, thus lowering their ability to catch inclusions and to prevent their adherence to the nozzle wall.

When argon gas is injected into a slide-gate nozzle through the pores (with typical average diameter of 25~40μm) in the refractory material of the nozzle [6, 7, 26], or via machined or laser cut holes (with typical diameter of 0.2~0.4mm) on the wall [6, 26, 27], the formation of the bubbles is associated with the growth of a liquid-gas interface in an environment subjected to the highly turbulent shearing flow of the liquid steel. The injected gas forms a succession of bubbles which break away from the solid-liquid-gas interface, join the stream of the liquid steel, and thereafter travel as separate entities in the liquid. Or, the injected gas may form a gas sheet along the wall. This possibility is one of several suggested mechanisms for argon injection to deter the clogging in nozzles [6, 11]. We want to know when each happen.

2.2 Literature Review

For bubble formation in liquid metals, some experimental works have been reported on gas-stirred vessels in which gas is injected from an upward facing orifice or tube submerged in quiescent liquid. The frequency of bubble formation was measured by using pressure pulse [28, 29], resistance probe [30, 31], or acoustic device [32]. The mean bubble sizes are then derived from the known gas injection flow rate and the measured frequency of bubble formation. Efforts on direct observation of bubble formation in liquid metal were also made by using X-ray cinematography technique [33, 34]. Little work has been reported on bubble formation in flowing liquid metals such as in tundish nozzles. Surface tension and contact angle between the gas, liquid and solid surfaces is also very important to bubble formation. Recently, Wang et al [35] studied the effect of wettability on air bubble formation using water model experiments in which gas was injected through porous refractory into an acrylic tube with flowing water. Wettability as changed by waxing the porous refractory. On the waxed surface, the bubbles tended to coalesce together and form a gas curtain along the wall and then break into many uneven-sized bubbles after travel certain distances. On an un-waxed surface, even-sized bubbles formed and detached from the wall to join the liquid flow. No theoretical modeling work has been reported on bubble formation in metallic systems.

On the other hand, extensive bubble formation studies have been done on aqueous systems, both experimentally and theoretically, as reviewed by Kumar and Kuloor (1970) [36], Clift et al. (1978) [37], Tsuge (1986) [38], and Rabiger and Vogelpohl (1986) [39]. Most of those works are about bubble formation in stagnant liquid. The theoretical studies of bubble formation can be divided into two categories: analytical spherical bubble models and discretized non-spherical bubble models. The spherical bubble model assumes the spherical shape of the bubble throughout the bubble growth. The bubble size at detachment is obtained by solving force balance equation and/or bubble motion equation. The forces in equations are evaluated on the whole growing bubble. Two of many significant contributions are the one-stage model by Davidson and Schuler [40] and the two-stage model by Kumar and Kuloor [41]. The spherical bubble models have to use empirical criteria for determining the instant of detachment. In contrast, non-spherical bubble models have been developed [42-45] that are based on a local pressure/force balance at the gas/liquid interface. In these models, the bubble surface is divided into many two-dimensional axis-symmetric elements. For each element, two motion equations, one in the radial direction and the other vertical direction, are solved to give its radial and vertical velocities and then the position of the element. The bubble growth and bubble detachment is determined by calculating the (non-spherical) shape of the bubble during its formation. These models are therefore advantageous because they do not require the assumption of bubble detachment criteria, but not applicable to asymmetric conditions such as with shearing flowing liquid. Direct simulation of bubble formation process using CFD technology was reported by Hong et al. [46] who numerically simulated the formation of a single bubble chain in stagnant liquid by tracking the movement of the gas-liquid interface using the VOF (Volume of Fluid) method [47].

Only a few works [48-50] were reported on bubble formation in flowing liquid condition. In these models, the analytical spherical bubble models of bubble formation in stagnant liquid are modified to accommodate the uniform liquid flow condition by including an additional drag force due to the flowing liquid in the equation of motion. More empirical parameters are introduced in order to match the experimental results, limiting the extension of these models to different conditions.

None of these previous models can be directly applied to the current case -- bubble formation in tundish nozzles, in which the gas is horizontally injected through the tiny holes on the inner wall of the nozzle into highly turbulent downward-flowing liquid.

2.3 Water Model Experiments

Water model experiments are performed to investigate the bubble formation in flow conditions that incorporate the essential phenomena in tundish nozzle flow. These include high velocity flow of liquid along the wall, which shears the growing bubbles. Direct image visualization and inspection are used to test the effects of liquid velocity, gas injection flow rate, gas injection hole size, and gas composition on the bubble size, shape, frequency, and size distribution. In addition to quantifying these important parameters, the results of these water experiments also serve to validate the theoretical model developed later.

2.3.1 Experimental Apparatus and Procedure

Figure 2.1 shows a schematic of the water experimental apparatus. Water flows down from an upper tank that simulates a tundish, through a vertical tube that simulates a tundish nozzle, to a tank at the bottom that simulates a casting mold. The gas (air, helium, or argon) is injected through a plastic tube attached to a hollow needle inserted horizontally into a square 35mm X 35mm Plexiglas tube. Water is made to flow vertically for conditions approximating those in a tundish nozzle. The needle outlet is flush with the nozzle wall to simulate a pierced hole on the inner wall of a nozzle. Three different-sized needles are used to examine the effect of the gas injection orifice diameter (0.2, 0.3, and 0.4 mm). The gas flow controller is adjusted to achieve volumetric gas flow rates of 0.17 ~ 6.0ml/s per orifice. Water flow rate is adjusted by partially blocking the bottom of the nozzle. The average water velocity varies from 0.6m/s to 3.1m/s which corresponds to the pipe Reynolds number of 21,000 ~ 109,000.

The water velocity is obtained by measuring the average velocity of the tracing particles that are purposely added to the water. The formation of bubbles is recorded by a high-speed video camera at 4500 frames per second. Each recorded test contains 1000 frame images accounting for 0.22 second measuring time. The head of liquid, defined as the vertical distance between the top surface of the liquid in the upper tank to the needle, is about 500mm and drops less than 20mm during video taping, owing to the short measurement time. The behavior of bubbles exiting the needle is studied by inspecting the video images frame by frame. The frequency (f) of bubble formation is determined by counting the number of the bubbles generated at the exit of the injection needle during the recorded time period. The mean bubble volume (V_b) is easily converted from the known gas injection volumetric flow rate (Q_g), via

$$V_b = \frac{Q_g}{f} \tag{2.1}$$

An equivalent average bubble diameter is calculated assuming a spherical bubble, or

$$D_b = \left(\frac{6Q_g}{\pi f}\right)^{1/3} \tag{2.2}$$

Bubbles sizes are also measured directly from individual video image in order to validate this procedure and to check the bubble size deviation from its average value.

In some testing cases, a second needle is inserted into the nozzle wall 12.5mm downstream the first needle in order to study the interaction between bubbles from the adjacent gas injection sites.

2.3.2 Bubble Size in Stagnant Liquid

Experiments are first performed with stagnant water where previous measurements and models are available for comparison. This was accomplished simply by closing the opening at the bottom of the tube. Although most previous works are based on bubble formation from an upward facing orifice or nozzle, some authors [32, 36] observed that the bubble sizes from a horizontal orifice were almost the same as those from an upward facing orifice submerged in stagnant liquid. Figure 2.2 shows the measured bubble diameters together with a prediction using Iguchi's empirical correlation [34].

It can be seen that bubble sizes increase with increasing gas injection flow rate. For the same gas injection rate, a bigger injection orifice produces larger bubbles. At high gas injection rate, larger bubbles emerge from larger diameter orifices. However, orifice size becomes less important at small gas injection rate. The agreement between the experiment data and Iguchi's correlation prediction is reasonably good. This suggests that Iguchi's empirical correlation, which is based on relatively large gas injection flow rates and vertical injection, also applies to the horizontal injection and relatively lower gas flow rates of this work.

2.3.3 Bubble Size in Flowing Liquid

Experiments are next performed with gas injection into flowing water. The measured mean bubble sizes are plotted in Figure 2.3. Each point in Figure 2.3 represents the mean bubble diameter for one test case with a particular gas injection flow rate, water velocity and gas injection hole size. In addition, the maximum and minimum bubble sizes, obtained by directly measuring the video images for the corresponding case, are shown as "error bars" for each point. Also shown on the figure is the symbol (circle, triangle or square) representing the corresponding mode that will be discussed later in this section.

Figure 2.3 shows that the mean bubble size increases with increasing gas flow rate and decreasing water velocity. Comparing Figures 2.2 and 2.3, it can be seen that at the same gas injection rate, the bubble size in flowing liquid is much smaller than in stagnant liquid. This becomes much clearer when the bubble volumes for stagnant liquid and flowing liquid are plotted together, as shown in Figure 2.4. Physically, the smaller bubble size in flowing liquid is natural because the drag force due to the shearing liquid flow acts to shear the bubbles away from the tip of the gas injection hole into the liquid stream before they grow to the mature sizes found in stagnant liquid. The higher the velocity of the shearing liquid flow, the smaller the detached bubbles are. The volumes of the bubbles formed in flowing water, in Figure 2.4, are about 5 ~ 8 times smaller in volume than those in stagnant water.

All of the experimental data shown in Figures 2.3 and 2.4 are collected for air. Argon and helium are also used in the experiments to investigate the effect of different gas composition. Figure 2.5 shows that the measured mean bubble diameters for three different gases (air, argon and helium) are about the same. Thus, the gas composition has little influence on bubble sizes.

It appears that bubble size is also relatively independent of gas injection hole size. This can be seen when the mean bubble diameters in Figure 2.3 are re-plotted for fixed water velocity, which is illustrated later as comparing with the model predictions in Figure 2.16. This observation is different from that in stagnant liquid, where bubble size is larger for larger gas injection hole. This suggests that the shearing force due to the flowing liquid dominates over other effects related to the hole size such as surface tension force.

Figures 2.2-2.5 show that data collected with increasing water velocity generally also has increasing gas flow. This choice of conditions was an unplanned consequence of the greater water flow inducing lower pressure at the orifice, with consequently higher gas flow rate. The higher-speed flowing liquid acts to aspirate more gas into the nozzle. This observation illustrates the important relationship between liquid pressure and gas flow rate that should be considered when investigating real systems.

2.3.4 Bubble Formation Mode

It is observed that the initial shape of the bubble exiting the gas injection hole falls into one of four distinct modes, as shown in the representative recorded images of Figure 2.6. Figure 2.7 shows the series of outlines of two typical cases illustrating the formation process of bubbles, corresponding to two different modes, based on tracing the recorded photo series shown in Figure 2.8.

For low velocity water flows (less than 1m/s) and small gas injection rates (less than 2ml/s), Mode I is observed. In this mode, uniform-sized spherical bubbles form at the tip of the gas injection hole. They elongate slightly before discretely detaching from the hole and joining the liquid stream, as spherical bubbles again seen in Figure 2.7 top. There is no interaction between the bubbles from the hole of the upper injection needle and the bubbles from the holes of the lower needle if it exists.

At the other extreme, Mode IV is observed for high velocity water flows (more than 1.6m/s) and very large gas injection rates (more than 10ml/s). In this mode, each bubble elongates down along the wall, forming a gas curtain, and the curtain merges with the gas from the lower needle, if it exists, to form a long continuous gas curtain. The curtain eventually becomes unstable when its thickness becomes too great and it breaks up into many different size bubbles. Their size ranges from a few that are very large to others that are very tiny. For the range of gas flow of practical interest, this regime is not expected.

Mode III is observed for high water flow conditions flows (more than 1.6m/s) and for practical gas injection flow range (less than 6ml/s). Mode III is similar to Mode IV except that there is insufficient gas flow to maintain a continuous gas curtain, so gaps form. Before detaching from the gas injection hole, Figure 2.7 (bottom) documents that the bubbles elongate about 2 times. The bubbles then elongate even more down along the wall and stay attached on the wall for some distance after disconnecting from the gas injection hole.

Mode II is a transitional mode between Modes I and III in which the injected gas is elongated along the wall but soon detaches from the wall. If a second gas injection hole exists, the bubbles from the upper hole in Mode II will not coalesce with the bubbles from the lower needle. Bubbles sizes in Mode II are still relatively uniform compared to those in Modes III and IV.

In addition to the mean bubble size measured, Figure 2.3 also shows the mode and the bubble size deviation from the mean value, using error bars to represent the size range for each experimental case. All data under 0.9m/s water velocity fall into Mode I and have very small size range, which corresponds to the relatively uniform spherical bubbles detaching near the tip of the hole. This is similar to observation in stagnant liquid. Most data under 1.4m/s water velocity fall into Mode II and have slightly larger size range. For the cases of liquid velocity at 1.9m/s and 2.5m/s, all of the data fall into Mode III and have huge size range, which corresponds to the discontinuous gas curtain broken up into uneven-sized bubbles. The bubble size is as small as 0.5mm in diameter. The continuous gas curtain in Mode IV is observed only at very high gas injection flow rate (Q_g > 10 ml/s per hole), which is beyond the practical range of interest, so is not shown in the plots.

For Mode III cases, no continuous gas curtain along the wall was observed for those experiments with single needle gas injection. However, those elongated bubbles, after disconnecting from the gas injection hole, still attach and travel along the wall for a certain distance before they finally detach the wall and join the liquid stream, as seen in Figure 2.6 and

Figure 2.7 (Bottom). If they meet injected gas from the lower downstream hole before detaching the wall, the two bubble streams coalesce to form larger elongated bubbles. In a real-life tundish nozzle with hundreds of pierced holes or thousands of tiny pores on porous refractory, a continuous gas curtain might be expected on the gas injection section of the inner wall of the nozzle for Mode III. In fact, the argon gas injected into the liquid steel has much bigger tendency to fall into Mode III and to form a gas curtain on the refractory wall due to the much larger surface tension of the liquid steel and the non-wetting behavior of the liquid steel on the refractory material. The experiments also show that no matter what bubble formation mode, the injected gas will eventually detach from the wall, break up into discrete bubbles and join the liquid stream. Therefore, there will be no gas curtain in the tundish nozzle after a certain distance from the gas injection section.

It is found that when plotting each experimental data point with the ratio of gas flow rate to mean liquid velocity (Q_g/U) as y axis and the gas injection flow rate (Q_g) as x axis, the different bubble formation modes fall into separate regions, as shown in Figure 2.9.

2.3.5 Bubble Elongation Measurement

Bubble shape is observed to grow and elongate during the formation process. To quantify the effects of the gas flow rate and liquid velocity on bubble elongation, the vertical elongation length (L) is measured at the instant of the detachment of the bubble from its injection hole, as shown in Figure 2.10(A). The measured bubble elongation lengths (L) are plotted in Figure 2.10(B). The effects become clear when plotting the elongation factor, e_d, defined as the ratio of the elongation length (L) and the equivalent diameter of the bubble (D_b)

$$e_d = \frac{L}{D_b} \tag{2.3}$$

As shown in Figure 2.11(A), the elongation factor mainly depends on liquid velocity, and is relatively independent of the gas injection flow rate. Bubbles elongate slightly more at higher liquid velocity. Figure 2.11(B) illustrates this effect of liquid velocity on the measured average elongation factors. These four data points are well fitted with a simple quadratic function,

$$e_d = 0.78592 + 0.70797U - 0.12793U^2 \tag{2.4}$$

which can be used to estimate the elongation factor at arbitrary liquid velocity rather than those test velocities.

2.3.6 Contact Angle Measurement

Contact angles are measured for the purpose of evaluating the surface tension force, which is used later in the model to predict bubble size. The relation between the contact angles and surface tension force are detailed in Appendix A.

The static contact angle is defined by the profile adopted by a liquid drop resting in equilibrium on a flat horizontal surface, and was measured to be 50° for the current water experiment. The transverse flowing liquid makes the contact angles no longer uniform along the bubble-solid contact circumference. At the upstream of the bubble, the contact angle increases to θ_a, defined as the advancing contact angle, and at the downstream of the bubble, the contact angle decreases to θ_r, defined as the receding contact angle, shown in Figures 2.12 (A).

Table 2.1 shows the measured mean contact angles in the water experiments. Generally speaking, the advancing contact angle θ_a increases with increasing liquid velocity, and the receding contact angle θ_r decreases with increasing liquid velocity. The effect of gas flow rate is relatively small. Contact angle function, f_θ, defined as

$$f_\theta = \sin\theta_o\left(\cos\theta_r - \cos\theta_a\right) \tag{2.5}$$

contains all contact angle terms in the surface tension force equation (Equation A.11),

In liquid steel-argon system, the surface tension force might have more influence on bubble formation behavior due to significant increase in surface tension coefficient. Unfortunately, except for the static contact angle, which is much larger for steel-argon system (θ_O =150°) [54] than for water-air system (θ_O =50°), the advancing and receding contact angles needed in Equation 2.5 are unknown due to lacking experimental data. Estimations on advancing and receding contact angles can be made for elongated argon bubbles in flowing steel, based on the observation in the air-water system. The advancing contact angle θ_a should be larger than the static contact angle θ_O (150°) and increases with increasing liquid velocity, but it can not be larger than 180°. The receding contact angle θ_r should be smaller than the static contact angle and decreases with increasing liquid velocity. It is found from the estimations that the contact angle function f_θ might have close values for the steel-argon and water-air systems even though all three contact angles (θ_O, θ_a and θ_r) are very different between the two systems. For example, if θ_a =155°(>θ_O =150°) and θ_r =124°(>θ_O =150°) , the contact angle function for the steel-argon system will have the same value (f_θ *=0.30)* as for the water-air system at liquid velocity U=0.9m/s.

The contact angle function f_θ increases with increasing liquid velocity, as shown in Figure 2.12(B). The four data points are well fitted with a simple quadratic function,

$$f_\theta(U) = -0.06079 + 0.33109U + 0.078773U^2 \tag{2.6}$$

Equation 2.6 can be used to estimate the value of the contact angle function at the liquid velocity rather than those tests.

2.4 Mathematical Model to Predict Bubble Size

Bubble formation in vertical flowing liquid is very different from the classic bubble formation problem in which the bubble forms at the end of an upward facing orifice or tube submerged in stagnant liquid. In continuous casting process, argon gas is injected into the nozzle horizontally through tiny holes on the inner wall of the nozzle. The injected gas encounters liquid steel flowing downward across its path. The downward shearing liquid flow of interest to nozzle injection is highly turbulent, with a Reynolds number of about 100,000. This turbulent flow exerts a strong shear force on the forming bubble, which greatly affects its formation. Unlike bubble formation in stagnant liquid, in which buoyancy force is the major driving force for bubble detachment, the buoyancy force now acts to resist the premature detachment of the bubble against the drag force of liquid momentum. Thus, previous bubble models can not be directly applied. In developing an analytical model in this work for nozzle injection, the basic ideas from the classic spherical bubble models in stagnant liquid are followed, which are based on balancing the forces acting on the growing bubble and setting a proper bubble detachment criteria.

2.4.1 Forces Acting on a Growing Bubble

Correct evaluation of the fundamental forces acting on the growing bubble is essential for an accurate analytical model of bubble formation that can be extrapolated to other systems. A schematic of the fundamental forces acting on a growing bubble is shown in Figure 2.13. The forces of liquid drag, buoyancy, and surface tension are now discussed in turn.

Drag force due to flowing liquid F_D

The drag force exerted by the flowing liquid onto the growing bubble, F_D, depends on the liquid velocity. The mean liquid velocity (U) in the nozzle is assumed to be known. Since the growth and detachment of the bubble all occur near the wall and the shearing effect of the flowing liquid creates small bubbles, the steep velocity gradient encountered by the forming bubble are very important. This liquid velocity profile at the wall is needed for accurate evaluation of the drag force. Of the many formulas for velocity profile of a fully developed turbulent flow in a pipe, the most convenient for the current purpose is the seventh root law profile [52]

$$u = 1.235U\left(\frac{y}{D_N / 2}\right)^{1/7} \tag{2.7}$$

where y is the distance from the wall, D_N is the nozzle diameter, and U is the mean vertical liquid velocity in the nozzle. The average liquid velocity across the growing bubble, $\bar{u}$, depends on the instantaneous bubble size and is estimated from

$$\bar{u} = \frac{1}{2r}\int_{y=0}^{y=2r} u\,dy = 1.3173U\frac{r^{1/7}}{D_N^{1/7}} \tag{2.8}$$

where r is the equivalent horizontal radius of the forming bubble. The drag force acting on the growing bubble, F_D, is

$$F_D = C_D \frac{1}{2}\rho_l \bar{u}^2 \pi r^2 \tag{2.9}$$

Assuming the bubble Reynolds number, Re_{bub}, is less than 3×10^5, the drag coefficient C_D is[37]

$$C_D = \frac{24}{\mathrm{Re}_{bub}}(1 + 0.15\,\mathrm{Re}_{bub}{}^{0.687}) + 0.42 / (1 + 4.25\times10^4\,\mathrm{Re}_{bub}^{-1.16}) \tag{2.10}$$

where Re_{bub} is defined by

$$\mathrm{Re}_{bub} = \frac{\bar{u}D}{\upsilon} \tag{2.11}$$

where D is the equivalent bubble diameter and υ is the kinematic viscosity of the liquid.

Buoyancy force F_B

Buoyancy force acts upward and resists the drag force due to the liquid momentum.

$$F_B = V_b(\rho_l - \rho_g)g = \frac{1}{6}\pi D^3(\rho_l - \rho_g)g \tag{2.12}$$

Surface tension force F_S

Surface tension force acts to keep the bubble attached to the wall. The vertical component acts upward to resist drag of the bubble that elongates its shape below the gas injection hole, and is given by [53].

$$F_{Sz} = \frac{\pi}{4} D\sigma \sin\theta_O(\cos\theta_r - \cos\theta_a) \tag{2.13}$$

where σ is the surface tension coefficient. Derivation of Equation 2.13 is detailed in Appendix A. The values for θ_O, θ_r and θ_a were measured from the video.

Figure 2.14 shows how those three fundamental forces change with the bubble size. Other forces, such as the inertial force due to the rate of change of momentum of the growing bubble, are believed to be negligible.

2.4.2 Two-Stage Model for Bubble Formation in Flowing Liquid

A two-stage model is developed to predict the size of the bubbles formed during nozzle injection. The bubble formation is assumed take place in two idealized stages, the expansion stage and the elongation stage, as shown in Figure 2.15.

Expansion stage

During the expansion stage, the forming bubble expands while holding onto the tip of the gas injection. This stage is assumed to end when the downward forces are first able to balance the upward force. That is,

$$F_D = F_B + F_{Sz} \tag{2.14}$$

The shape of the bubble during this stage is not considered until at the instant of the force balance when it is assumed to be spherical. Substituting Equations 2.9, 2.12 and 2.13 into Equation 2.14 yields

$$C_D \frac{1}{2}\rho_l \bar{u}^2 \pi r^2 = \frac{4}{3}\pi r^3(\rho_l - \rho_g)g + \frac{1}{2}\pi r\sigma \sin\theta_O(\cos\theta_r - \cos\theta_a) \tag{2.15}$$

In Equation 2.15, $\bar{u}$ depends on *r*, which is unknown in advance. Thus, Equation 2.15 is solved for *r* by trial and error to yield r_e, which is the equivalent radius of the bubble at the end of the expansion stage.

Elongation stage

As the bubble continues to grow, the downward force exceeds the upward forces on the bubble. This makes the growing bubble begin to move downward along with the liquid flow. The bubble keeps expanding since it still connects to the gas injection hole, and at the same time it gets elongated due to the shearing effect of the liquid flow.

The shape of the bubble in the elongation stage is idealized as ellipsoidal. The connection to the injection hole is assumed through a thin neck, thus the volume in the neck can be neglected. The two horizontal radii of the ellipsoid (r_x and r_y) are assumed to be the same to simplify the problem, that is,

$$r_x = r_y = r \tag{2.16}$$

and the vertical radius of the ellipsoid (r_z) accounts for the effect of the bubble elongation and is related to the equivalent bubble diameter (D) and the elongation factor (e) by

$$r_z = \frac{1}{2} eD \tag{2.17}$$

The elongation factor should match the measurement defined in Equation 2.3 at the instant of the bubble detachment from its gas injection hole, or

$$r_{zd} = \frac{1}{2} L = \frac{1}{2} e_d D_b \tag{2.18}$$

where r_{zd} is the vertical radius of the ellipsoid bubble at the instant of the detachment.

The instantaneous equivalent diameter (D) of the bubble is related to the instantaneous horizontal radius (r) of the ellipsoid and the instantaneous elongation factor (e) by

$$\frac{1}{6}\pi D^3 = \frac{4}{3}\pi\, r^2 r_z = \frac{4}{3}\pi\, r^2 \left(\frac{1}{2} e\, D\right) \qquad \text{or}$$

$$D = 2r\sqrt{e} \tag{2.19}$$

The bubble gets more elongated as it grows bigger. The bottom of the ellipsoidal bubble is assumed to travel along with the liquid at the average velocity $\bar{u}$, defined in Equation 2.8. Criterion to end this final stage of bubble growth is the detachment of the bubble from the gas injection hole when the bubble elongates to the measured elongation at detachment. This corresponds to the time when the vertical distance traveled by the fluid, from point A to B, equals the critical length at the instant of bubble detachment, as shown in Figure 2.15(B).

$$\int_{t_e}^{t_d} \bar{u}\, dt = e_d D_b + \frac{d}{2} - r_e \tag{2.20}$$

Substituting Equation 2.19 into Equation 2.20 yields

$$\int_{t_e}^{t_d} \bar{u}\, dt = 2 r_d e_d^{3/2} + \frac{d}{2} - r_e \tag{2.21}$$

where t_e and t_d are the bubble growing times at the end of the expansion stage and the instant of bubble detachment respectively. r_d is the horizontal radius at the detachment. The bubble growing time (t) is related to the instantaneous horizontal radius of the growing ellipsoidal bubble (r) by volume conservation, which assumes that pressure and temperature are sufficient uniform to avoid compressibility effects.

$$Q_g t = \frac{1}{6}\pi D^3 \tag{2.22}$$

Substituting Equation 2.19 into Equation 2.22 yields

$$t = \frac{4\pi}{3Q_g} r^3 e^{3/2} \tag{2.23}$$

Also knowing

$$e = \begin{cases} 1 & at \quad r = r_e \\ e_d & at \quad r = r_d \end{cases} \tag{2.24}$$

the elongation factor at can be approximated by a linear function

$$e = ar + b \qquad\qquad at \quad r_e < r < r_d \tag{2.25}$$

The values of the constant a and b can be derived by satisfying the conditions in Equation 2.24:

$$a = \frac{e_d - 1}{r_d - r_e} \tag{2.26}$$

$$b = \frac{r_d - e_d r_e}{r_d - r_e} \tag{2.27}$$

From Equation 2.23 and Equation 2.25,

$$dt = d\left(\frac{4\pi}{3Q_g} r^3 e^{3/2}\right) = \frac{4\pi}{Q_g}\left(r^2 (ar+b)^{3/2} + \frac{ar^3}{2}(ar+b)^{1/2}\right)dr \tag{2.28}$$

Substituting Equation 2.8 and Equation 2.28 into Equation 2.21 yields

$$5.2692\frac{\pi U}{Q_g D_N^{1/7}}\int_{r_e}^{r_d}\left(r^{2\frac{1}{7}}(ar+b)^{\frac{3}{2}} + \frac{ar^{3\frac{1}{7}}}{2}(ar+b)^{1/2}\right)dr = 2r_d e_d^{3/2} + \frac{d}{2} - r_e \tag{2.29}$$

It should be noted that there are no adjustable parameters in this model. The elongation factor at the instant of the bubble detachment (e_d) and the contact angle function (f_θ) depend on the mean liquid velocity (U), and are obtained from the experimental measurements, shown in Figures 2.11 and 2.12. To extend the model for the arbitrary liquid velocity beyond the test, the extrapolated quadratic function, Equations 2.4 and 2.6, are used in the model.

Equation 2.29 are solved iteratively by trial and error for the horizontal radius of the ellipsoidal bubble at the instant of detachment from the gas injection hole, r_d, which is the only unknown in this equation, using a program written in MATLAB detailed in Appendix B. The equivalent bubble diameter is then converted from Equation 2.19 to

$$D_b = 2r_d\sqrt{e_d} \tag{2.30}$$

2.4.3 Comparing with Measurements

The bubble diameters predicted by the two-stage model are shown in Figure 2.16, along with the measured mean bubble diameters. The physical properties of the fluids and operating conditions used in calculation are summarized in Table 2.2

Figure 2.16 shows that the match between the model prediction and the experimental data is reasonably good, although the predicted slopes (dD/dQ_g) appear to be slightly smaller than experimental results. This means the model may slightly over-predict the bubble size for the low gas injection flow rates and under-predict the bubble size for the high gas flow rates. Figure 2.16 shows the same trends of the effects of the liquid velocity and gas flow rate on bubble sizes as observed during the experiments, that is, the mean bubble size increases with increasing gas injection flow rate and decreasing shearing liquid velocity.

Figure 2.16 shows that the gas injection hole size rarely affects the bubble size at high liquid velocity ($U \geq 1.4$m/s). This agrees with the water experiments that could hardly tell the difference for the data measured from different hole sizes. However, at relatively low liquid velocity, as shown in the plot for U=0.9m/s in Figure 2.16, the influence of the hole size becomes slightly obvious, and the larger gas injection hole generates slightly larger bubbles. This match the trends observed in the experiments for the stagnant liquid condition, which showed an important effect of gas injection hole size on bubble size.

The two-stage model also predicts a negligible effect of the gas density that again matches the experimental measurements. The gas density appears only in the buoyancy term in the force balance Equation 2.15 in the form of $(\rho_l$-$\rho_g)$, which is easy to see being negligible compared with the liquid velocity.

There still exist some discrepancies between the predictions and measurements, as shown in Figure 2.15. Random errors found in the experiments are likely one of the main sources. The experiments were performed at highly turbulent flow conditions (experimental Reynolds numbers range from 21,000 to 109,000), which is transient and random in nature. The recorded 1000 frame images for each case are for the period of only 0.22 second, which is not long enough to make a good time average.

2.5. Argon Bubble Sizes in Liquid Steel

2.5.1 Difference between Steel-Argon and Water-Air Systems

In order to use the two-stage model developed above and validated for a water-air system to predict the bubble size in the liquid steel-argon system in tundish nozzles, it is important to understand the difference between the two systems. As seen in Table 2.2, there is big difference in physical properties between the steel-argon system and water-air system. For example, the surface tension coefficient for the liquid steel-argon system is more than 16 times of that of the water-air system. The density of the liquid steel is 7 times of the water density. The effects of these physical properties on bubble formation are incorporated in the two–stage model.

Except for the static contact angle, which is much larger for steel-argon system than for water-air system [54], the advancing and receding contact angles needed in Equation 2.15 are unknown for the liquid steel-argon system due to lacking experimental data. As discussed in Section 2.3.6, the contact angle function f_θ $(=sin\theta_o(cos\theta_r-cos\theta_a))$ from the water experiment might be close to the steel-argon system, thus adopted in calculation, as shown in Table 2.2.

Measurements [34] and calculation (Appendix C) show that gas injected through the "hot" ceramic wall heats up to 99% of the liquid steel temperature even before it hits the liquid steel. Thus, the argon gas injection flow rate used in the model is the "hot" argon flow rate.

2.5.2 Predicting Bubble Size in Tundish Nozzles

The two-stage model is used to predict argon bubble sizes in liquid steel in a typical tundish nozzle with 78mm bore diameter. Air bubble sizes in water is also predicted for the same conditions, as shown in the rightmost column of Table 2.2, for direct comparison. The predictions are presented in Figure 2.17, showing the predicted bubble diameter vs. gas injection flow rate under different liquid velocities. The argon bubble size increases with increasing gas flow rate and decreasing liquid velocity, same trends as the air bubble size in water. In general, argon bubbles generated in liquid steel are predicted to be larger than air bubbles in water. The difference becomes more significant at lower liquid velocity and smaller gas flow rate. For the practical interested range of the liquid velocity in tundish nozzles (0.7~1.2m/s), the difference in bubble size between the two systems is sometimes significant. For example, a typical tundish nozzle with 140 holes and 7 SLPM argon injection on UTN has 3.5 ml/s hot argon flow rate for each hole. At the mean liquid velocity of 0.7m/s, the diameters of the argon bubbles in liquid steel are about 1.5 times of those air bubbles in water, and the corresponding volumes of the argon bubbles are 3.4 times of those of air bubbles.

The reason for larger bubbles predicted in the steel-argon system is mainly due to the great difference in liquid density and surface tension coefficient in steel-argon system. This make the drag force and surface tension force acting on the forming argon bubbles in liquid steel much larger than those forces on the forming air bubble in water, under the same flow conditions. Since the increase in surface tension force is more than two times of the increase in drag force, the force balance of Equation 2.15 will be satisfied at a larger bubble size r_e at the end of the expansion stage when compared to the water-air system. At very high liquid velocity, the drag force due to the flowing liquid become so dominant that increase in surface tension force becomes less important to the bubble formation behavior and thus the difference in bubble sizes become smaller for the two systems.

Figure 2.18 plots the predicted bubble size for varying liquid velocity at a few fixed gas flow rates for both systems. The two-stage model could not handle the very low liquid velocity conditions. The program in Appendix B blowups at U<0.5m/s for water-air system and U<0.7m/s for steel-argon system. Physically, this is because that at very low velocity downward liquid flow, the downward drag force might not be able to balance the upward buoyancy force and surface tension force. The bubble might go upward. The model need modification to deal with the upward moving situation, in which the advancing contact angle and receding contact angle switch positions and the surface tension force change its direction. The steel-argon system blowups at higher liquid velocity due to its much higher surface tension than water-air system.

Since the ratio of the liquid and gas density for steel-argon system ($\rho_l/\rho_g = 10^4$) is one order higher than for water-air system ($\rho_l/\rho_g = 10^3$), gas density should have no effect on argon bubble size in liquid steel for the same reason as in water-air system. The effect of the gas injection hole on argon bubble size is similar like air bubbles in water, although it is not plotted here.

2.5.3 Discussion

The elongation factor and contact angle function f_θ obtained from the water model experiment, are directly employed for the tundish nozzle conditions due to lacking the experimental data for liquid steel-argon system. The mean argon bubble size in liquid steel predicted with the two-stage model is conservative or under-predicted due to the difference in wettability. The non-wetting property of liquid metal on ceramics nozzle wall, in contrast to the aqueous wetting system, makes the forming bubble tend to spread more over the wall, which has been observed by other authors [32, 34, 35]. The spreading bubble might have a larger elongation factor in this system. This will likely result in an under-predicted bubble size.

On the other hand, the tendency for argon bubbles to spread over the ceramics nozzle wall makes the bubble formation mode fall into Mode II or III region at lower liquid velocity than water-air system. Therefore, the argon bubbles should have larger tendency to have uneven sizes when detaching from the wall.

The two-stage model predicts only the average bubble size, but not other important gas bubble behavior such as bubble formation mode, bubble shape, bubble size deviation, bubble coalescence and break-up. Direct numerical simulation of bubble formation process by tracking the movement of the gas-liquid interface is a potential method to overcome these limitations. Simulation of a single bubble chain in stagnant liquid using the VOF method has been reported [46] to agree well with the experimental results in a real time sequence. However, numerical simulation of argon bubble formation in a tundish nozzle condition is still a challenge, likely due to the complex effects of turbulence, boundary layer, surface tension and wettability.

2.6 Summary

Water experiments are performed to study bubble formation from a horizontal oriented hole facing a shearing downward turbulent liquid flow, approximating conditions in a tundish nozzle. The effects of various parameters such as liquid velocity, gas injection flow rate, hole diameter, and gas density on bubble formation behavior such as bubble size, injected gas mode have been investigated. An analytical two-stage model based on force balance and bubble formation sequence is developed to predict the bubble size at detachment from it gas injection hole. Model predictions show good agreement with the measurements. The model is then used to predict the size of the argon bubbles generated in liquid steel of a tundish nozzle. Specific findings include:

- The mean bubble size increases with increasing gas injection flow rate.
- The mean bubble size increases with decreasing shearing liquid velocity.
- The mean bubble size in flowing liquid is significantly smaller than in stagnant liquid.
- The mean bubble size is relatively independent of gas injection hole size, especially at high liquid velocity
- The gas composition has little influence on bubble size.
- Bubble formation falls into one of the four different modes, depending primarily on the velocity of the flowing liquid and secondarily on the gas flow rate.
- In Mode I (low liquid speed and small gas flow rate), uniform-sized bubbles form and detach from the wall. In Mode III (high liquid speed), the injected gas elongates down along the wall and breaks into uneven sized bubbles. Mode II is intermediate between

Mode I and Mode III. In Mode IV (high liquid speed and high gas flow rate), the gas elongates a long distance down the nozzle walls, forming a sheet before breaking up.

- Compared to water-air system, argon bubbles in liquid steel should tend to spread more over the ceramic nozzle wall in liquid steel and fall into Mode II or III region. Thus, the argon bubbles likely have a larger tendency to have non-uniform sizes when detaching from the wall.
- Argon bubbles generated in liquid steel should be larger than air bubbles in water for the same flow conditions. The difference should become more significant at lower liquid velocity and smaller gas injection flow rate.

Table 2.1 Average contact angles measured in the water experiments

Average liquid velocity (m/s)	Static contact angle θ_O (°)	Advancing contact angle θ_a (°)	Receding contact angle θ_r (°)	Contact angle function $f_\theta = sin\theta_O(cos\theta_r - cos\theta_a)$
0.9	50	64	35	0.30
1.4	50	82	29	0.56
1.9	50	101	22	0.85
2.5	50	134	27	1.26

Table 2.2 Physical properties and operating conditions used in the two-stage model

Parameters	Symbol	Unit	Water-Air System for matching measurements	Steel-Argon System	Water-Air System for comparison
Liquid density	ρ_l	Kg/m^3	water: 1000	liquid steel: 7021	water: 1000
Gas density	ρ_g	Kg/m^3	air: 1.29	hot argon: 0.27	air: 1.29
Liquid viscosity	μ_l	kg/(ms)	water: 0.001	liquid steel: 0.0056	water: 0.001
Gas viscosity	μ_g	kg/(ms)	air: 1.7E-5	hot argon: 7.42E-5	air: 1.7E-5
Surface tension coefficient	σ	N/m	0.073	1.192	0.073
Gas injection flow rate/pore	Q_g	ml/s	air: 0.1 ~ 6 ml/s	hot argon: 0.1 ~ 6 ml/s	air: 0.1 ~ 6 ml/s
Nozzle diameter	D_n	mm	35	78	78
Diameter of gas injection hole	d	mm	0.2, 0.3, 0.4	0.2, 0.3, 0.4	0.2, 0.3, 0.4
Average velocity of the liquid	U	m/s	0.9, 1.4, 1.9, 2.5	0.7, 0.9, 1.4 1.9, 2.5	0.7, 0.9, 1.4 1.9, 2.5
Elongation factor at detachment	e_d		1.32, 1.53, 1.67, 1.76	$e_d(U) = 0.78592 + 0.70797U - 0.12793U^2$	
Contact angle function $sin\theta_o(cos\theta_r - cos\theta_a)$	f_θ		0.30, 0.56 0.85, 1.26	$f_\theta(U) = -0.06079 + 0.33109U + 0.078773U^2$	

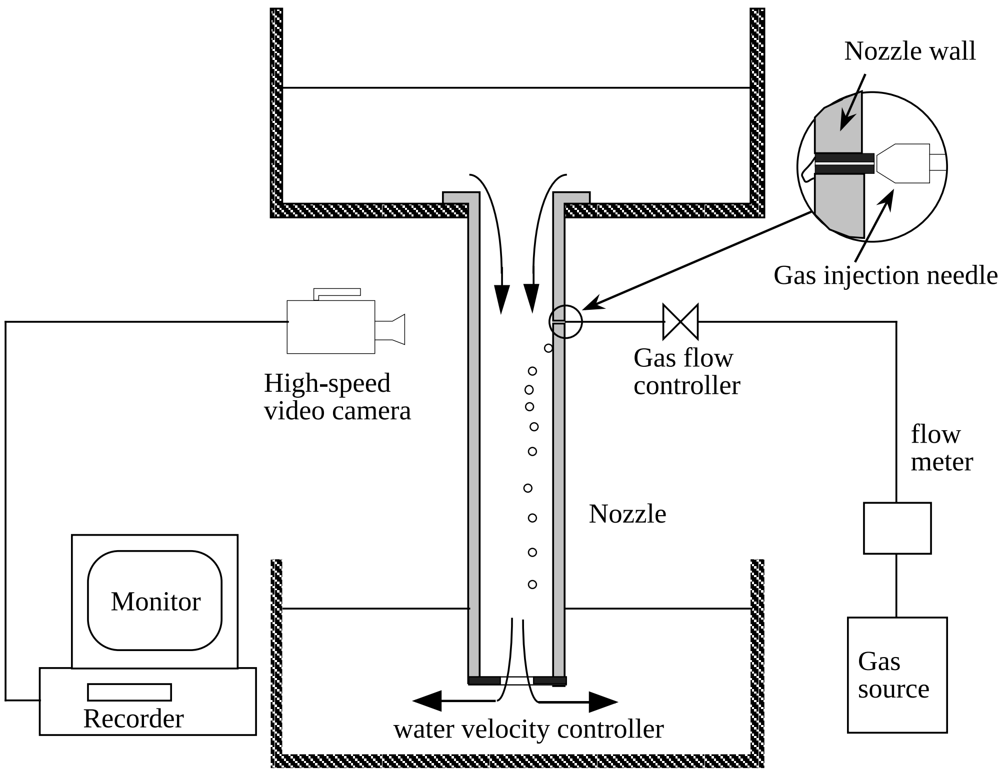

Figure 2.1 Schematic of water experiment for bubble formation study

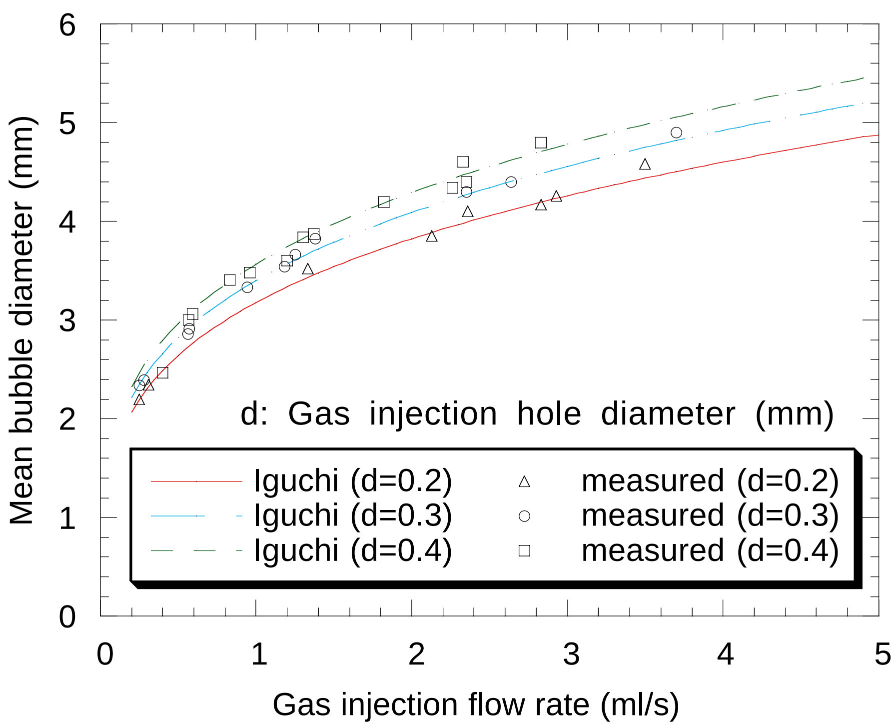

Figure 2.2 Measured air bubble sizes in stagnant water and prediction from Iguchi's empirical correlation [34]

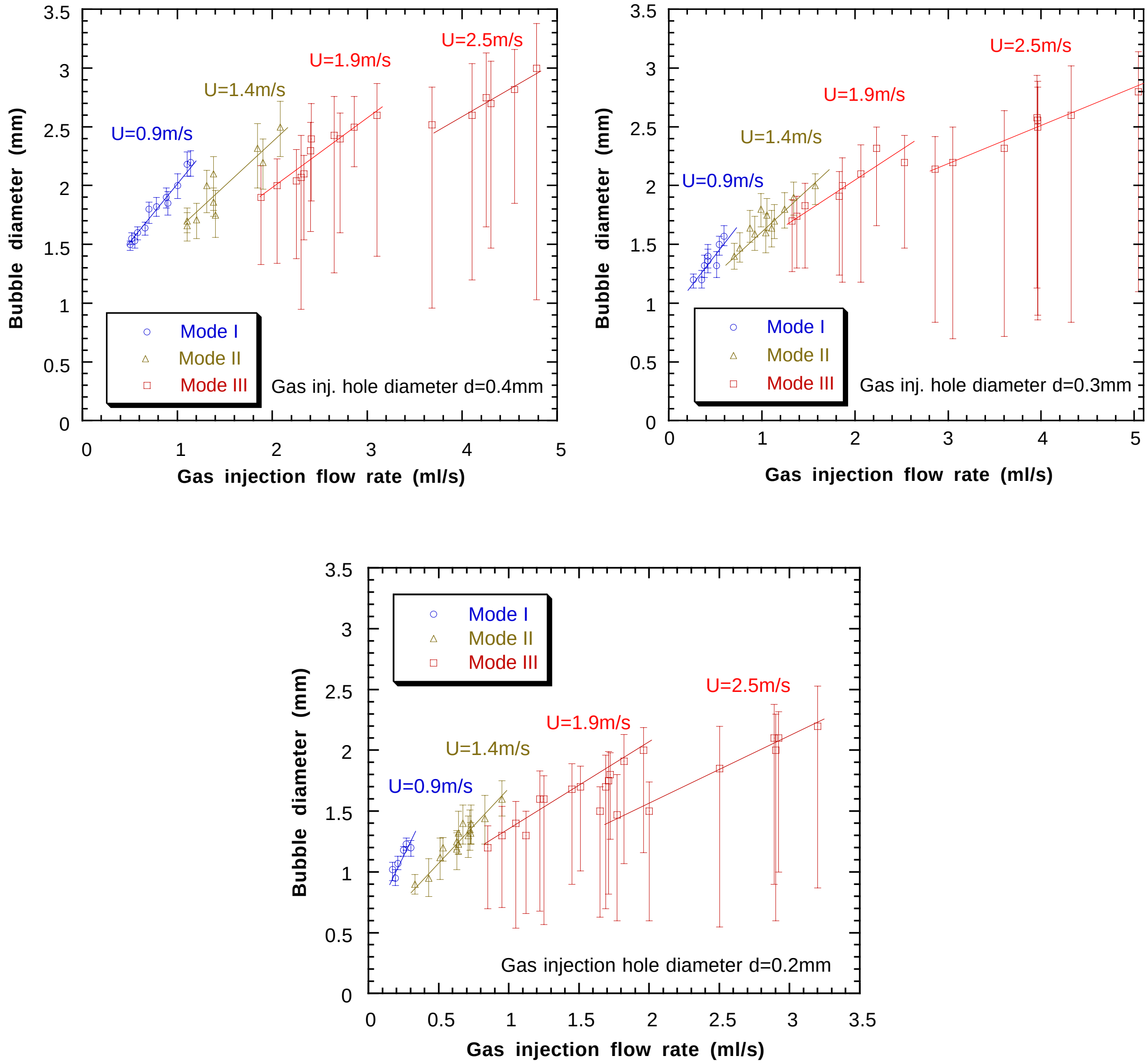

Figure 2.3 Measured air bubble sizes under different gas injection flow rate and water velocity and the effect of the modes to bubble size deviation to their mean values

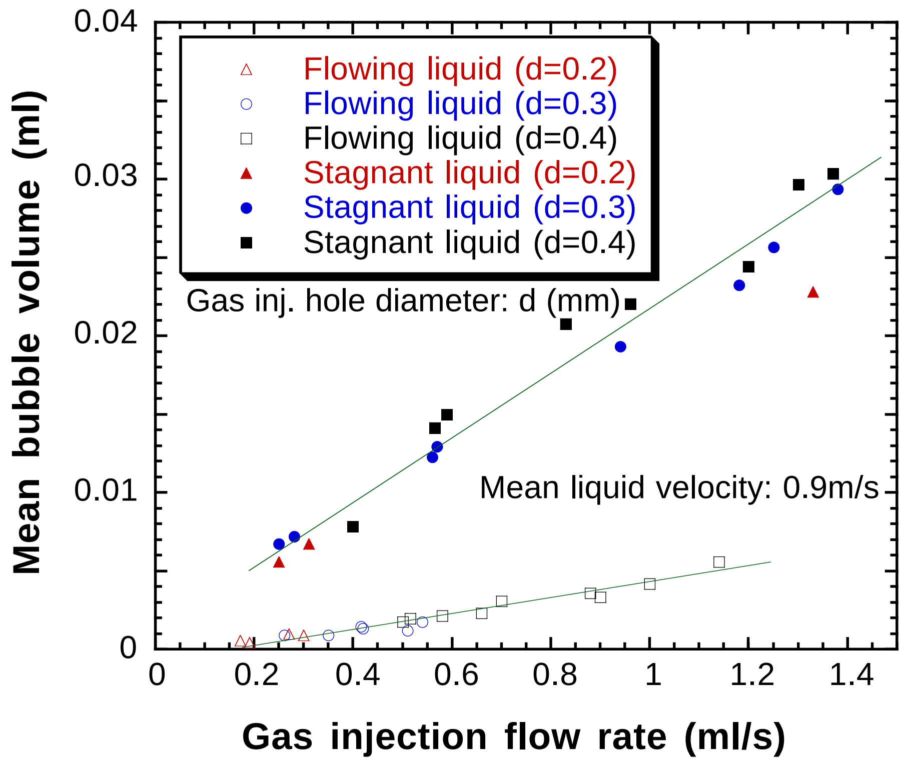

Figure 2.4 Comparison of air bubble volumes in stagnant liquid and flowing liquid

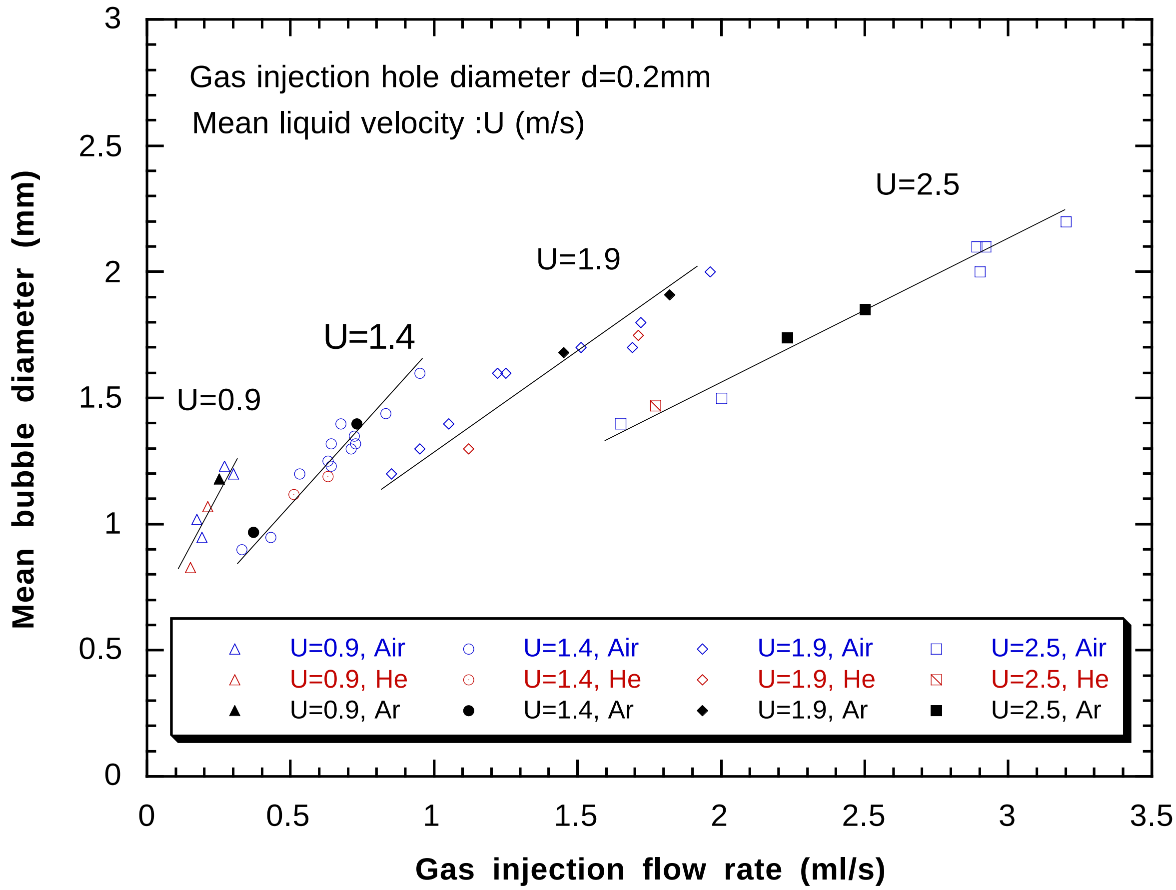

Figure 2.5 Effect of gas composition, gas flow rate and liquid velocity on bubble size

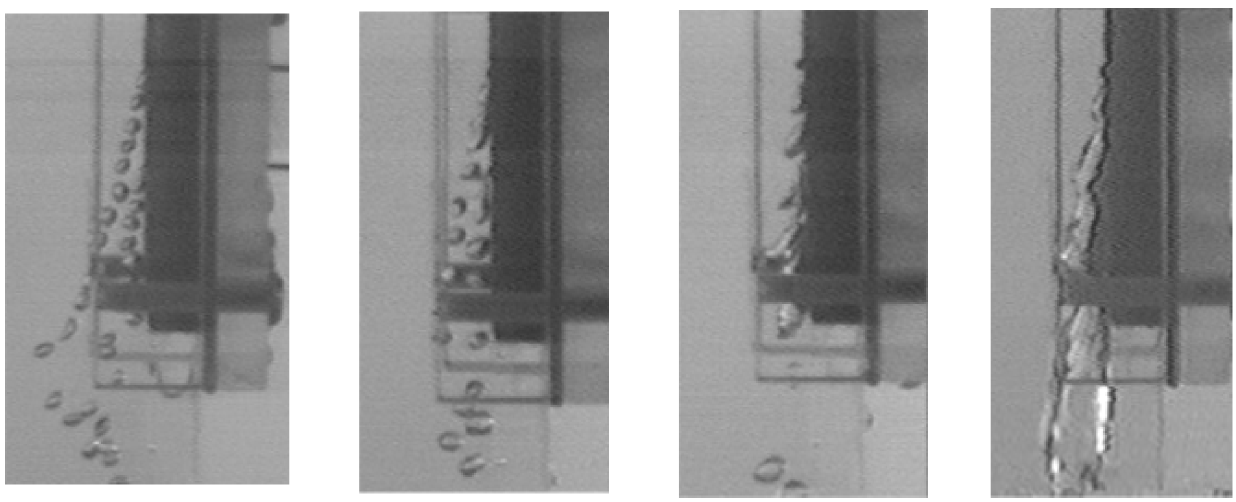

Mode I Mode II Mode III Mode IV

Figure 2.6 Photograph of the four bubble formation modes observed in the experiments

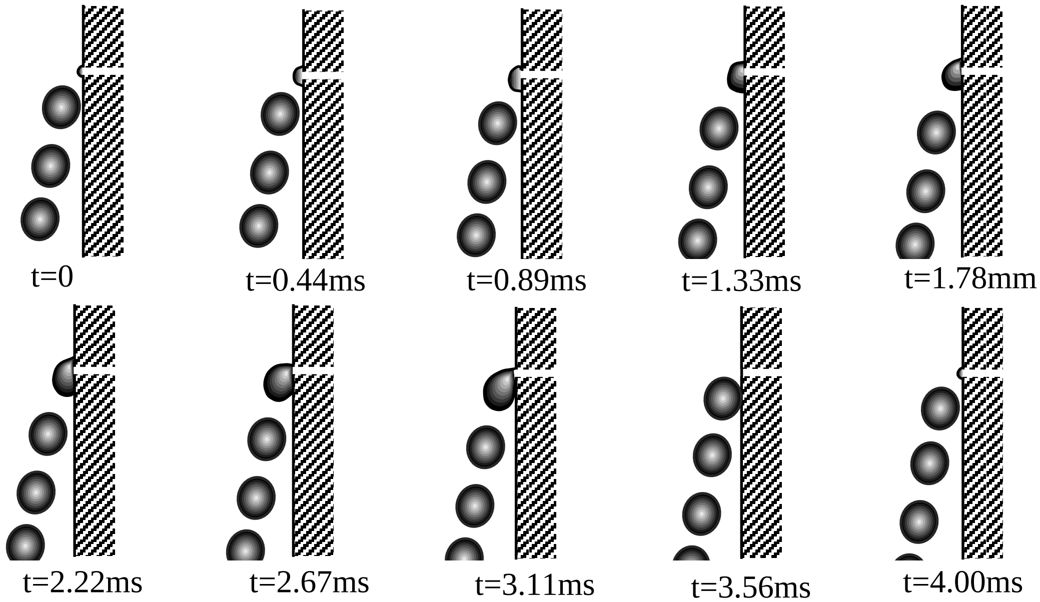

Mode I (U=0.9m/s, Q_G=0.5ml/s, d=0.4mm), Bubble frequency f=293s^{-1}
Equivalent bubble diameter: measured: 1.51mm, predicted: 1.53mm

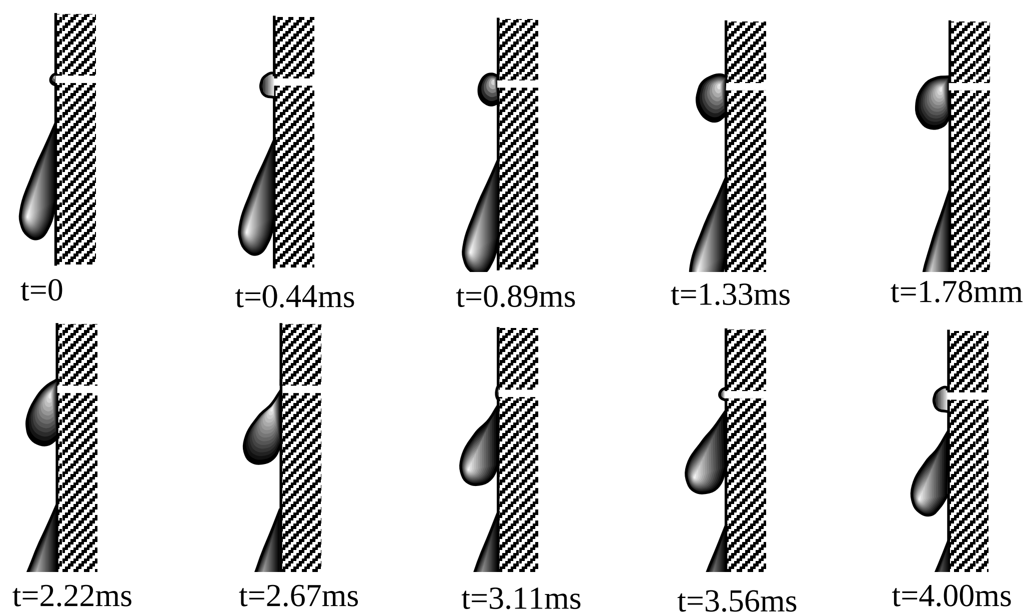

Mode III (U=1.9m/s, Q_G=1.86ml/s, d=0.3mm), Bubble frequency f=444s^{-1}
Equivalent bubble diameter: measured: 2.0mm, predicted:1.95mm

Figure 2.7 Traced bubble formation process for Mode I and Mode III

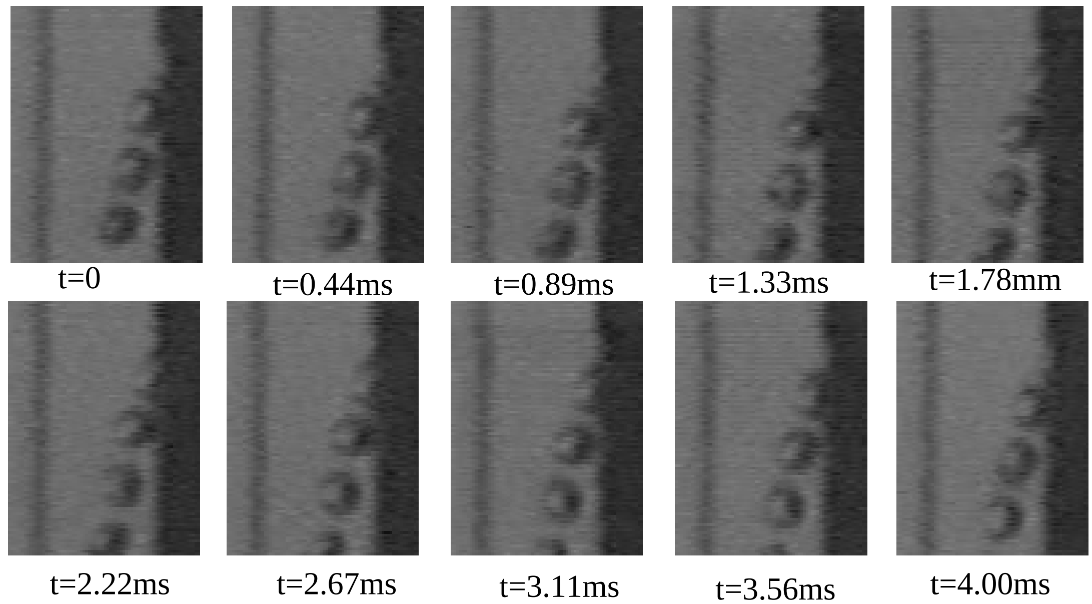

Mode I (U=0.9m/s, Q_G=0.5ml/s, d=0.4mm), Bubble frequency f=293s^{-1}
Equivalent bubble diameter: measured: 1.51mm, predicted: 1.53mm

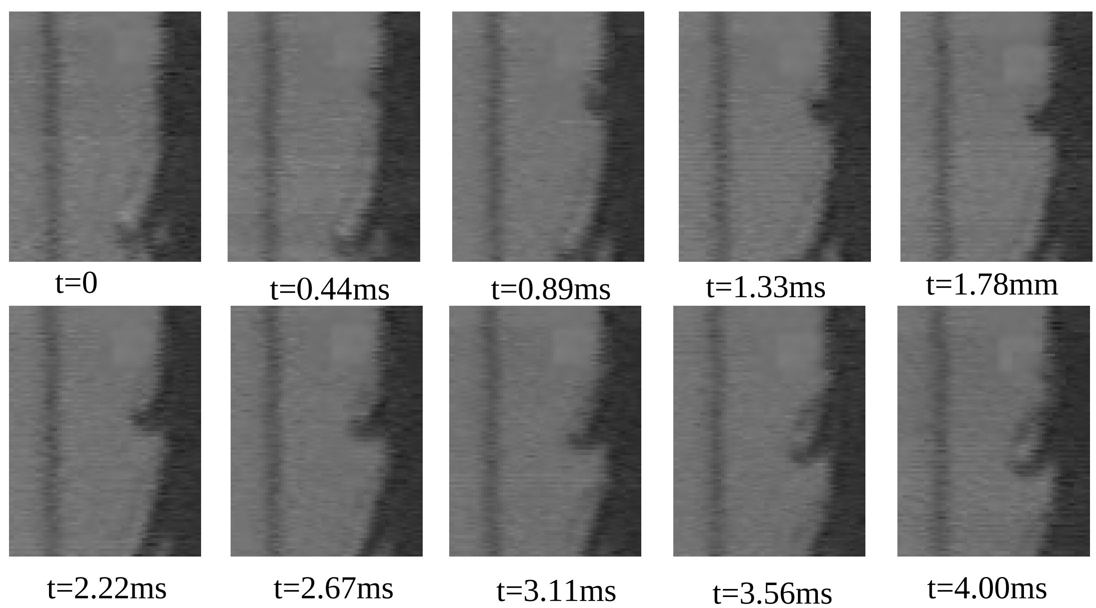

Mode III (U=1.9m/s, Q_G=1.86ml/s, d=0.3mm), Bubble frequency f=444s^{-1}
Equivalent bubble diameter: measured: 2.0mm, predicted:1.95mm

Figure 2.8 Photo series showing the traced bubble formation process for Mode I and Mode III

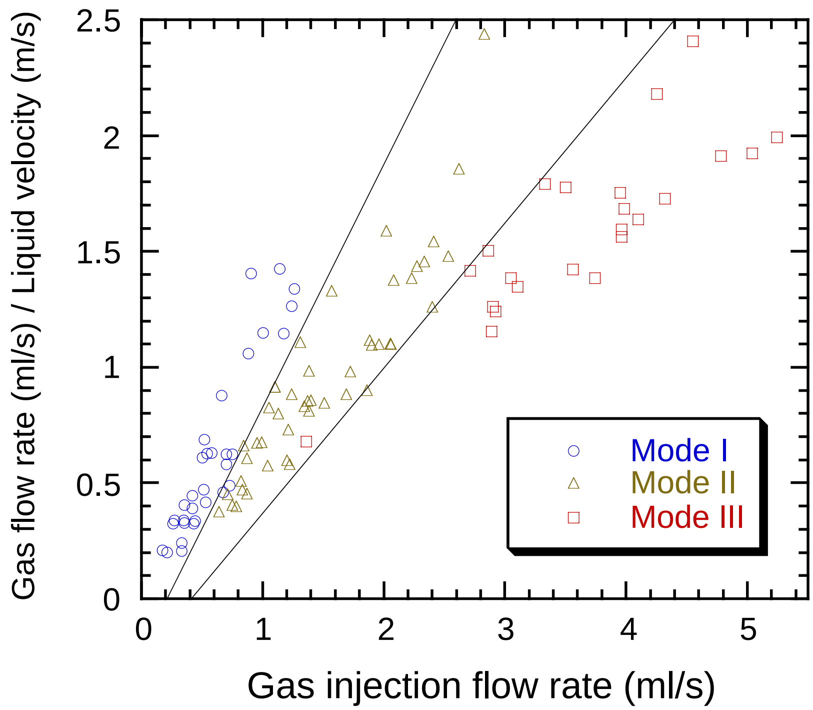

Figure 2.9 Bubble formation modes and their relation with liquid velocity and gas injection flow rate

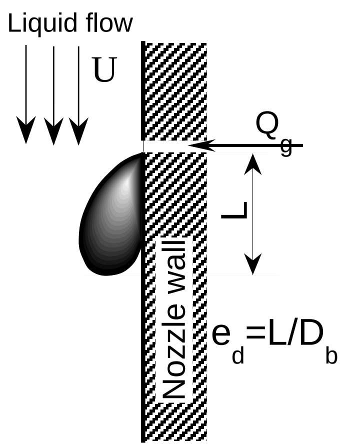

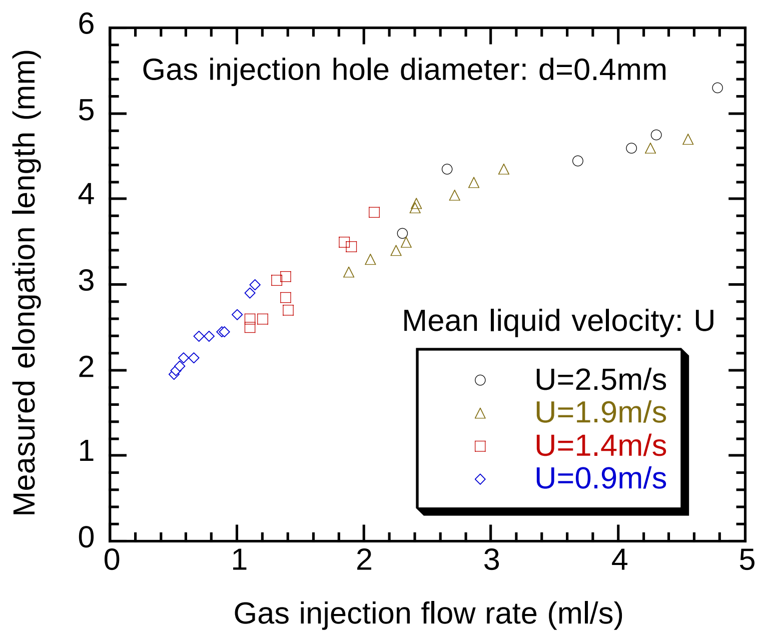

(A) Schematic of the measurement

(B) Measured elongations (*L*)

Figure 2.10 Bubble elongation length at instant of bubble detachment from the gas injection hole

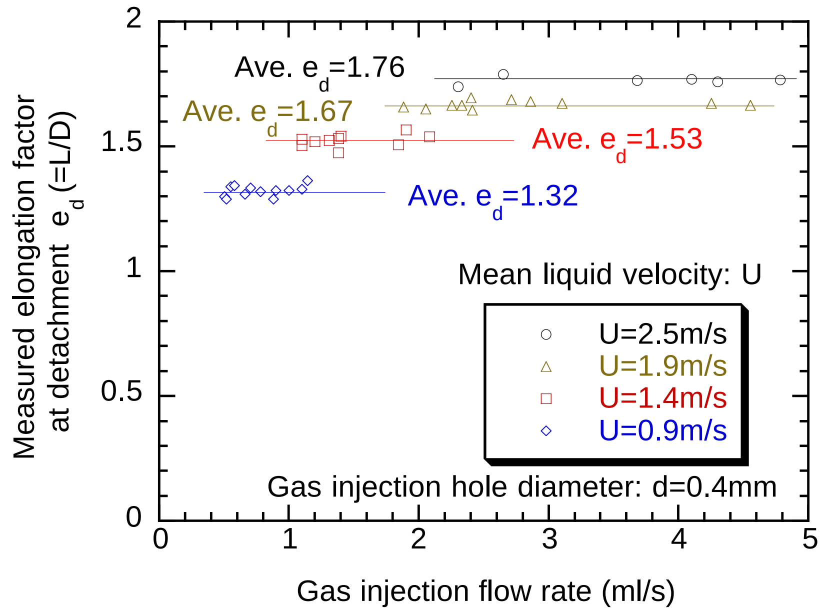

(A)

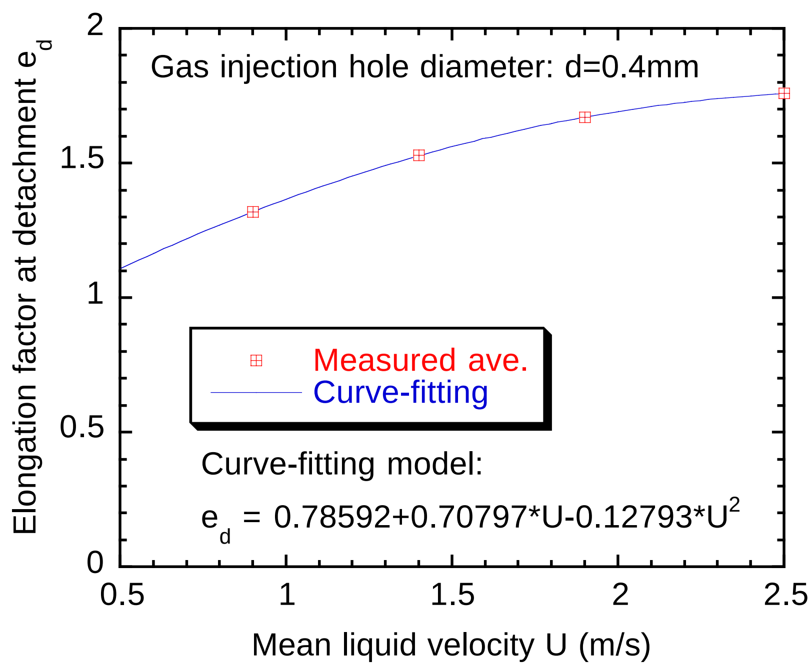

(B)

Figure 2.11 Measured average elongation factor at bubble detachment (A) and its extrapolation (B)

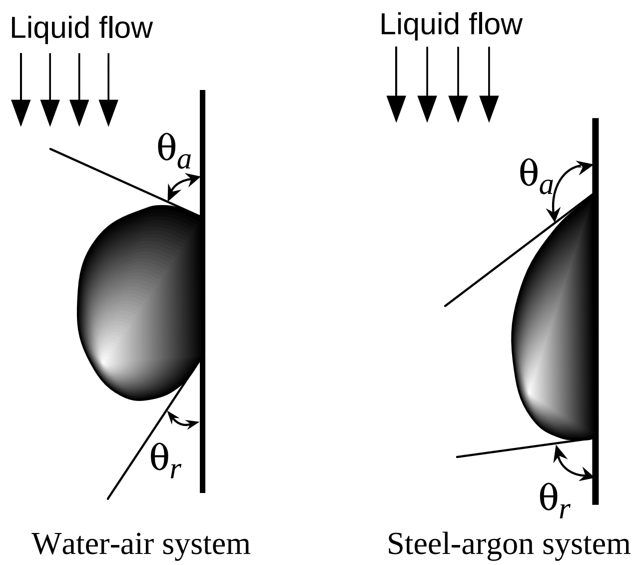

(A)

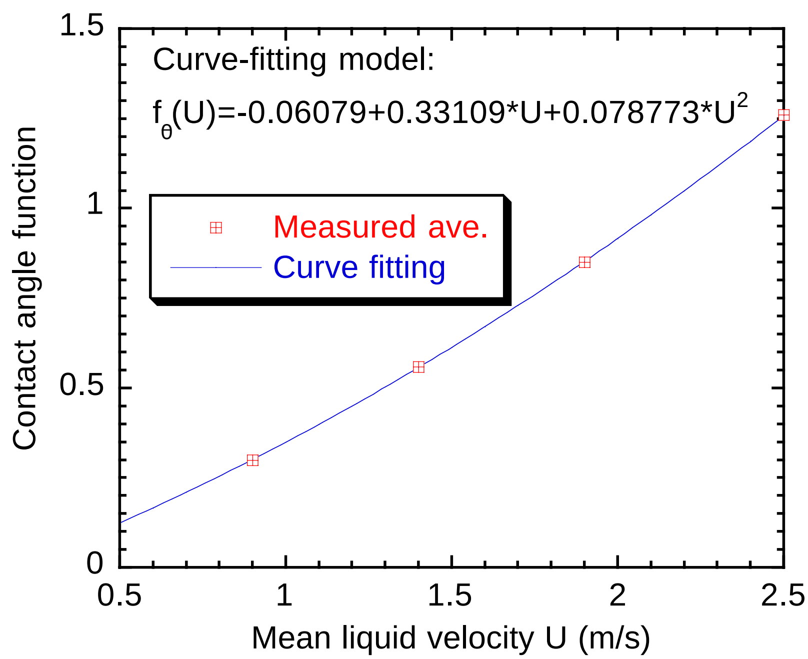

(B)

Figure 2.12 Advancing and receding contact angles (A) and contact angle function extrapolation (B)

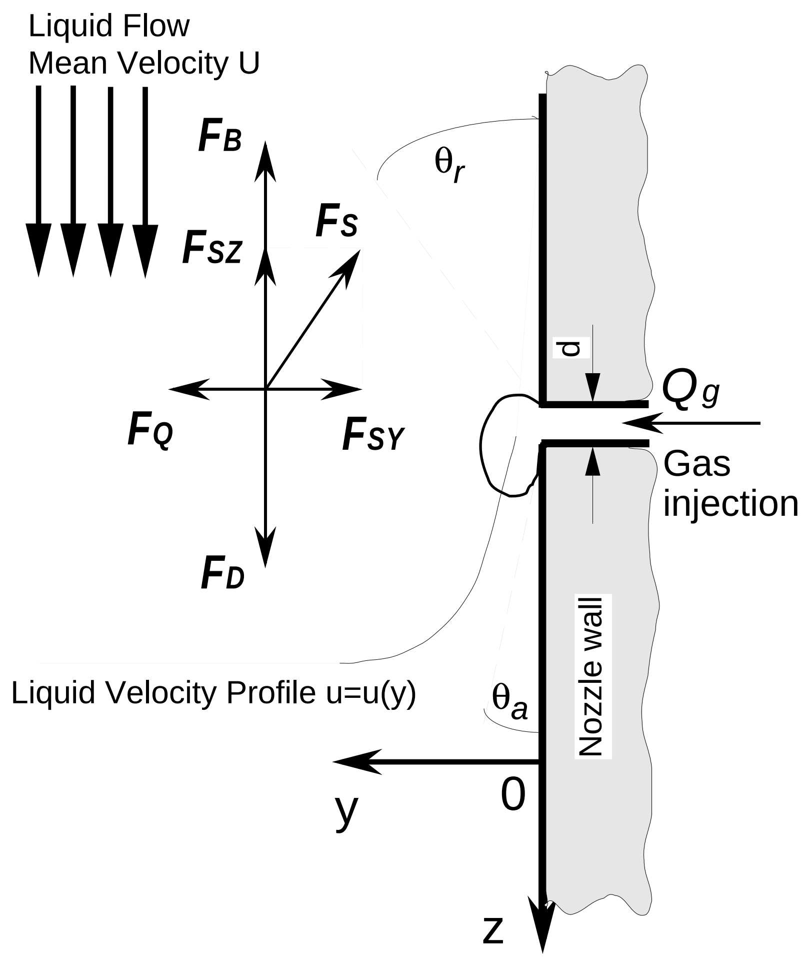

Figure 2.13 Schematic of forces acting on a growing bubble and liquid velocity profile near wall region in the expansion stage

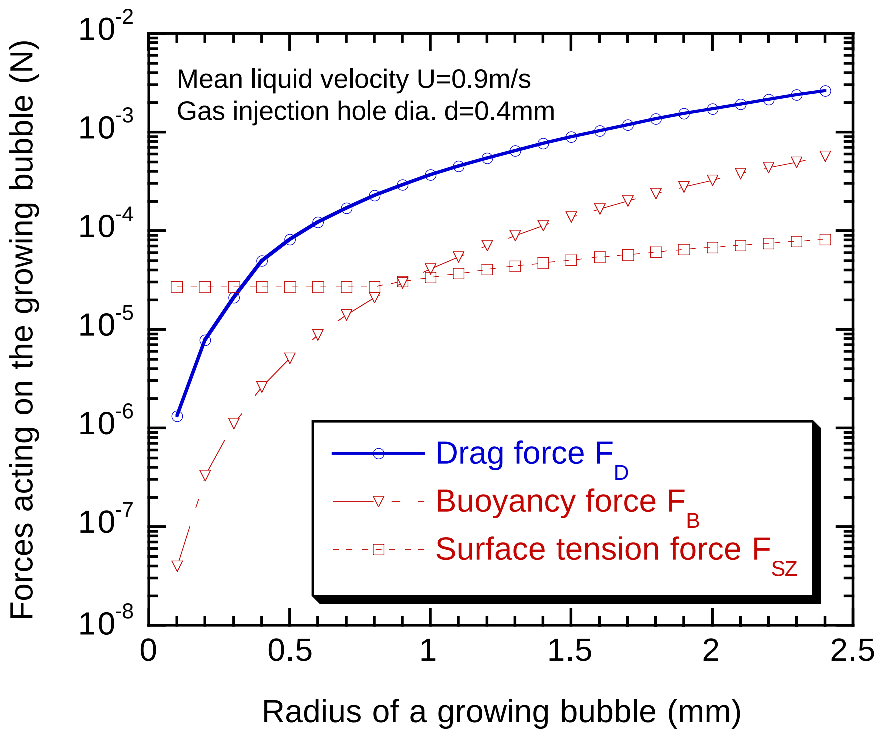

Figure 2.14 Evolution of vertical forces acting on a growing bubble with increasing bubble size

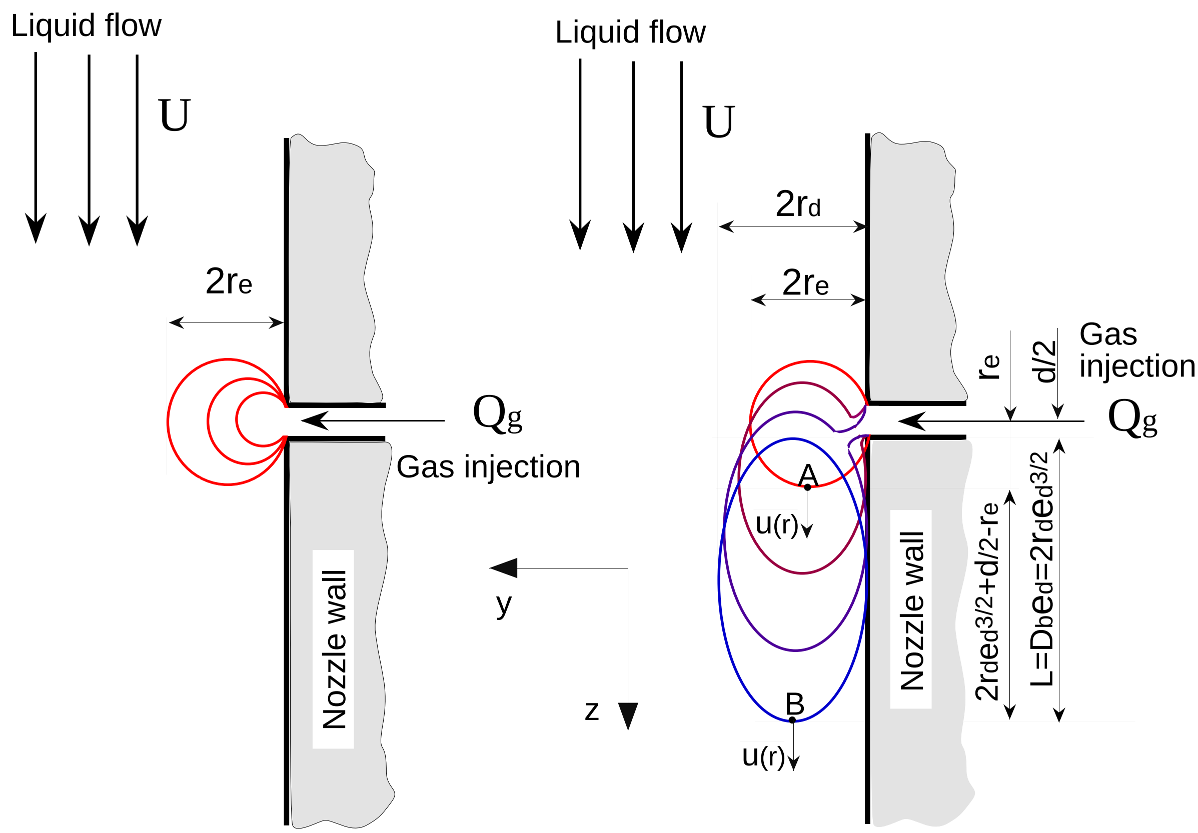

(A) Expansion stage

(B) Elongation stage

Figure 2.15 Idealized sequence of bubble formation in the two stage model

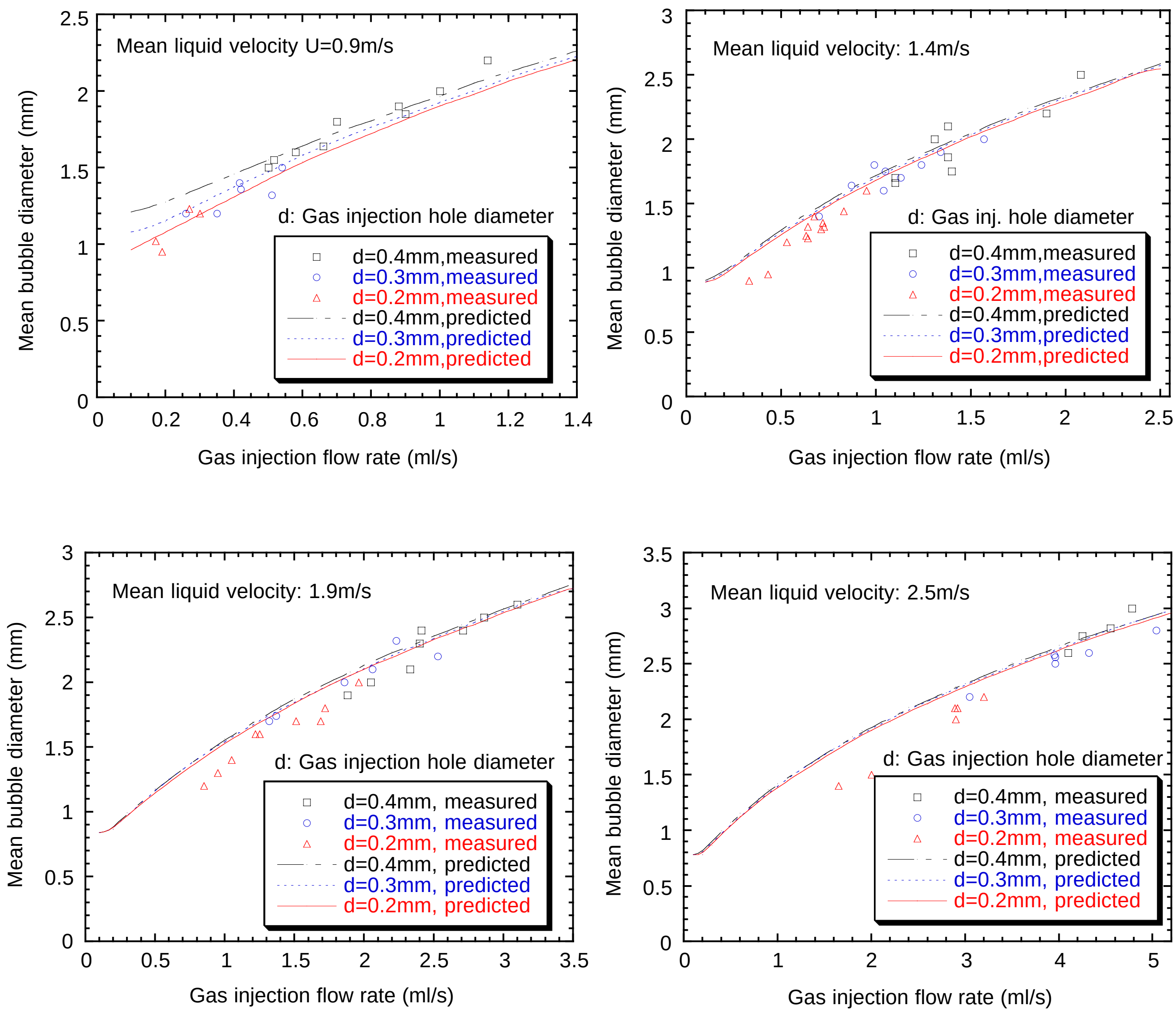

Figure 2.16 Comparison of the predicted air bubble sizes in water with measurements

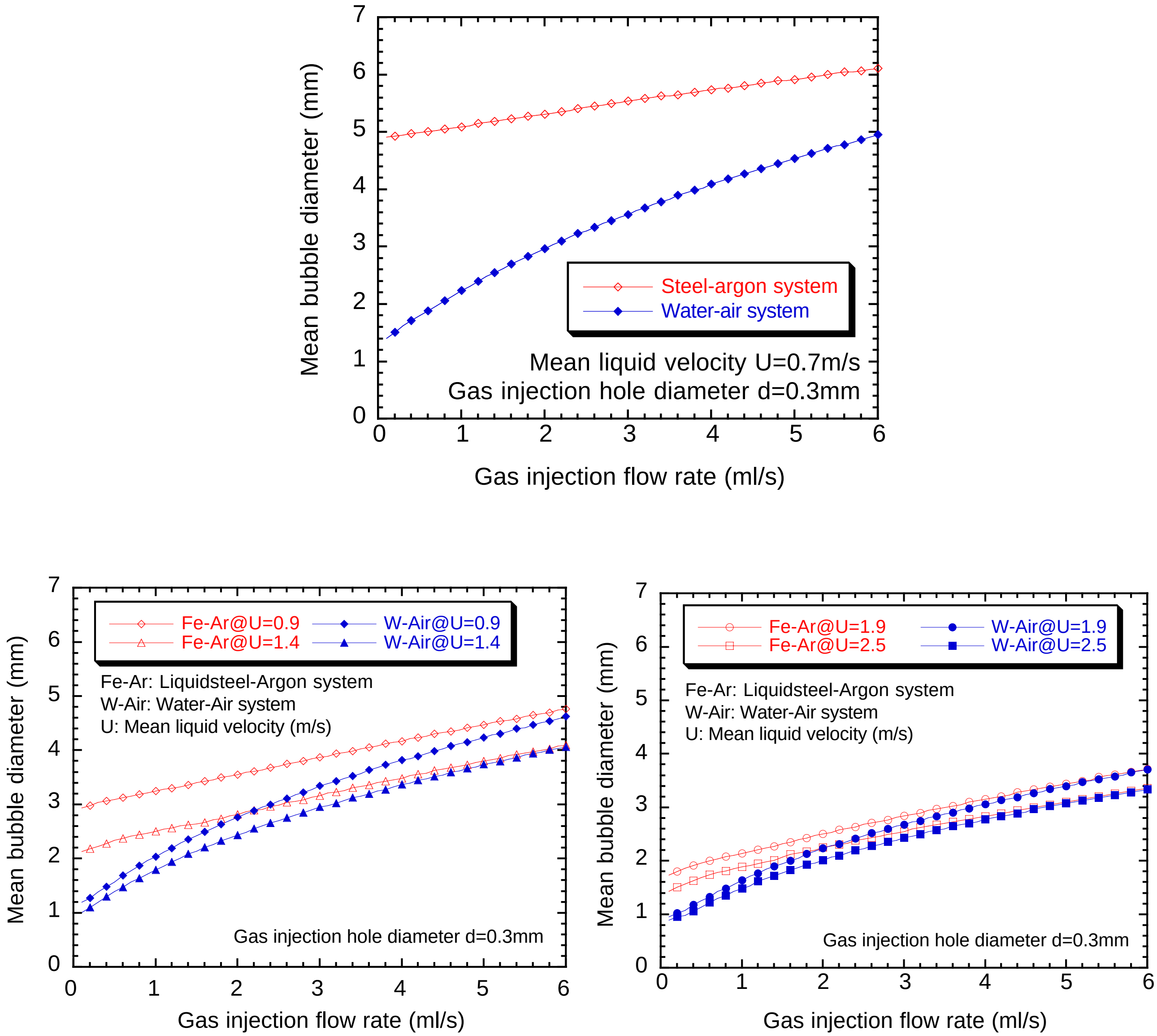

Figure 2.17 Comparison of the predicted argon bubble diameters in liquid steel with air bubble diameters in water

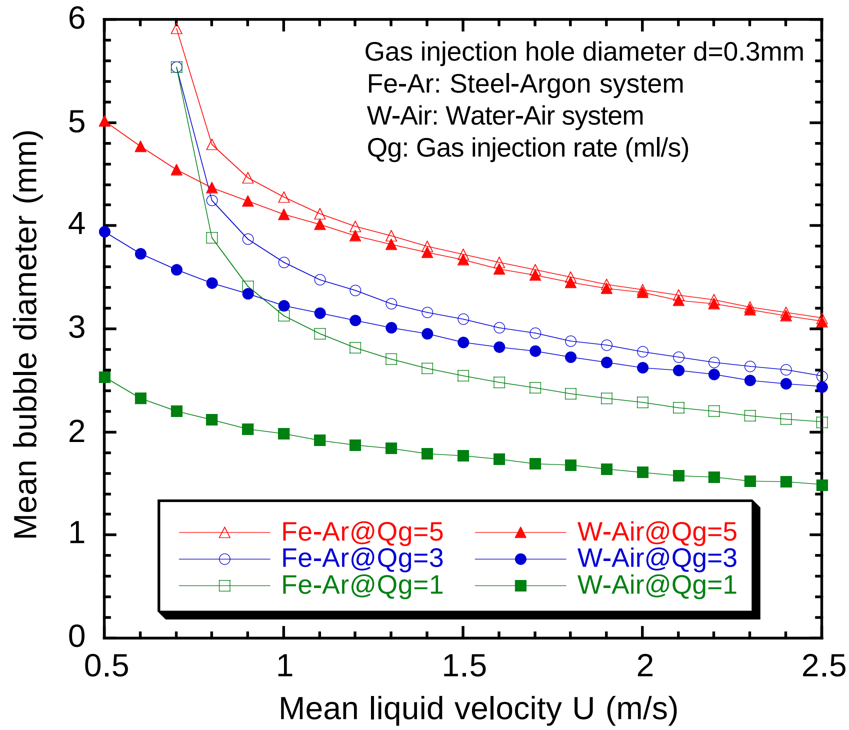

Figure 2.18 Effect of the mean liquid velocity and gas flow rate on argon bubble in liquid steel and air bubble in water

CHAPTER 3. TWO-PHASE FLOW IN SLIDE-GATE NOZZLES

3.1 Previous Work

Previous works on modeling flow in nozzles have focused on single-phase flow. Hershey, Najjar and Thomas [1, 55] assessed the accuracy of the two- and three-dimensional finite-element simulations of the single-phase flow in a bifurcated submerged entry nozzle (SEN) through comparison with velocity measurements and water modeling observations. They demonstrated the reasonable accuracy of separating the nozzle and mold calculations and using 2-D simulations for some symmetrical flows. Their work was later extended [17] to perform an extensive parametric study of single-phase symmetrical flow in the nozzle. Wang [18] employed a 3-D finite-element single-phase model of a complete tundish nozzle (including the upper tundish nozzle, the slide-gate, and the SEN) to confirm the asymmetrical flow caused by the slide gate. Yao [19] used a finite-volume method to model flow through the SEN and the mold together.

Experimental works have reported the importance of two-phase flow in nozzles when argon injected. Tsai [56] observed the partial vacuum pressure at the upper portion of SEN in the water experiments, and found that proper argon injection might avoid the vacuum pressure and hence reduce the air aspiration. Heaslip et al. [57] performed water model experiments to investigate the use of injected gas to carry alloying elements into the liquid. Burty et al. [16] observed a flow pattern transition from dispersed bubbly flow to “annular” flow where gas and liquid separates. A criterion for this transition was developed based on water model experiments through stopper-rod nozzles that depends on both gas flow rate and liquid flow. Sjöström et al. [58] performed an experimental study of argon injection and the aspiration of air into a stopper rod using liquid steel, and found that air aspiration could be reduced by increasing the argon flow rate or pressurizing the stopper. Little work has been reported on the mathematical modeling of the two-phase flow in nozzles, although some studies have been published on the two-phase flow in the ladle [59, 60] and mold [21, 22].

Several different methods have been developed to simulate multiphase flow in continuous casting process. Thomas et al. [10] tracked the trajectories of individual bubbles through the liquid steel in a mold using a Lagrangian approach for particle transport. The effect of the argon bubbles on the steel flow pattern was neglected, so, the results only apply to low argon flow rates. Bessho et al. [21] and Thomas and Huang [22] modeled the gas-liquid flow in the mold by solving the 3-D, incompressible, steady-state, mass and momentum conservation equations for the liquid phase. The buoyancy effect of the gas bubbles was taken into account by adding an extra force term in the liquid momentum equation in the vertical direction. Bubble dispersion in the gas–liquid mixture due to turbulent transport and diffusion was modeled by solving a transport equation for the continuum gas volume fraction. To simplify the problem, no momentum equation was solved for the gas phase. Instead, the bubbles were assumed to reach their steady-state terminal velocity immediately upon entering the domain. An enhancement on this procedure is the Eulerian "homogeneous model" [61, 62] which still solves only a single set of transport equations, but adopts mixture properties where the density and viscosity are proportional to the volume fraction of the phases. The volume fractions are function of space and sum to one on each cell.

Another form of multiphase flow models [47] solves the transport equations only for liquid phase. The gas-liquid interface is defined by a transport equation and diffusion across the interface is prevented. The volume fractions are equal to one or zero everywhere except the interface. This method is usually used for free surface flows and stratified flows, tracking movement of gas-liquid interface such as the case of non-dispersed flow or tracking individual bubble formation [46], and might be suitable for modeling annual flow in nozzles.

Creech [24] investigated the turbulent flow of liquid steel and argon bubble in the mold using the multi-fluid Eulerian multiphase model, in which one velocity field for the liquid steel and a separate velocity field for the gas phase are solved. The momentum equation for each phase is affected by the other phase through inter-phase drag terms. This approach is adopted in current work.

3.2 Model Formulation

The nozzle controls the flow pattern developed in the mold by governing the speed, direction, swirl and other characteristics of the liquid jet entering the mold. The computational domain for simulating flow through a typical slide-gate nozzle is shown in Figure 3.1 with its boundary conditions. The top of the nozzle is attached to the bottom of a tundish and the outlet ports of the nozzle exit into the continuous casting mold.

3.2.1 Governing Equations

Flow in this nozzle is inherently three-dimensional, two-phase and highly turbulent. The Reynolds number, based on the nozzle bore diameter (D_N), is typically of the order of 10^5. A multi-fluid Eulerian multiphase model is used to simulate the time-average flow of argon bubbles in liquid steel. Each phase has its own set of continuity and momentum equations. Coupling is achieved through an empirical inter-phase drag between liquid steel and argon bubbles.

The governing equations of mass and momentum balance for the liquid phase are:

$$\frac{\partial\left(v_{li} f_l\right)}{\partial x_i} = 0 \tag{3.1}$$

$$\rho_l \frac{\partial\left(v_{lj} v_{li} f_l\right)}{\partial x_j} = -f_l \frac{\partial p_l}{\partial x_i} + \frac{\partial}{\partial x_j}\left[f_l(\mu_l + \mu_t)\left(\frac{\partial v_{li}}{\partial x_j} + \frac{\partial v_{lj}}{\partial x_i}\right)\right] + c_{lg}\left(v_{gi} - v_{li}\right) \tag{3.2}$$

and for the gas phase

$$\frac{\partial\left(v_{gi} f_g\right)}{\partial x_i} = 0 \tag{3.3}$$

$$\rho_g \frac{\partial\left(v_{gj} v_{gi} f_g\right)}{\partial x_j} = -f_g \frac{\partial p_g}{\partial x_i} + \frac{\partial}{\partial x_j}\left[f_g \mu_g \left(\frac{\partial v_{gi}}{\partial x_j} + \frac{\partial v_{gj}}{\partial x_i}\right)\right] + f_g(\rho_l - \rho_g) g_i + c_{lg}\left(v_{li} - v_{gi}\right) \tag{3.4}$$

where the indices i and j = 1,2,3 represent the x, y and z directions, $v_i = \{u, v, w\}$, subscript l donates the liquid phase and subscript g the gas phase, f is volume fraction, ρ is density, μ is molecular viscosity and μ_t is the turbulent (or eddy) viscosity. Repeated indices imply summation. Because the density of the gas is 3~4 orders of magnitude smaller than that of the liquid, turbulence in the gas phase is neglected. The standard, two-equation K-ε turbulence model is chosen for the liquid phase, which requires the solution of two additional transport equations to find the turbulent kinetic energy, K, and the turbulent dissipation, ε, fields [63],

$$\rho_l \frac{\partial\left(f_l v_{lj} K\right)}{\partial x_j} = \frac{\partial}{\partial x_j}\left(f_l\left(\mu_l + \frac{\mu_t}{\sigma_k}\right)\frac{\partial K}{\partial x_j}\right) + \mu_t f_l \frac{\partial v_j}{\partial x_i}\left(\frac{\partial v_i}{\partial x_j} + \frac{\partial v_j}{\partial x_i}\right) - \rho_l f_l \varepsilon \tag{3.5}$$

$$\rho_l \frac{\partial\left(f_l v_{lj} \varepsilon\right)}{\partial x_j} = \frac{\partial}{\partial x_j}\left(f_l\left(\mu_l + \frac{\mu_t}{\sigma_\varepsilon}\right)\frac{\partial \varepsilon}{\partial x_j}\right) + C_1 \frac{\varepsilon}{K} \mu_t f_l \frac{\partial v_j}{\partial x_i}\left(\frac{\partial v_i}{\partial x_j} + \frac{\partial v_j}{\partial x_i}\right) - C_2 \rho_l f_l \frac{\varepsilon^2}{K} \tag{3.6}$$

The turbulent viscosity μ_t is calculated from the turbulent kinetic energy and dissipation by

$$\mu_t = C_\mu \rho_l \frac{K^2}{\varepsilon} \tag{3.7}$$

The above equations contain five empirical constants that appear to produce reasonable behavior for a wide range of flow [64] when given standard values as follows:

$$C_1 = 1.44,\ \ C_2 = 1.92,\ C_\mu = 0.09,\ \sigma_K = 1.00,\ \sigma_\varepsilon = 1.30$$

There is an obvious constraint that the volume fractions sums to unity

$$f_l + f_g = 1 \tag{3.8}$$

Equations 3.1 to 3.8 represent 12 equations with 13 unknowns (*u, v, w, p, f for each phase, and* μ_t*, K,* ε for turbulence). The final equation needed to close the system is given by a simple constraint that both phases share the same pressure field:

$$p_l = p_g = p \tag{3.9}$$

The last term of the momentum equations (Equation 3.2 and 3.4) describes inter-phase momentum transfer between the liquid steel and argon bubbles. Here, c_{lg} denotes the inter-phase momentum exchange coefficient, which is related to the relative velocity of the two phases by

$$c_{lg} = \frac{3}{4}\frac{C_D}{D} f_g \rho_l \left| v_{li} - v_{gi} \right| \tag{3.10}$$

where D is the bubble diameter. The non-dimensional drag coefficient C_D is a function of the bubble Reynolds number, defined as Re_{bub}

$$Re_{bub} = \frac{\rho_l \left| v_l - v_g \right| D}{\mu_l} \tag{3.11}$$

The function $C_D(Re_{bub})$ is determined experimentally, and is known as the drag curve. Analysis of the results revealed that most bubbles in this study are in the Stokes regime, with a few in the Allen regime,

Stokes regime [37], $0 \le Re_{bub} \le 0.2$

$$C_D = \frac{24}{Re_{bub}} \tag{3.12}$$

and Allen regime [37], $0 \le Re_{bub} \le 500 \sim 1000$,

$$C_D = \frac{24}{Re_{bub}}\left(1 + 0.15 Re_{bub}{}^{0.687}\right) \tag{3.13}$$

3.2.2 Boundary Conditions

Liquid inlet

Over the plane at the top of the nozzle, velocity is fixed according to the chosen flow rate. A uniform normal velocity profile is assumed, which is a reasonable approximation of the 1/7 power-law profile expected in turbulent pipe flow. Turbulent kinetic energy and turbulent dissipation at the inlet are specified using the semi-empirical relations for pipe flow [65]. The volume fraction of the liquid is unity at the top boundary.

Gas injection

Argon gas is injected along the lower portion of the inner surface of the upper tundish nozzle (UTN) wall. At this boundary, normal velocity for the gas phase is specified from the gas flow rate divided by the region area. The liquid fraction is set as zero. Calculations in Appendix C show that gas injected through the “hot” ceramic wall heats up to 99% of the molten steel temperature even before it hits the liquid steel. Thus, the argon gas injection flow rate used in the numerical model is the “hot” argon flow rate. This is simply the product of the “cold” argon flow rate measured at the standard conditions (STP of 25˚C and 1 atmosphere pressure) and the factor of gas volume expansion due to temperature and pressure change, which is about 5 [23]. The most relevant measure of gas flow rate is the hot percentage. This measure is defined as the ratio of the hot argon to the total (steel and argon) volumetric flow rates.

Wall boundary

The boundary condition at the nozzle wall is the standard K-ε "wall law". This approach can capture the steep velocity gradient in the near-wall boundary layer without using excessive grid refinement. Normal velocity components are set to zero and the tangential velocity profile is defined by an empirical correlation based on the shear stress [62]

$$V_t = -\left(C_\mu^{1/2} K\right)^{1/2} y^+ \qquad \text{for} \qquad y^+ < y_0^+ \tag{3.14a}$$

$$V_t = \frac{-\left(C_\mu^{1/2} K\right)^{1/2}}{\kappa} \log\left(E y^+\right) \qquad \text{for} \qquad y^+ \geq y_0^+ \tag{3.14b}$$

where V_t is the velocity tangential to the wall, E is the log-layer constant (9.7930), κ is the Von-Karman constant (0.419), y_0^+ is the cross over point between the viscous sub-layer and the logarithmic region, and is the upper root of

$$y_0^+ = \frac{1}{\kappa} \log\left(E y_0^+\right) \tag{3.15a}$$

and y^+ is the non-dimensional distance normal to the wall,

$$y^+ = \frac{\left(\rho_l C_\mu^{1/2} K\right)^{1/2}}{\mu_l} n \tag{3.15b}$$

where n is the distance normal to the wall. More details on the wall law implementation can be found elsewhere [62].

Outlet ports

Setting proper boundary conditions at the outlet ports of the nozzle is difficult because flow is not fully developed. This problem can be avoided by extending the modeling domain into the mold, but this greatly increases the computational requirements. Previous modeling of single-phase 2-D flow in nozzles has demonstrated the accuracy of setting zero normal gradients for all variables on the outlet ports [1, 17, 55]. Results from this approach compared favorably with experimental observation and with a combined SEN/mold model [1, 17].

This work also adopts zero normal gradients for all variables except pressure, which is fixed to the hydrostatic pressure based on the SEN submergence depth. This reference pressure is reasonably close to the actual pressure at the nozzle ports, and has little influence on the solution except for convergence. The alternate "mass flow boundary" condition in CFX is unreasonable for this problem because it requires the mass flow rate from each port to be specified and always produces vertical jet angles of 0˚.

3.2.3 Solution Method

A multi-block, numerical grid with body-fitted coordinates is used to create the complex geometry of the nozzle domain. The typical slide-gate nozzle geometry shown in Figure 3.1 has 74 blocks. The governing equations (Equations 3.1~3.8) are discretized using the finite difference method and solved using the commercial finite difference program CFX version 4.2 by AEA Technology [62].

Grid resolution is chosen to allow both accurate prediction and economical computing resource. Figure 3.2 illustrates sections through three different grid resolutions investigated: coarse, standard, and refined, with 17,028, 34,000, and 126,448 total cells respectively. The CPU times for 1000 iterations are 1.33, 2.45 and 9.42 hours respectively on the SGI Origin 2000 supercomputer at NCSA at University of Illinois at Urbana-Champaign. Figure 3.3 compares the solutions of velocity and volume fraction at the vertical centerlines along the entire nozzle and along the port outlet plane. The coarse grid predicts different profiles from which the standard and refined grids do, especially the volume fraction. Predictions with the standard grid are reasonably close to those of the refined grid but require only a quarter of the CPU time the refined grid needs. Thus the standard grid was chosen as optimal for the remainder of this work.

To achieve faster convergence, a single-phase solution is obtained first and used as an initial guess for the two-phase flow simulation. For some cases with high percentage of gas injection volume fraction, the gas injection flow rate must be gradually increased to avoid convergence problems. For most cases, 1000 to 2000 iterations are needed to achieve a fully converged solution with scaled residuals of less than 10^{-4}. The scaled residual is the ratio of the residual at the current iteration to that of the second iteration. A typical convergence history for all of the scaled residuals is shown in Figure 3.4(A). The solution value history of each variable at a monitoring point (x=0.0299m, y=0.0627m, z=0.0664m) is shown in Figure 3.4(B). The predicted values become very stable after 400 iterations while all scaled residuals fall below 10^{-4}.

A common problem in turbulent flow simulation is rapid divergence, where the residuals suddenly increase to extremely large numbers and the solver crashes. This problem is usually due to the cross diffusion terms in the K transport equation (Equation 3.5) that contain ε and the terms in ε equation (Equation 3.6) that contain K. This divergence can be avoided by "deferred correction" in CFX [62], which turns off these terms for the first 500 iterations and then linearly increases them to their full values by the end of the next 500 iterations.

3.2.4 Typical Simulation Results

Simulation results for the nozzle in Figure 3.1 with the standard grid in Figure 3.2 and the Standard conditions in Table 3.1 are plotted in Figures 3.5, 3.6 and 3.7, showing velocity vectors, argon gas distribution and pressure distribution respectively. Recirculation zones are found in three regions: 1) immediately under the slide plate, 2) in the cavity of the slide-gate, and 3) in the upper portion of the nozzle ports, as shown in Figure 3.5. In each of these regions, the velocities are relatively low at the recirculation center, and a relatively high volume fraction of gas is collected, as shown in Figure 3.6. The highest liquid velocity region is found through the slide-gate due to the throttling effect.

The flow conditions leaving the nozzle ports directly affect flow in mold and therefore the steel quality. The jets flow out of the ports with a strong vortex or swirl, as shown in Figures 3.5(B) and (C). Each jet splits into two parts as it leaves the port: 1) a strong downward jet of molten steel which contains very little gas, and 2) a weaker jet from the upper portion of the port. The latter contains a high percentage of gas and is directed upward due to the buoyancy of the bubbles. The vortex pattern and the swirl rotational direction depend on many factors such as the slide-gate opening size, slide-gate orientation, nozzle geometry, gas injection, as well as clogging, and will be further discussed later.

Figure 3.7 shows a shaded contour plot of the pressure distribution. While regulating the liquid steel flow, the slide-gate creates a local flow restriction which generates a large pressure drop. The lowest pressure is found in SEN just beneath the slide gate, so joint sealing is very important there to avoid air aspiration if a vacuum occurs. A vacuum occurs if minimum pressure inside the nozzle falls below zero (gage). The minimum pressure is affected by argon injection, tundish bath depth, casting speed, gate opening and clogging, and addressed in Chapter 4. The pressure plot in Figure 3.7 is also an example of a successful avoidance of a vacuum with the help of argon injection.

3.2.5 Multiple Steady-State Solutions

The highly turbulent flow in nozzles is inherently time-dependent. The flow patterns predicted with the steady-state turbulent flow model shown in Equations 3.1-3.9 are time-averaged behavior. In previous experimental studies [1], three different jet vortex patterns were observed to be relatively stable. The flow pattern periodically “flipped” between a single clockwise strong swirl, a single counterclockwise strong swirl, or two small symmetric swirls, as observed directly into the port. The pattern with two small symmetric swirls was most unstable and lasted the shortest time between ”flipping”. This time-dependent behavior can be captured by the CFX steady-state turbulent flow simulation.

Figure 3.8 shows the vortex patterns predicted in a full 3-D SEN for the conditions of Hershey et al [1]. All three patterns in Figure 3.8 are fully converged solutions for the same simulation condition except for the initial guess for the velocity field. Starting from a symmetric initial guess of zero velocity generates two small symmetric swirls, as shown in Figure 3.8(C). This matches the solution obtained in earlier work with symmetry imposed [1]. An initial guess with small horizontal velocity components to the right converges to a solution with one large counterclockwise swirl and one small clockwise swirl at the center plane. When flow exits the port, the flow pattern evolves into a single vortex rotating counterclockwise, as shown in Figure 3.8(A). Switching the initial velocity components to the left reverses the resulting vortex pattern, as shown in Figure 3.8(B). These different converged solutions to the same problem likely represent local minima in the residual error space. When such multiple solutions are encountered, convergence difficulties are likely. This situation appears to occur in nature also, which explains the transient oscillation between flow patterns observed in the water models.

In this work, the full nozzle domain is always modeled for two reasons. Firstly, the slide-gate nozzle often has little symmetry to exploit than SEN (for example, a 45° orientated slide-gate has no symmetry at all). Secondly, modeling a quarter of the SEN based on the geometric symmetry forces the solution to converge to the symmetric flow pattern, so multiple solutions cannot be observed. The present finding of multiple steady flow patterns suggests that slight changes in operating conditions (such as gate opening and clogging) are likely to cause great changes in the most stable flow pattern, especially when near critical conditions.

3.2.6 Jet Characteristics

The tundish nozzle affects the steel quality through its influence on flow pattern in the mold. As a step towards investigating the effect of nozzle design and operation conditions on the flow pattern in the mold, the jet characteristics are quantified here in terms of average jet angle, jet speed, back-flow zone, and biased mass flow. The jet characteristics are calculated from the numerical solution at the port outlet plane. These jet properties are computed using weighted averages based on the local outward flow rate. The values associated with the low-velocity back-flow zone (where flow reenters the nozzle) are ignored. These definitions follow those of previous work for single–phase flow [17], with modifications to account for the gas phase. The local flow rate corresponds to the local liquid velocity magnitude at cell *i* of the nozzle port.

Liquid velocity magnitude at cell i of the nozzle port:

$$U_i = \sqrt{\left(u_l\right)_i^2 + \left(v_l\right)_i^2 + \left(w_l\right)_i^2} \tag{3.16}$$

Weighted average liquid velocity at the nozzle port in the x-direction:

$$\overline{u_l} = \frac{\sum\limits_{i\ (if\ outflow)} \left[\left(u_l\right)_i U_i (\Delta y)_i (\Delta z)_i (f_l)_i\right]}{\sum\limits_{i\ (if\ outflow)} \left[U_i (\Delta y)_i (\Delta z)_i (f_l)_i\right]} \tag{3.17}$$

Weighted average liquid velocity at the nozzle port in the y-direction:

$$\overline{v_l} = \frac{\sum_{i\ (if\ outflow)} \left[(v_l)_i U_i (\Delta y)_i (\Delta z)_i (f_l)_i \right]}{\sum_{i\ (if\ outflow)} \left[U_i (\Delta y)_i (\Delta z)_i (f_l)_i \right]} \tag{3.18}$$

Weighted average liquid velocity at the nozzle port in the z-direction:

$$\overline{w_l} = \frac{\sum_{i\ (if\ outflow)} \left[(w_l)_i U_i (\Delta y)_i (\Delta z)_i (f_l)_i \right]}{\sum_{i\ (if\ outflow)} \left[U_i (\Delta y)_i (\Delta z)_i (f_l)_i \right]} \tag{3.19}$$

Weighted average turbulence energy at the nozzle port:

$$\overline{K} = \frac{\sum_{i\ (if\ outflow)} \left[K_i U_i (\Delta y)_i (\Delta z)_i (f_l)_i \right]}{\sum_{i\ (if\ outflow)} \left[U_i (\Delta y)_i (\Delta z)_i (f_l)_i \right]} \tag{3.20}$$

Weighted average turbulence dissipation at the nozzle port:

$$\overline{\varepsilon} = \frac{\sum_{i\ (if\ outflow)} \left[\varepsilon_i U_i (\Delta y)_i (\Delta z)_i (f_l)_i \right]}{\sum_{i\ (if\ outflow)} \left[U_i (\Delta y)_i (\Delta z)_i (f_l)_i \right]} \tag{3.21}$$

Vertical Jet Angle:

$$\theta_{zx} = \tan^{-1}\left(\frac{\overline{w_l}}{\overline{u_l}} \right) = \tan^{-1}\left(\frac{\sum_{i\ (if\ outflow)} \left[(w_l)_i U_i (\Delta y)_i (\Delta z)_i (f_l)_i \right]}{\sum_{i\ (if\ outflow)} \left[(u_l)_i U_i (\Delta y)_i (\Delta z)_i (f_l)_i \right]} \right) \tag{3.22}$$

Downward angles are defined to be positive.

Horizontal Jet Angle:

$$\theta_{yx} = \tan^{-1}\left(\frac{\overline{v_l}}{\overline{u_l}} \right) = \tan^{-1}\left(\frac{\sum_{i\ (if\ outflow)} \left[(v_l)_i U_i (\Delta y)_i (\Delta z)_i (f_l)_i \right]}{\sum_{i\ (if\ outflow)} \left[(u_l)_i U_i (\Delta y)_i (\Delta z)_i (f_l)_i \right]} \right) \tag{3.23}$$

Angles toward the wide face opposite the gate opening are defined to be positive (Figure 3.20).

Jet Speed:

$$U_{jet} = \sqrt{\left(\overline{u_l}\right)^2 + \left(\overline{v_l}\right)^2 + \left(\overline{w_l}\right)^2} \tag{3.24}$$

Back-flow zone fraction:

$$\eta = \frac{\sum_{all\ i}\left[(\Delta y)_i(\Delta z)_i\right] - \sum_{i\ (if\ outflow)}\left[(\Delta y)_i(\Delta z)_i\right]}{\sum_{all\ i}\left[(\Delta y)_i(\Delta z)_i\right]} \tag{3.25}$$

where Δy and Δz are the lengths of the cell sides, $(u_l)_i$, $(v_l)_i$, and $(w_l)_i$ are the liquid velocity components in the x, y, and z directions, and $(f_l\ )_i$ is the liquid volume fraction in cell *i*. The summation operation Σ is performed on all cells at the port exit plane with outward flow.

3.3 Model Validation

3.3.1 Water Model Experiments and PIV Measurements

To verify the computational model, flow visualization and velocity measurement were made using a 0.4-scale water model of the tundish, nozzle and mold of the caster at LTV Steel (Cleveland, OH). This "water caster" is a transparent plastic representation of an actual slab caster used in LTV Steel at 0.4 scale, with its strand length shortened to 0.95m. The physical model has three 35mm-holes spaced 180mm apart at the bottom of the wide face to allow removal of water at a volume flow rate corresponding to the casting speed. Figure 3.9 shows the photo of the water caster. The nozzle geometry is shown in Table 3.1 as "0.4-Scale PIV Nozzle".

The PIV (Particle Image Velocimetry) system developed by DANTEC Measurement Technology was used to measure the velocity field at the plane of interest near the nozzle port. Figure 3.10 shows a schematic of PIV system. In PIV, a pulsed laser light sheet is used to illuminate a plane through flow field seeded with tracer particles small enough to accurately follow the flow. The positions of the particles are recorded with a digital CCD (Charged Coupled

Device) camera at each instant the light sheet is pulsed, yielding an “exposure”. The images from two successive exposures are processed to match up individual particles and calculate the vector displacement of each. Knowing the time interval between the two exposures (1.5 ms), the velocity of each particle can be calculated and the velocities are combined to produce an instantaneous velocity field. In this work, this procedure was repeated every 0.533 second to obtain the complete history of the fluctuating velocity field under nominally steady conditions. To obtain a time-averaged or “steady” velocity field, the results from 50 exposures were averaged. Errors in matching up particles sometimes produce abnormal huge velocities at a single point, which are easy to recognize. Thus, before averaging, the vector plot of each exposure is examined and each abnormal vector is replaced by the average of its four normal neighbors. If the abnormal vector is at the nozzle port, only the neighbors on the outside of the nozzle port are averaged to obtain the replacement vector, because velocities inside the nozzle cannot be accurately measured.

Since the PIV measurement generates a planar velocity vector field that does not include the v-component of the velocity (y-direction, perpendicular to the light sheet), the resulting speed measurements should be compared with calculated magnitudes based only on the u- and w-velocity components. To evaluate the direction of the jet exiting the port, a “slice jet angle” is calculated from an arithmetic average of the angles of all vectors along the port exit in the particular slice illuminated by the laser light sheet:

$$\theta_{zx-slice} = \frac{1}{N}\sum_{i=1}^{n}\tan^{-1}\left(\frac{(w_l)_i}{(u_l)_i}\right) \tag{3.26}$$

where N is the number of measuring points (PIV vectors or computational cells) on the given slice through the domain at the nozzle port exit.

Figure 3.11 shows typical speed histories measured at two points along the port outlet centerline, one at the middle and the other at the bottom. The corresponding time average values are also given.

3.3.2 Flow Pattern Observations

Flow patterns observed in the experiments can be directly compared to the numerical simulation. Close agreement between the experiments and the numerical model was achieved. In both the water experiments and model predictions, three main recirculation zones are observed inside the slide-gate nozzle: in the cavity of the middle gate plate, below the throttling gate plate, and at the nozzle ports. High gas concentration collects in these recirculation zones. In both the simulation and the water experiments, the jet exits the ports with a single strong vortex.

No obvious "back-flow" at the nozzle port was observed for the nozzle in this experiment. This matches the numerical computation for the PIV Nozzle, which predicts only outward flow at the nozzle ports (η=0, Equation 3.25). The predicted flow field superposed on gas distribution at the SEN port is shown in Figure 3.12. This "no back flow" behavior differs from the predictions for the Standard Nozzle in this work, where η=8%~40% depending on operation conditions, which matches previous findings for the typical nozzles [1, 10, 17, 18]. This is due to the special design of the 0.4 Scale PIV Nozzle, which has a steep angle of the upper port edge (40°down) relative to the lower port edges (15°down). This can be clearly seen when comparing simulated flow patterns at the port between this test nozzle and the nozzle with modified port edges (15°down for both upper and lower port, as "regular port angle" design), as seen in Figure 3.13. The only difference between the two simulations is the port angle design at the upper edge of the port. The steep upper-port-edge directs the liquid flow along the port wall, thus avoid the back-flow, as seen in Figure 3.13(A), whereas a back-flow zone is developed at the upper portion of the port for the "regular port angle" design, as shown in Figure 3.13(B).

The jet entering the mold is directed approximately 29° down, as seen in the photograph of Figure 3.14. This is very close to the value of 27.8° down calculated from the numerical simulation results using Equation 3.22. The vortex pattern is very stable, rotating clockwise when looking directly into the left port, as shown in Figure 3.12. This swirl is caused by the 90° slide-gate, which directs flow down the front of the nozzle bore.

3.3.3 Velocity Comparisons

A quantitative comparison between the PIV measurements and the simulation results is made on the jet at the nozzle port exit. Unfortunately, the flow field inside the plastic nozzle could not be reliably measured, due to the curvature of the nozzle wall and partial opacity from the machining cut. Figure 3.15(A) shows time-averaged vector plots of the PIV-measured flow field just outside the nozzle port. The simulated vector plots are shown in Figure 3.15(B) for comparison. The corresponding liquid velocity magnitudes at the port are compared in Figure 3.15(C). Also marked on Figure 3.15(C) are the slice jet angles defined in Equation 3.26, which is different from the overall average vertical jet angle defined in Equation 3.22. The upper part of Figure 3.15 shows the slice jet angle for the slice C-C through the nozzle center-plane (y=0) is downward. The lower part of Figure 3.15 shows upward flow near the port edge (at y=12mm). The jet in this slice is upward even though the overall jet is downward. This is consistent with the 3-D swirl of the jet.

The match of the velocity magnitude and the slice jet angle between the PIV measurement and the model prediction is satisfactory except that the velocity predictions are consistently slightly larger than the measurements. This might be due to the fact that the location of the pulsed laser light sheet was manually adjusted by naked eyes during the PIV experiments, and thus might not lie exactly in the desired positions. Figure 3.16 shows how the velocity magnitude is sensitive to the slice location due to the 3-D effect of the jet vortex.

3.4 Model Discussion

3.4.1 Dispersed Bubble Assumption

The Eulerian multi-fluid model employed in this work assumes that the gas bubbles (disperse phase) to be spherical and to mix with liquid (continuous phase), bubble coalescence or breakup can not be modeled with this method. This model is suitable for the bubbly flow where gas bubble and liquid well mix but not suitable for the annular flow where the gas and liquid separate. The experimental studies [16] show that the bubbly-annular flow transition occurs at high gas volume fraction, specifically, 32-46% hot gas for the Standard Nozzle and conditions in Table 3.1. The annual flow pattern in nozzle creates strong perturbations in mold meniscus and should be avoided. In practice, gas injection rate is limited by its effect on flow pattern, and is usually less than 30% in volume. Therefore, the Eulerian multi-fluid model is suitable for practical casting conditions.

Wide range of the argon gas injection volume fraction (up to 44%) is simulated for the Standard Nozzle in Table 3.1 with a 45° gate orientation, using the Eulerian multi-fluid model. Figure 3.17 shows the argon volume fraction profiles across the nozzle bore on the wide face center plane at three different vertical positions. Figure 3.17(A) shows the profile at gas injection region (UTN, z=1000mm) where pure gas is found near the wall and pure liquid is found in the central region of the nozzle. High gas concentration develops toward the center with increasing gas injection rate. Figure 3.17(B) and 3.17(C) shows asymmetric profile to the SEN centerline due to the off-center blocking effect of slide-gate. Figure 3.17(B) shows the profile under the blocking gate plate (z=800mm) where a swirl forms. The highest gas collection is found in the center of the swirl instead of on the wall. Figure 3.17(C) shows the profile at the middle of SEN (z=400mm) where the profile becomes more symmetric to the centerline relative to the Figure 3.17(B). The dispersed model can neither simulate the ideal annular flow profile, nor predict the trend to annular flow. In following parametric study detailed in later section of this chapter and next chapter, the gas injection volume fraction is no more than 28%, corresponding to the bubbly flow for all cases.

3.4.2 Split-Jet Calculation

The jet characteristics defined in Equations 3.20-3.25 are weighted average on the whole port, However, two separate jets may form on the same port, depending on nozzle geometry, argon injection and the swirl effect by slide-gate, as seen in Figure 3.5. The downward jet is usually an asymmetric strong vortex, containing small amount of gas, and the upward jet with high percentage of gas flow from the very top of the port. The back flow zone is between the two jets and the position changes with flow pattern. It is possible to calculate the characteristics of the two jets on each port separately rather than treat the whole outward flow as one average jet.

Since the two-jet pattern varies from case to case, it is difficult to find a universal definition to divide the two jets. Next, one simulation case is taken as an example to illustrate the way to calculate the split jets separately. The simulated case has a 45° gate orientation and 28% (hot) argon gas injection volume fraction. The nozzle geometry and other conditions are the same as the Standard Nozzle in Table 3.1. The velocity vector plots for both ports are shown in Figure 3.18, including the 3-D view.

The split of the jet into a downward-jet and an upward-jet is based on flow pattern observation, shown as the jet division line in Figure 3.18. The back flow zones do not belong to either jet. Calculation of the characteristics for each jet still employs the weighted average method defined in Equations 3.20-3.25, but the summation is applied on each jet region (Upward-jet or Downward-jet), and the back flow zone is still ignored. The split-jet calculation results, together with the overall one-jet average results are tabulated in Table 3.2. Following observation can be made from the table.

- Upward jets have very large upward jet angle (over 20°).
- The vertical jet angle for downward jets are steeper than that of overall average for one-jet, but still shallower than the port angle. This shows that buoyancy also has great influence on both downward and upward jets.
- Both downward jet and upward jet are away from the center plane, but toward different side of the wide face. The downward jets are toward the gate opening side and the upward jets are toward the opposite of the gate opening side.
- Although the upward jets take more than 30% of the area on each port, their ratios of the carried liquid flow are much less than those of the downward jets (8.7% for the left port and 9.2% for the right port). This is due to high gas volume fraction in the upward jet regions.
- Over 70% of the gas is carried by the upward jets.
- Most liquid is carried by the downward jets, which have dominant influence on the overall average values. This is shown by the much closer jet angles of the overall average jet to the downward jet than to the upward jets.

Jet division is somehow arbitrary, as shown in Figure 3.18, and case-dependent because of the swirling behavior of the jets. It is difficult to implement a general scheme to split and calculate the jet characteristics as for the single overall jet. Therefore, in the following parametric study on effect of the casting operation conditions and nozzle design on flow, the overall weighted average scheme, defined in Equations 3.20-3.25, are employed for jet characteristics calculation.

3.5 Parametric Studies

The 3-D finite difference model is employed to perform extensive parametric studies to investigate the effects of casting operation conditions including gas injection, slide-gate orientation, casting speed, gate opening and bubble size and nozzle port design including port angle and port shape on flow pattern.

A non-clogging condition is assumed for all simulation cases in this work. The effect of clogging, including initial clogging and severe clogging, is addressed in Chapter 4.

3.5.1 Effect of Argon Gas Injection

Gas collects at the upper portion of the nozzle ports whenever a back flow zone exists, as shown by the high gas concentration there in Figure 3.6. For ports with no back flow such as the nozzle in the validation experiments shown in Figure 3.12, gas collects instead in the central region of the jet swirl. In both cases, gas affects the flow pattern of the jet.

The effect of gas on the flow pattern can be seen more clearly when the jets with and without gas are directly compared, as shown in Figure 3.19. Both simulation cases have geometry and conditions in Table 3.1 with the 45° gate orientation. Without gas, some low-velocity flow reenters the upper portion of the nozzle ports. When gas is injected and the casting speed is kept constant, the flow must accelerate to accommodate the space taken by the gas. This greatly increases the turbulence and changes the vortex pattern exiting the ports. Some of the gas bubbles are carried by the downward jet but most of the bubbles exit from the upper portion of the ports. This second jet is directed upward due to the buoyancy. This matches the observation in the water model experiments.

The effects of gas injection will naturally change with the argon injection flow rate, and is also affected by other variables such as slide-gate orientation and casting speed. Quantitative analysis is detailed in the analysis of the jet characteristics together with the effects of slide-gate orientation and casting speed in the next few sections.

3.5.2 Effect of Slide-Gate Orientation

The slide-gate is used to regulate the steel flow rate by adjusting its position to control the opening size. However, the off-center blocking effect generates asymmetric flow that directly affects the flow pattern in the mold. Three typical slide-gate orientations, illustrated in Figure 3.20, are investigated here. For the 0° orientation, the slide-gate moves parallel to the wide face of the mold, so asymmetric jets flow from the two outlet ports. For the 90° orientation, the slide-gate moves perpendicular to the wide face of the mold. This avoids obvious asymmetry but generates strong swirl and may also generate asymmetry in the horizontal plane. The 45° orientation is a compromise design between these two extremes.

The simulated flow patterns for the three slide-gate orientations at the center planes and view into the ports are shown in Figures 3.21 and 3.22 for the conditions shown in Table 3.1. The simulated gas distribution for each of these three cases is shown in Figures 3.23-3.25 respectively. Jet properties at the port outlets are compared in Figures 3.26-3.31.

For the 0° orientation, more steel (over 60%) flows from the left port, which is the side opposite to the gate opening. This uneven flow distribution causes the biased flow in the mold, with associated quality problems. A much larger back flow zone is found at the right port (32%) than at the left port (11%). Two symmetric small vortices form at the center plane, as shown in

Figure 3.21(B), and evolve into almost straight jets exiting the ports, as seen in Figure 3.22 for the 0° orientation. A high gas concentration collects at the upper portion of the ports. This gas exits the nozzle from the very top of the port, forming a separate upward jet in addition to the main downward jet containing very little gas.

The 90° orientation gate generates symmetric flow from the two ports, so avoids left-right flow pattern in the mold. However, a single strong vortex develops through the entire nozzle that extends a strong swirl component to the jet leaving both ports. The swirling jets move toward the wide face opposite to the gate opening, as indicated by the horizontal jet angle in Figure 3.20. Most of the gas exits the nozzle from the very top of the port at the gate opening side, forming a separate upward jet.

The 45° orientation gate creates only a slight improvement on the left-right biased flow through the two ports, relative to the 0° orientation. About 58% liquid flows from the left port. The back flow zone at the right port drops to 24%, and the left port is the same as the 0° orientation (11%). Furthermore, the jet vortex pattern creates flow asymmetries in the horizontal plane that are very close to that found for the 90° orientation configuration.

The combined effects of slide-gate orientation and gas injection, on the jet are quantified by the weighted-average characteristics at the port, defined in Equations 3.20-3.25. The trends are plotted in Figures 3.26-3.31. Each point on those plots represents one simulation performed on the Standard Nozzle for the operation conditions in Table 3.1, except for the gas flow rate and the slide-gate orientation.

Vertical jet angle

The vertical jet angle measures when the overall average jet flow is directed. A positive vertical jet angle corresponds to a downward jet. It is noticed that the vertical jet angle is only slightly steeper than the port angle for the no gas condition. With increasing gas injection, the buoyancy bends the average jet upward. The jet angle becomes even shallower than the port angle of the nozzle when the gas exceeds. This observation differs from that of previous single–phase flow modeling [1] which found the jet angle always to be much steeper downward than the port angle. This is likely due to the shallower port height and the increased port thickness of this particular nozzle geometry.

Increasing gas injection flow rate gives buoyancy to the jet, so that it is directed less downward when it leaves the nozzle. This is quantified by the decrease in vertical jet angle seen in Figure 3.26. For 0° and 45° orientation without gas, the vertical jet angles at the left port are shallower than at the right port (on the gate opening side). The 45° orientation shows only a limited improvement in reducing the asymmetry of the jet angles between the two ports. On the other hand, gas injection may reduce the asymmetry for both 0° and 45° orientations. Without gas, both 0° and 45° orientations have shallower vertical jet angles at the left port and steeper jet angles at the right ports relative to those with 90° orientation.

Horizontal jet angle

The horizontal jet angle reflects how the average jet flow may deviate away from the center plane of the mold wide face. A positive horizontal jet angle in Figure 3.27 corresponds to a deviation toward the wide face opposite of the gate opening, as shown in Figure 3.20.

For the 0° orientation, the average horizontal jet angle is always zero due to symmetry, although the jet splits toward both wide faces. The 90° and 45° orientation configurations have significant horizontal jet angles due to the strong asymmetric vortex leaving the ports. On average the flow is directed toward the wide face opposite to the gate opening. For a typical slab 8”x60”, the jet will still impinge mainly on the narrow face even for the worst asymmetry (5.3°).

Without gas, the largest horizontal jet angle occurs at the left port of the 45° orientation, no improvement on flow symmetry. With gas injection above 8%, the horizontal jet angle is greatest for the 90° orientation, which has the strongest swirl component. Horizontal jet angle decreases with increasing gas flow rate.

Jet speed

The jet speed defined in Equation 3.24 and plotted in Figure 3.28 is the weighted-average of liquid velocities flowing out of the port. For a fixed liquid flow rate, jet speed increases with increasing back flow zone size and gas injection rate. For the 0° and 45° orientations, the jet speed at the left port is smaller than at the right port, whereas 90° orientation gives symmetric jet speed for both ports. The jet speed for 90° orientation is the smallest among three orientation cases, while 0° orientation has the largest jet speed.

Figure 3.28 also shows slightly increasing jet speed with increasing gas flow rate. This is because the same liquid flow rate is assumed for all simulation cases. It should be noted that gas injection only increases the local liquid velocity, but not the liquid mass flow rate out of the ports. This acceleration of the liquid is due to less space available when the injected gas takes some.

Back-flow zone fraction

The back-flow fraction is the area of the nozzle port where flow reenters the nozzle relative to the total port area. Back-flow commonly occurs at the upper portion of the nozzle port, as shown in Figures 323-3.25.

Figure 3.29 shows that the back-flow zone fractions at the left port are much smaller than at the right port for 0° and 45° orientations. The larger back-flow zone develops at the gate opening side. For all cases, the back-flow zone decreases with increasing gas flow rate.

It was observed in water modeling [18] that unsteady periodic pulsing of the jets at the ports increased with larger back flow zones. This may increase surface level fluctuations and other problems in the mold.

Biased mass flow

Biased or asymmetric mass flow refers to the difference in flow rate out of the two ports due to the off-center throttling effect of the slide-gate. Figure 3.30 shows the liquid and gas mass flows out of the left port; the rest of the mass flow leaves the right port.

The 0° orientation naturally generates the most biased mass flow with over 60% of the liquid mass flow leaving the left port, whereas the 90° orientation gives an unbiased 50%. This agrees with Wang's observation for single-phase flow [18]. The 45° orientation is supposed to improve the symmetry, but the results show about 58% of the liquid exits the left port for all studied cases. This negligible improvement contrast with Wang's finding [18] and suggests that effect of orientation on the biased mass flow may vary with nozzle design. Gas injection has very little influence on the biased liquid flow, although the gas flow tends to become more symmetrical with increasing gas injection.

Turbulence kinetic energy

The turbulence of the jets increases with gas injection, as shown by the average turbulence kinetic energy (K) results in Figure 3.31. The highly swirling jets of the 90° orientation generate the largest turbulence energy (K) of the three orientations. The average turbulence dissipation rates, not shown here, have the same trend as the turbulence kinetic energy.

3.5.3 Effect of Casting Speed

High casting speed means high productivity, thus is always one of the main concerns to the steel-making industry. Three casting speed conditions are simulated in the parametric studies. Besides the normal casting speed (1m/min) for the standard condition in Table 3.1, the other two are intermediate casting speed (1.5m/min) and super high casting speed (2.3 m/min) separately.

All casting speeds refer to 8”x52” slab. All simulated cases here have the same gate orientation (45°) and fixed gate opening (F_L=50%). Casting speed can be adjusted by changing either slide-gate opening or tundish bath depth. Therefore, the casting speed changes discussed here are achieved by adjusting the liquid head in tundish. The slide-gate opening will be addressed separately. In this way, effects of the casting speed, tundish height, slide-gate opening, gas injection etc. can be isolated and investigated independently.

The effects of casting speed, together with the effects of gas injection, on the jet are quantified by the weighted-average jet characteristics, which are plotted in Figures 3.32-3.37. Each point on those plots represents one simulation performed on the Standard Nozzle for operation conditions in Table 3.1, except for the fixed 45° orientation and varying casting speed and gas flow rates. For single-phase flow, the casting speed has little influence on the jet characteristics that represent the flow patterns such as vertical jet angle, horizontal jet angle, back flow zone and biased mass flow. This is shown as almost constant values for all different casting speed at zero gas volume fraction in Figures 3.32, 3.33, 3.35 and 3.36. Jet speed and turbulence energy naturally increase with increasing casting speed, as shown in Figures 3.34 and 3.37. This agrees with previous finds from the single-phase flow studies [1, 17].

With gas injection, vertical jet angle becomes shallower with increasing gas injection due to the gas buoyancy, and horizontal jet angle and back flow zone become smaller with increasing gas injection. This effect of the gas becomes less influential with increasing casting speed, shown as the jet property values closer to those in zero-gas condition seen in Figures 3.32, 3.33 and 3.35. Physically, this may be explained as that the buoyancy due to gas injection and the liquid momentum compete with each other, and the liquid momentum dominates over buoyancy as casting speed increases. Both casting speed and gas injection have little influence on biased mass flow, as seen in Figure 3.36. For a constant gas injection volume fraction (NOT gas flow rate), increasing casting speed produces steeper downward jet angle, larger horizontal jet angle, larger back flow zone, higher casting speed and stronger turbulence.

3.5.4 Effect of Slide-Gate Opening

Five different gate opening fractions are simulated in this parametric study, ranging from F_L=40% to full opening (F_L=100%). Slide gate opening fraction F_L is a linear fraction of the opening distance, defined as the ratio of the displacement of the throttling plate (relative to the just-fully closed position) to the bore diameter of the SEN, as shown in Figure 3.38. This measure can be converted to other definitions of gate opening, such as displacement relative to a reference position, F_P , which is usually used in the plant, by

$$F_P = (1 - M)F_L + M \tag{3.27}$$

where
$$M = \frac{T - D}{T} \tag{3.28}$$

The most relevant way to denote gate opening is via the area fraction, F_A, found by

$$F_A = \frac{2}{\pi}\cos^{-1}\left(1 - F_L\right) - \frac{2}{\pi}\left(1 - F_L\right)\sqrt{1 - \left(1 - F_L\right)^2} \tag{3.29}$$

Figure 3.39 shows the converted F_A and F_P for two typical off-set fractions, where M=24% for Inland Steel and M=41.7% for LTV Steel. All five cases have the same geometry and conditions for the Standard Nozzle in Table 3.1 except for gate opening. All cases are run with the same casting speed and no clogging. In practice, gate opening is adjusted to compensate for clogging build-up in order to maintain a constant casting speed.

The jet characteristics for all five simulations are plotted in Figure 3.40. The horizontal jet angle decreases with increasing gate opening, and approaches zero as opening approaches 100%, as shown in Figure 3.40(A). This is natural because the off-center blocking effect decreases as gate opening approaches the symmetrical full open condition. All other jet characteristics are found to have maximum or minimum values near the gate opening F_L=60% (about 50% area fraction). The vertical jet angle first increases with increasing gate opening. However, when gate opening (F_L) is over 60%, the vertical jet angle decreases with increasing gate opening. The jet speed and back flow zone have these same trends while the turbulence energy and dissipation have opposite trends. This critical gate opening F_L=60% matches the gate opening for the worst vacuum, which will be addressed in Chapter 4.

3.5.5 Effect of Bubble Size

The effect of bubble size was investigated by increasing bubble diameter from 1mm to 3mm and 5 mm for the Standard Nozzle and conditions in Table 3.1. Important jet characteristics are compared in Figure 3.41.

Larger bubbles cause a shallower vertical jet angle due to their greater buoyancy. This effect becomes more significant at higher argon injection flow rate. The horizontal jet angle increases only slightly with increasing bubble size. Bigger bubbles tend to reduce the size of the back flow zone but enhance turbulence, especially at high gas flow rate.

3.5.6 Effect of Nozzle Port Design

The effects of nozzle design parameters, including the shape, angle, height, width and thickness of the ports and the bottom geometry, on flow pattern in SEN and jet characteristics have been reported for single-phase flow with the finite element models [17]. A parametric study here investigates the effect of port angle and port shape with argon gas injection.

Nozzle port angle

Three different vertical port angles (15° up, 15° down and 25° down) are simulated for the Standard Nozzle and conditions in Table 3.1. Figure 3.42 compares the predicted flow patterns in the wide face and at the outlet port. The calculated jet characteristics are plotted in Figure 3.43. It can been seen that the port angle greatly changes the flow pattern, vertical jet angle and back flow zone fraction. A steeper downward port angle generates a steeper downward jet angle. This is consistent with previous findings without gas [1, 17]. The vertical jet angle is consistently a few degrees shallower than the port angle, owing to the gas buoyancy. Without gas, the jet angle is steeper downward than the port angle, although for this nozzle geometry, the difference was very slight.

The upward port angle generates an average jet angle (18.6° upward) directed even more upward than the port angle (15° upward). This shows the important influence of gas buoyancy on the flow. The horizontal jet angle and back flow zone are similar for the 15° up and 15° down ports. However, with 25° down ports, the back flow zone disappears and the average horizontal jet angle drops to almost zero. The turbulence energy are unaffected by port angle.

Nozzle port shape

Three different port shape designs (78mmx78mm square, 64mmx95mm rectangle, and 55mmx122mm slender rectangle) are simulated for the Standard Nozzle and conditions in Table 3.1. All three designs have the same port area and same port angle (15° downward). The flow patterns are compared in Figure 3.44 and the jet characteristics in Figure 3.45.

Port shape greatly changes the vertical jet angle. The square port generates the shallowest jet. The jet from the rectangular (64x95) port is angled about the same as the port angle. The slender rectangle (50x122) port produces a very steep downward jet (27.8°down) despite the high gas injection rate (16%). All three designs have small horizontal jet angles (< 3°) which decrease slightly as the port shape becomes more slender. The square port splits off the largest upward jet, and also has the largest back flow zone and jet speed among the three designs. Both rectangle port designs have much smaller back flow zones, showing a large single swirl covering over 90% of the port area. The slender rectangle port has a slightly larger back flow zone than the rectangular port.

3.6 Pressure Drop across Nozzle

The pressure drop across the nozzle can be output from the pressure solution for each case of the foregoing parametric studies. Figure 3.46(A) shows the effects of gas injection flow rate and gate orientations on pressure drops across the nozzle. It can be seen that the gate orientation has very little influence on the pressure drop. The pressure drop linearly increases with increasing gas injection. This is due to the extra resistance to the downward liquid flow by the gas buoyancy. The pressure drop increases with increasing casting speed for a fixed gate opening, as shown in Figure 3.46(B), and decreases with increasing gate opening for a fixed casting speed, as shown in Figure 3.46(C). This is simply because the flow resistance increases with increasing flow rate and decreasing gate opening.

The pressure solutions also reveal that the pressure drops across the nozzle rarely change with bubble size, port angle and port shape although they might greatly change the flow pattern and jet characteristics.

Pressure drop across the nozzle is related to tundish bath depth and other operation conditions [66, 67]. The development of this relationship model is detailed in the next chapter.

3.7 Using Jet Solution in Mold Flow Modeling

Flow in the mold is often modeled separately from the nozzle to simplify mesh generation [22, 23, 55, 68, 69]. The nozzle port is then the inlet boundary of the mold domain. The inlet boundary condition can be obtained from the flow simulation result for the corresponding nozzle.

There are three ways to implement this inlet boundary condition for mold simulation. First, the overall average jet characteristics, defined in Equations 3.20-3.25, are directly used as the inlet boundary conditions. Specifically, a uniform velocity with the value of the jet speed directed in the vertical and horizontal jet angles is specified on the outflow region or the lower part of the nozzle outlet port. The turbulence energy K and dissipation ε for the inlet are the weighted average values for the jet. A uniform gas volume fraction is assumed for the whole inlet boundary. This method is simple to specify and also a reasonable approximation for the symmetric low-gas flow, such as found in 0° gate orientation or stopper-rod nozzles. For those symmetric low-gas jet flows, the upper portion of the port is usually pure back flow zone and the symmetric swirls are relatively weak as they develop to the port.

For those cases with two separate jets on the same port, which are often found for the 45° or 90° gate orientation with high gas flow rate, the split-jet calculation can be used as the inlet boundary conditions for the mold flow simulation. The inlet boundary is divided into 3 contingent sections, the upper section for the upward jet, the lower section for the downward jet, and the middle section for the back flow zone. The section size depends on the occupied area fraction for the corresponding jet. The average jet properties for the upward jet are specified on the upper section, and the average jet properties for the downward jet are specified on the lower section. Each section still has its uniform velocity, jet angles, gas volume fraction, and turbulence properties, therefore easy to implement. A zero velocity boundary is set for the back flow zone in the middle section.

Another method is to use the nozzle simulation results directly for the inlet boundary conditions for the mold, by inputting the numerical solution (velocity components for liquid and gas, volume fraction, and turbulence properties) for each cell on the port. This can be easily implemented in a self-developed CFD program and can also be done using a user subroutine for a commercial CFD program. The meshes for the nozzle port and for the mold inlet should be exactly same so no interpolation is needed. This method avoids simplification for the jet thus can improve modeling accuracy. Of course, the nozzle and mold can be combined to model to avoid this problem, but that may cause other difficulties in mesh generation and convergence, and need more computational resources.

3.8 Summary

The two-phase turbulent flow of liquid steel and argon bubbles in a slide-gate nozzle can be simulated with Eulerian multiphase multi-fluid model using a three-dimensional finite difference method. Model predictions agree both qualitatively and quantitatively with the measurements conducted using PIV (Particle Image Velocimetry) on a 0.4-scale water model. The model is suitable for the dispersed bubbly flow that covers the whole practical range of gas injection rate. A weighted average scheme for the overall outflow is developed to quantify the jet characteristics such as jet angle, jet speed, back flow zone fraction, turbulence and biased mass flow. It is possible to calculate the characteristics of the split jets on each port separately rather than treat the whole outward flow as one average jet. The model is employed to perform extensive parametric studies to investigate the effects of casting operation conditions such as gas injection, slide-gate orientation, casting speed and gate opening, and nozzle port design including port angle and port shape on flow pattern. The effects are quantified using weighted average jet characteristics. The main findings are summarized below:

- Gas injection greatly affects the flow pattern and jet characteristics. Increasing gas injection bends the jet upward, enhances turbulence level, and reduces back flow zone size. A small mount of the gas bubbles are carried by the downward liquid jet while most argon bubbles exit the nozzle from the upper portion of the ports, forming a separate upward jet due to the gas buoyancy.

- Effect of gas injection becomes less influential with increasing casting speed.
- For the single-phase flow, casting speed has little influence on those jet characteristics that represent the flow pattern such as vertical jet angle, horizontal jet angle, back flow zone and biased mass flow.
- The off-center blocking effect of the slide-gate generates asymmetric flow.
- The 0° gate orientation generates the worst biased flow between the left and right ports. Specifically, the port on the gate opening side has a steeper jet angle, much larger back flow zone and less than 40% of the liquid mass flow.
- The 90° gate orientation generates strong swirl and asymmetry in the other plane, with a horizontal jet angle that directs the average jet toward the wide face opposite the gate opening side.
- The 90° gate orientation generates strong swirl on the jet that likely has a great effect on flow in the mold.
- The 45° gate orientation appears to be a poor compromise because it has all the asymmetries of both 0° and 90° design at almost same levels.
- The horizontal jet angle decreases with increasing gate opening, and becomes zero for the full opening. The vertical jet angle, jet speed and back flow zone reach their maximum values near gate opening F_L=60%, and decrease as the gate opening away from this critical region.
- Increasing gas injection seems to reduce the asymmetry slightly. Larger bubbles have more influence on the flow pattern for a given gas fraction due to their greater buoyancy.

- Port angle and port shape both have great influence on the flow. The vertical jet angle becomes steeper with steeper port angle and more slender port shape.
- Pressure drop across the nozzle is insensitive to slide-gate orientation, bubble size and port design. However, pressure drop increases with increasing gas injection, increasing casting speed, and decreasing gate opening.

Table 3.1 Nozzle dimension and operation conditions

Dimension & Condition	Standard Nozzle	0.4 Scale PIV Nozzle	Validation Nozzle A	Validation Nozzle B
UTN top diameter (mm)	114	28	115	100
UTN length (mm)	241.5	132	260	310
Gate thickness(mm)	63	18	45	45
Gate diameter(mm)	78	28	75	70
Shroud holder thickness (mm)	100	18	100	66
SEN length (mm)	748	344	703	776
SEN bore diameter (mm)	78	32	91~96	80
SEN submerged depth (mm)	200	71-80	120~ 220	165
Port width X height(mmXmm)	78X78	31X32	75X75	78X78
Port thickness(mm)	29	11	30	28.5
Port angle (down)	15°	40° upper edge 15° lower edge	35°	15°
Recessed bottom well depth (mm)	12	4.8	12	12
Slide gate orientation	90°	90°	90°	90°
Gate opening (F_L)	50%	52%		52%
Casting speed (V_C) (m/min, 8"x52"slab)	1			1.21
Liquid flow rate (l/min)	268.4	42.4		324.8
Tundish depth (H_T) (m)		0.4~0.41	1.125	0.927
Argon injection flow rate (Q_G) (SLPM)	10	2.6	7~10	14
Argon injection (hot) volume fraction f_g	16%	5.8%		17.7%
Argon bubble diameter (D) (mm)	1	1	1	1

Table 3.2 Comparison of the overall average one-jet and the split-jets

Port	Left Port			Right Port		
Jet mode	Split-jets		One-jet	Split-jets		One-jet
Jet	Upward jet	Downward jet	Overall one-jet	Upward jet	Downward jet	Overall one-jet
Vertical jet angle	21.65° upward	8.30° downward	4.55° downward	20.59° upward	7.86° downward	2.41° downward
Jet speed (m/s)	0.56	0.81	0.76	0.67	0.87	0.81
Horizontal jet angle *	-4.70°	1.86°	1.06	-1.43	2.89	2.09
Back flow zone fraction			8.3%			20.1%
Area fraction of port occupied by jet	34.0%	57.7%	91.7%	31.3%	48.6%	79.9%
Liquid flow fraction carried by jet	8.7%	48.1%	56.8%	9.2%	34.0%	43.2%
Jet gas fraction on the port	61.5%	10.9%	25.8%	61.3%	11.7%	30.7%
Gas flow fraction carried by jet	35.8%	15.1%	50.9%	37.5%	11.6%	49.1%

* Horizontal jet angle > 0 : toward the wide face opposite the opening of the gate

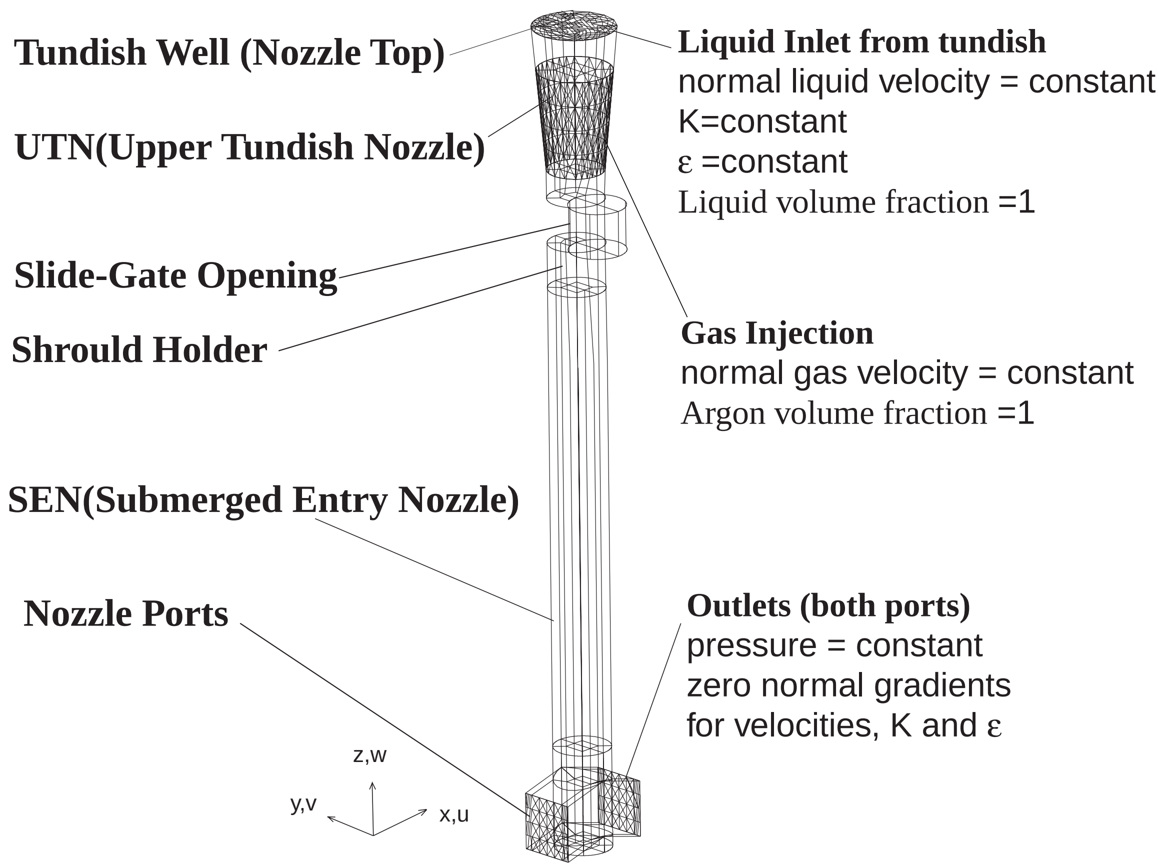

Figure 3.1 Computational domain and boundary conditions for the standard nozzle

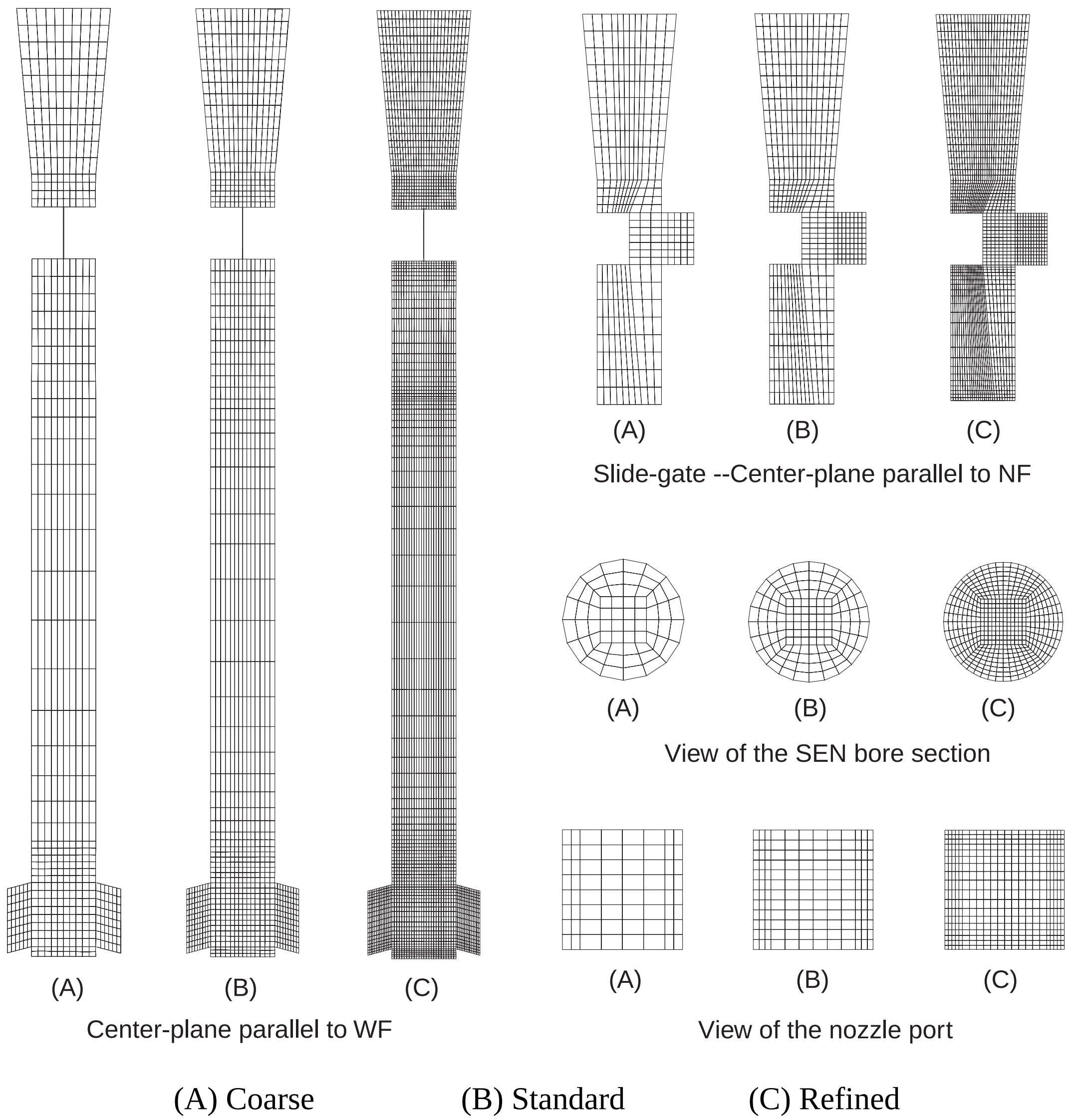

Figure 3.2 Grid resolution employed

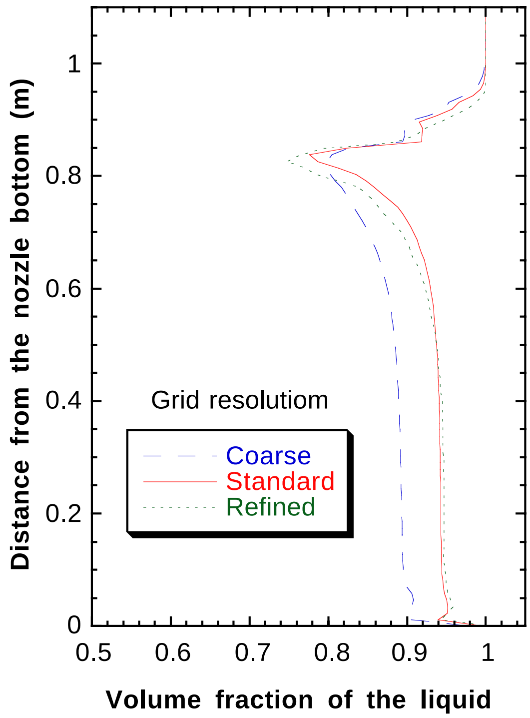

(A) along vertical z-axis of the nozzle

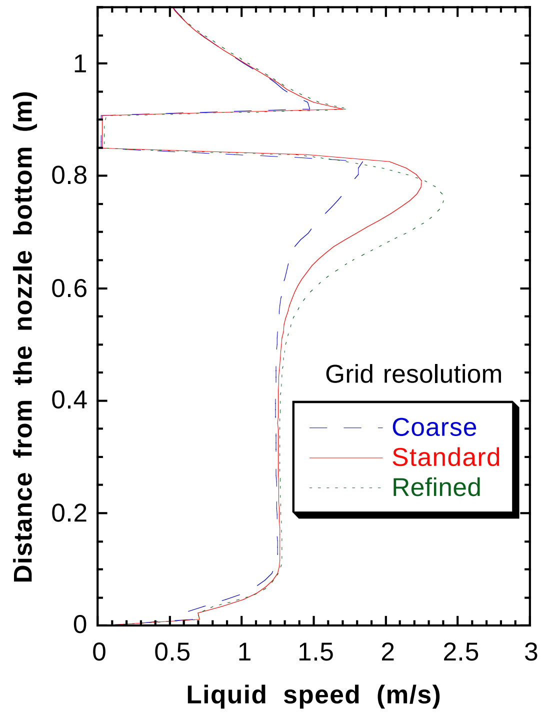

(B) along vertical z-axis of the nozzle

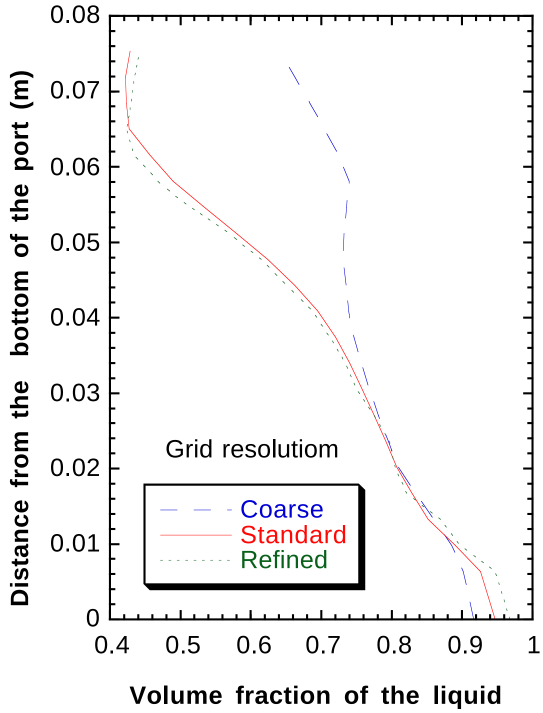

(C) along vertical centerline on the port

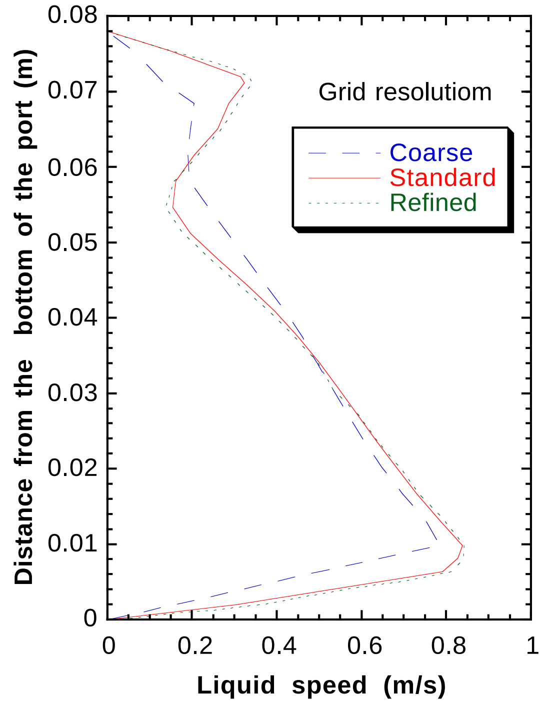

(D) along vertical centerline on the port

Figure 3.3 Model predictions for various grid resolutions

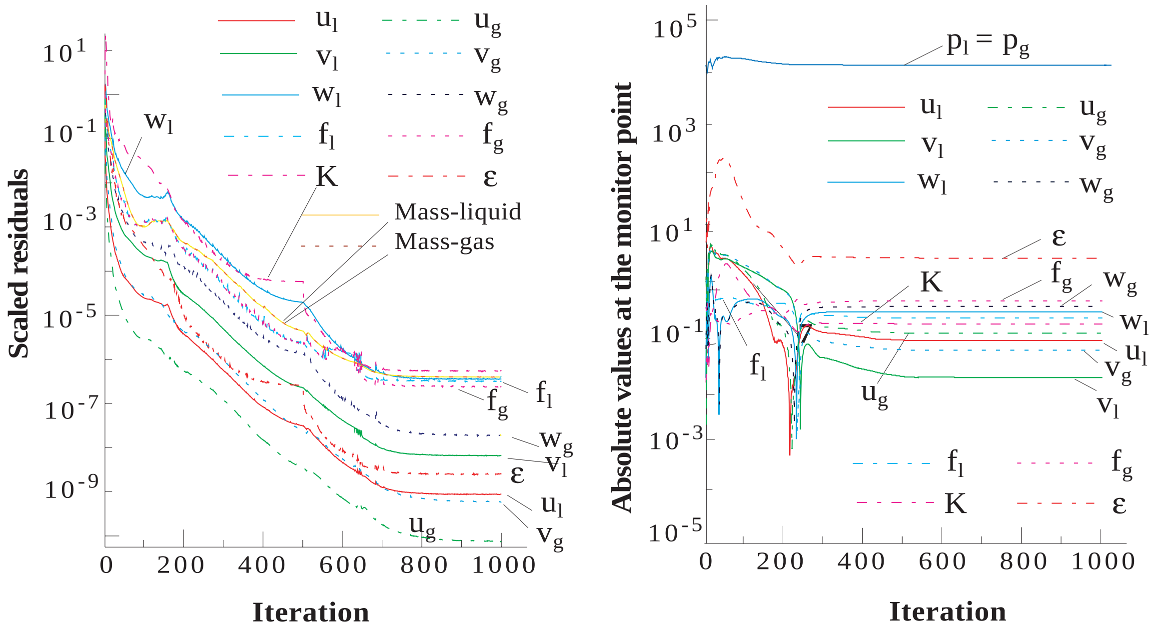

(A) Scaled residual history (B) Values history at the monitor point

Figure 3.4 Convergence history for a typical 2-phase turbulence flow simulation run

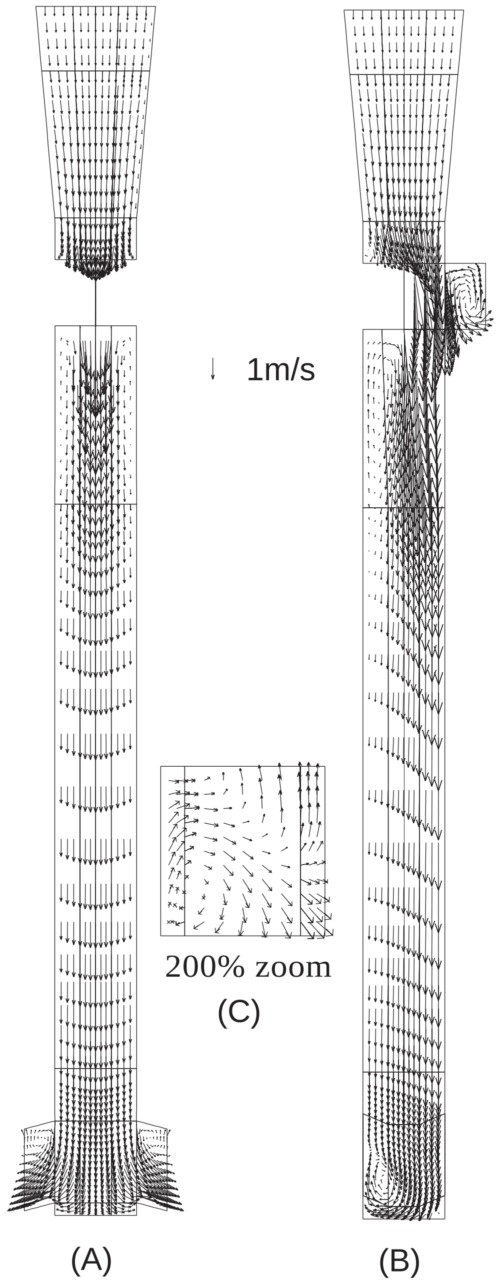

(A) Center plane parallel to WF (B) Center plane parallel to NF
(C) Port view, look into the left port (200% zoom)

Figure 3.5 Simulated flow field for the standard nozzle and conditions in Table3.1

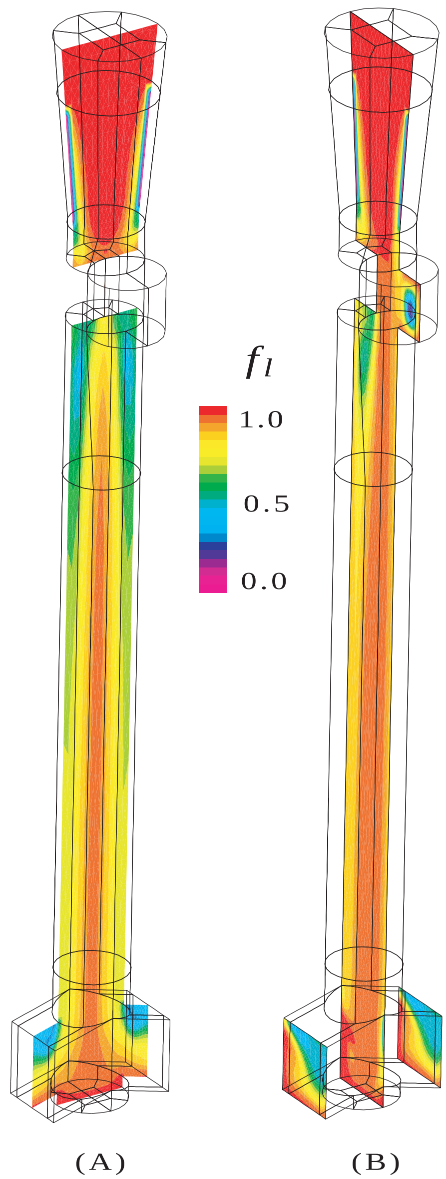

(A) Center plane parallel to WF (B) Port planes and center plane parallel to NF

Figure 3.6 Predicted argon gas distribution for the standard nozzle and conditions in Table 3.1

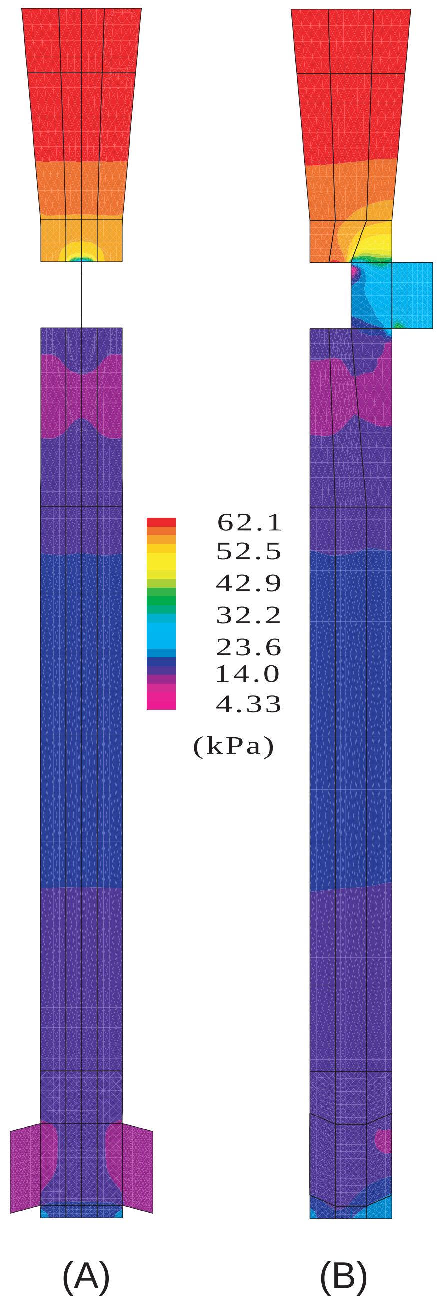

(A) Center plane parallel to WF (B) Center plane parallel to NF

Figure 3.7 Predicted pressure distribution for the standard nozzle and conditions in Table 3.1

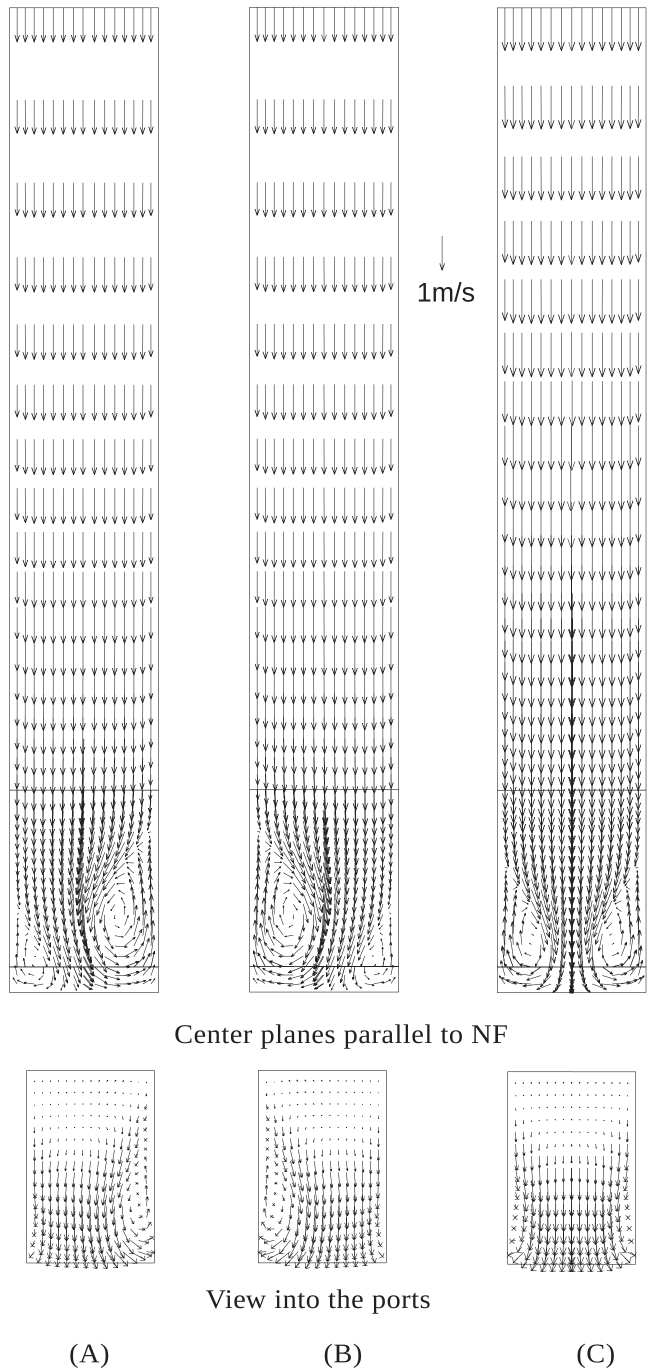

Figure 3.8 Predicted three vortex patterns for SEN under different initial conditions

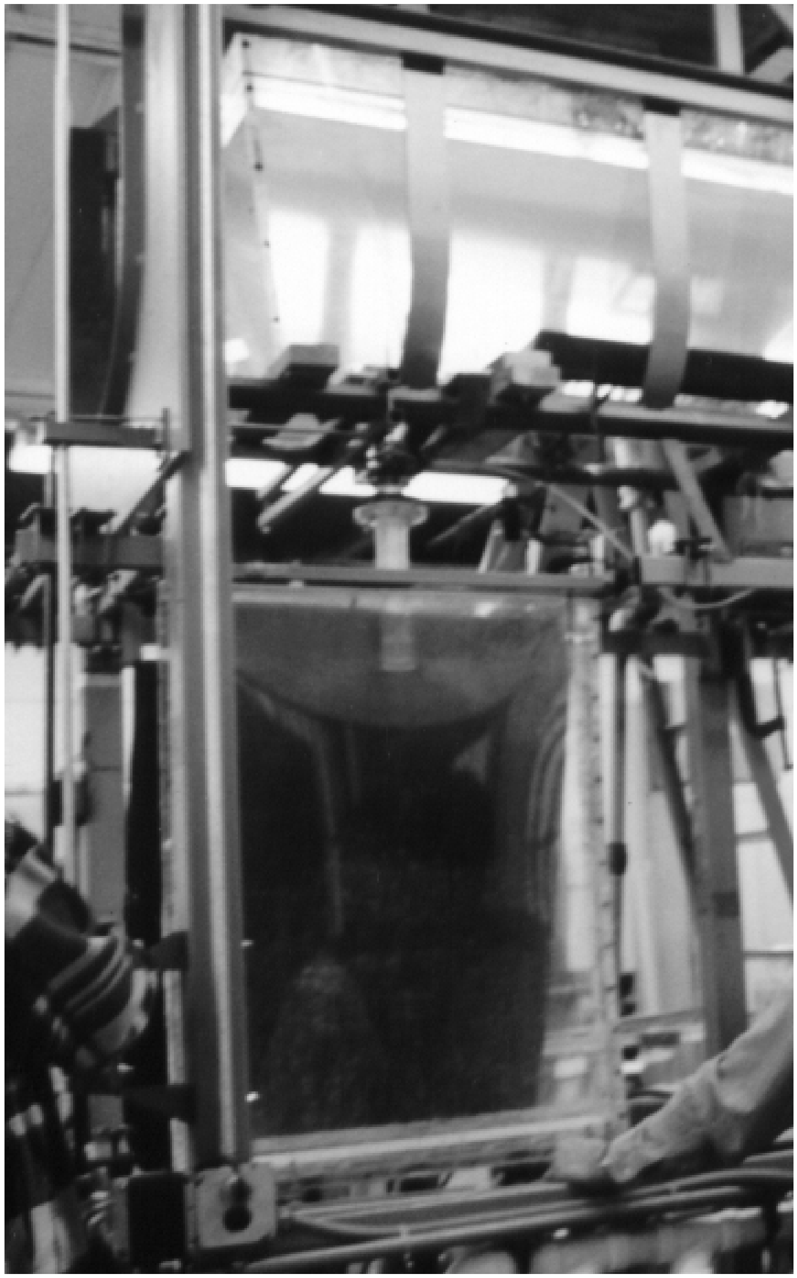

Figure 3.9 Photograph of the 0.4 scale “water caster” used in the experiments

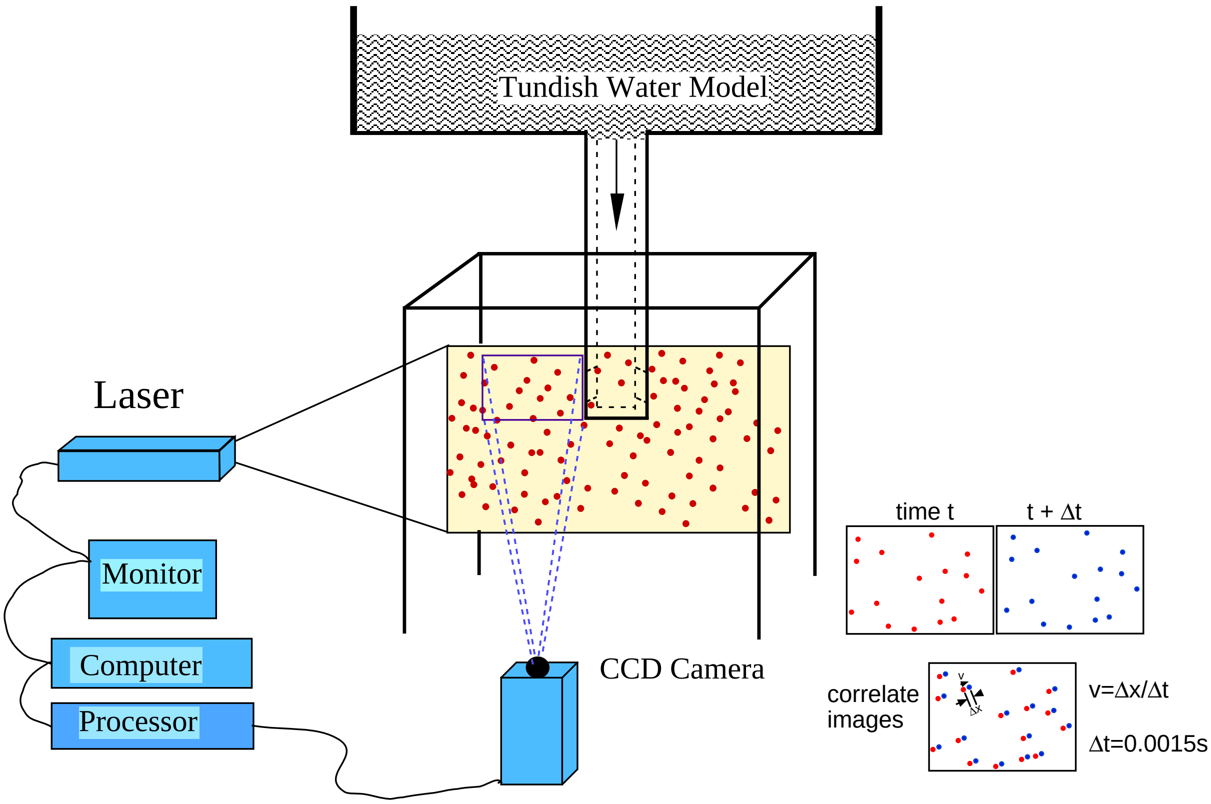

Figure 3.10 Schematic of PIV (Particle Image Velocimetry) system

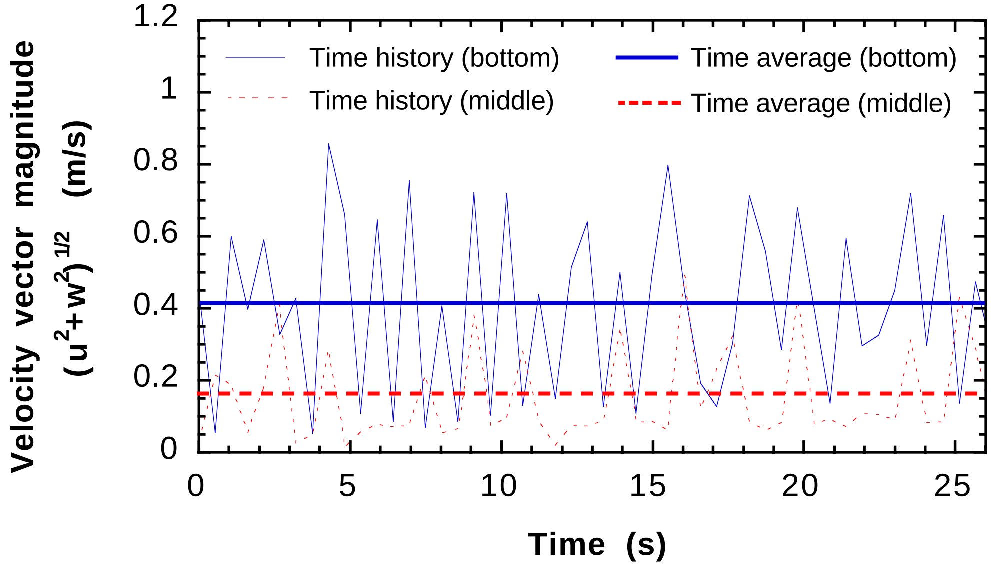

Figure 3.11 Time history records of PIV measurements of the velocity magnitude

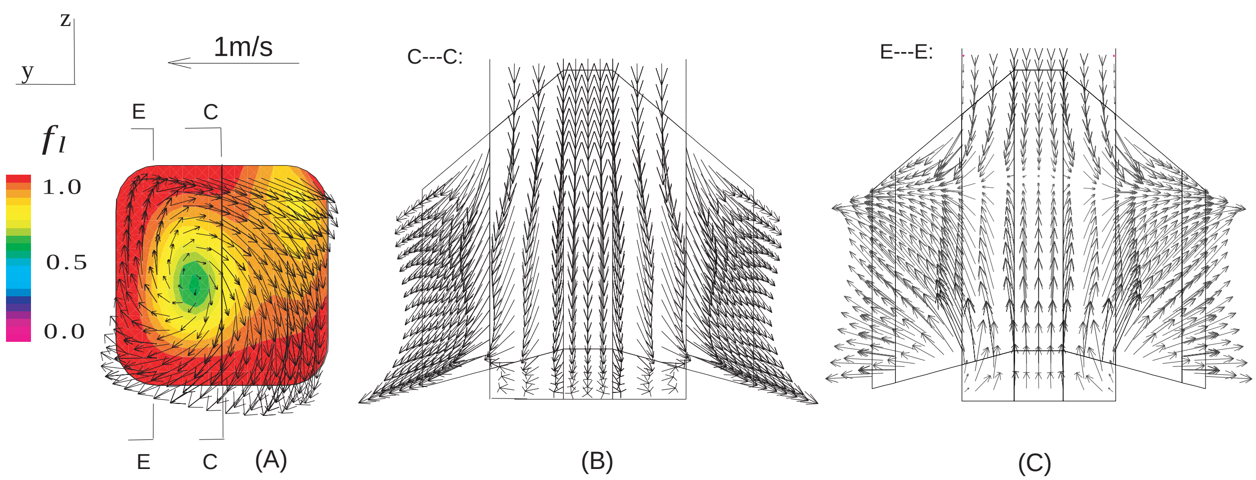

(A) end view from the left port (B) center-plane parallel to the wide face
(C) 12 mm from center-plane, parallel to the wide face

Figure 3.12 Predicted flow pattern and gas distribution at SEN port for PIV nozzle

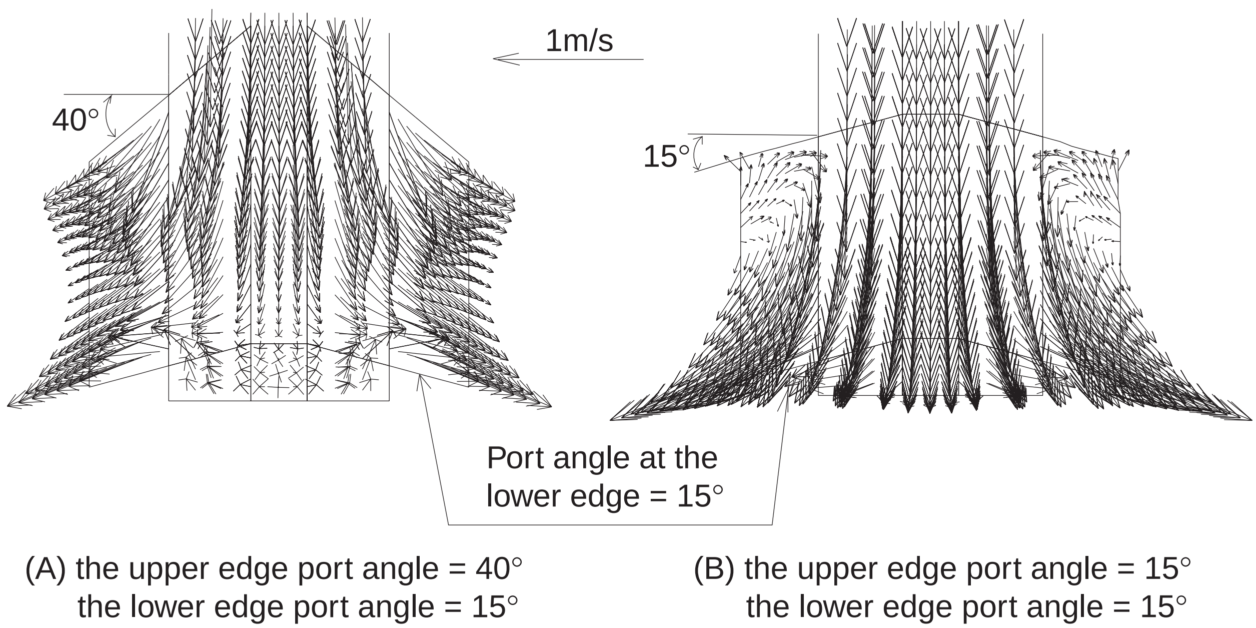

Figure 3.13 Effect of the upper edge port angle on back flow zone (y=3mm plane)

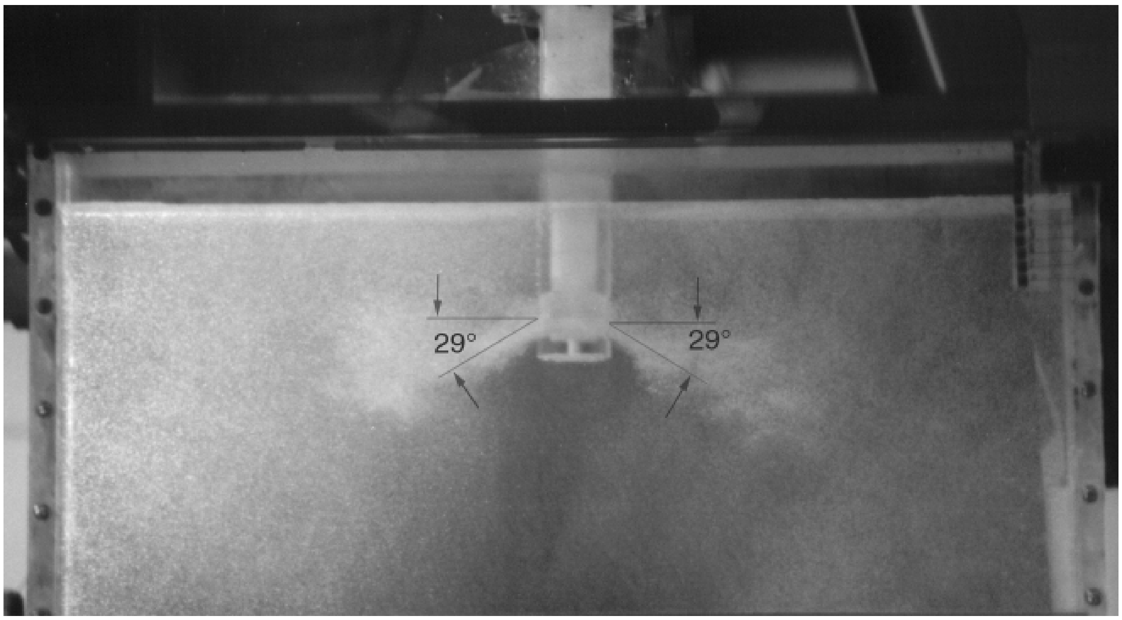

Figure 3.14 Flow pattern and jet photo showing vertical jet angle in water model experiment

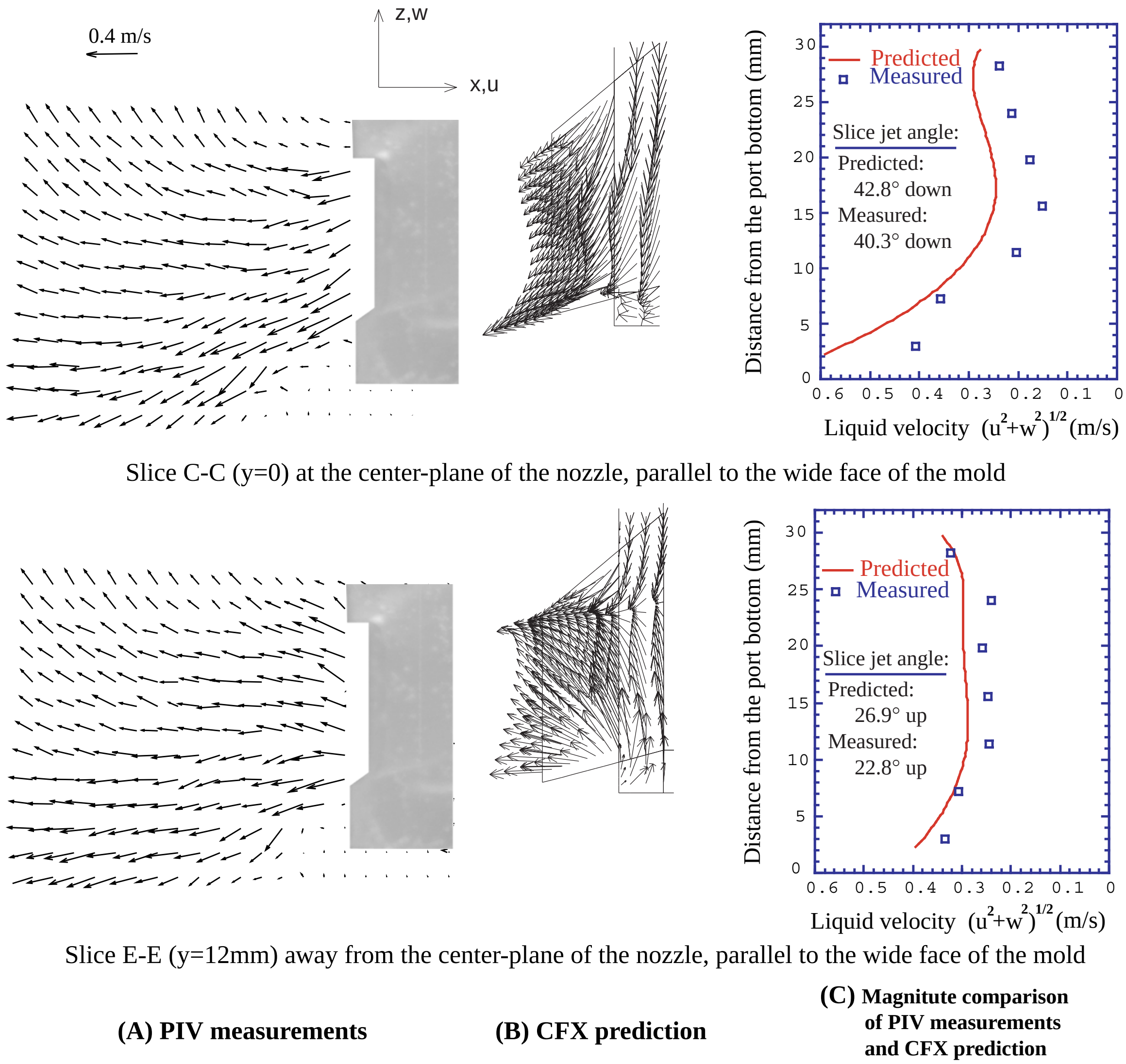

Figure 3.15 Comparison of PIV measurements and model prediction

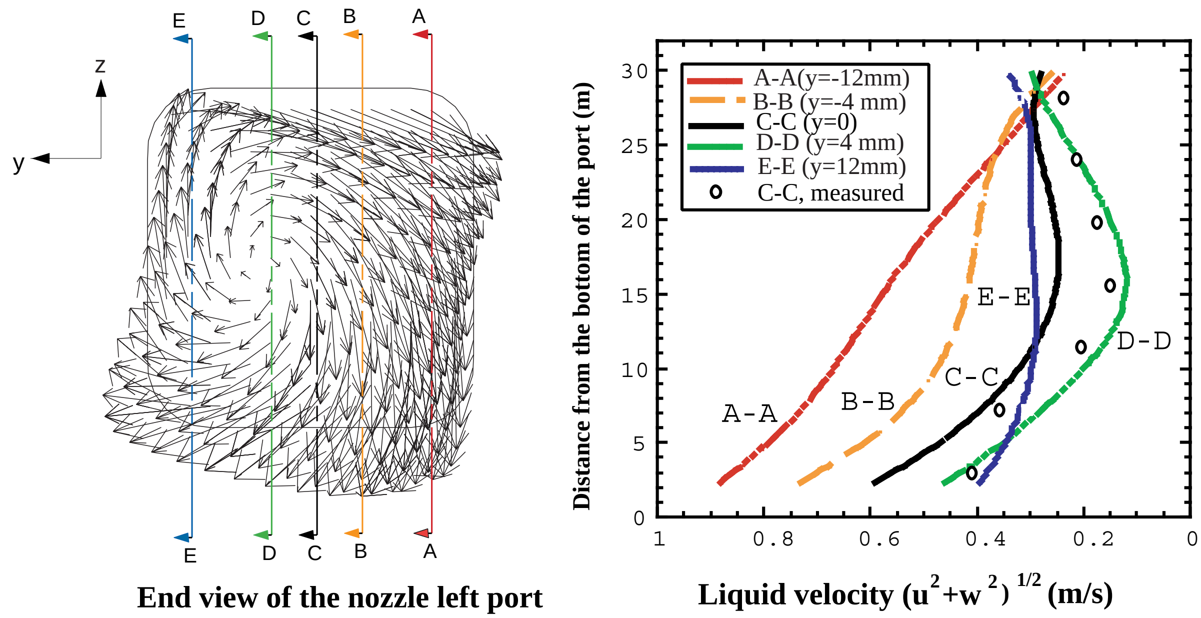

Figure 3.16 Vortex pattern at pot outlet and velocity profiles at different vertical slices of the nozzle port

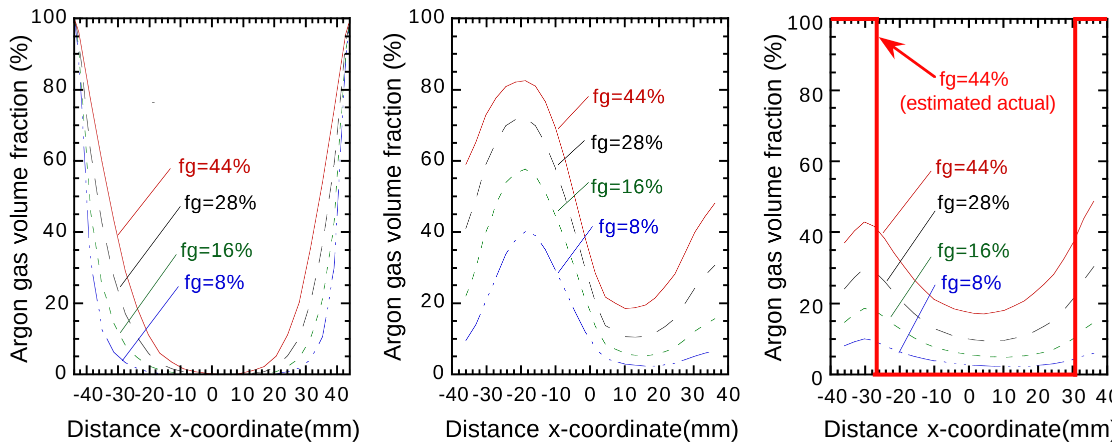

(A) gas injection region
z=1000mm

(B) below slide-gate
z=800mm

(C) middle of SEN
z=400mm

z—distance from the bottom of the nozzle

Figure 3.17 Effect of gas injection on gas volume fraction across nozzle bore on wide face center plane (45° gate orientation, 8~44% hot argon, F_L=50%, V_C=1m/min)

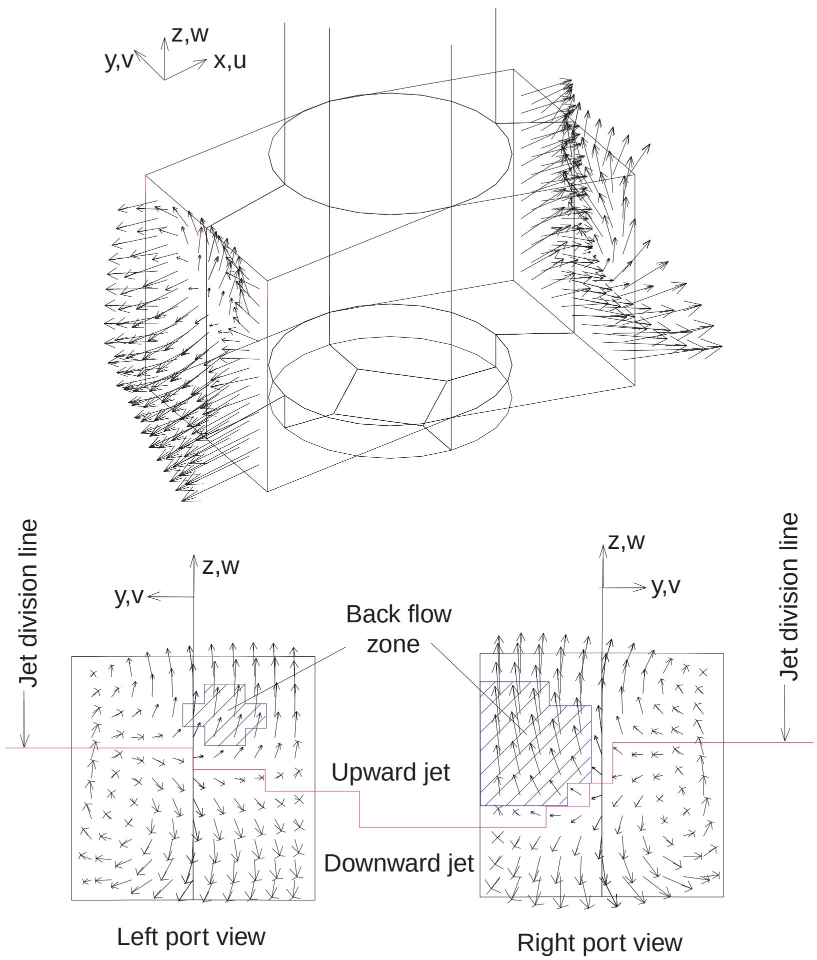

Figure 3.18 Flow pattern showing upward jet, downward jet and back flow zone on port outlets of the standard nozzle (45° gate orientation, 28% hot argon, F_L=50%, V_C=1m/min)

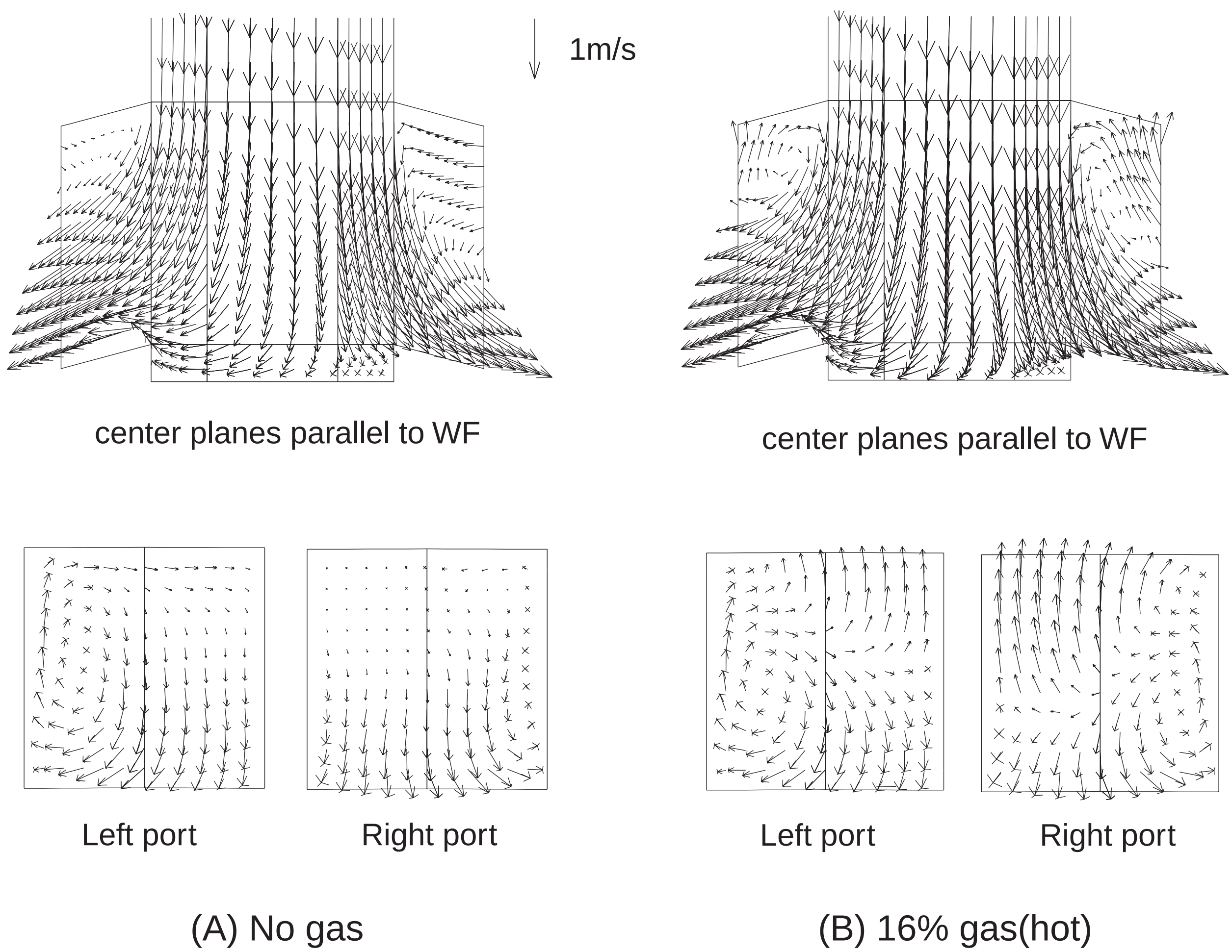

(V_C=1m/min, F_L=50%, 45° gate orientation)

Figure 3.19 Effect of argon gas injection on flow pattern in nozzle

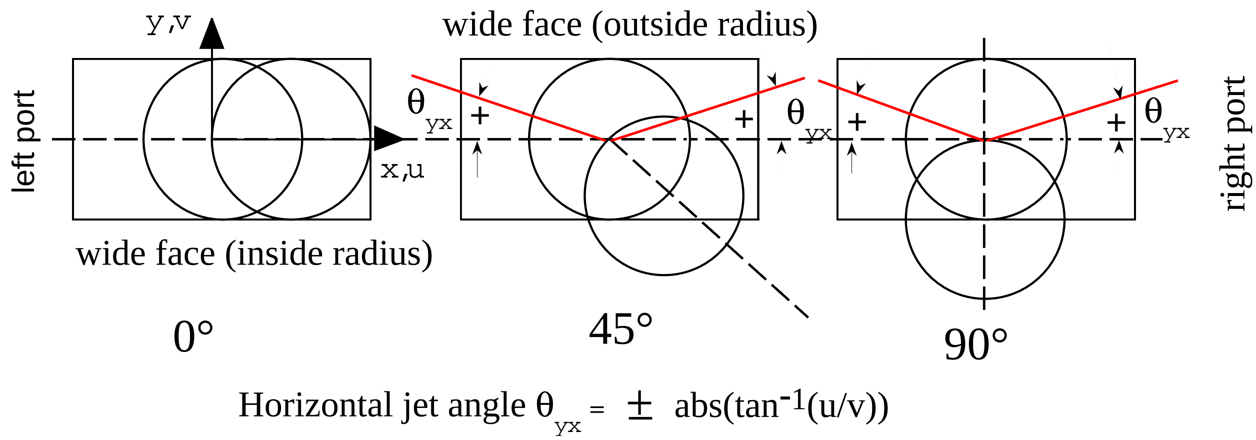

Figure 3.20 Schematic of the slide-gate orientation (top view) and horizontal jet angle

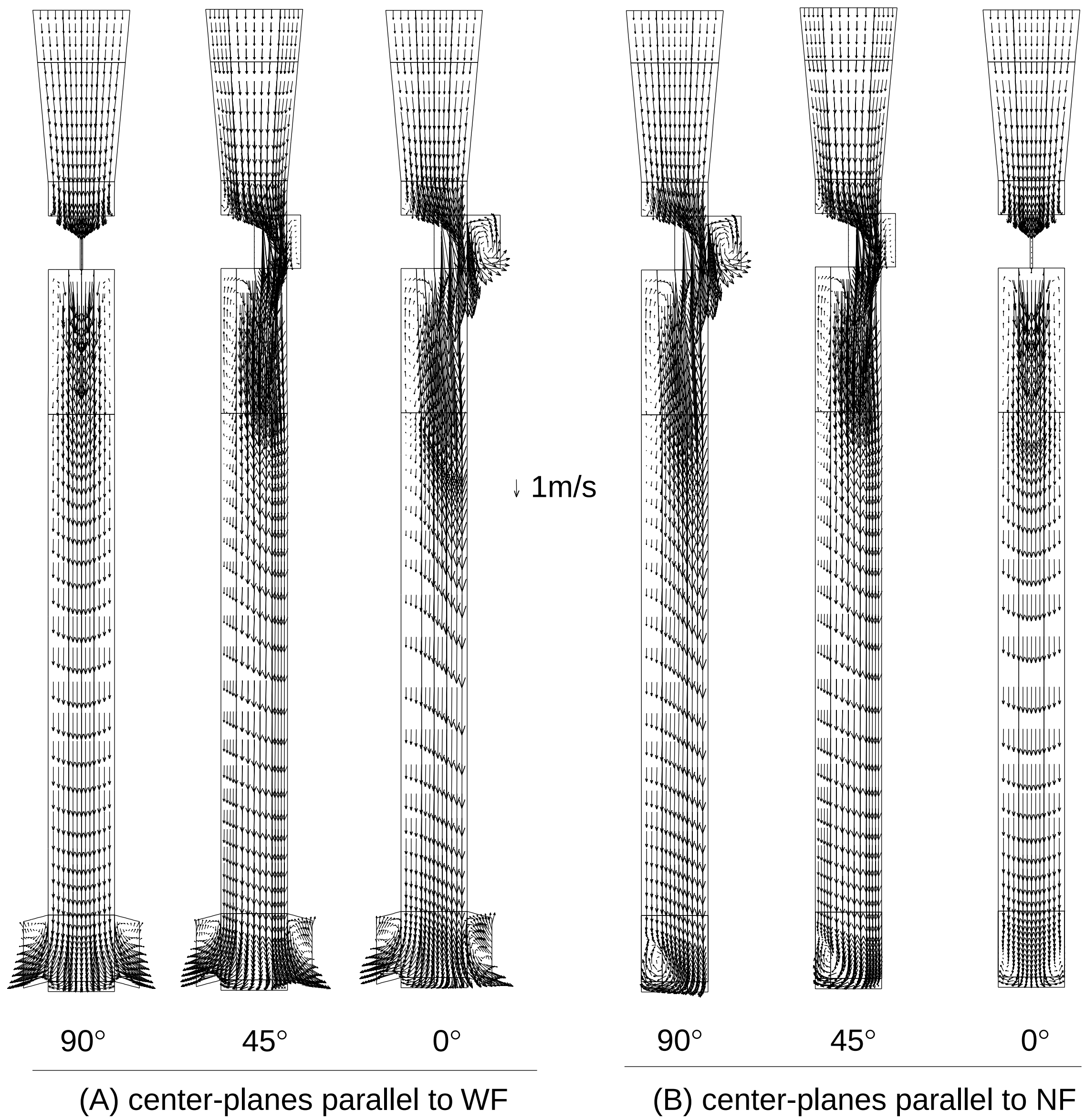

(V_C=1m/min, Q_G=10SLPM, f_g=16%(hot), F_L=50%,)

Figure 3.21 Flow field at the center planes for different gate orientations

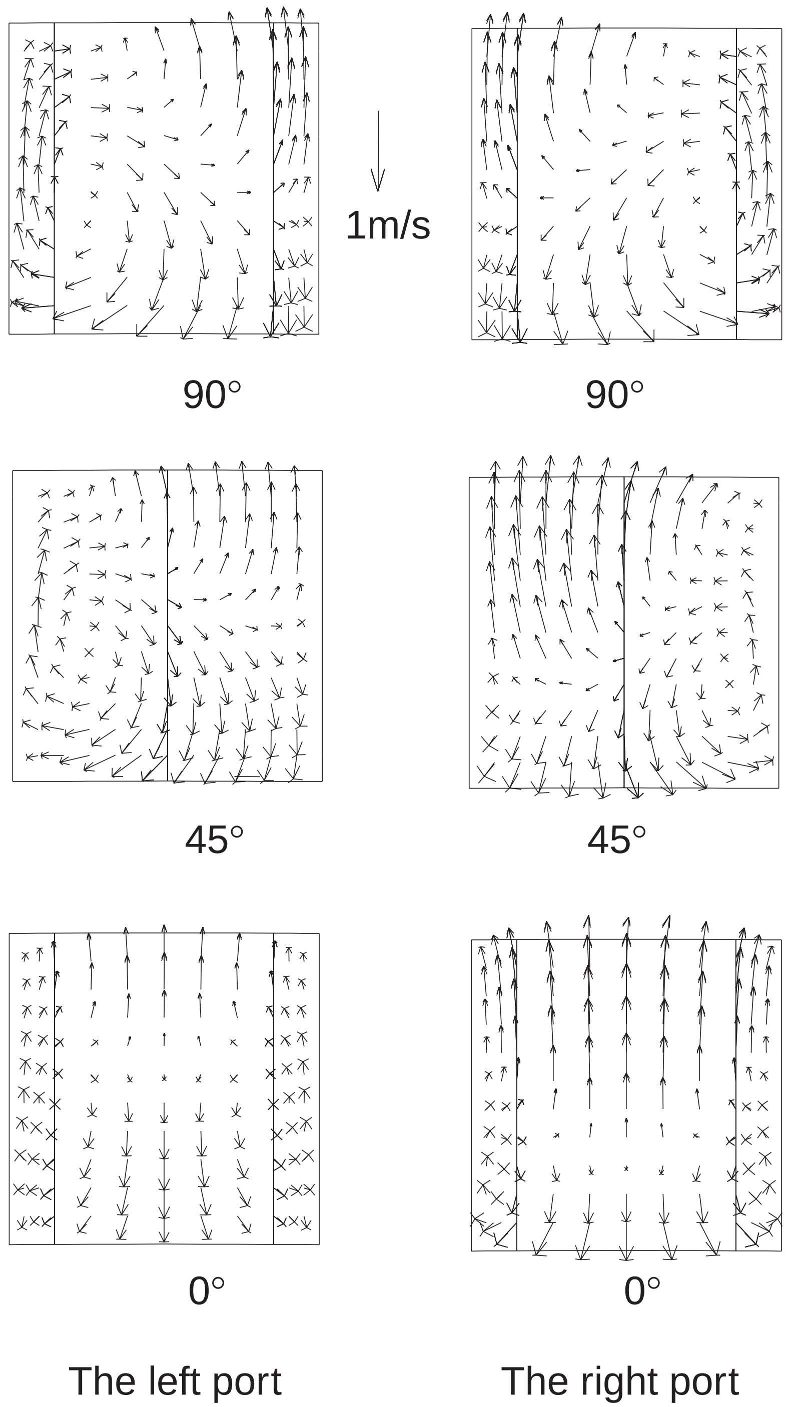

(V_C=1m/min, Q_G=10SLPM, f_g=16%(hot), F_L=50%,)

Figure 3.22 Flow field at the nozzle ports under different gate orientations

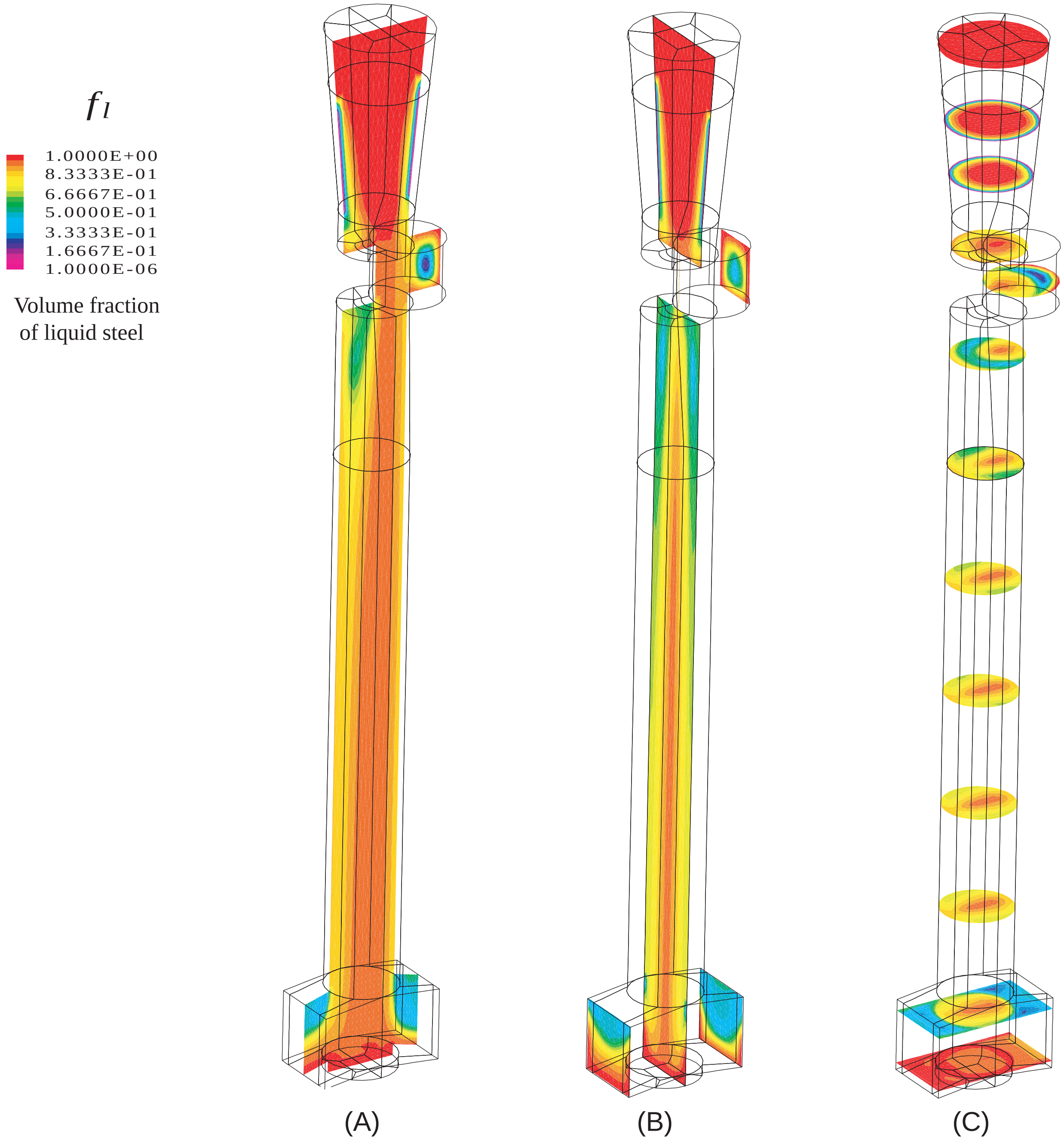

(A) x-z centerplane, parallel to the wide face
(B) y-z centerplane and two ports, all parallel to the narrow face
(C) some horizontal planes

Figure 3.23 Argon gas distribution in the standard nozzle with 0° gate orientation

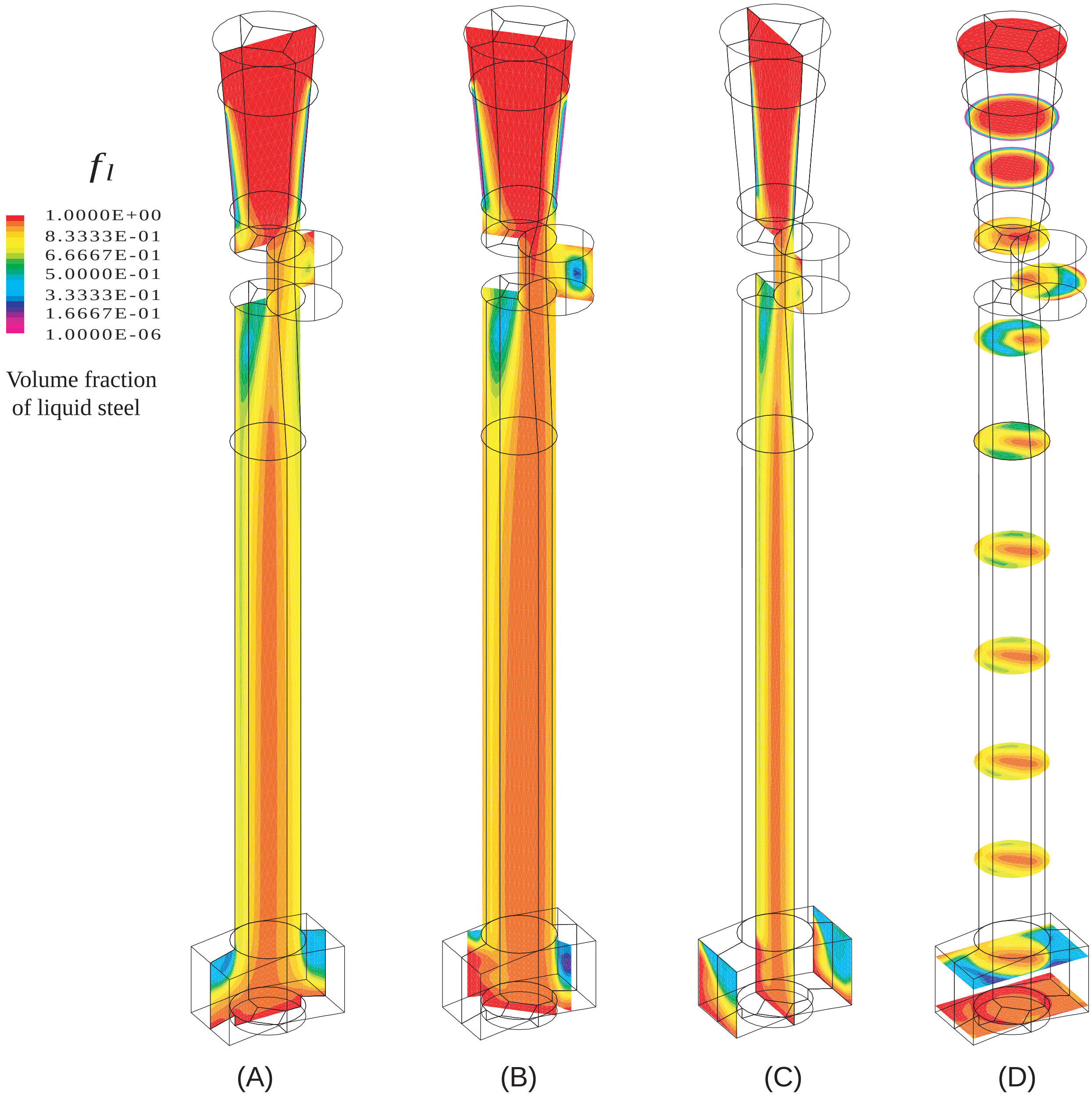

(A) x-z centerplane, parallel to the wide face
(B) vertical plane, through the center of the slide-gate cavity
(C) y-z centerplane and two ports, all parallel to the narrow face
(D) some horizontal planes

Figure 3.24 Argon gas distribution in the standard nozzle with 45° gate orientation

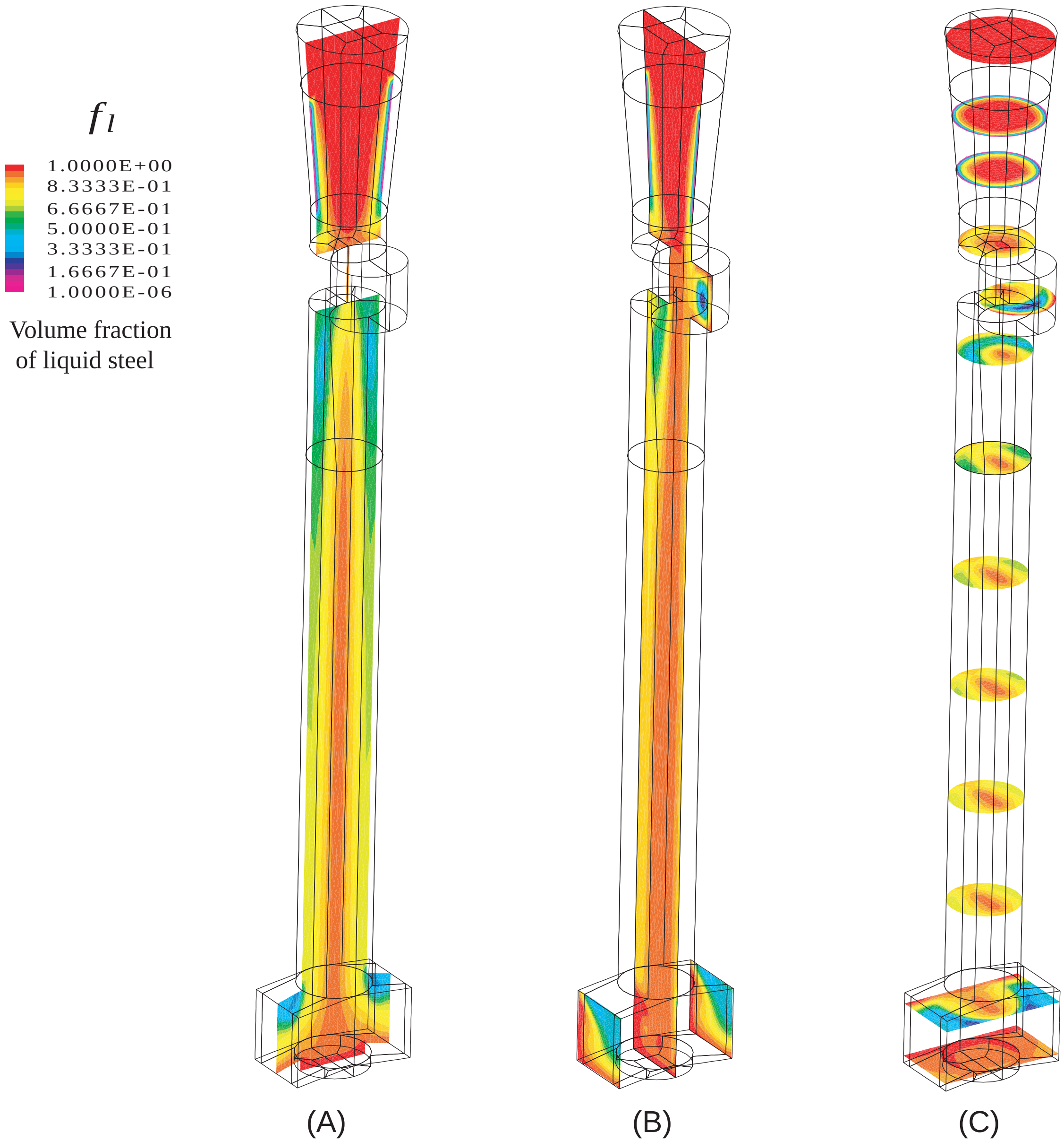

(A) x-z centerplane, parallel to the wide face
(B) y-z centerplane and two ports, all parallel to the narrow face
(C) some horizontal planes

Figure 3.25 Argon gas distribution in the standard nozzle with 90° gate orientation

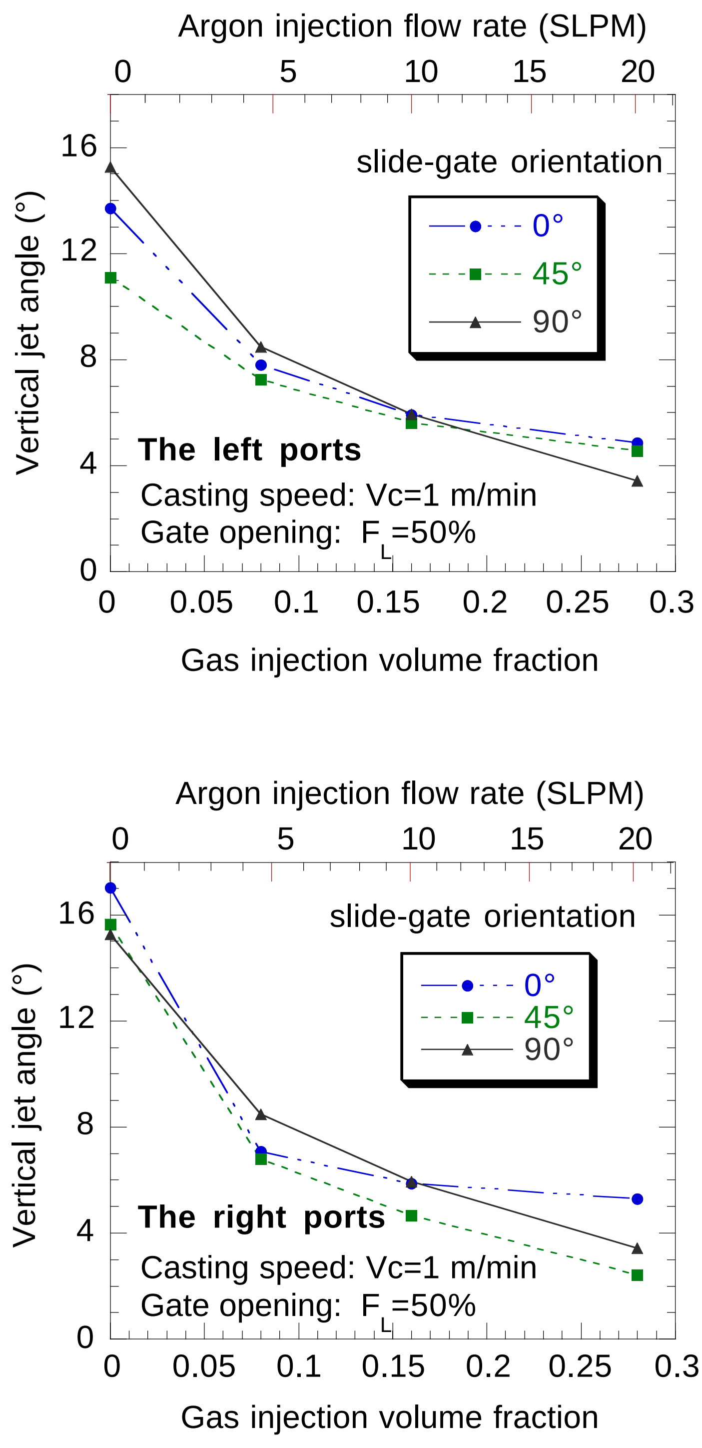

Figure 3.26 Effects of slide-gate orientation and gas injection on vertical jet angle

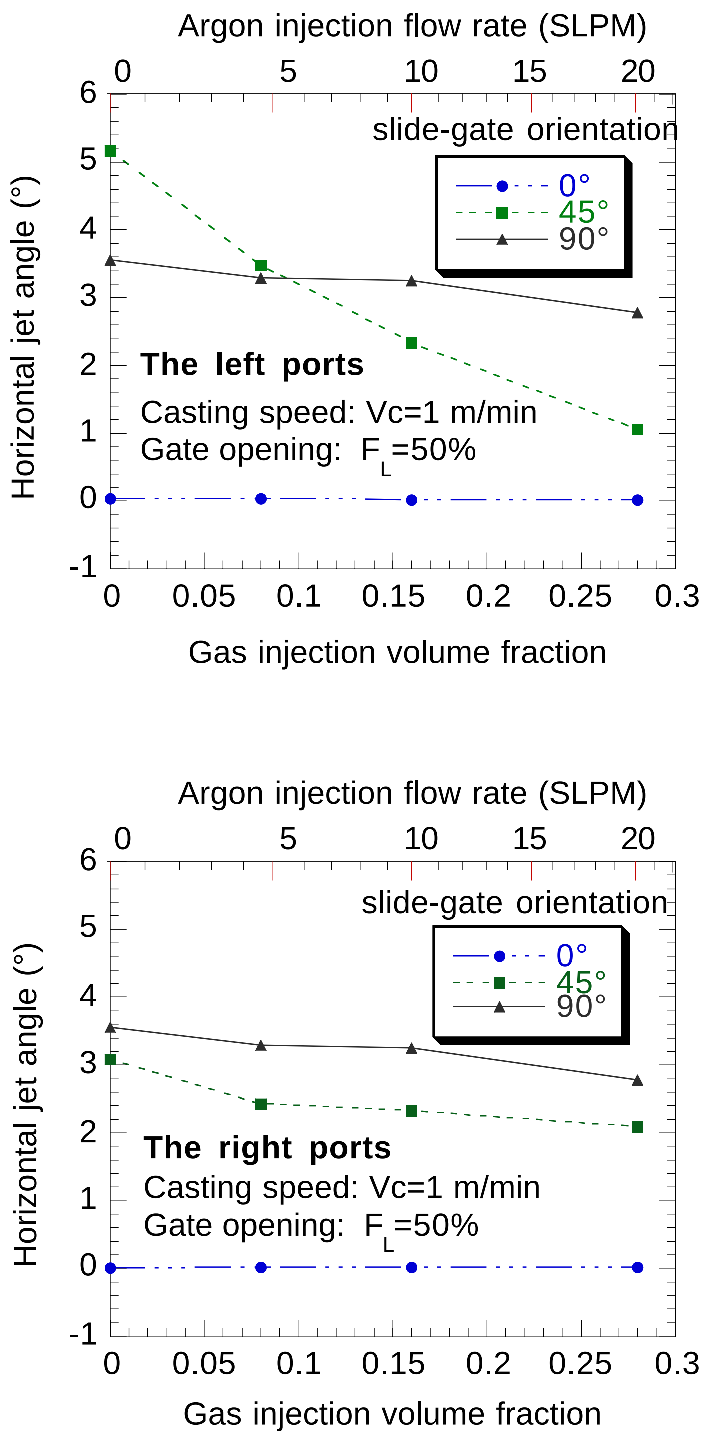

Figure 3.27 Effects of slide-gate orientation and gas injection on horizontal jet angle

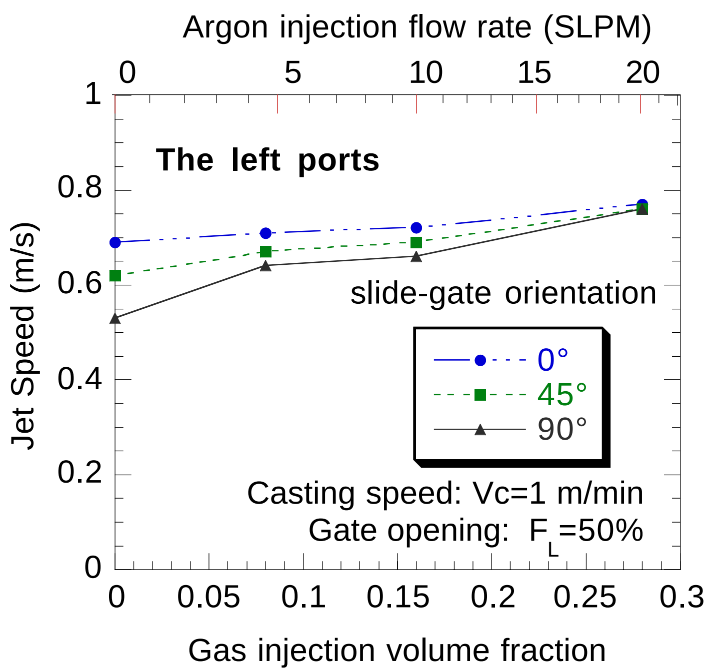

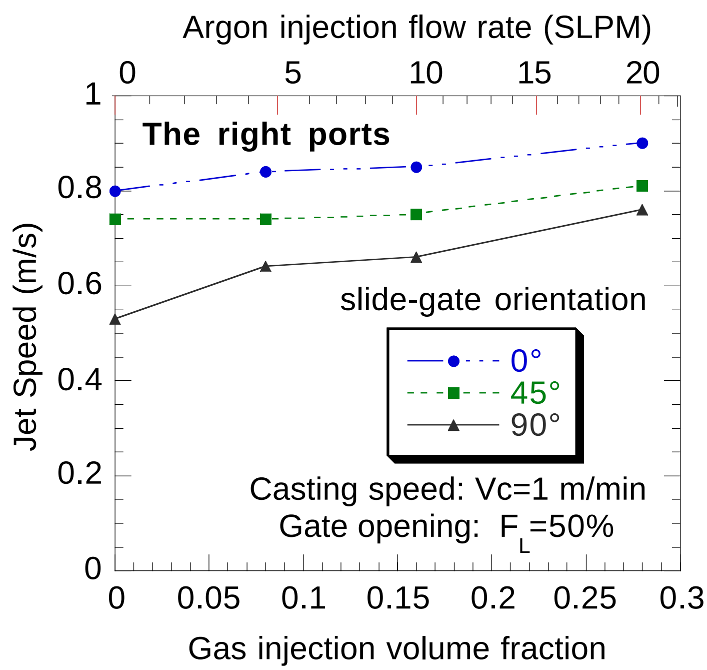

Figure 3.28 Effects of slide-gate orientation and gas injection on jet speed

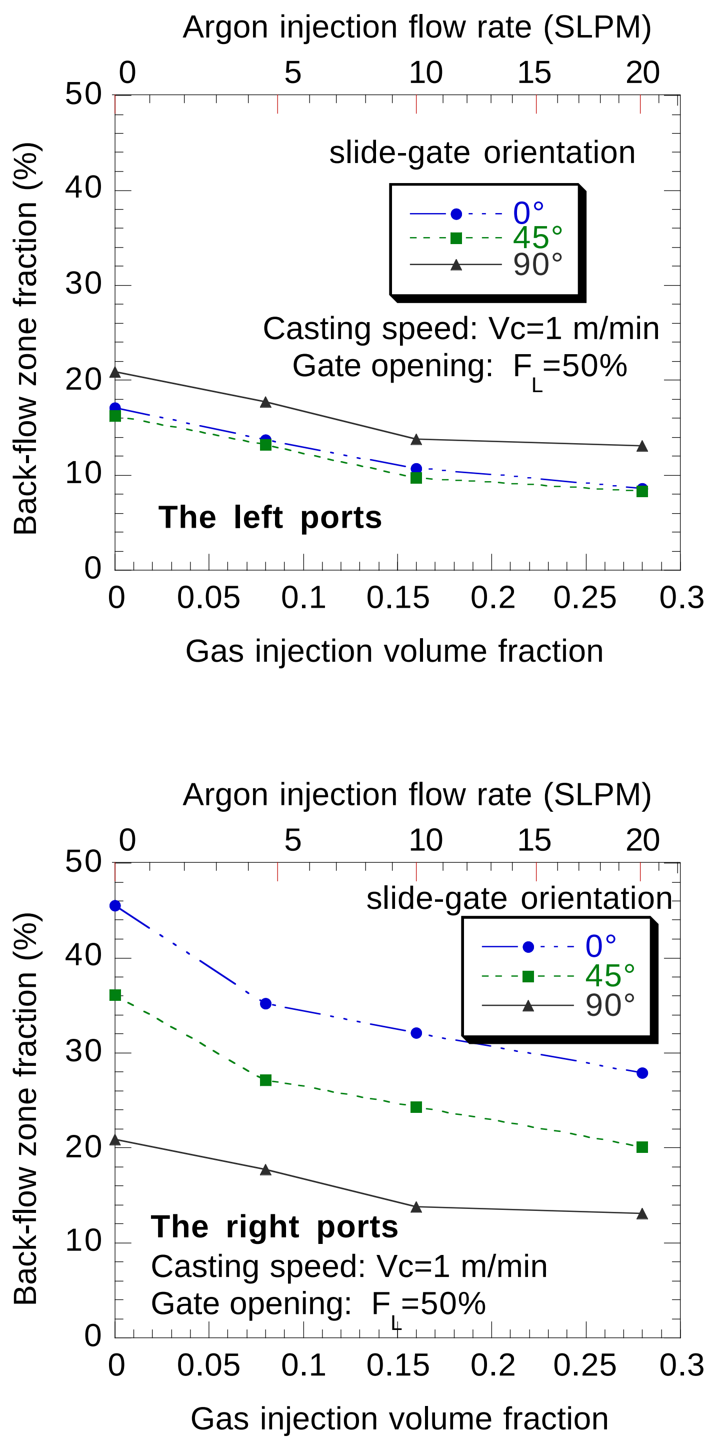

Figure 3.29 Effect of slide-gate orientation and gas injection on back flow zone

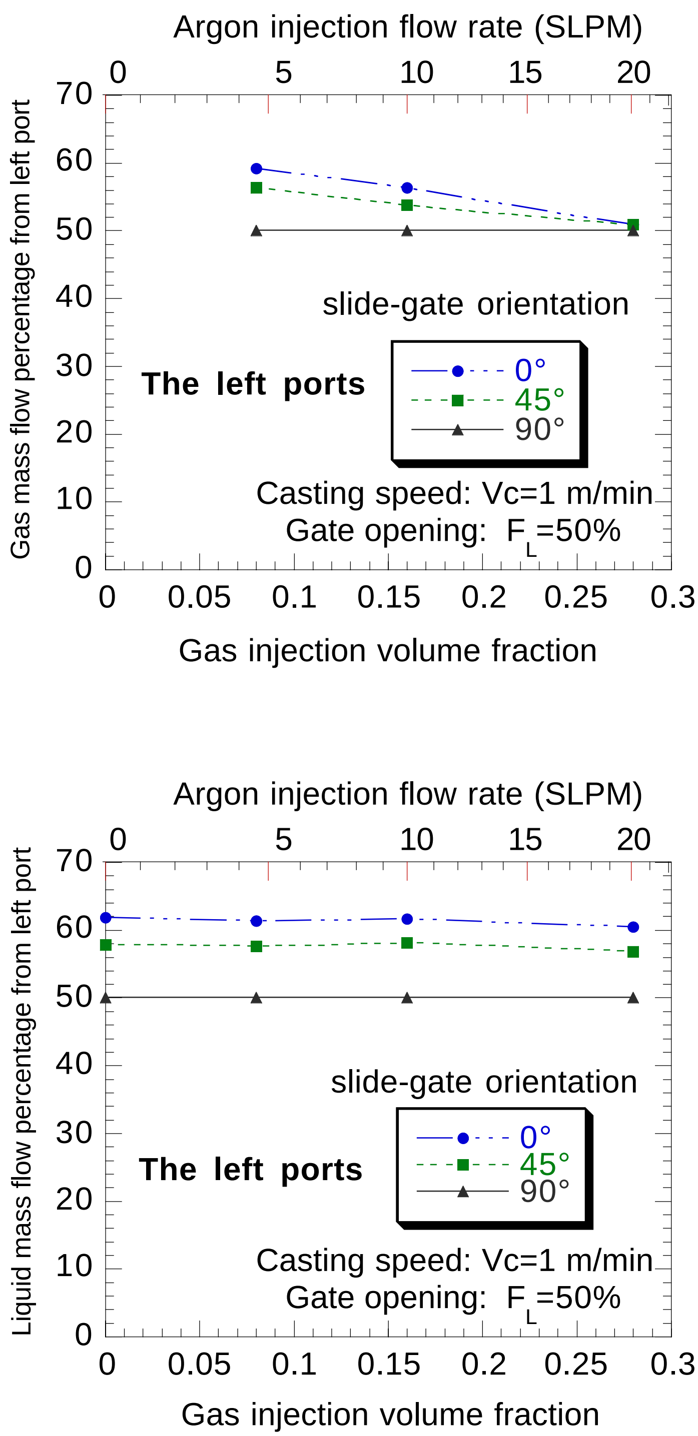

Figure 3.30 Effect of slide-gate orientation and gas injection on biased mass flow

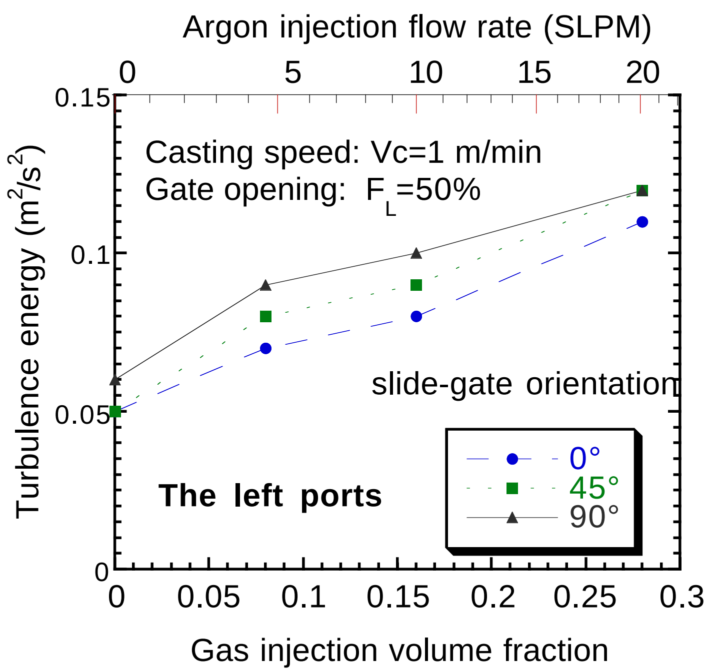

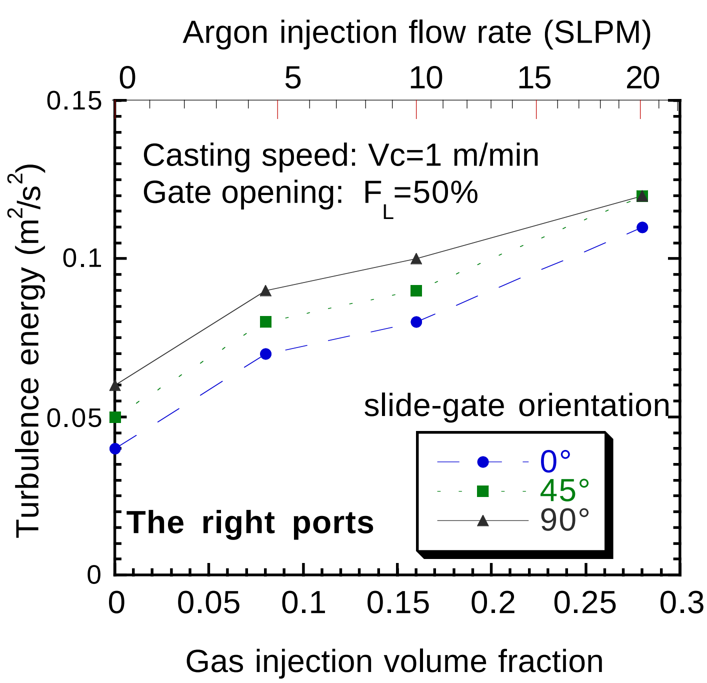

Figure 3.31 Effect of slide-gate orientation and gas injection on turbulence energy

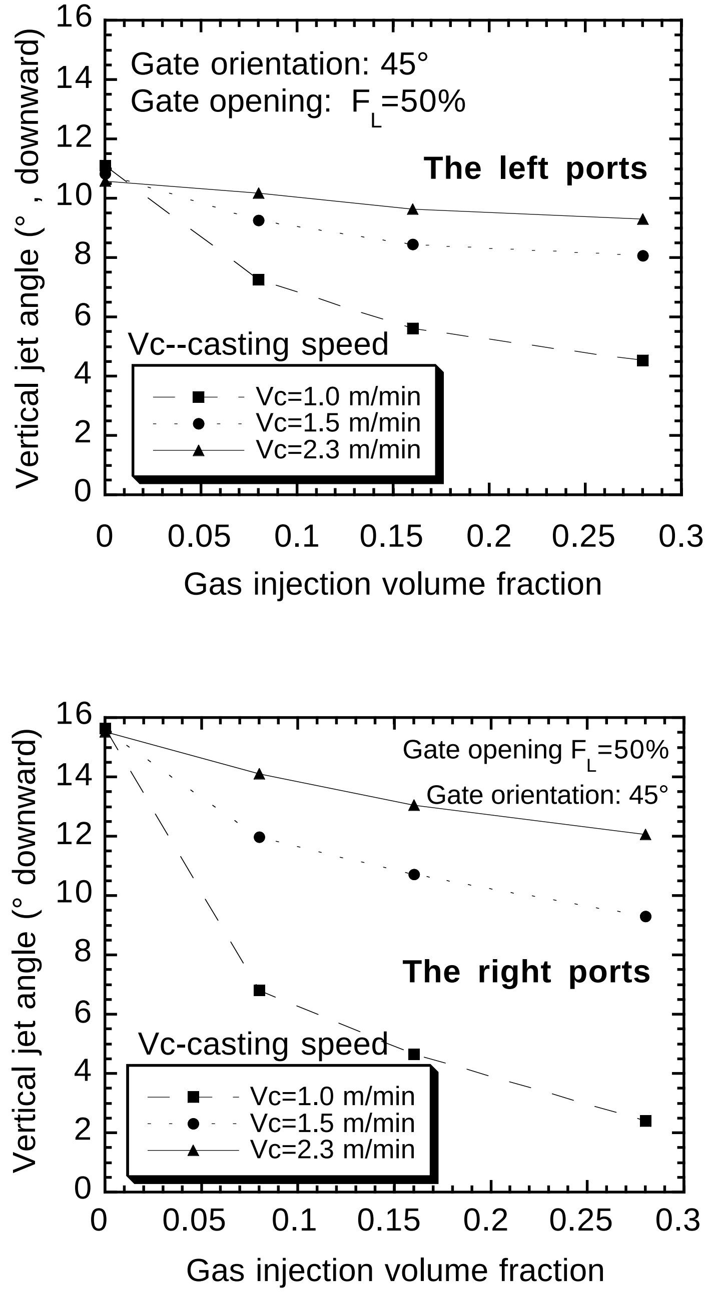

Figure 3.32 Effects of casting speed and gas injection on vertical jet angle

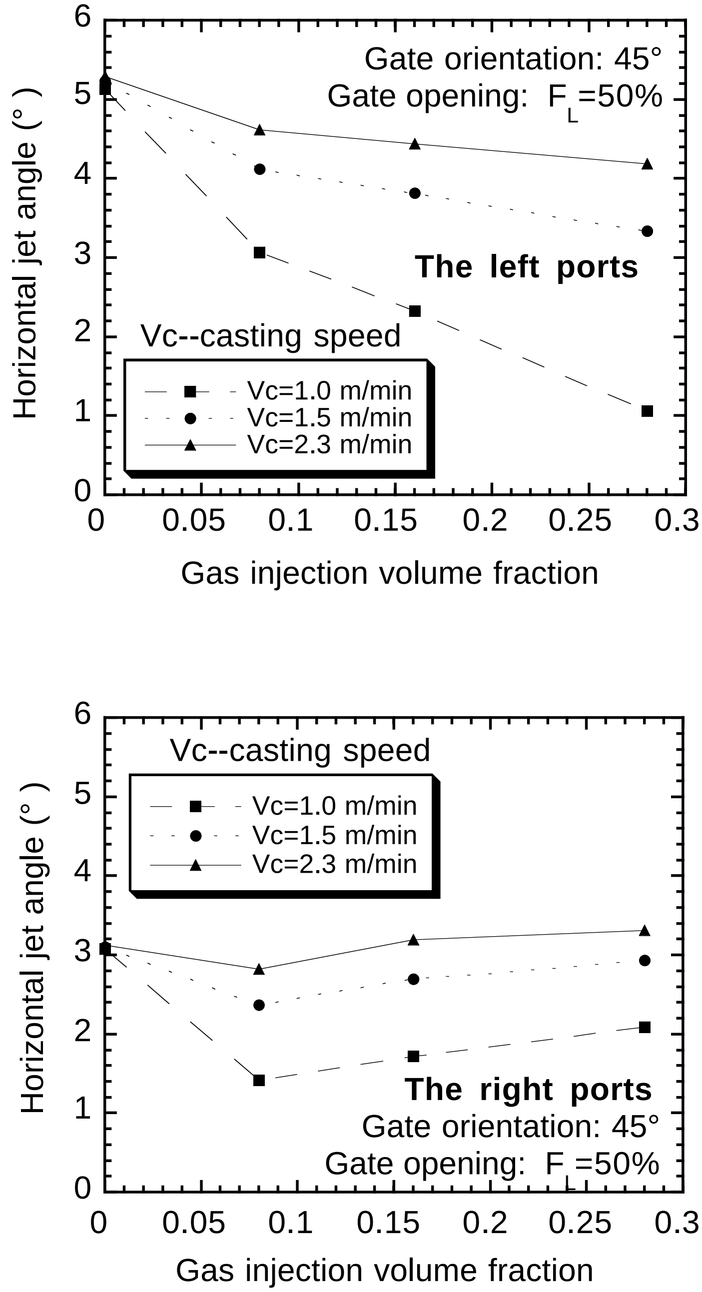

Figure 3.33 Effects of casting speed and gas injection on horizontal jet angle

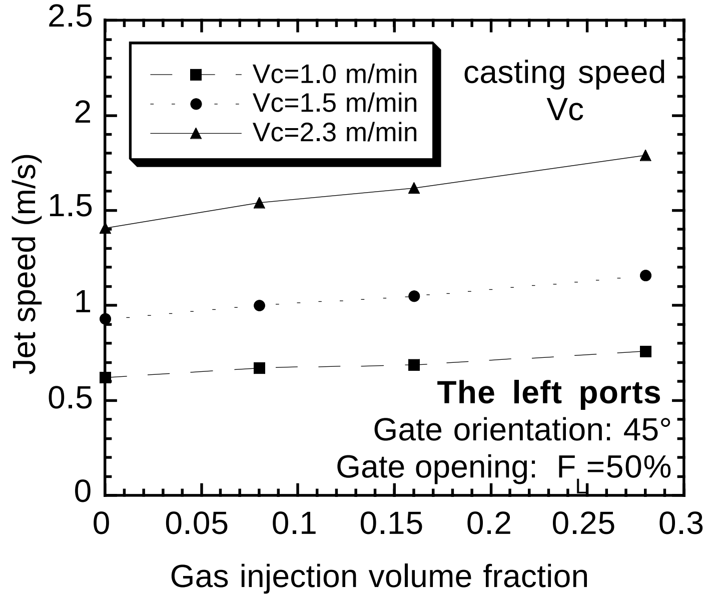

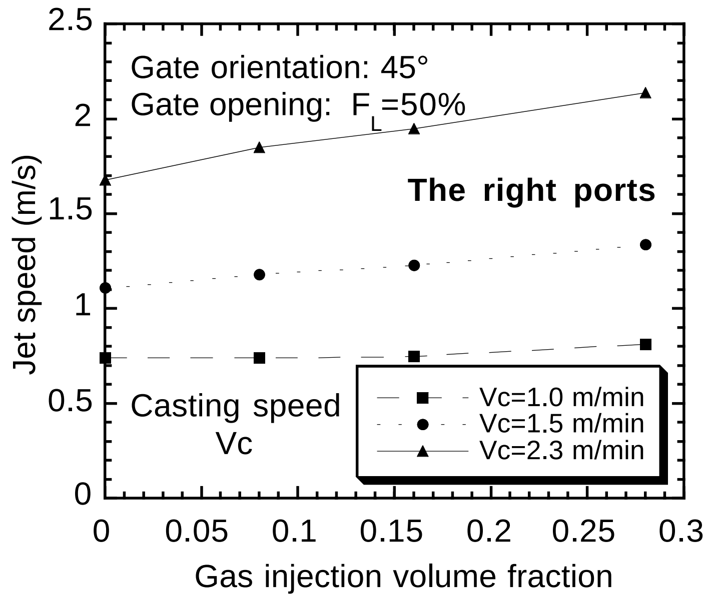

Figure 3.34 Effects of casting speed and gas injection on jet speed

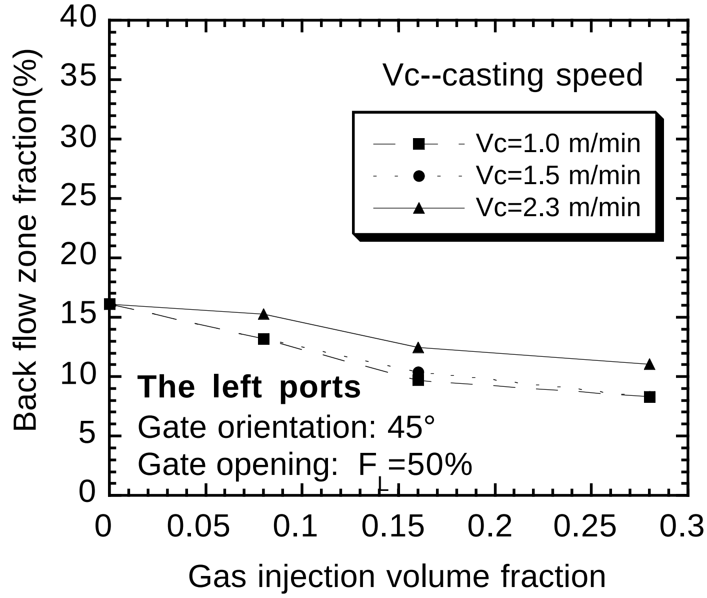

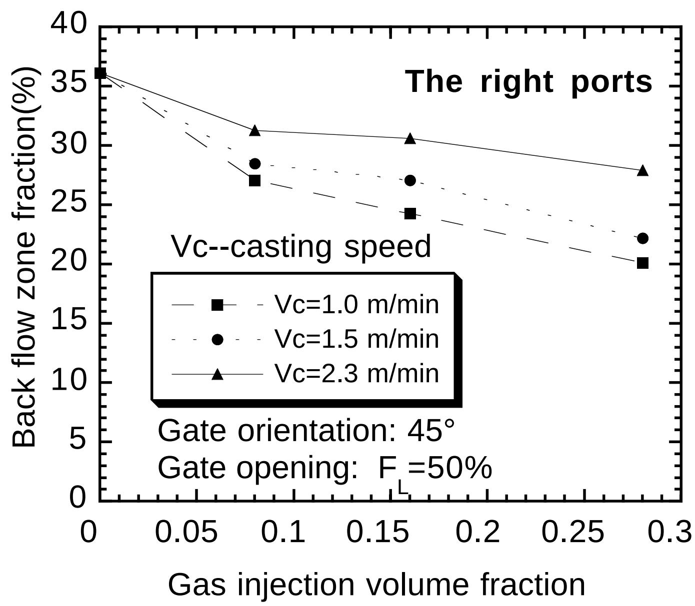

Figure 3.35 Effects of casting speed and gas injection on back flow zone

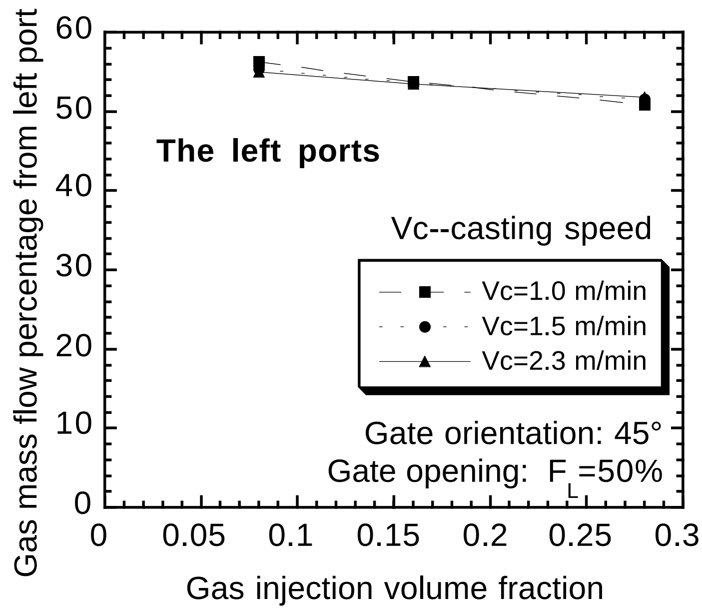

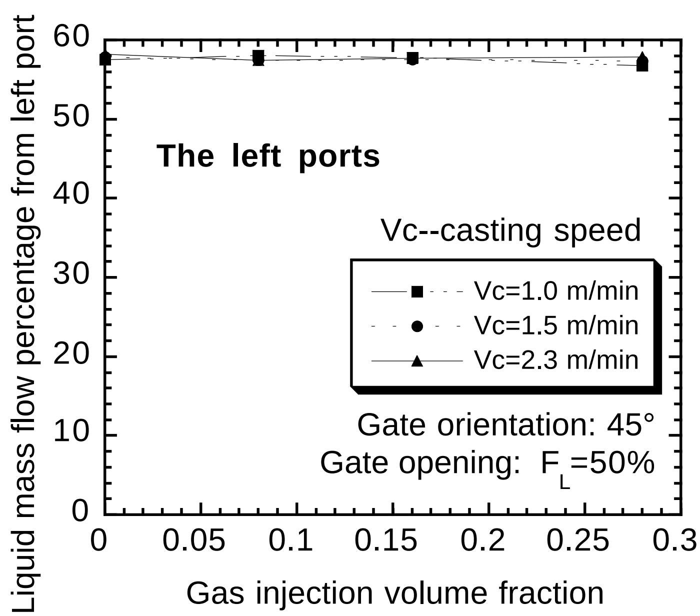

Figure 3.36 Effects of casting speed and gas injection on biased mass flow

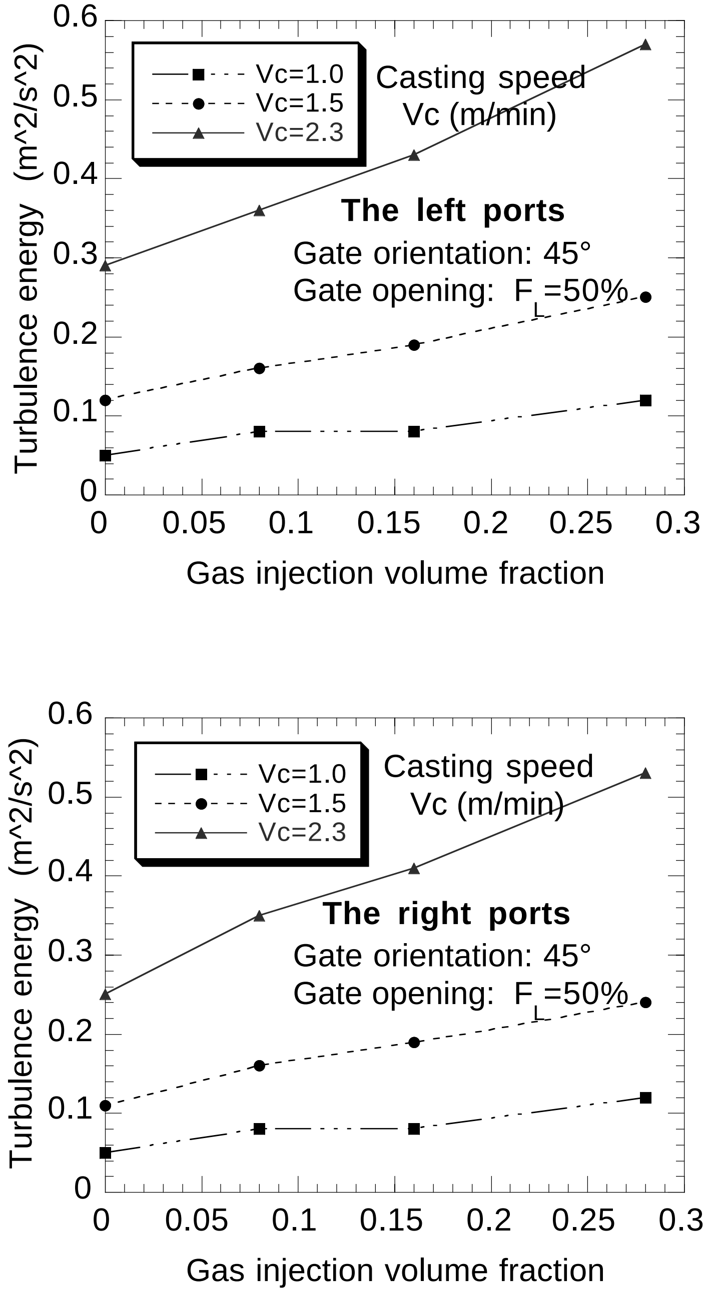

Figure 3.37 Effects of casting speed and gas injection on turbulence energy

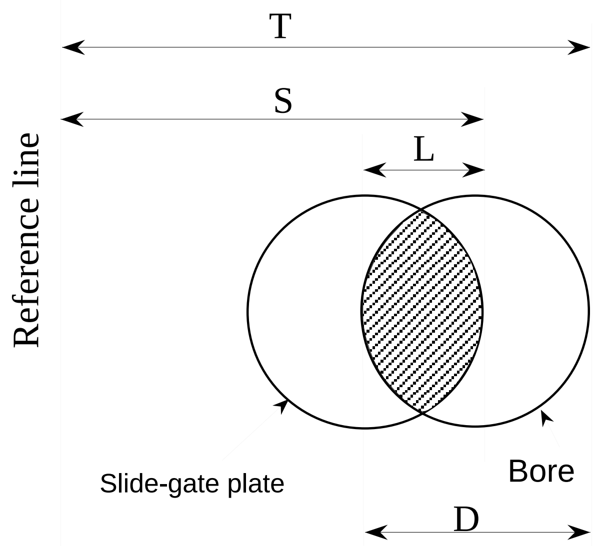

$$F_L = \frac{L}{D}$$

$$F_P = \frac{S}{T}$$

$$F_A = \frac{Shadow\ Area}{Bore\ Area}$$

$$F_P = (1 - M)F_L + M$$

$$M = \frac{T - D}{T}$$

Figure 3.38 Schematic of the definition of slide-gate opening for F_L , F_P and F_A

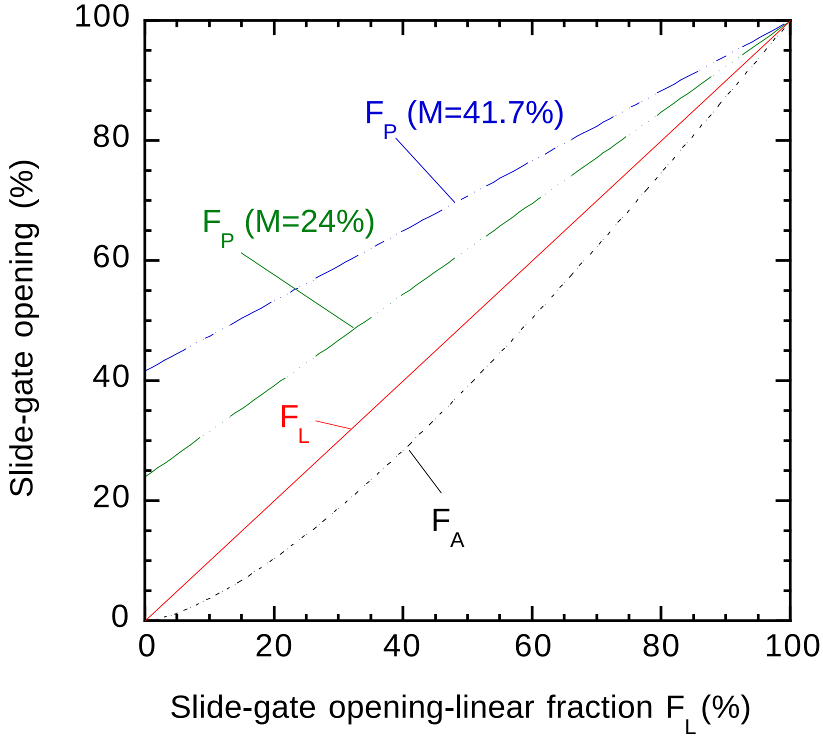

Figure 3.39 Relationship between different definitions for gate opening

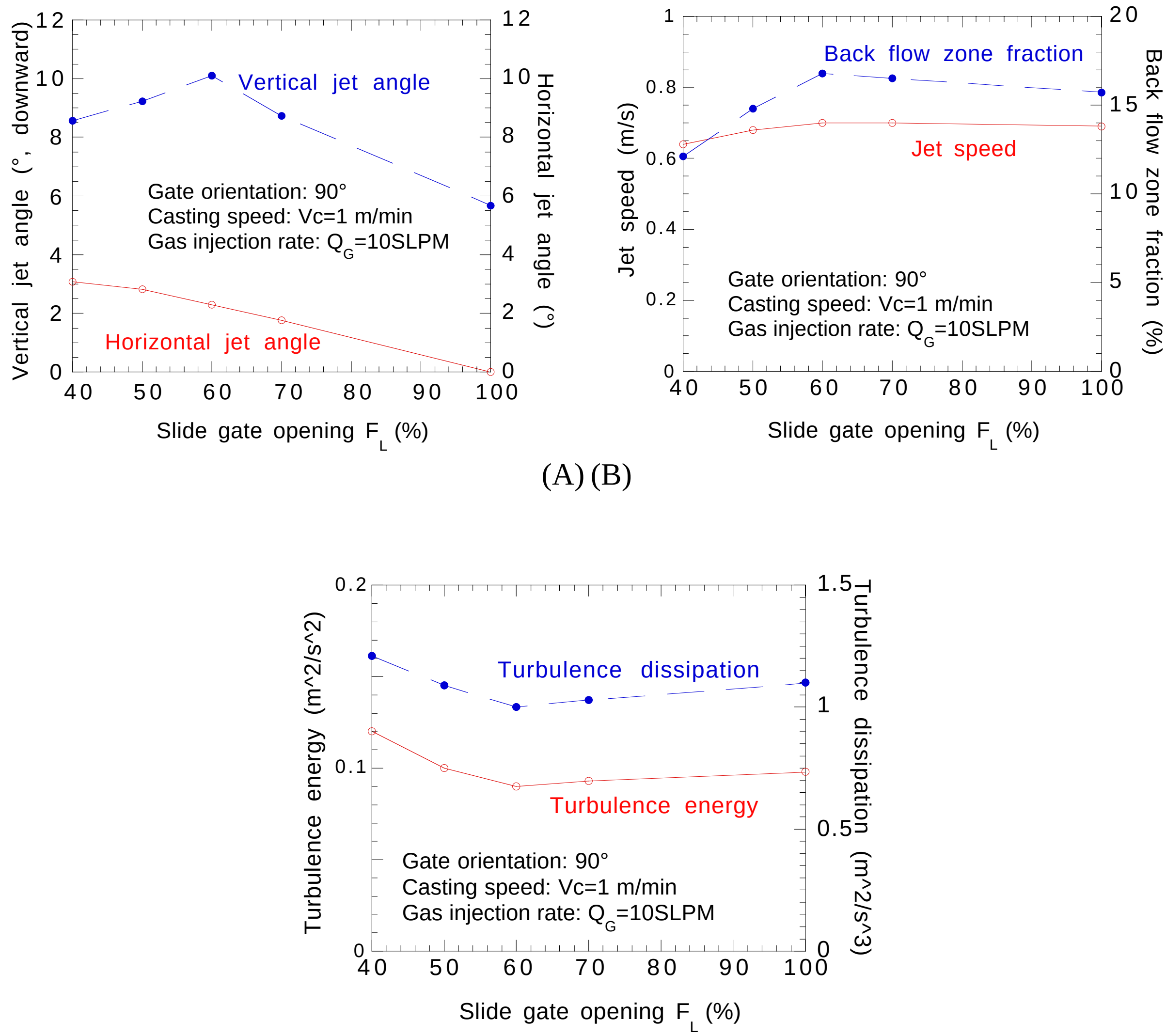

(A) (B)

(C)

Figure 3.40 Effects of gate opening on jet characteristics

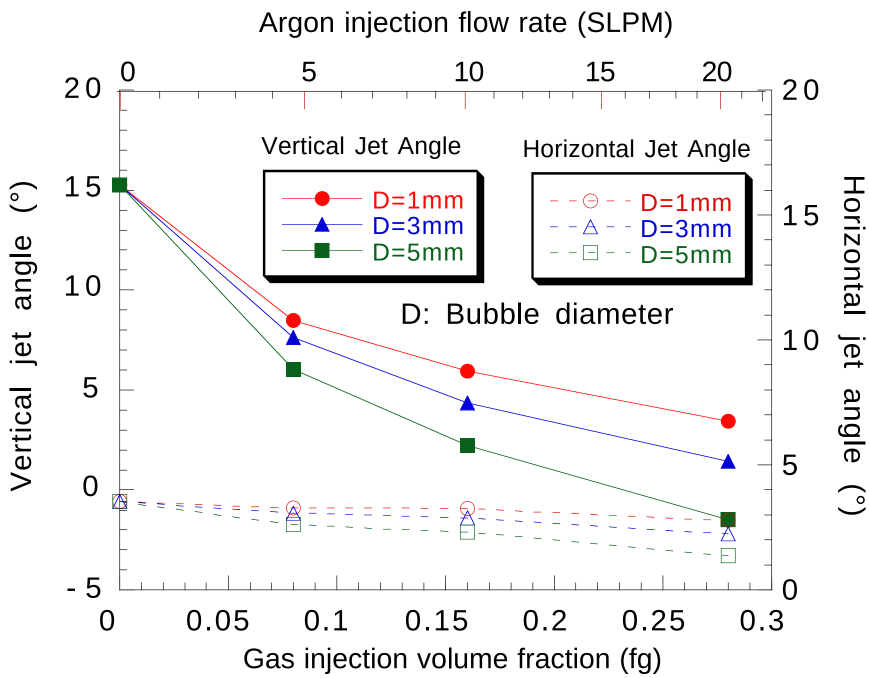

(A) Vertical and horizontal jet angles

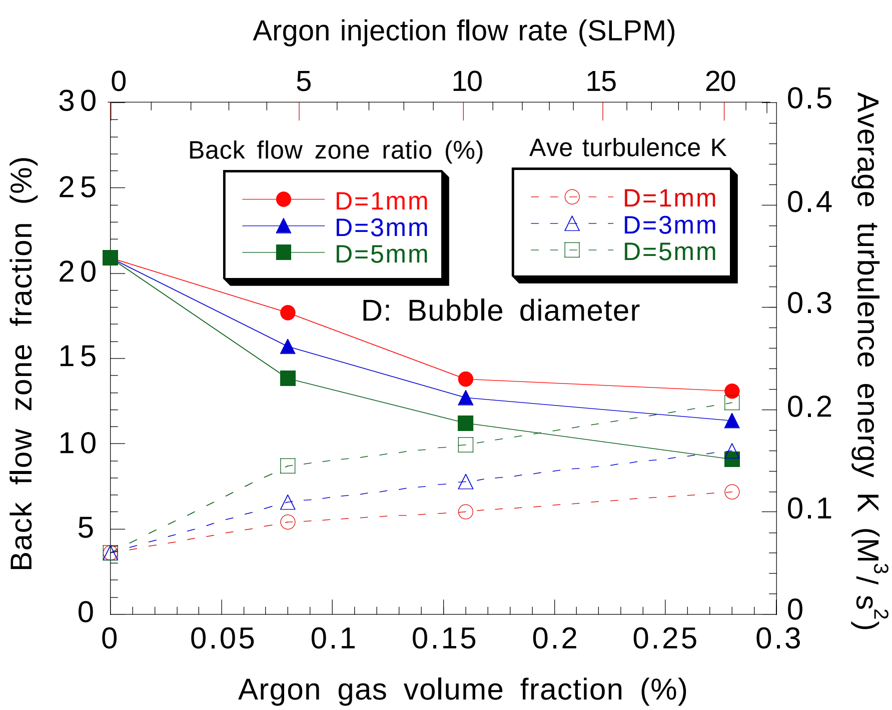

(B) Back flow zone and turbulence energy

(V_C=1m/min, F_L=50%, 90° gate orientation)

Figure 3.41 Effect of argon bubble size and gas injection on jet characteristics

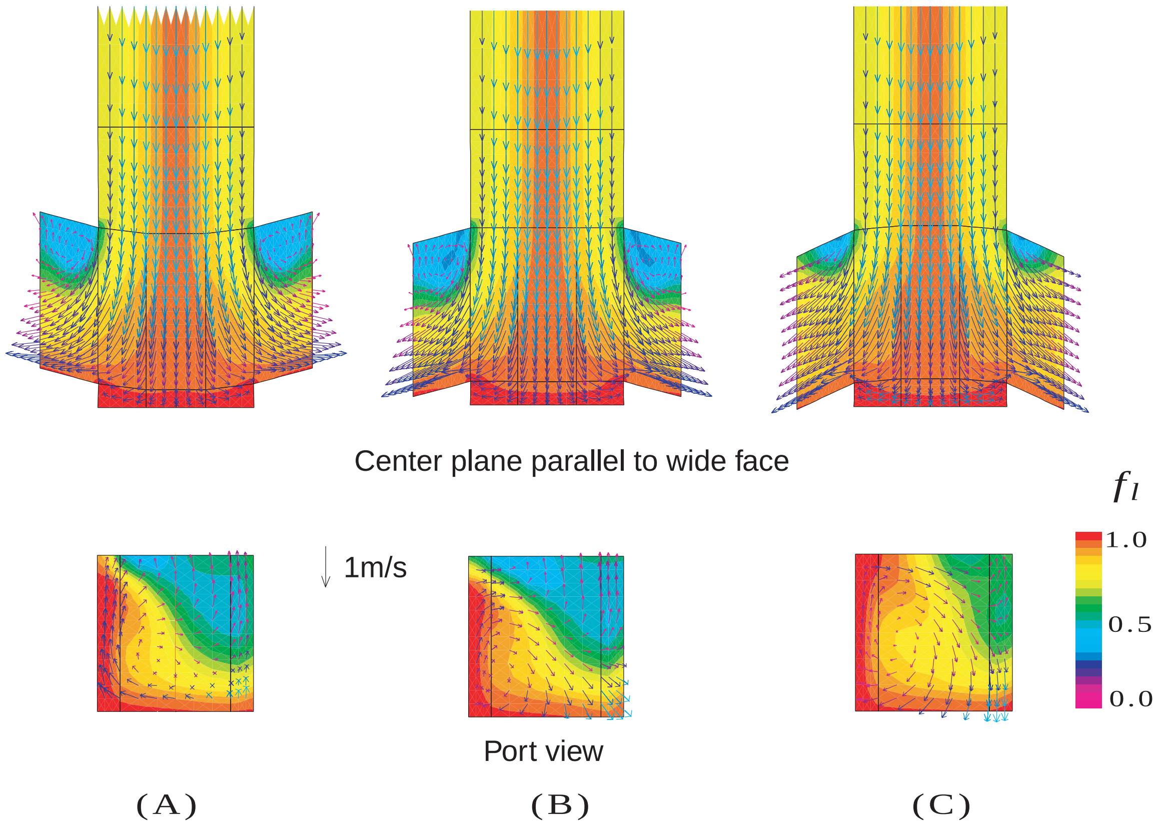

(V_C=1m/min, Q_G=10SLPM, f_g=16%(hot), F_L=50%, 90° gate orientation)

Figure 3.42 Liquid velocity fields superposed on liquid volume fraction at the center plane and port for different nozzle port angles (A)15° up (B) 15° down (C) 25° down

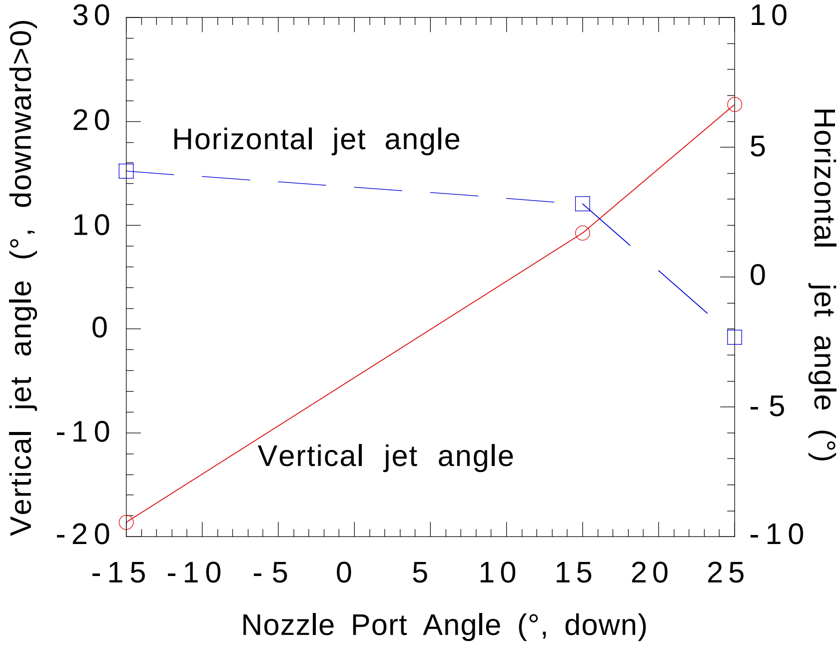

(A) Vertical and horizontal jet angles

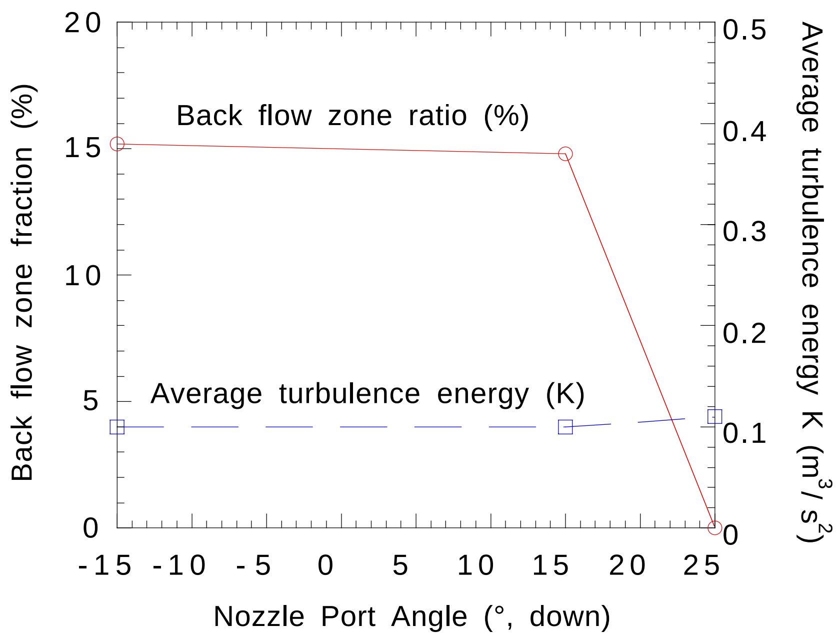

(B) Back flow zone and turbulence energy

(V_C=1m/min, Q_G=10SLPM, f_g=16%(hot), F_L=50%, 90° gate orientation)

Figure 3.43 Effect of nozzle port angle on jet characteristics

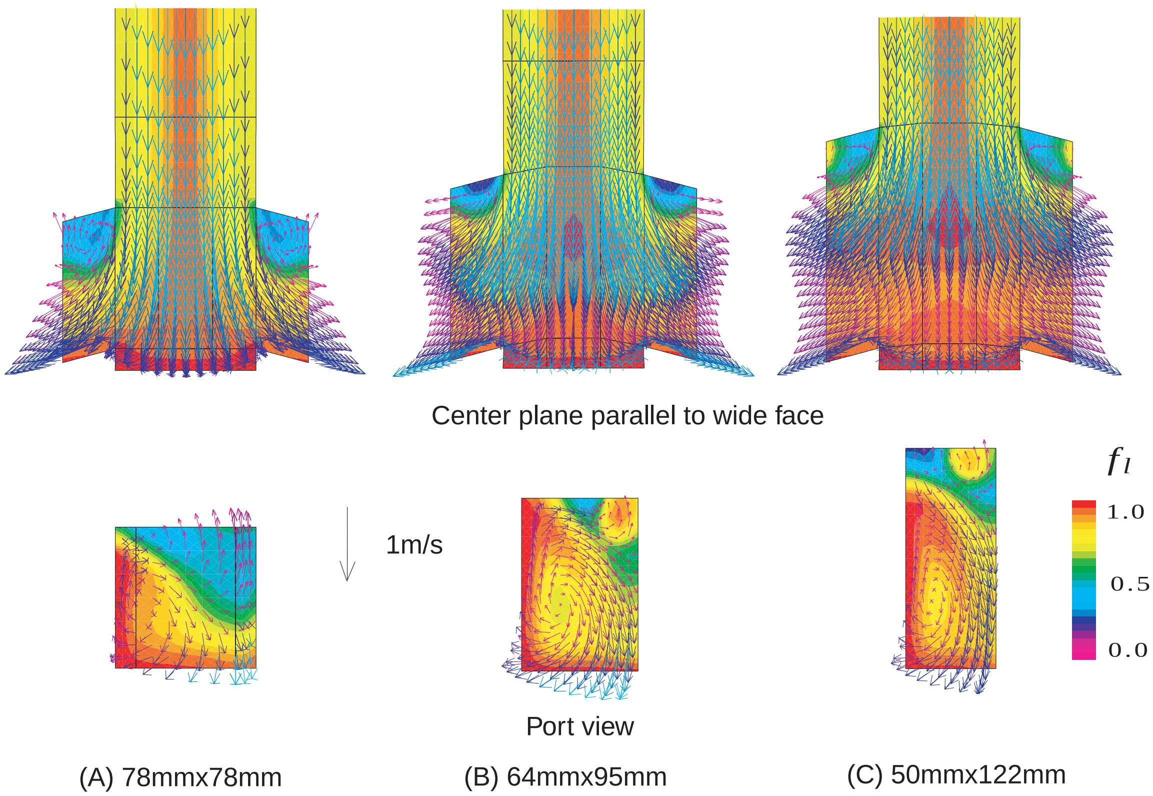

(V_C=1m/min, Q_G=10SLPM, f_g=16%(hot), F_L=50%, 90° gate orientation)

Figure 3.44 Liquid velocity fields superimposed on liquid volume fraction at center plane and port for different port shape designs

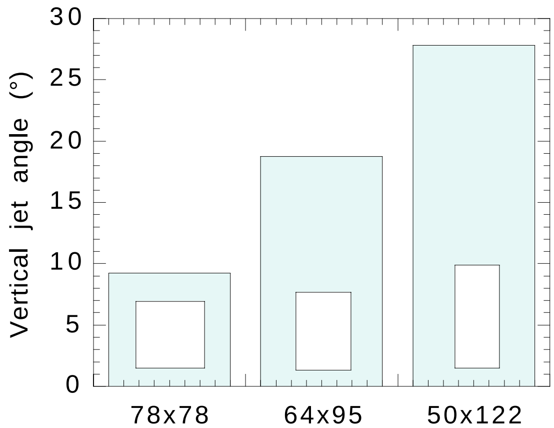

(A) Vertical jet angles

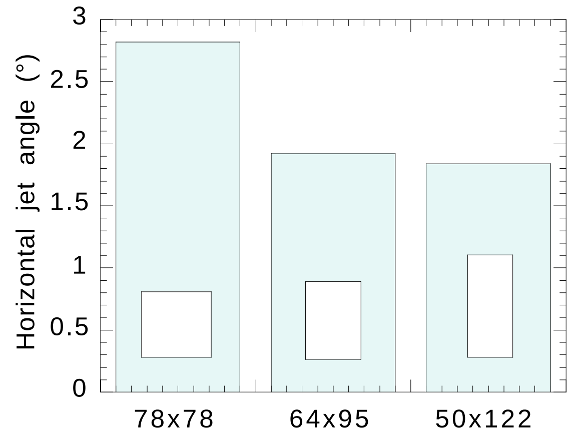

(B) Horizontal jet angle

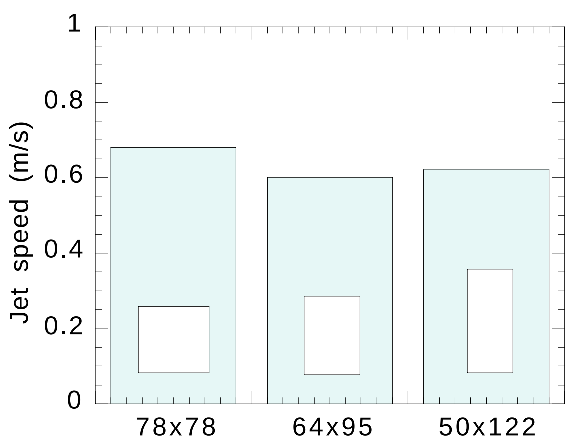

(C) Jet speed

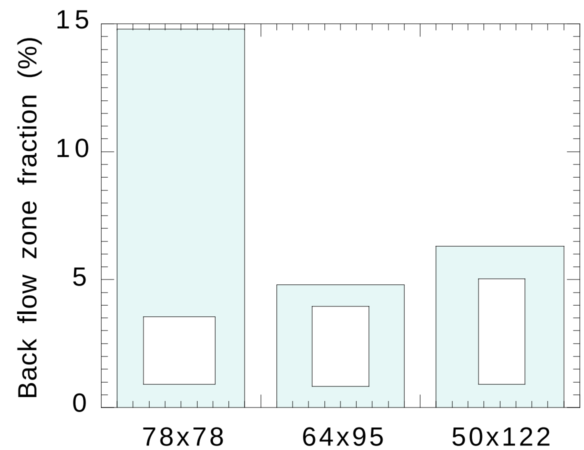

(D) Back flow zone ratio

(V_C=1m/min, F_L=50%, 90° gate orientation, 15° port angle)

Figure 3.45 Effect of port shape design on jet characteristics

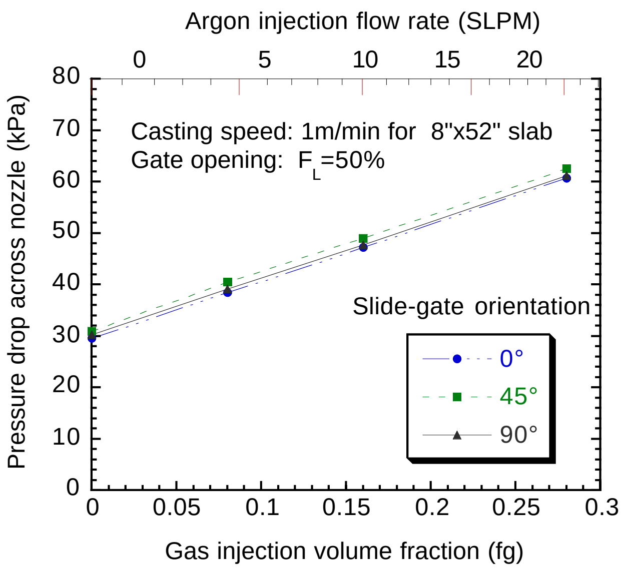

(A)

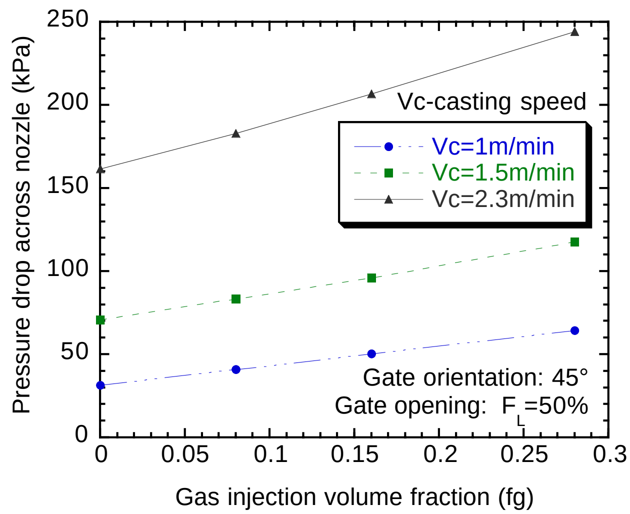

(B)

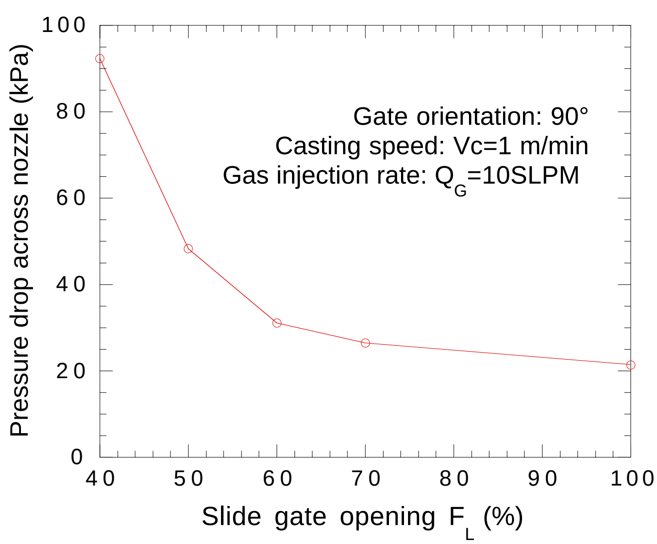

(C)

Figure 3.46 Effects of gas injection and slide-gate orientation (A), casting speed (B), and slide-gate opening (C) on pressure drop across the nozzle

CHAPTER 4. INTERRELATED EFFECTS OF CLOGGING, ARGON INJECTION AND CASTING CONDITIONS

4.1 Introduction

In each of the foregoing parametric studies, only the investigated variable changes while all other variables are kept constant in order to isolate the effect. This can be conveniently done in numerical simulation, but might differ from the real-life continuous casting process conditions, especially when the investigated variable is one of the operation conditions. In practice, the operation variables are often interrelated. Changing one variable usually causes corresponding changes in another variable. For example, a drop in tundish bath depth needs a corresponding increase in gate opening in order to maintain a constant casting speed. In fact, the plots in Figures 3.26~3.37 correspond to varying tundish bath depths. During a stable casting process, tundish bath depth and argon injection are usually kept constant, and gate opening is regulated to compensate for any unwanted effects, such as nozzle clogging, in order to maintain a constant casting speed.

Flow through the tundish nozzle is gravity-driven by the difference between the liquid levels of the tundish and mold top free surface. Flow rate or casting speed depends upon the tundish bath depth and the flow characteristics inside the nozzle. Tundish bath depth is related to the pressure drop across the nozzle, which can be predicted with the numerical simulation of the flow in the nozzle. To quantify the interrelated effect of those operation variables and to present trends that correspond with real-life operation conditions, a model describing the relationship between casting speed, gate opening, gas injection and tundish bath depth is developed, based on interpolation of the numerical simulation results.

Both clogging and argon injection may greatly affect the flow pattern in the nozzle, and subsequently in the mold, altering both the flow rate and flow symmetry, and causing quality problems. There is incentive to understand quantitatively how they are related to those operation variables.

Air aspiration through cracks and joints into the nozzle leads to reoxidation, which is an important cause of inclusions and clogging [15, 56]. Air aspiration is more likely if the pressure inside the nozzle drops below atmospheric pressure, creating a partial vacuum. While regulating the liquid steel flow, the slide-gate creates a local flow restriction, which generates a large pressure drop. This creates a low-pressure region right below the throttling plate, which often falls below 1 atm (0 gauge pressure). The minimum pressure is affected by argon injection, tundish bath depth, casting speed, gate opening and clogging. Predicting when a partial vacuum condition exists and choosing conditions to avoid it is one way to prevent this potential source of reoxidation products and the associated clogging and quality problems.

4.2 Model Formulation

A model to investigate the interrelated effects of casting variables on the minimum pressure in nozzle is developed in four stages. Firstly, the 3-D finite-difference model developed and validated in previous chapter is used to perform a parametric study. Then, the output pressure drops are converted to tundish bath depths and the results are curve fit with simple equations. Next, these equations are inverted to make the tundish bath depth an independent variable and to allow presentation of the results for arbitrary practical conditions. Finally, the predicted minimum pressure results are combined with the inverse model, so that they also can be presented for practical casting conditions.

4.2.1 Parametric Study with 3-D Finite Difference Model

The 3-D finite difference model is employed to simulate the turbulent flow of liquid steel with argon bubbles in a typical slide-gate nozzle, and to perform an extensive parametric study of various variables, including casting speed, gate opening, argon injection flow rate and nozzle bore diameter. Over 150 simulations are performed in the parametric study. All of the runs are based on the Standard Nozzle in Figure 3.1 with the standard geometry and operating conditions given in Table 3.1. This nozzle is typical of a conventional slab casting operation. It has a 90° orientation slide-gate. Thus, the right and left sides of the mold are nominally symmetrical. This orientation has the least bias flow between the two ports, so is widely adopted in practice.

The simulation conditions for the parametric study are listed in Table 4.1. Casting speed V_C refers to a typical size of the continuous-cast steel slab (8"x52") and can be easily converted into liquid steel flow rate through the nozzle or to casting speed for a different sized slab. Slide gate opening fraction F_L is a linear fraction of the opening distance, defined in Chapter 3.5.4. Argon is injected into the upper tundish nozzle (UTN) at the "cold" flow rate Q_G measured at the standard conditions (STP of 25˚C and 1 atmosphere pressure). The corresponding "hot" argon flow rate is used in the numerical simulation. Nozzle bore diameter D_N refers to the diameter of the circular opening in the slide-gate, which is assumed to be the same as the inner diameter of the SEN and bottom of the UTN. Decreasing D_N also approximates the effect of severe clogging when alumina builds up uniformly in the radial direction. Four different nozzle diameters are simulated in this work, shown in Table 4.1. In order to isolate the effect of D_N and better approximate the uniform clogging buildup, all nozzles keep the same axial dimensions as the Standard Nozzle. The ports are proportionally scaled, however, to keep the same square shape for all bore sizes.

The simulation conditions given in Table 4.1 cover most of the practical casting operation ranges. Figure 4.1(a) shows a typical shaded contour plot of the pressure distribution in the Standard Nozzle from the 3-D finite-difference model simulation. Figure 4.1(b) shows the pressure profile along the nozzle, for a few cases with different gate openings. The path follows the nozzle centerline from the nozzle top to point O at the center of the port section and then along the line from point O to the port outlet. It can be seen that the biggest pressure drop occurs across the slide gate, due to the throttling effect. The lowest pressure is found where the slide gate joins the SEN, so joint sealing is very important there to avoid air aspiration if a vacuum occurs. Increasing gate opening results in smaller flow resistance and thus less pressure drop.

4.2.2 Multivariable Curve Fitting

In order to interpolate the results of the parametric study over a continuous range of operating conditions, equations were sought to curve-fit the data points from the parametric studies with the 3-D model described in the previous section. Flow through the nozzle is driven by gravity so the pressure drop calculated across the nozzle corresponds to the pressure head given by the tundish bath depth, H_T. The relationship derived from Bernoulli's equation, is

$$H_T = \frac{\Delta p + \rho_l g H_{SEN} + \frac{1}{2}\rho_l (U_B^2 - U_C^2)}{\rho_l g} \tag{4.1}$$

where Δp is the overall pressure-drop across the nozzle which can be directly output from the numerical simulation, H_{SEN} is the SEN submerged depth, U_B is the average velocity at the top inlet of the nozzle and U_C is the average jet velocity at the nozzle port, which is a weighted average of the liquid flow exiting the port. The derivation of Equation 4.1 is straightforward and detailed in Appendix D.

The calculated tundish bath depths (H_T) are plotted as a function of the other process variables, in Figures 4.2(A-D). Each point in these plots represents one simulation case. Equations to relate tundish bath depths (H_T) with those variables were obtained by fitting the points in Figures 4.2(A-D) using a multiple-variable curve fitting procedure, which is briefly described below.

First, the form of the equation is chosen for each variable. Figure 4.2(A) shows that the H_T *vs.* V_C data fits well with a quadratic polynomial function. The H_T *vs.* Q_G data shown in Figure 4.2(B) fits well with a simple linear function, and the H_T *vs.* D_N data in Figure 4.2(C) fits well with a cubic function. A single simple function could not be found to fit the H_T *vs.* F_L data in Figure 4.2(D) over the whole F_L range. Thus, these data were split into two regions, with a quadratic function for $F_L \leq 60\%$ and a linear function for $F_L \geq 60\%$. Putting these relations together yields the overall relation:

$$H_T = \left(a_1 V_C^2 + a_2 V_C + a_3\right)\left(a_4 F_L^2 + a_5 F_L + a_6\right)\left(a_7 Q_G + a_8\right)\left(a_9 D_N^3 + a_{10} D_N^2 + a_{11} D_N + a_{12}\right) \quad \text{for } F_L \leq 60\% \tag{4.2a}$$

$$H_T = \left(a_{13} V_C^2 + a_{14} V_C + a_{15}\right)\left(a_{16} F_L + a_{17}\right)\left(a_{18} Q_G + a_{19}\right)\left(a_{20} D_N^3 + a_{21} D_N^2 + a_{22} D_N + a_{23}\right) \quad \text{for } F_L \geq 60\% \tag{4.2b}$$

where the a_i (i=1~23) are unknown constants. Each numerical simulation case generates one set of data (H_T, V_C, F_L, Q_G, D_N), and corresponds to one equation for constant a_i.

Theoretically, 23 equations or simulation cases are needed to solve for the 23 unknown constants in Equations 4.2. Because far more than 23 cases were simulated (Table 4.1), a least square curve fitting technique is needed to find a_I values that minimize the sum of the distance of each data point from its fitting curve. However, Equations 4.2 represent a set of the nonlinear equations for the unknowns a_I and are difficult to solve for a least square solution.

Equations 4.2 can be expanded to yield a new pair of equations with a new group of total of 72 and 48 unknowns respectively

$$
\begin{aligned}
H_T = {} & c_1 + c_2V_C + c_3F_L + c_4Q_G + c_5V_CF_L + c_6V_CQ_G + c_7F_LQ_G + c_8V_CF_LQ_G + c_9V_C^2 + c_{10}F_L^2 \\
& + c_{11}V_CF_L^2 + c_{12}V_C^2F_L + c_{13}V_C^2Q_G + c_{14}F_L^2Q_G + c_{15}V_C^2F_L^2 + c_{16}V_CF_L^2Q_G \\
& + c_{17}V_C^2F_LQ_G + c_{18}V_C^2F_L^2Q_G \\
& + c_{19}D_N + c_{20}V_CD_N + c_{21}F_LD_N + c_{22}Q_GD_N + c_{23}V_CF_LD_N + c_{24}V_CQ_GD_N + c_{25}F_LQ_GD_N \\
& + c_{26}V_CF_LQ_GD_N + c_{27}V_C^2D_N + c_{28}F_L^2D_N \\
& + c_{29}V_CF_L^2D_N + c_{30}V_C^2F_LD_N + c_{31}V_C^2Q_GD_N + c_{32}F_L^2Q_GD_N + c_{33}V_C^2F_L^2D_N + c_{34}V_CF_L^2Q_GD_N \\
& + c_{35}V_C^2F_LQ_GD_N + c_{36}V_C^2F_L^2Q_GD_N \\
& + c_{37}D_N^2 + c_{38}V_CD_N^2 + c_{39}F_LD_N^2 + c_{40}Q_GD_N^2 + c_{41}V_CF_LD_N^2 + c_{42}V_CQ_GD_N^2 + c_{43}F_LQ_GD_N^2 \\
& + c_{44}V_CF_LQ_GD_N^2 + c_{45}V_C^2D_N^2 + c_{46}F_L^2D_N^2 \\
& + c_{47}V_CF_L^2D_N^2 + c_{48}V_C^2F_LD_N^2 + c_{49}V_C^2Q_GD_N^2 + c_{50}F_L^2Q_GD_N^2 + c_{51}V_C^2F_L^2D_N^2 + c_{52}V_CF_L^2Q_GD_N^2 \\
& + c_{53}V_C^2F_LQ_GD_N^2 + c_{54}V_C^2F_L^2Q_GD_N^2 \\
& + c_{55}D_N^3 + c_{56}V_CD_N^3 + c_{57}F_LD_N^3 + c_{58}Q_GD_N^3 + c_{59}V_CF_LD_N^3 + c_{60}V_CQ_GD_N^3 + c_{61}F_LQ_GD_N^3 \\
& + c_{62}V_CF_LQ_GD_N^3 + c_{63}V_C^2D_N^3 + c_{64}F_L^2D_N^3 \\
& + c_{65}V_CF_L^2D_N^3 + c_{66}V_C^2F_LD_N^3 + c_{67}V_C^2Q_GD_N^3 + c_{68}F_L^2Q_GD_N^3 + c_{69}V_C^2F_L^2D_N^3 + c_{70}V_CF_L^2Q_GD_N^3 \\
& + c_{71}V_C^2F_LQ_GD_N^3 + c_{72}V_C^2F_L^2Q_GD_N^3
\end{aligned}
$$

$$\text{for} \quad F_L \leq 60\% \qquad (4.3a)$$

$$
\begin{aligned}
H_T = {} & c_{73} + c_{74}V_C + c_{75}F_L + c_{76}Q_G + c_{77}V_CF_L + c_{78}V_CQ_G + c_{79}F_LQ_G \\
& + c_{80}V_CF_LQ_G + c_{81}V_C^2 + c_{82}V_C^2F_L + c_{83}V_C^2Q_G + c_{84}V_C^2F_LQ_G \\
& + c_{85}D_N + c_{86}V_CD_N + c_{87}F_LD_N + c_{88}Q_GD_N + c_{89}V_CF_LD_N + c_{90}V_CQ_GD_N + c_{91}F_LQ_GD_N
\end{aligned}
$$

$$+ c_{92}V_C F_L Q_G D_N + c_{93}V_C^2 D_N + c_{94}V_C^2 F_L D_N + c_{95}V_C^2 Q_G D_N + c_{96}V_C^2 F_L Q_G D_N$$

$$+ c_{97}D_N^2 + c_{98}V_C D_N^2 + c_{99}F_L D_N^2 + c_{100}Q_G D_N^2 + c_{101}V_C F_L D_N^2 + c_{102}V_C Q_G D_N^2 + c_{103}F_L Q_G D_N^2$$

$$+ c_{104}V_C F_L Q_G D_N^2 + c_{105}V_C^2 D_N^2 + c_{106}V_C^2 F_L D_N^2 + c_{107}V_C^2 Q_G D_N^2 + c_{108}V_C^2 F_L Q_G D_N^2$$

$$+ c_{109}D_N^3 + c_{110}V_C D_N^3 + c_{111}F_L D_N^3 + c_{112}Q_G D_N^3 + c_{113}V_C F_L D_N^3 + c_{114}V_C Q_G D_N^3 + c_{115}F_L Q_G D_N^3$$

$$+ c_{116}V_C F_L Q_G D_N^3 + c_{117}V_C^2 D_N^3 + c_{118}V_C^2 F_L D_N^3 + c_{119}V_C^2 Q_G D_N^3 + c_{120}V_C^2 F_L Q_G D_N^3$$

$$\text{for } F_L \geq 60\% \qquad (4.3\text{b})$$

where c_i (i=1, 2,…, 120) are the new group of unknowns. The important difference between the original Equations 4.2 and the expanded Equations 4.3 is that the latter are linear equations for the unknowns. The least square solution for the linear equations can be solved using the Normal Equation Method [70]. The solution procedure is the same as that for the relative simpler form of the Equation 4.2 and the corresponding expanded equation reported in the earlier work [66], in which a fixed nozzle bore diameter was assumed and therefore there were much less unknowns (30 total).

The close match in Figures 4.2(A-D) between the lines from Equation 4.3 and some of the points from the computational model indicates the accuracy of this fit.

4.2.3 Inverse Models

For a given nozzle geometry and clogging status, the four basic casting process variables: casting speed, argon injection flow rate, gate opening and tundish bath depth are related. Choosing values for any three of these variables intrinsically determines the fourth.

Plots in Figure 4.2 are inconvenient to apply in practice because the tundish bath depth is generally not a dependent variable but usually kept constant during a stable continuous casting process. In order to determine and present the results in arbitrary practical ways, Equation 4.3 is inverted into three other forms with either V_C, Q_G, or F_L as the dependent variable (instead of H_T). The obtained "inverse models" can then be easily used to study how the process variables are related to each other. The derivation of these inverse models is straight forward, as shown below.

For the example of fixed tundish bath depth (H_T), fixed gate opening (F_L) less than 60%, and fixed argon injection flow rate (Q_G), Equation 4.3a can be rewritten as:

$$aV_C^2 + bV_C + c = 0 \tag{4.4}$$

where

$$\begin{aligned} a = {} & c_9 + c_{12}F_L + c_{13}Q_G + c_{15}F_L^2 + c_{17}F_LQ_G + c_{18}F_L^2Q_G \\ & + c_{27}D_N + c_{30}F_LD_N + c_{31}Q_GD_N + c_{33}F_L^2D_N + c_{35}F_LQ_GD_N + c_{36}F_L^2Q_GD_N \\ & + c_{45}D_N^2 + c_{48}F_LD_N^2 + c_{49}Q_GD_N^2 + c_{51}F_L^2D_N^2 + c_{53}F_LQ_GD_N^2 + c_{54}F_L^2Q_GD_N^2 \\ & + c_{63}D_N^3 + c_{66}F_LD_N^3 + c_{67}Q_GD_N^3 + c_{69}F_L^2D_N^3 + c_{71}F_LQ_GD_N^3 + c_{72}F_L^2Q_GD_N^3 \end{aligned} \tag{4.5a}$$

$$\begin{aligned} b = {} & c_2 + c_5F_L + c_6Q_G + c_{11}F_L^2 + c_8F_LQ_G + c_{16}F_L^2Q_G \\ & + c_{20}D_N + c_{23}F_LD_N + c_{24}Q_GD_N + c_{29}F_L^2D_N + c_{26}F_LQ_GD_N + c_{34}F_L^2Q_GD_N \\ & + c_{38}D_N^2 + c_{41}F_LD_N^2 + c_{42}Q_GD_N^2 + c_{47}F_L^2D_N^2 + c_{44}F_LQ_GD_N^2 + c_{52}F_L^2Q_GD_N^2 \\ & + c_{56}D_N^3 + c_{59}F_LD_N^3 + c_{60}Q_GD_N^3 + c_{65}F_L^2D_N^3 + c_{62}F_LQ_GD_N^3 + c_{70}F_L^2Q_GD_N^3 \end{aligned} \tag{4.5b}$$

$$\begin{aligned} c = {} & c_1 + c_3F_L + c_4Q_G + c_{10}F_L^2 + c_7F_LQ_G + c_{14}F_L^2Q_G - H_T \\ & + c_{19}D_N + c_{21}F_LD_N + c_{22}Q_GD_N + c_{28}F_L^2D_N + c_{25}F_LQ_GD_N + c_{32}F_L^2Q_GD_N \\ & + c_{37}D_N^2 + c_{39}F_LD_N^2 + c_{40}Q_GD_N^2 + c_{46}F_L^2D_N^2 + c_{43}F_LQ_GD_N^2 + c_{50}F_L^2Q_GD_N^2 \\ & + c_{55}D_N^3 + c_{57}F_LD_N^3 + c_{58}Q_GD_N^3 + c_{64}F_L^2D_N^3 + c_{61}F_LQ_GD_N^3 + c_{68}F_L^2Q_GD_N^3 \end{aligned} \tag{4.5c}$$

The theoretical casting speed is then obtained from:

$$V_C = \frac{-b + \sqrt{b^2 - 4ac}}{2a} \qquad \text{for} \quad F_L \le 60\% \tag{4.6}$$

The other root is always negative, which is physically incorrect. Similar equations are derived and detailed in Appendix E for gate openings greater than 60% and for F_L, Q_G, or D_N as the dependent variables.

Figure 4.3 and 4.4 shows typical plots with two of the inverse models. The following observations can be made from examination of Figures 4.2-4.4:

- For a given nozzle geometry and gas flow rate, higher casting speed results from a deeper tundish bath depth (constant gate opening) or a larger gate opening (constant bath depth).
- Casting speed is more sensitive to a change in bath depth at low casting speed than at high casting speed.
- Casting speed is more sensitive to a change in bath depth at large gate opening than at small gate opening.
- Casting speed is more sensitive to gate opening when maintaining a high casting speed.
- For a fixed tundish bath depth, increasing argon injection will slightly slow down the casting speed unless the gate opening increases to compensate.
- For a fixed gas flow rate, the percent gas increases greatly at low casting speeds, resulting in large buoyancy forces which reduces the effectiveness of the gate opening and make it difficult to drain the tundish.
- The extent of clogging condition can be inferred by comparing the measured steel flow rate with the value predicted by the inverse model for the given geometry, tundish bath depth, gas flow rate and percent gate opening.

4.2.4 Combined Model

The same multivariable curve-fitting method used to find Equation 4.2 can be employed to develop equations to predict trends for other important nozzle flow characteristics under practical operating conditions. Such characteristics include the lowest pressure in the nozzle (air aspiration), bias flow due to the slide-gate throttling, and the properties of the jets exiting the nozzle ports.

As an example, a model is now developed to predict the lowest pressure in the nozzle. When the lowest pressure in nozzle is below atmospheric pressure, air aspiration may occur if the joints are not properly sealed. In the 3-D numerical simulations, the reference ambient pressure is set to zero. Therefore, a negative pressure predicted in the simulation implies the existence of a partial vacuum (less than one atmosphere) which suggests a tendency for air aspiration.

For each 3-D simulation case in Table 4.1, the lowest pressure in the nozzle is recorded. The results are then curve-fit to produce an equation for the lowest pressure, P_L, as a function of the four independent variables, V_C, F_L, Q_G, and D_N.

As shown in Figure 4.5, the P_L *vs.* V_C data fits well with a quadratic function, *the* P_L *vs.* Q_G data fits well with a linear function, the P_L *vs.* D_N data fits well with a cubic function, and the P_L *vs.* F_L data must be split into two different linear regions for $F_L \leq 70\%$ and $F_L \geq 70\%$. The overall relationship can be written as

$$P_L = \left(b_1 V_C^2 + b_2 V_C + b_3\right)\left(b_4 F_L + b_5\right)\left(b_6 Q_G + b_7\right)\left(b_8 D_N^3 + b_9 D_N^2 + b_{10} D_N + b_{11}\right)$$

$$\text{for} \quad F_L \leq 70\% \qquad (4.7\text{a})$$

$$P_L = \left(b_{12} V_C^2 + b_{13} V_C + b_{14}\right)\left(b_{15} F_L + b_{16}\right)\left(b_{17} Q_G + b_{18}\right)\left(b_{19} D_N^3 + b_{20} D_N^2 + b_{21} D_N + b_{22}\right)$$

$$\text{for} \quad F_L \geq 70\% \qquad (4.7\text{b})$$

where the b_i (i=1-22) are unknown constants. Like for Equations 4.2, Equations 4.7 are expanded to yield a new pair of linear equations for a new group of total of 96 new fitting constants, as detailed in Appendix F. The new fitting constants are solved using the same least square curve fitting procedure as for Equations 4.5.

The close match in Figures 4.5(A-D) between the lines from Equations 4.7 and some of the points from the computational model indicates the accuracy of this fit. Using two different linear functions to fit the P_L *vs.* F_L data produces sharp transitions, observed at F_L=70% in Figure 4.5(d). A smoother transition could be obtained if more data between F_L=70% and F_L=100% were generated and a higher-order fitting model were employed for P_L *vs.* F_L.

It should be cautioned that all of the curves in Figures 4.5(A-D) correspond to varying tundish bath depths. This makes this presentation of the results difficult to interpret. In practice, the tundish bath depth is usually kept at a relatively constant level. It is the gate opening that is continuously adjusted to compensate for changes in the other variables, such as clogging and gas flow rate in order to maintain a constant casting speed. To better present the minimum pressure results in Equation 4.7 under these practical conditions, it is combined with one of the inverse models derived in the last section. Specifically, the inverse model for F_L as a function of V_C, H_T, Q_G, and D_N is simply inserted to replace F_L in Equations 4.7. This yields the combined model expressing P_L as a function of these same four practical independent variables. The results are presented in the later section on air aspiration.

4.3 Comparing with Plant Measurements

To verify the curve-fitting model and the corresponding inverse model, the predictions from the inverse model are compared with the measurements on an operating steel slab casting machine. Using Validation Nozzle A in Table 3.1, gate opening positions were recorded for different steel throughputs over several months [71]. Figure 4.6 shows the several thousand data points thus obtained. Only first heats in a sequence were recorded in order to minimize the effect of clogging. The tundish bath depth was held constant (H_T=1.125m) for these data, and the argon injection ranged from 7 to 10 SLPM. Since the measurements were recorded with different units from the Table 4.1 for the inverse model, the model predictions require conversion of F_L to the plant definition of gate opening F_P and casting speed to steel throughput Q_{Fe} by

$$F_P = (1\text{-}24\%)F_L + 24\% \qquad (4.8)$$

and

$$Q_{Fe}(tonne/min)=1.8788\ V_C(m/min) \qquad (4.9)$$

The geometry of the Validation Nozzle A is not exactly the same as the Standard Nozzle on which the inverse model predictions are based, but it is reasonably close. In addition to the inverse model prediction, additional numerical simulations using CFX were performed for the actual geometry of the Validation Nozzle A in Table 3.1. These results also are shown in Figure 4.6 as three big dots.

Figure 4.6 shows that the CFX results are very close to the inverse model predictions, despite the slight difference in nozzle geometry. In addition to validating both models, this suggests that the inverse model derived from the Standard Nozzle is applicable to other practical conditions, as long as the nozzle geometry is reasonably close. This is due to the fact that the pressure drop across the nozzle mainly depends on flow resistance. Port design may greatly affects the jet properties exiting the nozzle [17], but rarely affects the pressure drop, therefore the fitting model.

Both predictions from the inverse model and CFX simulation match the larger extreme of the range of measured gate opening percentage for a given steel throughput. The decreased gate opening often experienced in the plant is likely due to the following reasons:

- Less argon flow in the plant (7~10 SLPM vs. 10 SLPM) needs smaller opening to accommodate the same liquid flow.
- Rounded edge geometry likely found in the plant nozzles may cause less pressure drop than the sharp edge in new or simulated nozzles, so need less opening to achieve the same flow.
- The initial clogging experienced during the first heat may reduce the gate opening required for a given steel throughput. This is because, before it starts to restrict the flow channel, the streamlining effect of the initial clogging may reduce the overall pressure loss across nozzle. The last two factors will be further discussed in the next section.
- K-ε turbulence model uncertainty might be another source for lack of fit.

4.4 Effect of Clogging

4.4.1 Initial Clogging and Edge Sharpness

In both numerical simulations and experiments, three recirculation zones are observed in the vicinity of the slide-gate [18, 66]. One is created in the cavity of the slide-gate itself and the other two are located just above and below the throttling plate. In these recirculation zones, the flow is turbulent and the gas concentration is high. These recirculation zones and the sharp edges of the slide gate surfaces both may create an extra resistance to flow. Slight erosion by the flowing steel may round off the ceramic corners. In addition, it is known that clogging tends to buildup initially in the recirculation regions [18]. Because of this, the initial clogging might not impede the flow and instead may decrease the flow resistance by streamlining the flow path. This may decrease the total pressure drop across the nozzle.

To investigate these phenomena, four simulations were performed using the 3-D finite difference model for the cases illustrated in Figure 4.7. The geometry and casting conditions, given in Table 3.1 for Validation Nozzle B, were chosen to match conditions where measurements were available for comparison [72]. All four cases are the same, except for the geometry near the slide gate. The first case, Figure 4.7(a) has sharp edges similar to the Standard Nozzle simulated in the foregoing parametric study. The next case, shown in Figure 4.7(b), has the four slide gate edges rounded with a 3mm radius. The final two cases have the recirculation regions partially filled in to represent two different amounts of initial clogging with alumina reinforced by solidified steel. One case, Figure 4.7(c), has solid clog material in the gate cavity and around the throttling gate and smooth surfaces in the upper SEN. The final case, Figure 4.7(d), has extra clogging at the same places but with more buildup around the gate.

From the numerical simulation results, the corresponding tundish bath depth for each case was calculated using Equation 4.1. These values are compared in Figure 4.8 with the measured tundish bath depth. The standard sharp-edge case with no clogging has the largest pressure drop, so requires the greatest bath depth. Rounding the edges of the throttling plates reduces the pressure drop across the gate plates and lowers the required tundish head by 18%. The initial clogging is even more effective at streamlining the liquid steel flow around the slide-gate, decreases the recirculation loops and lowers the pressure loss. The initial clogging of Figure 4.8(c) reduces the required tundish bath depth by 24%, relative to the standard sharp, non-clogged case. Further increasing the initial clogging, case Figure 4.8(d), decreases the required tundish bath depth by 36%, which is even lower than the measured value of 0.927m. The clogging condition for the measurement is unknown. The measurement was taken at the first heat, so it is likely to have some initial clogging buildup around the slide-gate recirculation regions.

The clogging condition and edge roundness affects not only the pressure drop across the nozzle but also the flow pattern exiting the ports into the mold. Figure 4.9 shows the simulated flow pattern at the center plane parallel to the mold narrow face. Difference such as edge roundness and clogging around the slide gate greatly change the flow pattern in the SEN as well as the jets out of the ports. The jets are seen to vary from two small symmetric swirls to a single large swirl which can switch rotational directions. Thus, a slight change in clogging can suddenly change the jet characteristics exiting the port. This will produce a transient fluctuation in flow in the mold cavity which could be very detrimental to steel quality. This result provides further evidence of problems caused even by initial nozzle clogging.

4.4.2 Severe Clogging

With increasing alumina buildup, the clogging, instead of streamlining the flow, begins to restrict the flow channel and to create extra flow resistance. The gate opening then must increase to maintain constant liquid steel flow rate through the nozzle. The effect of clogging on the flow depends on both the clogging status (how much alumina deposits) and the clogging shape (where and how the alumina deposits). It has been observed that clogging often builds up relatively uniformly in the radial direction and acts to reduce the diameter of the nozzle bore [6, 73]. Based on this fact, a way to investigate the effect of this type of clogging is simply to reduce the bore diameter. Figure 4.2(C) shows that decreasing the bore size, i.e., increasing clogging, requires the tundish liquid level to increase in order to maintain the same flow rate at a constant gate opening. Using the inverse model for gate opening F_L, the effect of the clogging/decreasing bore size is quantified for practical conditions in Figure 4.10.

Figure 4.10(A) shows how gate opening must increase to accommodate clogging (or decreasing bore size) in order to maintain a constant flow rate for a fixed tundish level. Figure

4.10(b) shows how the steel flow rate decreases if the gate opening percentage does not change. It can be seen that the gate opening is much less sensitive to clogging when the bore diameter is large. Thus, clogging may be difficult to detect from gate changes until it is very severe and the gate opening increases above 60%.

4.5 Effect of Air Aspiration

4.5.1 Lowest Pressure in Nozzle

One of the suggested mechanisms for the beneficial effect of argon injection in reducing nozzle clogging is that the argon generates positive pressure in the nozzle [6]. Avoiding a partial vacuum in the nozzle should make it less likely for air to be drawn in through any cracks, joints, or sealing problems in the nozzle, with the benefit of avoiding reoxidation. Numerical simulations in this work, Figure 4.5(B), and water modeling [56] both show that the minimum pressure in the nozzle can drop below zero in some circumstances, and that argon gas injection can raise that pressure above zero. The lowest pressure in the nozzle is also affected by the casting speed, gate opening, tundish bath depth, nozzle bore size (or extent of clogging), as shown in Figure 4.5. The combined fitting model (Equation 4.7) is now applied to study the effects of these variables on minimum pressure for the practical conditions of fixed tundish bath depth.

The lowest pressure in the nozzle is presented as a function of casting speed in Figure 4.11-4.13 for different argon injection rate and nozzle bore size and as a function of argon flow rate in Figure 4.14-4.15 for different casting speed respectively. All of these figures fix the tundish bath depth and allow gate opening to vary, which reflects realistic operation conditions. The corresponding gate openings, along with both “cold” and “hot” argon injection volume fractions, are also marked on Figures 4.11-4.15 for easy reference. The results in Figures 4.5 and

4.11-4.15 quantify how increasing argon injection and decreasing tundish bath depth both always tend to decrease the pressure drop across the slide gate, thereby raising the minimum pressure in the nozzle and making air aspiration less likely.

The effect of casting speed is complicated because of several competing effects. Higher flow rate tends to increase the pressure drop and vacuum problems. At the same time, increasing the flow rate allows the gate to open wider, which tends to alleviate the vacuum problems. The worst vacuum problems occur with the gate at about 60% open by distance or 50% open by area fraction, regardless of casting speed. Above 70% linear gate opening, the effect of decreasing the throttling effect with increased gate opening dominates, so that the vacuum problems are reduced with increasing casting speed. Below 50% gate opening, the effect of lowering casting speed dominates, so that the vacuum problems are reduced with decreasing speed. A further effect that helps to reduce vacuum problems at lower casting speed is that the gas percentage increases (for a fixed gas flow rate).

The common practice of employing oversized nozzle bores to accommodate some clogging forces the slide gate opening to close. Although this makes the opening fraction smaller, the opening area actually may increase slightly. Thus, the tendency for air aspiration due to vacuum problems will also decrease, so long as the linear opening fraction stays below 50%. However, this practice does generate increased turbulence and swirl at the nozzle port exits, so should be used with caution.

When the pressure drop across the gate is small and there is no vacuum problem, the minimum pressure in the nozzle moves to the nozzle ports. The port pressure depends mainly on SEN submerged depth.

4.5.2 Optimal Argon Flow

The minimum argon flow rate required to avoid any vacuum in the nozzle can be obtained by letting P_L=0 in Equation 4.7 and solving for Q_G. The results are plotted in Figure 4.16 and 4.17 as a function of casting speed at fixed tundish bath depth for tow different nozzle bore size, respectively. The top of these figures shows the corresponding slide gate opening. The results suggest ways to optimize argon flow to avoid air aspiration conditions in the nozzle.

Injecting argon gas sometimes enables the transition from an air aspiration condition to positive pressure in the nozzle. The minimum argon flow rate required to avoid a vacuum condition can be read from Figure 4.16 and 4.17. It increases greatly with tundish bath depth. For a given tundish bath depth, the minimum argon flow rate first rapidly increases with increasing casting speed, and then decreases with increasing casting speed. The most argon is needed for linear gate openings between 50%-70% for the reasons discussed earlier.

At low casting speed, (below 0.5m/min), or at low tundish levels (below 0.6m), no vacuum is predicted in the nozzle. Thus, argon injection is not needed under these conditions. During ladle transitions and at other times when either casting speed or tundish level is low, argon flow should be turned off or at least severely reduced. Besides saving argon, this avoids flow problems in the mold and possible gas bubble entrapment.

Figure 4.16 and 4.17 show that very large argon flow rates (over 20 SLPM) are needed to avoid a vacuum condition for high tundish level (deeper than 1.2m) and high casting speed (above 1.5m/min). Specifically, a 0.2m increase in tundish bath depth typically requires an additional 5 SLPM of argon to compensate the vacuum effect at high casting speeds. In practice, the argon injection flow rate is limited to a maximum of about 15 SLPM. This is because argon injection greatly changes the flow pattern in the mold [22, 23]. Excessive argon injection may cause a transition from “bubbly flow” to “annular" flow in the nozzle [16], create boiling action at the meniscus and cause quality problems [73]. Therefore, it is not feasible for argon injection to eliminate the vacuum in the nozzle when the tundish bath is deep and the casting speed is high. Other steps should be taken to avoid air aspiration. Besides improving the sealing at the joints (especially the joints between the slide-gate, the lower plate, and the SEN holder), other methods suggested by the model (Equation 4.7) include:

- Choose bore diameters according to the steel flow rate in order to avoid linear gate openings near 60%. To increase gate openings above 60%, a smaller nozzle bore diameter could be used, but this allows too little accommodation for clogging. To decrease gate openings to below 60%, a larger bore diameter is needed.
- Decrease tundish bath depth. A shallower tundish level has less pressure drop, so generates less vacuum tendency.

4.6 Conclusions

The turbulent flow of the liquid steel and argon bubbles in a slide-gate nozzle has been simulated with a verified three-dimensional finite difference model. The results are further processed using advanced multivariable curve fitting methods to relate casting speed, argon injection rate, slide-gate opening position, nozzle bore diameter and tundish bath depth to clogging and air aspiration potential.

Both rounding the nozzle edges due to erosion and initial clogging buildup are found to enhance the steel flow rate due to a streamlining effect. Only after severe clogging builds up is the flow eventually restricted so that the gate opening must increase to maintain the casting speed. However, the initial clogging and even edge rounding might greatly affect the flow pattern and jet characteristics. The extent of clogging can be predicted by comparing the measured steel flow rate to the prediction, leading to a “clogging index”.

The pressure drop generated across the partially-closed slide gate creates a partial vacuum just below the slide gate which tends to entrain air, leading to reoxidation problems. The worst vacuum appears to occur for 50%-70% linear gate opening (about 50% area fraction). Increasing argon injection helps to raise the lowest pressure and sometimes may avoid this vacuum. For shallow tundish bath depths or low casting speeds, the pressure is always positive, so argon should not be used. Less argon is needed if the nozzle bore size is chosen to avoid intermediate casting speeds so that the gate is either nearly fully open or is less than 50%. For high casting speeds, a 0.2m increase in tundish bath depth typically will require an additional 5 SLPM of argon to compensate the vacuum effect. In practice, argon injection is limited by its effect on the flow pattern, and may not be able to fully compensate the vacuum effect.

Table 4.1 Simulation conditions for the standard nozzle

Variable	Value	Notes
Casting Speed V_C (m/min)	0.2, 0.5, 1, 1.5, 2.0, 2.3	For 8”x52” slab
Gate Opening F_L (%)	40, 50, 60, 70, 100	Linear opening
Argon Flow Rate Q_G (SPLM)	0, 5, 10	“cold” argon
Nozzle Bore Diameter D_B (mm)	60, 70, 78, 90	Also simulates clogging

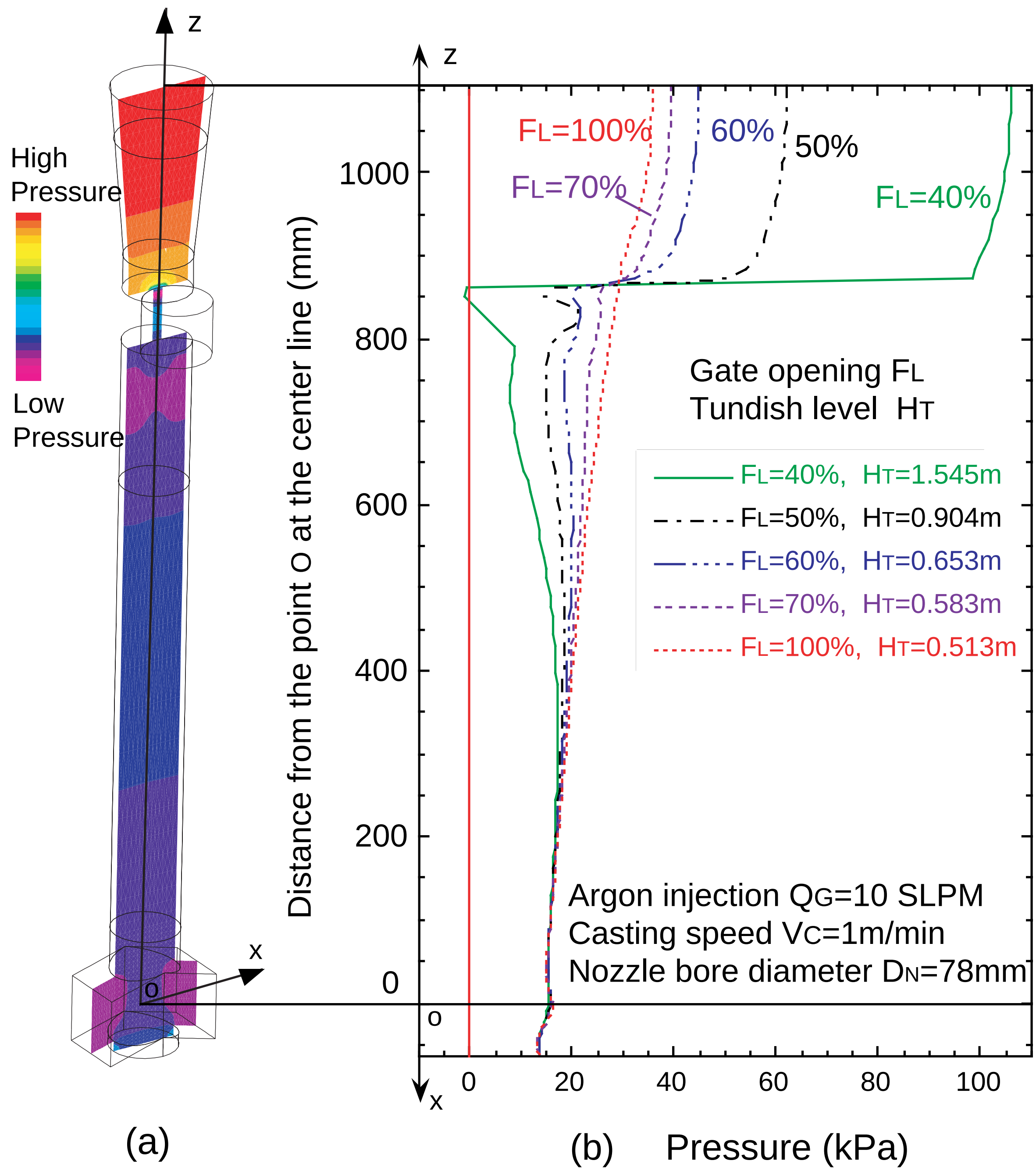

Figure 4.1 Pressure distribution in the standard nozzle, predicted by the 3-D finite difference model (a) shaded contour plot at the center-plane (b) pressure profile along the centerline (from top to outlet port)

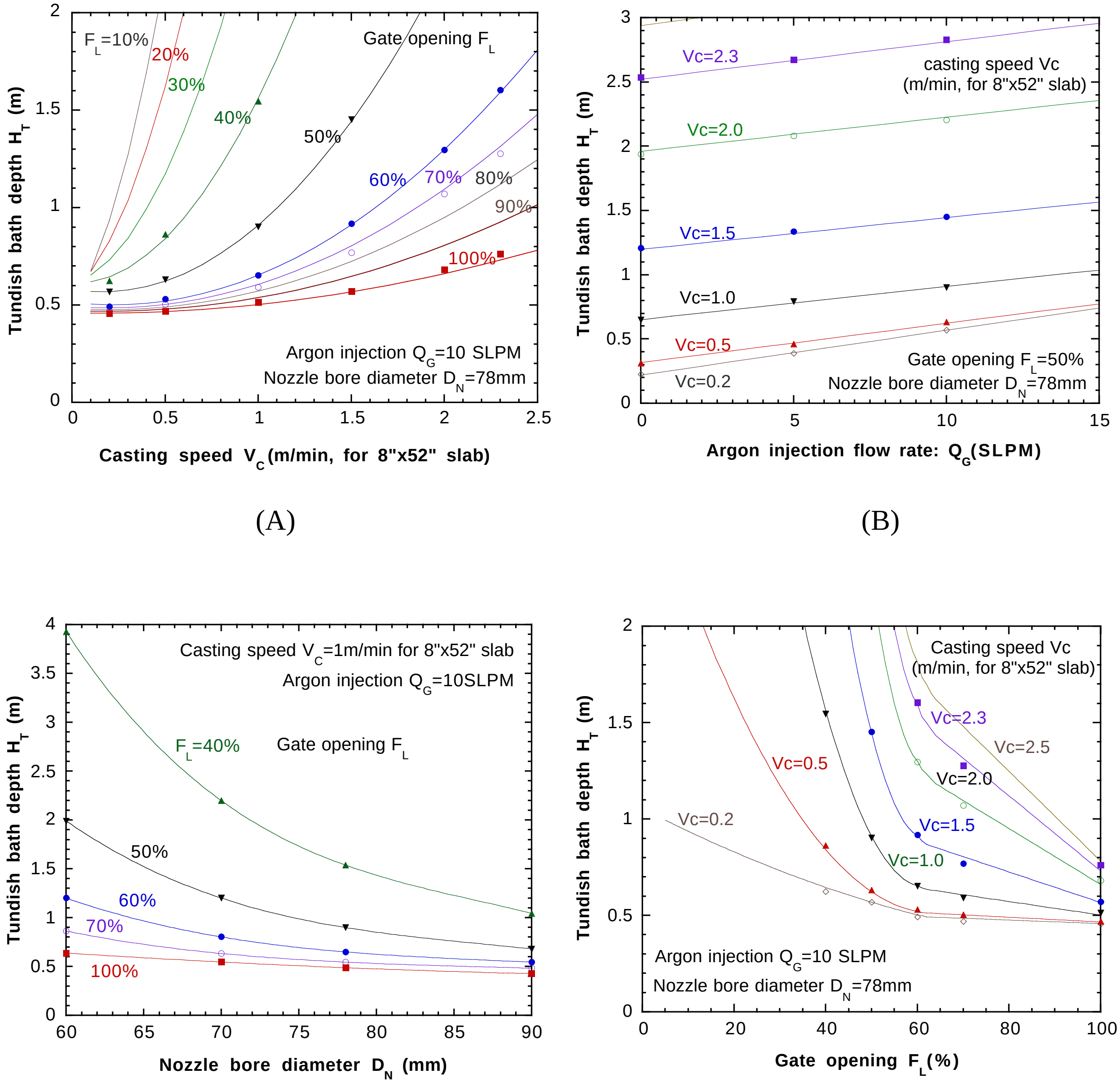

(A) (B)

(C) (D)

Figure 4.2 CFX data (points from Equation 4.1) and fitting curve (lines of Equation 4.2) showing effects of casting speed V_C, gate opening F_L, argon injection Q_G and nozzle bore size D_N on tundish bath depth H_T

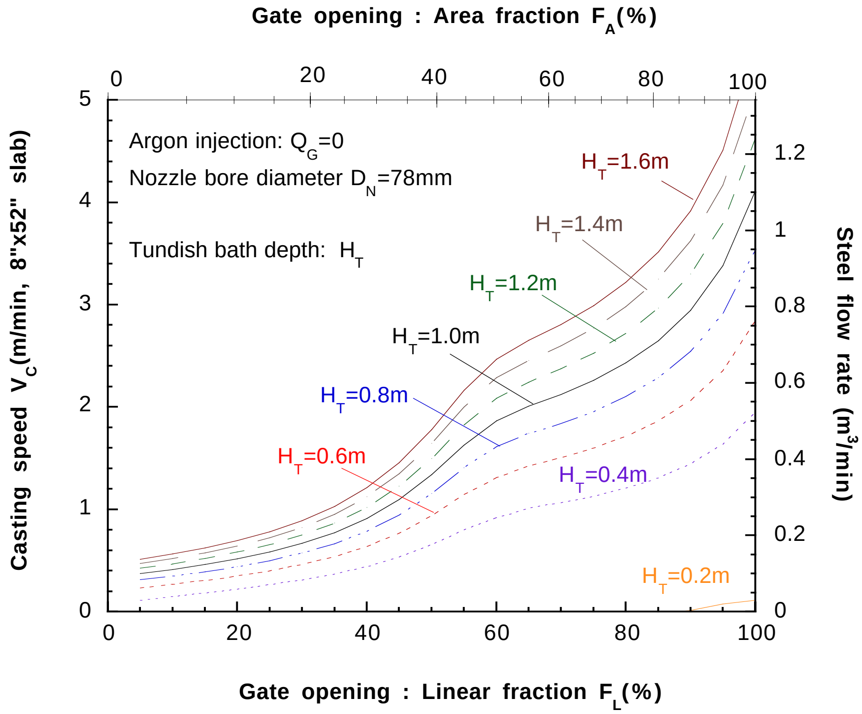

(A) Argon injection rate Q_G=0

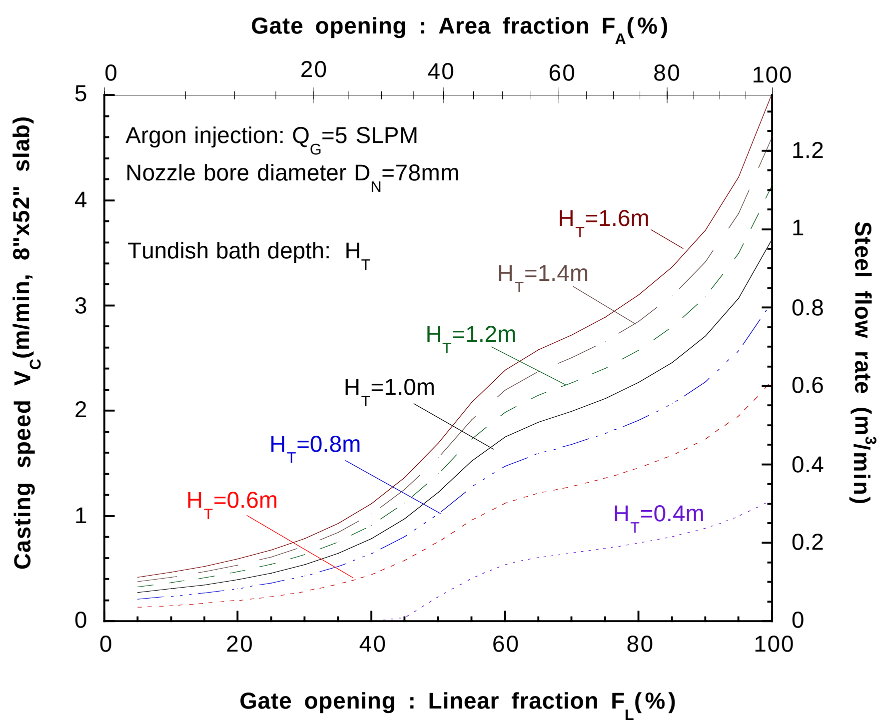

(B) Argon injection rate Q_G=5 SLPM

Figure 4.3 Inverse model plots showing effect of gate opening and tundish bath depth on casting speed (A) Argon injection rate Q_G=0, and (B) Argon injection rate Q_G=5 SLPM

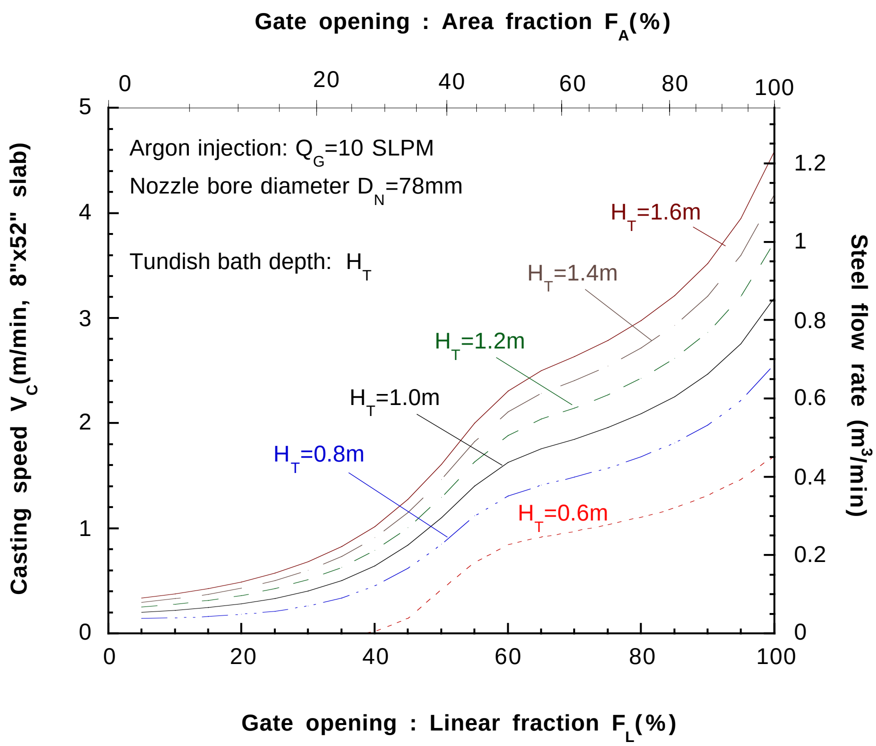

(C) Argon injection rate Q_G=10 SLPM

Figure 4.3 Inverse model plots showing effect of gate opening and tundish bath depth on casting speed (C) Argon injection rate Q_G=10 SLPM

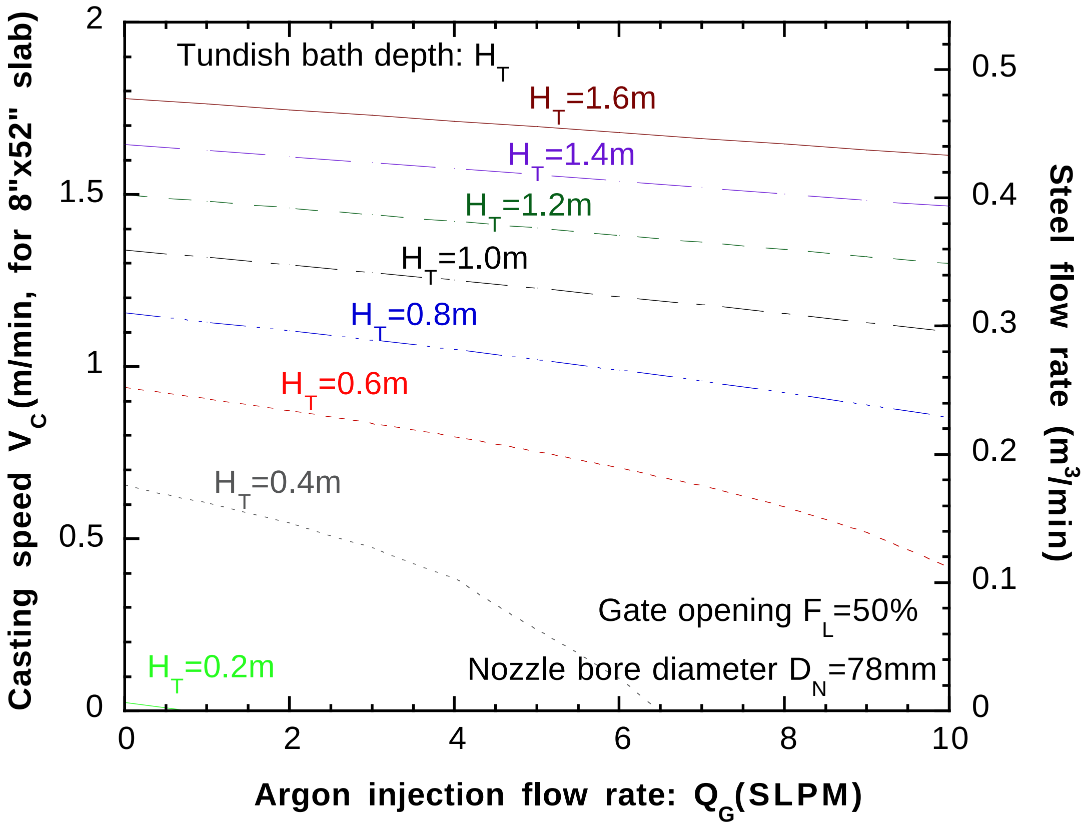

Figure 4.4 Inverse model plots showing effect of gas injection and tundish bath depth on casting speed

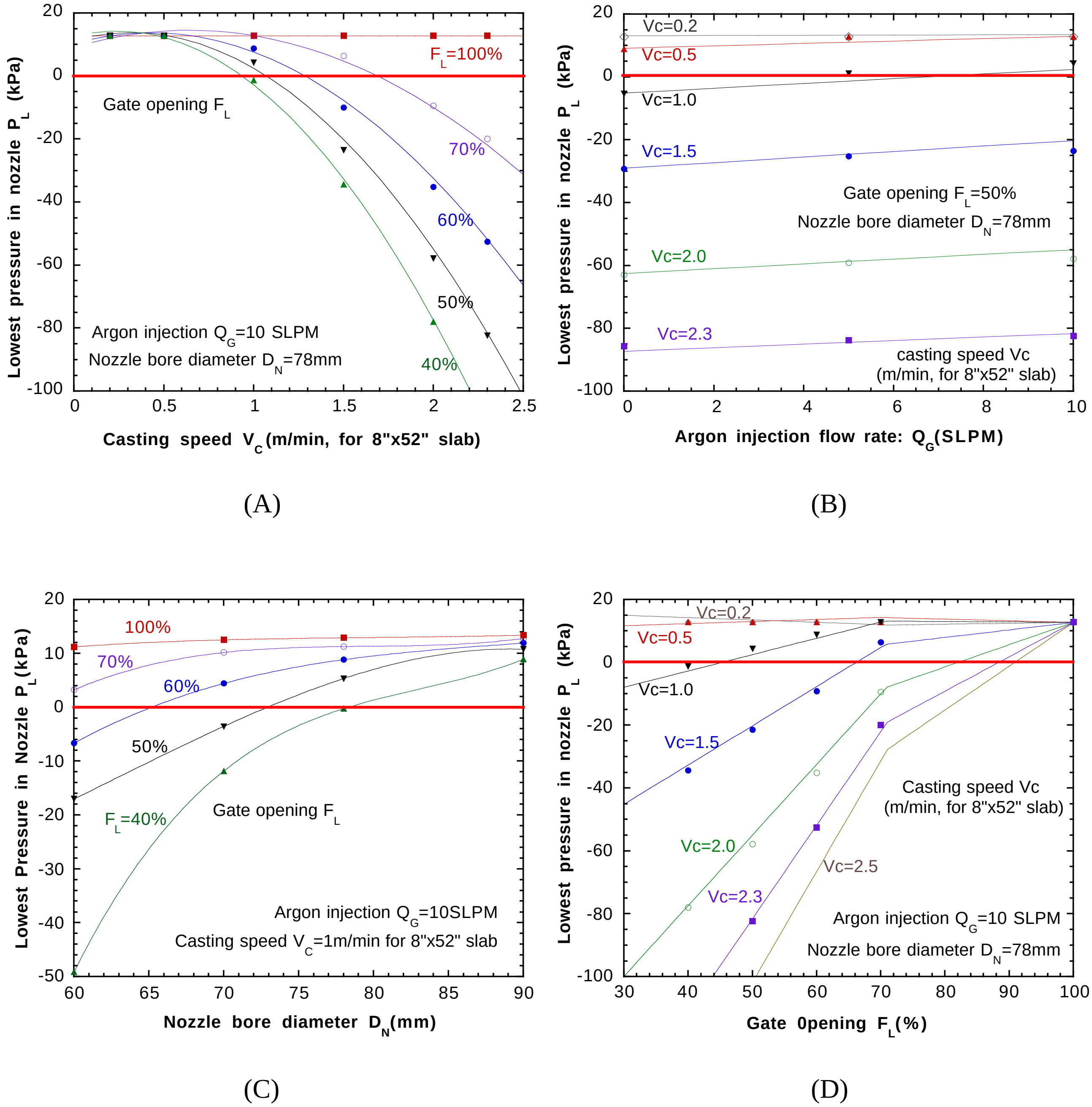

Figure 4.5 CFX data (points) and fitting curve (lines) showing effects of casting speed V_C, gate opening F_L, argon injection Q_G and nozzle bore size D_N on the lowest pressure P_L in nozzle (under varying tundish bath depth)

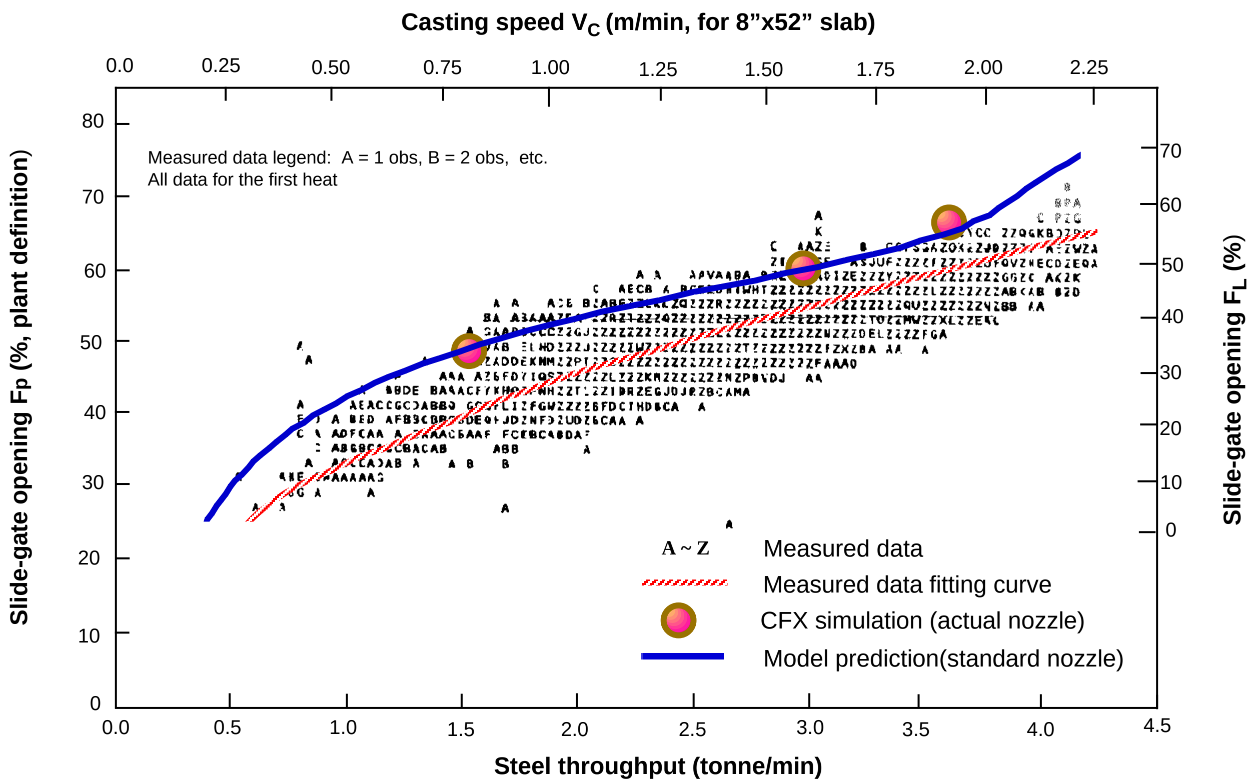

Figure 4.6 Comparison of the measurement and the model prediction

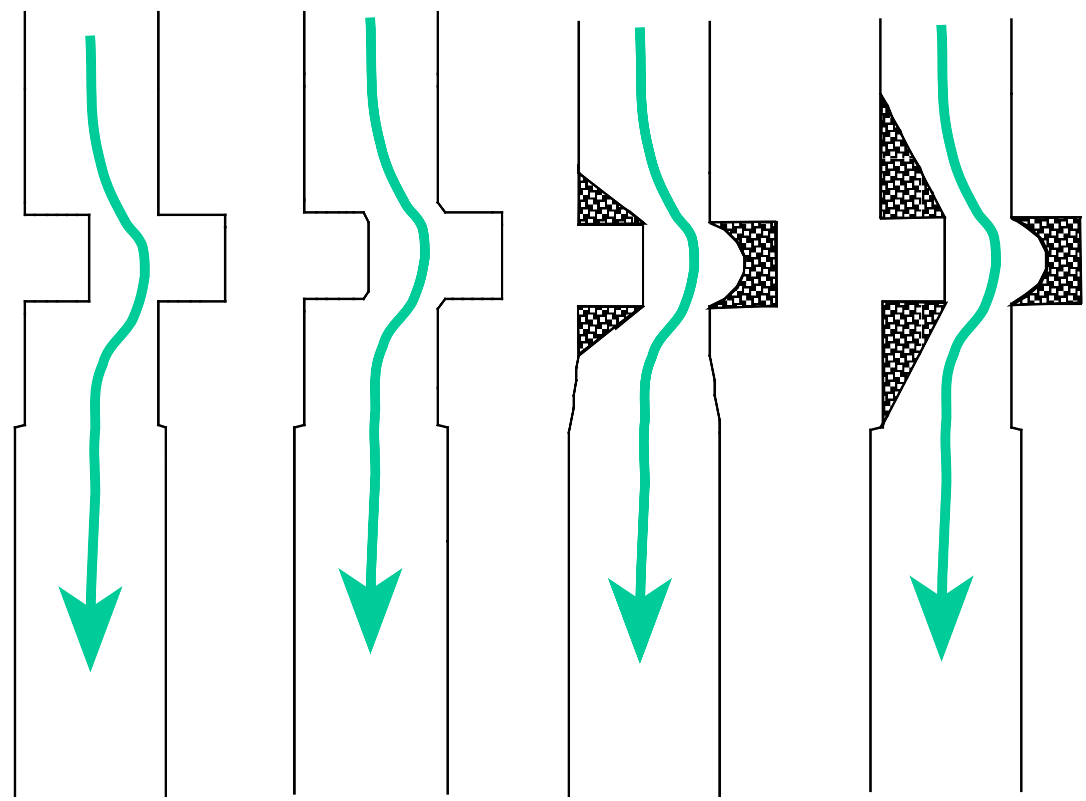

(a) Sharp edges (b) Rounded edges (c) Sharp edges with initial clogging (d)Sharp edges with more inital clogging

Figure 4.7 Schematic of initial clogging and rounded edges in the vicinity of the slide-gate (Validation Nozzle B)

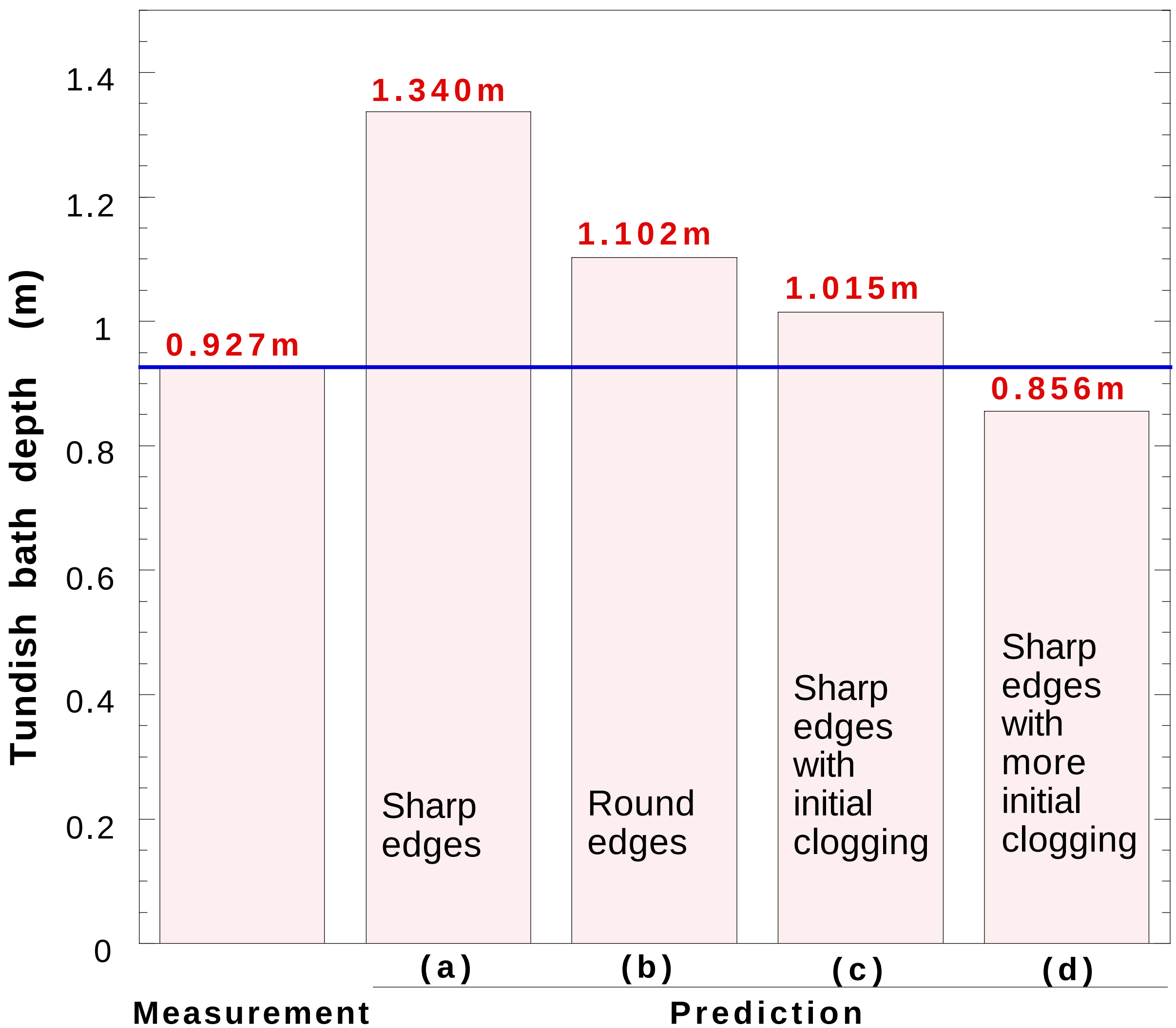

Figure 4.8 Effects of initial clogging and rounded edges on tundish bath depth (Validation Nozzle B)

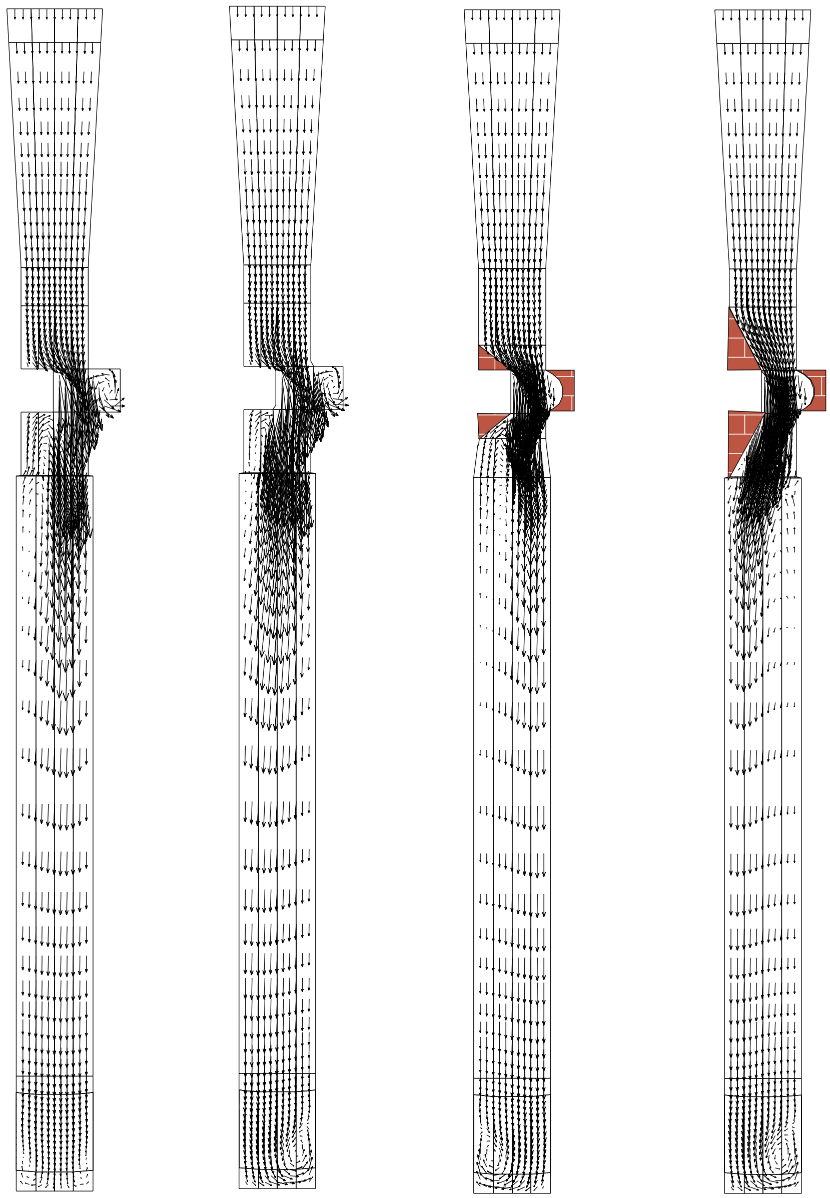

Figure 4.9 Effects of initial clogging and rounded edges on nozzle flow pattern (center plane parallel to the narrow face) for Validation Nozzle B

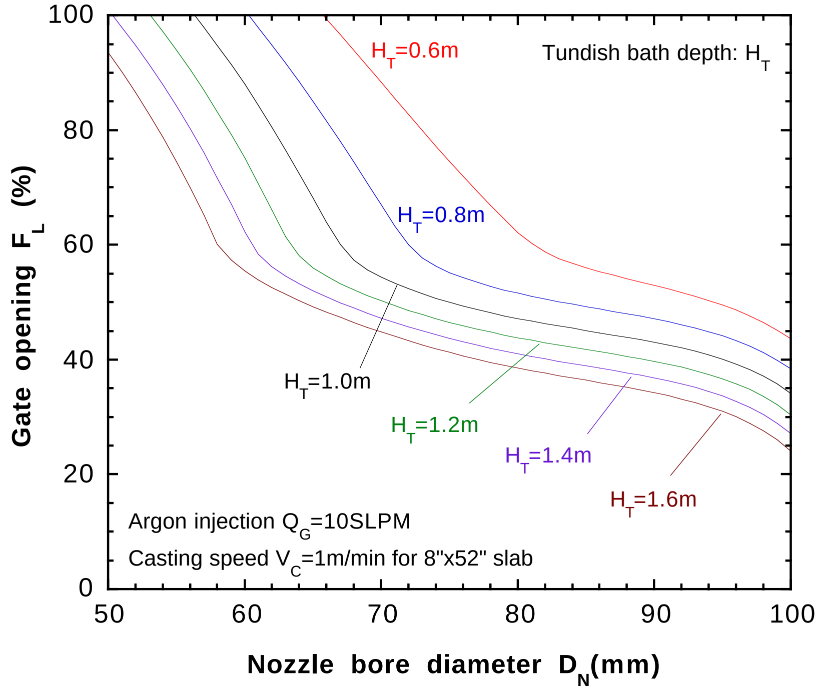

(A) Gate opening changes to accommodate clogging (decreased nozzle bore size) for fixed gas flow rate and casting speed

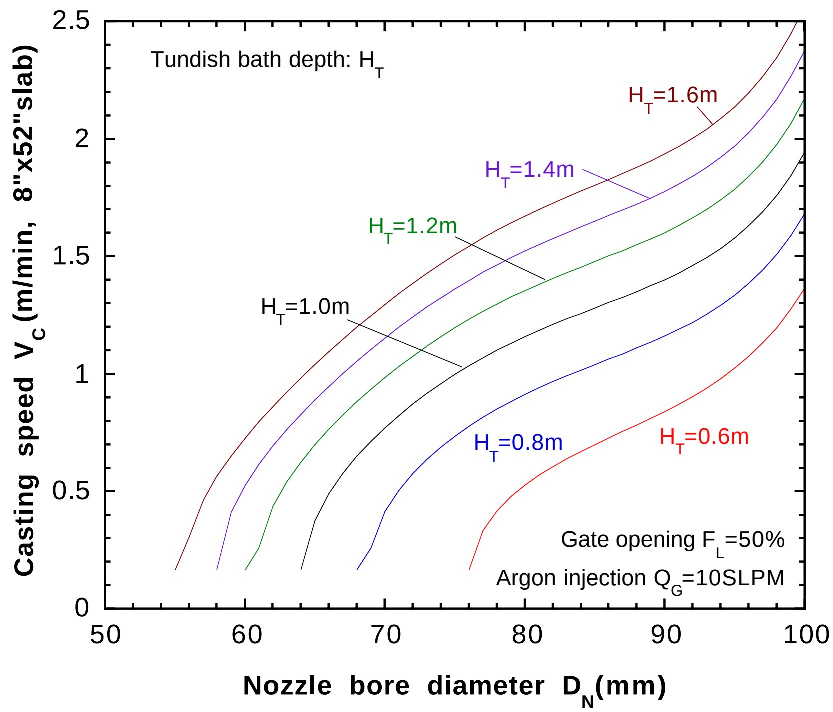

(B) Casting speed changes caused by clogging (or nozzle bore size change) for fixed gate opening

Figure 4.10 Effects of clogging or nozzle bore size

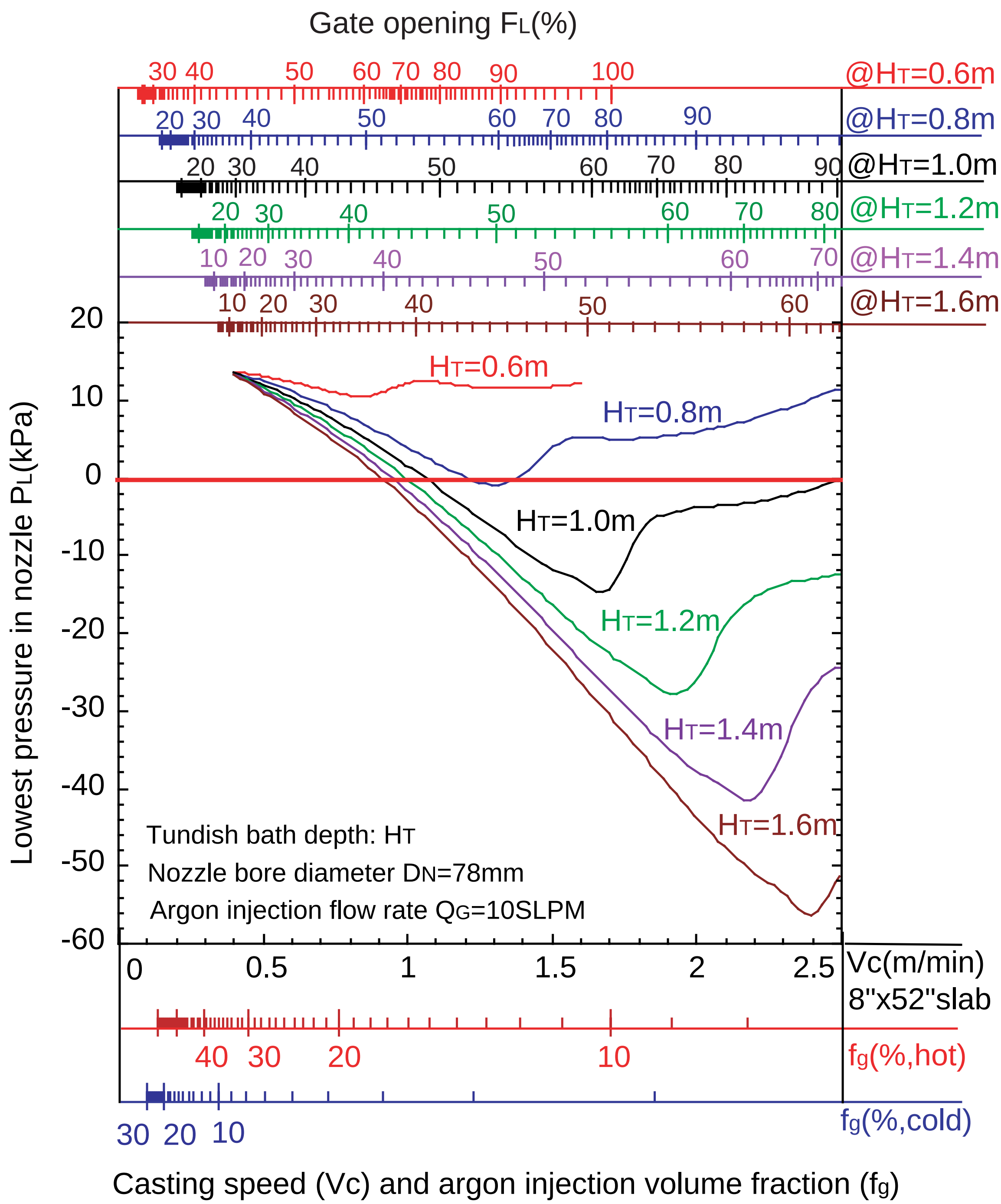

Figure 4.11 Effect of casting speed on minimum pressure in the nozzle for constant tundish bath depth and argon injection flow rate (Q_G=10SLPM, D_N=78mm)

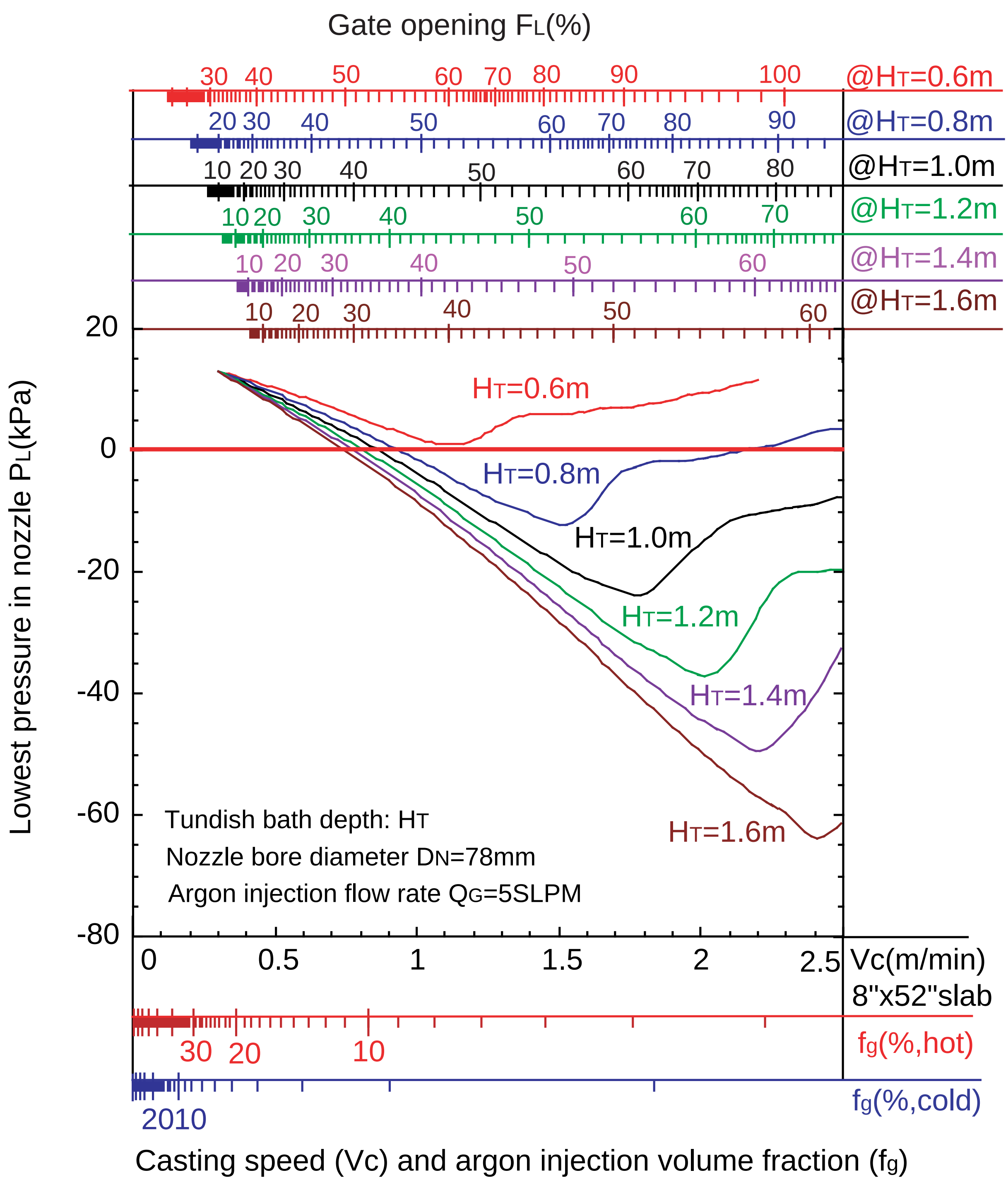

Figure 4.12 Effect of casting speed on minimum pressure in the nozzle for constant tundish bath depth and argon injection flow rate (Q_G=5SLPM, D_N=78mm)

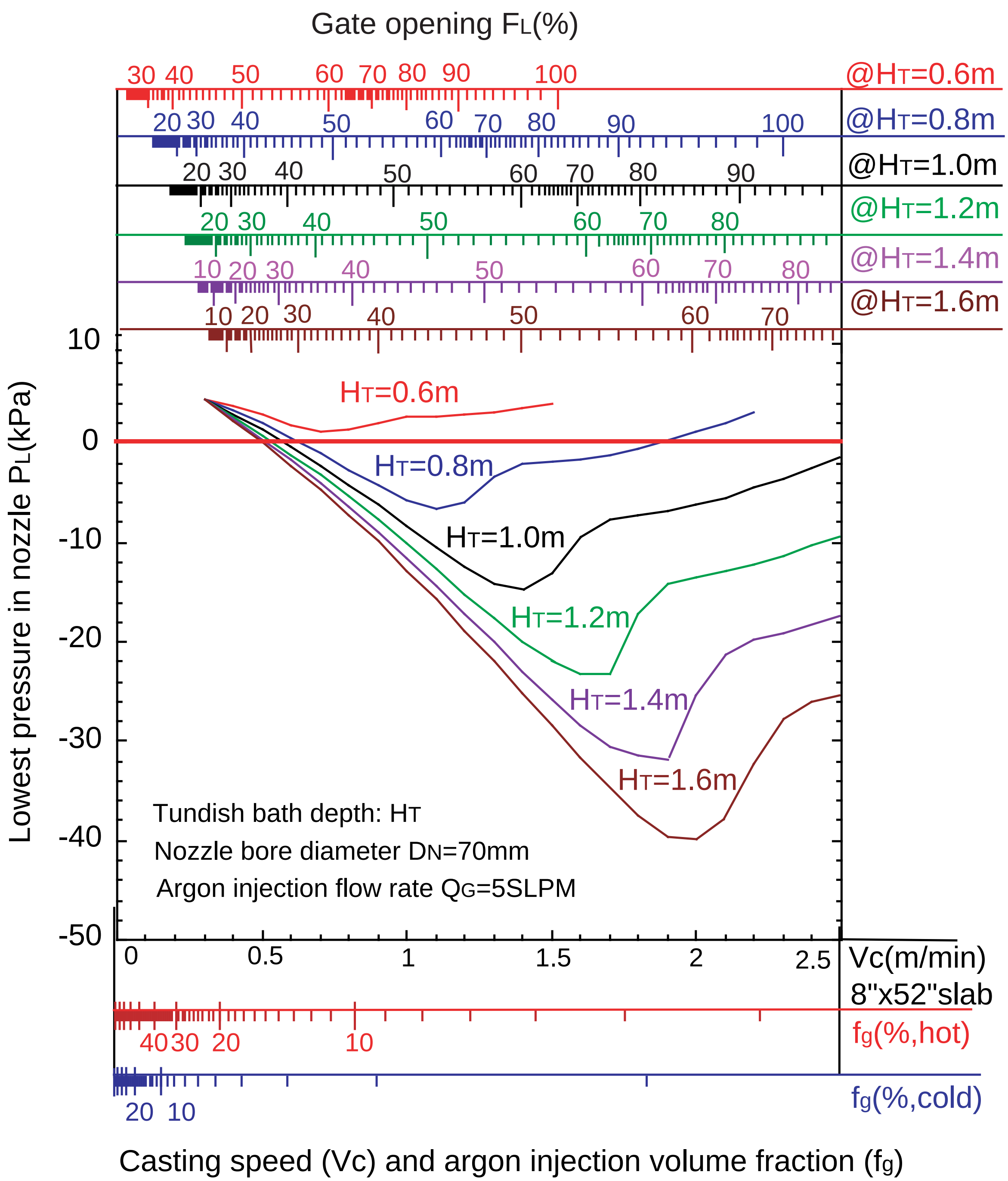

Figure 4.13 Effect of casting speed on minimum pressure in the nozzle for constant tundish bath depth and argon injection flow rate (Q_G=5SLPM, D_N=70mm)

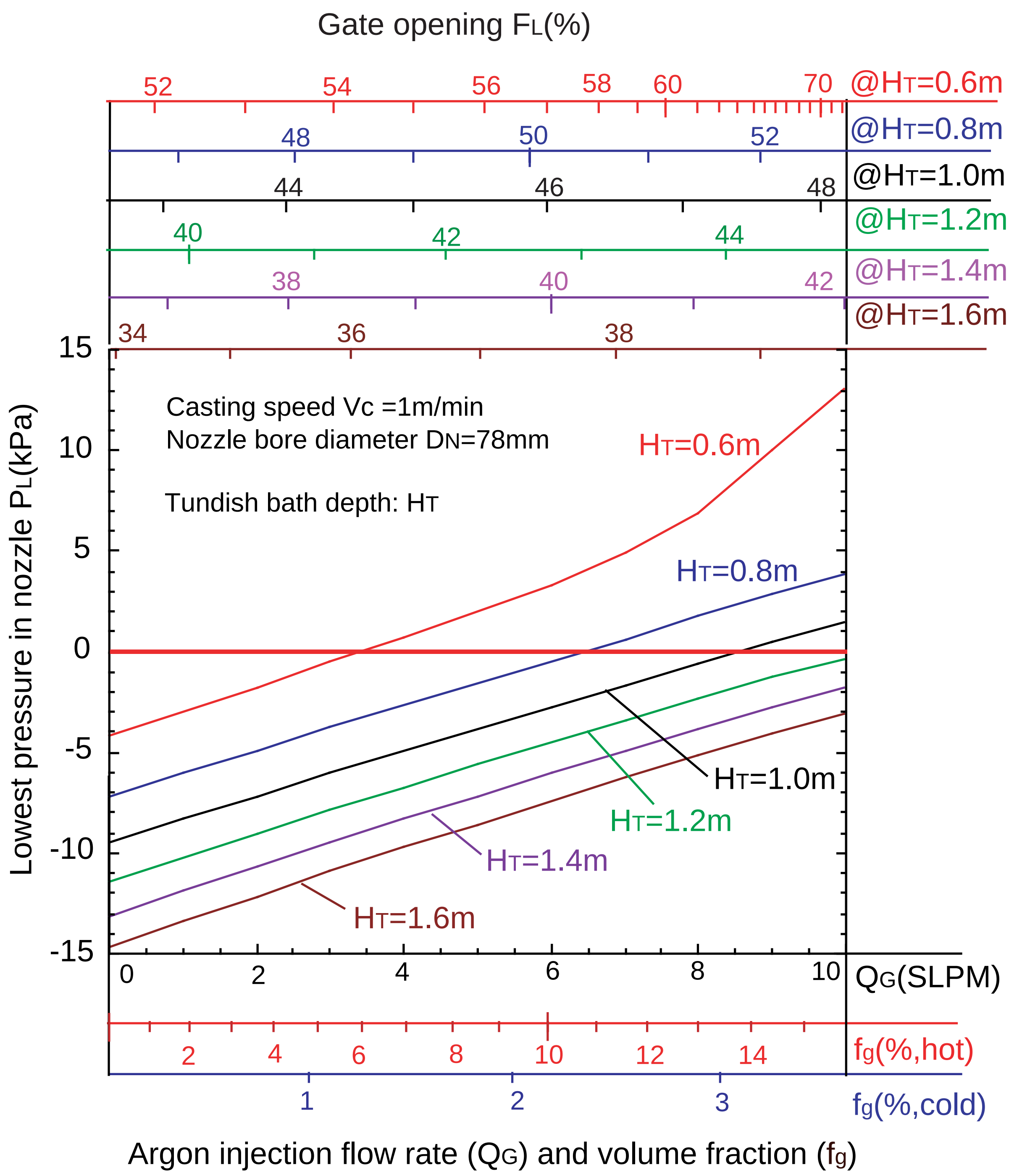

Figure 4.14 Effect of argon injection flow rate on minimum pressure in the nozzle for constant tundish bath depth and casting speed (V_C=1m/min, D_N=78mm)

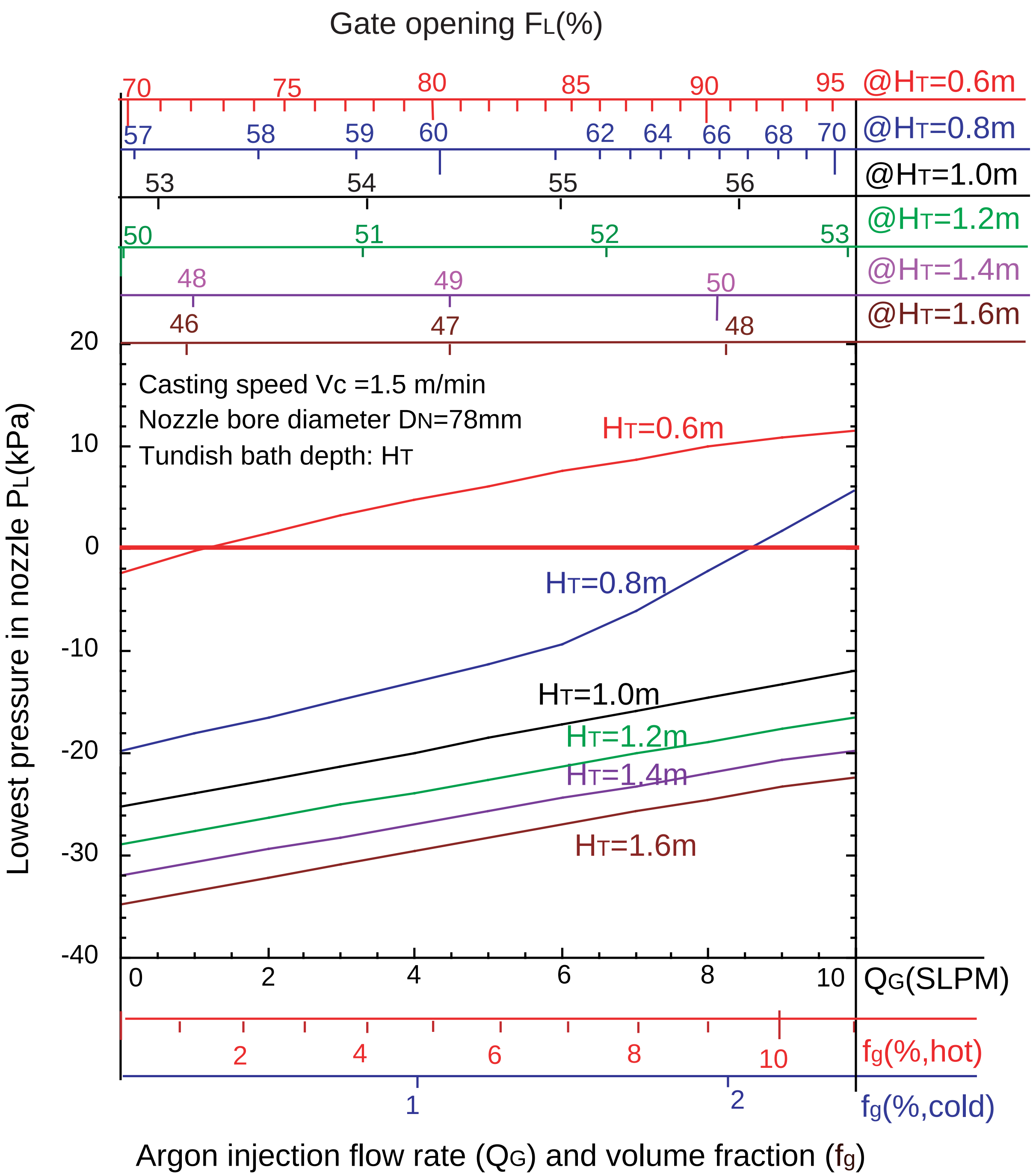

Figure 4.15 Effect of argon injection flow rate on minimum pressure in the nozzle for constant tundish bath depth and casting speed (V_C=1.5m/min, D_N=78mm)

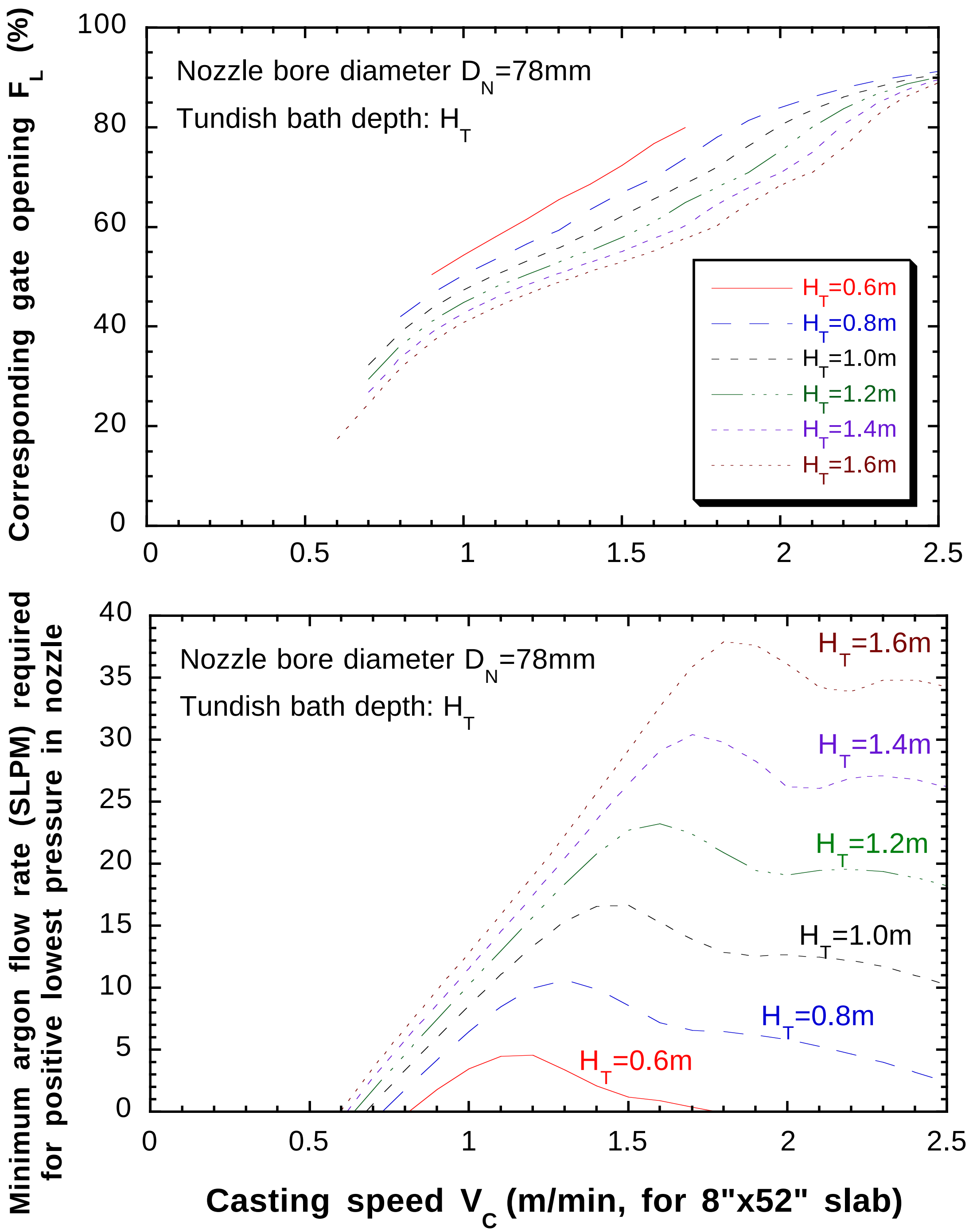

Figure 4.16 Effect of casting speed and tundish depth on minimum argon flow rate required for positive pressure in nozzle (bottom) and the corresponding gate opening (top) for D_N=78mm

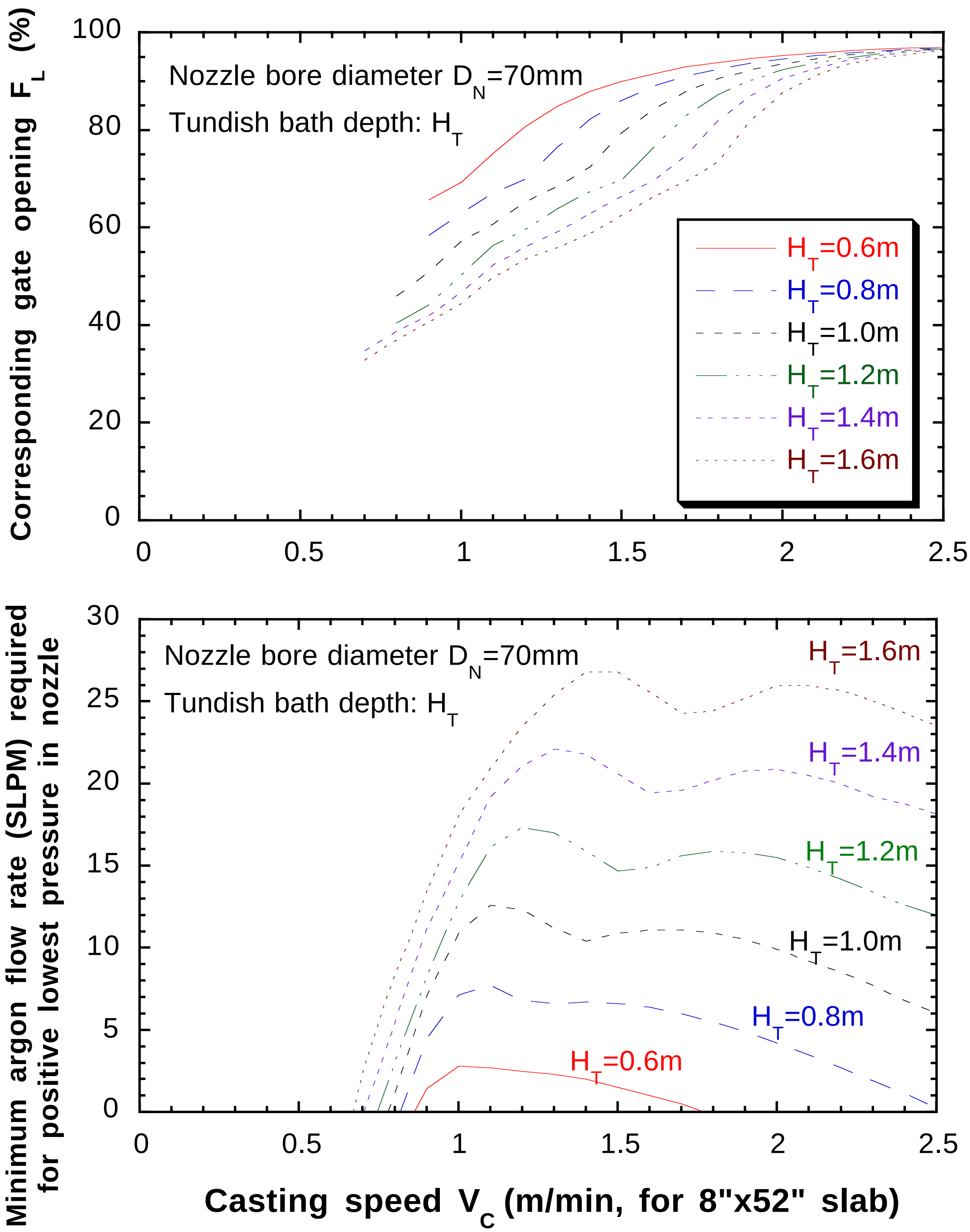

Figure 4.17 Effect of casting speed and tundish depth on minimum argon flow rate required for positive pressure in nozzle (bottom) and the corresponding gate opening (top) for D_N=70mm

CHAPTER 5. CONCLUSIONS

This work combines mathematical modeling and experiments to investigate the argon bubble behavior in slide-gate tundish nozzles and to analyze phenomena related to product defects and operational problems during the continuous casting of steel slabs. Water model experiments are performed to study bubble formation behavior in flow conditions approximating those in a slide-gate tundish nozzle of continuous casting process. An analytical model is developed to predict the bubble size. A three-dimensional finite difference model is developed to study the turbulent flow of liquid steel and argon bubbles in the slide-gate nozzles. Experiments are performed on a 0.4-scale water model to verify the computational model by comparing its prediction with velocity measurements using PIV (Particle Image Velocimetry) technology. A weighted average scheme for the outflow is developed to quantify the characteristics of the jets exiting the nozzles. The validated model is then employed to perform an extensive parametric study to investigate the effects of casting operation conditions and nozzle port design. The interrelated effects of nozzle clogging, argon injection, tundish bath depth, slide gate opening and nozzle bore diameter on the flow rate and pressure in tundish nozzles are quantified using an inverse model, based on interpolation of the numerical simulation results. The results are validated with measurements on operating steel continuous slab-casting machines, and presented for practical conditions.

5.1 Bubble Formation Study

Effects of various variables such as liquid velocity, gas injection flow rate, gas injection hole size and gas density are investigated. Predictions with the analytical model show good agreement with the measurements. Specific findings include:

- The mean bubble size increases with increasing gas injection flow rate.
- The mean bubble size increases with decreasing shearing liquid velocity.
- The mean bubble size in flowing liquid is significantly smaller than in stagnant liquid.
- The mean bubble size is relatively independent of gas injection hole size, especially at high liquid velocity.
- The composition of the gas has little influence on bubble size.
- Bubble formation falls into one of the four different modes, depending primarily on the velocity of the flowing liquid and secondarily on the gas flow rate.
- In Mode I (low liquid speed and small gas flow rate), uniform-sized bubbles form and detach from the tip of the gas injection hole. In Mode III (high liquid speed), the injected gas elongates down along the wall and breaks into uneven-sized bubbles. Mode II is intermediate between Mode I and Mode III. In Mode IV (high liquid speed and high gas flow rate), the gas elongates a long distance down the nozzle walls, forming a sheet before breaking up.
- Compared to water-air system, argon bubbles in liquid steel should tend to spread more over the ceramic nozzle wall in liquid steel and fall into Mode II or III region. Thus, the argon bubbles likely have a larger tendency to have non-uniform sizes when detaching from the wall.
- Argon bubbles generated in liquid steel should be larger than air bubbles in water for the same flow conditions. The difference should become more significant at lower liquid velocity and smaller gas injection flow rate.

5.2 Two-Phase Flow in Slide-Gate Nozzles

The turbulent flow of liquid steel and argon bubbles in a slide-gate tundish nozzle can be effectively modeled with the Eulerian multiphase multi-fluid model for the dispersed bubbly flow that covers the whole practical range of the gas injection rates, using a three-dimensional finite difference method. Effects of the casting operation conditions including gas injection, slide-gate orientation, gate opening and casting speed, and nozzle port design including port angle and port shape, on flow pattern are quantified using the weighted average jet characteristics such as jet angle, jet speed, back flow zone fraction, turbulence and biased mass flow. The main findings are summarized below:

- Argon gas injection greatly affects the flow pattern and jet characteristics. Increasing gas injection bends the jet angle upward, enhances the turbulence level, and reduces the back flow zone size. A small mount of the gas bubbles are carried by the downward liquid jet while most argon bubbles exit the nozzle from the upper portion of the outlet ports, forming a separate upward jet due to the gas buoyancy.
- Effect of gas injection becomes less influential with increasing casting speed.
- For the single-phase flow, casting speed has little influence on those jet characteristics that represent the flow pattern such as vertical jet angle, horizontal jet angle, back flow zone and biased mass flow.
- The off-center blocking effect of the slide-gate generates asymmetric flow.
- The 0° orientation generates the worst biased flow between the left and right ports. Specifically, the port on the gate opening side has a steeper jet angle, much larger back flow zone and less than 40% of the liquid mass flow.

- The 90° orientation generates strong swirl and asymmetry in the other plane, with a horizontal jet angle that directs the average jet toward the wide face opposite the gate opening side.
- The 90° orientation generates strong swirl on the jet that likely has a great effect on flow in the mold.
- The 45° orientation appears to be a poor compromise because it has all the asymmetries of both 0° and 90° design at almost same levels.
- The horizontal jet angle decreases with increasing gate opening, and becomes zero for the full opening. The vertical jet angle, jet speed and back flow zone reach their maximum values near gate opening F_L=60%, or about 50% area fraction, and decrease as the gate opening away from this critical region.
- Increasing gas injection seems to reduce the asymmetry slightly. Larger bubbles have more influence on flow pattern for a given gas fraction due to their greater buoyancy.
- Port angle and port shape both have great influence on the flow. The vertical jet angle becomes steeper with steeper port angle and more slender port shape.
- Pressure drop across the nozzle is insensitive to slide-gate orientation, bubble size and port design. However, pressure drop increases with increasing gas injection, increasing casting speed, and decreasing gate opening.
- Both rounding the nozzle edges due to erosion and initial clogging buildup are found to enhance the steel flow rate due to a streamlining effect. Only after severe clogging builds up is the flow eventually restricted so that the gate opening must increase to maintain the casting speed. However, the initial clogging and even edge rounding might greatly affect the flow pattern and jet characteristics.

5.3 Interrelated Effects of Clogging, Argon Injection and Casting Conditions

In practice, the continuous casting operation variables are interrelated. Changes in one variable usually cause corresponding changes in other variables. The interrelated effects of casting speed, argon injection rate, slide-gate opening position, nozzle bore diameter, clogging and tundish bath depth on flow rate and air aspiration potential are quantified using the advanced multivariable curve fitting and inverse models, based on interpolation of the numerical simulation results. Specific findings include:

- The pressure drop generated across the partially-closed slide gate creates a partial vacuum just beneath the slide gate which tends to entrain air, leading to reoxidation problems.
- The worst vacuum appears to occur for 50%-70% linear gate opening (about 50% area fraction).
- Increasing argon injection helps to raise the lowest pressure and sometimes may avoid this vacuum. For high casting speeds, a 0.2m increase in tundish bath depth typically will require an additional 5 SLPM of argon to compensate the vacuum effect. In practice, argon injection is limited by its effect on the flow pattern, and may not be able to fully compensate the vacuum effect.
- During ladle transitions and at other times when either casting speed or tundish level is low, argon flow should be turned off or at least severely reduced. Besides saving argon, this avoids flow problems in the mold and possible gas bubble entrapment.
- The extent of clogging can be predicted by comparing the measured steel flow rate to the prediction with the inverse models, leading to a “clogging index”.
- For a given nozzle geometry and gas flow rate, higher casting speed results from a deeper tundish bath depth (constant gate opening) or a larger gate opening (constant bath depth).

- Casting speed is more sensitive to a change in bath depth at low casting speed than at high casting speed.
- Casting speed is more sensitive to a change in bath depth at large gate opening than at small gate opening.
- Casting speed is more sensitive to gate opening when maintaining a high casting speed.
- For a fixed tundish bath depth, increasing argon injection will slightly slow down the casting speed unless the gate opening increases to compensate.

5.4 Mechanism for Argon Injection to Resist Nozzle Clogging

Even though the argon injection has been efficiently and widely employed to reduce nozzle clogging in continuous casting process for many years, its real working mechanism is still not fully understood. The suggested mechanisms include [6]:

- A film of argon is formed on the nozzle wall which prevents the inclusion from contacting the wall [11, 57, 74].
- The partial vacuum inside the nozzle is decreased which thereby reduces air aspiration through the nozzle [56, 57].
- Argon injection increases the turbulence and thereby causes the inclusion deposit to be flushed off [75].
- The argon bubbles flush the inclusions off the nozzle [57].
- The argon bubbles are believed to preferentially attach with inclusion particles, thus promoting their removal [23, 25].
- The argon bubbles promote the flotation of inclusions [Tai, 1985 #11].
- The argon prevents chemical reactions between steel and the refractory [Tai, 1985 #11].

The experimental and mathematical studies in this work found:

- The formation of gas film on the nozzle wall depends on liquid velocity, gas flow rate and gas injection holes/pores distribution. There is a big tendency for argon bubbles to spread over the ceramics nozzle wall and to form a gas film on the gas injection area. However, the gas film might not be present on the downstream section of the nozzle wall where no injection occurs.
- Argon injection does helps to raise the lowest pressure and thus reduce the vacuum in a nozzle. However, the injection rate is limited by its effect on the flow pattern, and may not be able to fully compensate the vacuum effect.
- Argon injection does increase the turbulence level in nozzle.

The clogging resistance by argon injection might contribute to the combined effects of all of these suggested mechanisms.

CHAPTER 6. SUGGESTIONS FOR FUTURE WORK

Although much progress has been made, a number of areas were identified during the course of this research that need further work to develop a better model for the continuous casting process.

Bubble formation study

The two-stage model developed in this work can predict only the mean bubble size but not other important bubble formation behavior such as bubble formation mode, bubble shape, interaction between bubbles, bubble size distribution, bubble coalescence and break-up. Numerical modeling is a potential tool to study those behaviors by simulating the bubble formation process via tracking the movement of the gas-liquid interface. A couple of work has been reported for small flow rate of gas injection in stagnant water [46]. The author of this work also successfully simulated the bubble formation process in stagnant liquid using VOF method, but the simulation for flowing liquid condition could not match the experimental measurements, likely due to the effects of turbulence, boundary layer and numerical problems.

The flow in a tundish nozzle is highly turbulent and the bubble formation frequency is high (200~600 bubbles per second for a typical pierced hole). The bubble size is relatively small and bubble formation occurs across the boundary layer at the wall. All of these facts suggest that the accuracy of the model for flow near the nozzle wall might be a key for successful future work on bubble formation in process simulation. On the numerical side, special attentions might be needed in choosing computational domain, grid resolution, reference pressure, time step, and solution algorithm to avoid the “stiff bubble problem” [76] and other numerical difficulties.

Experiments with argon injection into turbulent flowing liquid steel to study the bubble formation behavior are definitely the best way to validate the model for the continuous casting conditions. The experiments should be done if possible.

Turbulent flow of liquid steel and argon bubbles in nozzle and mold

The parametric studies in this work assume uniformed-sized bubbles being injected into nozzle in each case, which is a simplification of the actual situation. The bubble formation study reveals that bubble size is affected by bubble formation mode. Due to the high surface tension and non-wetting property of the liquid steel, the argon bubbles have a larger tendency to fall in Mode II or III, which generates non-uniform sized bubbles simultaneously. The multiphase model used in this work can be extended to account for the effect of multiple bubble sizes by specifying additional gas phases, each with a different bubble diameter.

By using the numerical solution for the jet exiting the nozzle port, found in this work, as the inlet boundary condition, flow in the mold can be modeled to investigate the swirl effect of the jet. The potential improvement on the accuracy of modeling flow in mold needs to be checked by comparing with the measurements on casters as well as the predictions using the weighted average jet values as the inlet boundary conditions. Modeling nozzle and mold together may also further improve the model accuracy.

Developing a model to predict the flow pattern transition from bubbly flow to annular flow in nozzle is also an important step to optimize the argon injection flow rate for reaching both good clogging-resistant performance and the required flow pattern.

The conclusions made from the parametric studies in this work need to be checked by implementing suggested changes in plant.

Interrelated effects of clogging, argon injection and casting conditions

The accuracy of the curve-fitting model and the inverse models, which describe the interrelated effects of nozzle clogging, argon injection, casting operation conditions, can be further improved with curve-fitting over more simulation data points, especially in the gate opening range of F_L=50%-80%. Higher order fitting models may be employed to obtain a smoother transition for the neighboring sub-regions of gate opening, thus to eliminate the glitches observed in the model transitional region.

Develop a proper clogging index model based on the inverse models in this work, and implement it in the plant to monitor the nozzle clogging status during the continuous casting process.

Further investigate the applicability of the inverse model, based on the Standard Nozzle in this work, to plant nozzles with different geometry.

There are still some uncertainties in pressure drop predictions. Pressure measurements are needed to further check the predictions.

Physical modeling

Water modeling has been widely used in the continuous casting industry to study the flow. Besides the transparency and low expense, one of the main reasons for using water modeling is that the kinematic viscosity of the liquid steel is nearly equal to that of the water. The two most important dimension groups, Reynolds number (*Re*) and Froude number (*Fr*), in a full-scale water model and in a steel caster are nearly identical due to this fact. This means that the measured flow pattern in a full-scale water model is directly correspondent with that in a steel caster. However, this is true only for the single-phase flow.

The introduction of the gas phase brings the effects of gas momentum and surface (interface) tension into the systems, which hence needs some new dimensionless groups to account for those effects. A preliminary similarity analysis is presented in Appendix G, which shows that there is no way to match all dimensionless groups at the same time due to the significant difference between the two systems. Thus, more physical experiments should be done with flowing steel in the plant and mathematical models could play more important role in understanding the continuous casting process. Two-phase water models are most useful only for the validation of the mathematical models.

APPENDIX A

SURFACE TENSION, CONTACT ANGLE AND WETTABILITY IN BUBBLE FORMATION STUDY

Surface Tension Coefficient

Surface tension is a physical property of a liquid. Surface tension coefficient is mainly dependent of composition and the temperature of the liquid. For liquid steel, its surface tension coefficient [54] are about 16~20 times that of water.

Contact Angle and Wettability

Contact angle is defined by the profile adopted by a liquid drop resting in equilibrium on a flat horizontal surface. The profile is governed by the balance between surface force and gravitational force, as shown in Figure A.1.

The relation between the contact angle and respective interfacial tensions (σ_{lg}, σ_{ls}, and σ_{sg}, we use σ in place of σ_{lg} in the other parts of the proposal) acting at the point of three-phase contact ("A" in Figure A.1), is given by the Young equation.

$$(\sigma_{sg} - \sigma_{ls}) = \sigma_{\mathrm{lg}} \cos\theta \qquad \text{(A.1)}$$

When θ=180°, the liquid is wholly non-wetting with respect to the particular solid, and conversely, for systems in which θ=0°, the solid is completely wetted by the liquid. Systems having values of $\theta > 90°$ or $\theta < 90°$ are described respectively as non-wetting (Figure A.1(A)) and wetting (Figure A.1(B)). Aqueous systems are typical wetting, whereas liquid metals are typical non-wetting.

For bubble formation problem, the profiles for the non-wetting and wetting systems can be converted to Figure A.1(C) and Figure A.1(D) respectively. It can be seen that in aqueous wetting system, the liquid wets the solids, and in metallic non-wetting system, the bubble tends to spread over the solid face.

Evaluation of the Surface Tension Force in Bubble Formation Study

Bubble formation in stagnant liquid

For a forming bubble in stagnant liquid, the surface tension force acts to hold the bubble from the detachment, against the buoyancy. The surface tension force in vertical direction (downward) is given by

$$F_{sx} = 2\pi a\sigma \cos\theta_O \qquad \text{(A.2)}$$

where a is the radius of the (bubble-solid) contact area. For aqueous wetting system, bubbles form at the inner circumference of the gas injection hole. Thus $2a = d$. In a good wetting system, usually $\theta_O << 90°$, thus $cos\theta_O \approx 1$. Equation A.2 can be simplified as:

$$F_{sx} = \pi d\sigma \qquad \text{(A.3)}$$

which were used by most previous bubble formation models in evaluating the surface tension forces for bubble injected into stagnant liquid condition.

Bubble formation in transverse flowing liquid

The transverse flowing liquid makes the contact angles no longer uniform along the bubble-solid contact circumference. At the upstream of the bubble, the contact angle increases to θ_a, as called the advancing contact angle, and at the downstream of the bubble, the contact angle decreases to θ_r, as called the receding contact angle, shown in Figures A.1(E) and (F).

The net surface tension force holding the bubble on the wall and resisting the drag force due to the flowing liquid was derived by Winterton [53] as described below:

The advancing angle θ_a the receding angle θ_r only give the contact angles at the two points on the bubble-solid contact line, the most upstream point and the most downstream point. At intermediate points on the contact line, the contact angles (θ) are assumed to meet following expressions (refer to Figure A.2)

$$\cos\theta = \cos\theta_o - (\cos\theta_o - \cos\theta_r)\cos\alpha \quad \text{for} \ -90° \le \alpha \le 90° \tag{A.4}$$

for the downstream half of the bubble, and

$$\cos\theta = \cos\theta_o - (\cos\theta_o - \cos\theta_a)\cos\beta \quad \text{for} \ -90° \le \beta \le 90° \tag{A.5}$$

for upstream half of the bubble, where θ_O is the static contact angle.

The Equations A.4 and A.5 give a smooth variation along the contact line and match the correction values of contact angles at $\alpha = 0$, $\alpha = \pm 90°$ and $\beta = 0$, $\beta = \pm 90°$.

At any intermediate point on the contact line, the surface tension force opposing the flow direction can be written as:

$$dF_{sx} = \sigma\ a\ \cos\theta\ \cos\alpha\ d\alpha \qquad \text{for} \ -90° \le \alpha \le 90° \tag{A.6}$$

$$dF_{sx} = \sigma\ a\ \cos\theta\ \cos\beta\ d\beta \qquad \text{for} \ -90° \le \beta \le 90° \tag{A.7}$$

The overall surface tension force is solved by integrating Equation (E.6) and (E.7):

$$F_{sx} = \int_{-90°}^{90°} \sigma\ a\ \cos\theta\ \cos\alpha\ d\alpha + \int_{-90°}^{90°} \sigma\ a\ \cos\theta\ \cos\beta\ d\beta \tag{A.8}$$

Plugging in Equations A.4 and A.5 yields

$$F_{sx} = \frac{\pi}{2}\sigma\ a\left(\cos\theta_r - \cos\theta_a\right) \tag{A.9}$$

Further assuming the diameter of the contact area is unchanged from the static case:

$$a = \frac{1}{2} D \sin\theta_o \tag{A.10}$$

where D is the bubble diameter so

$$F_{sx} = \frac{\pi}{4}\sigma\ D\ \sin\theta_o\left(\cos\theta_r - \cos\theta_a\right) \tag{A.11}$$

Equation A.11 is adopted in the two-stage model to evaluate the surface tension force in force balance equation of the expansion stage. The static contact angle θ_O, advancing angle θ_a and the receding angle θ_r are obtained experimentally.

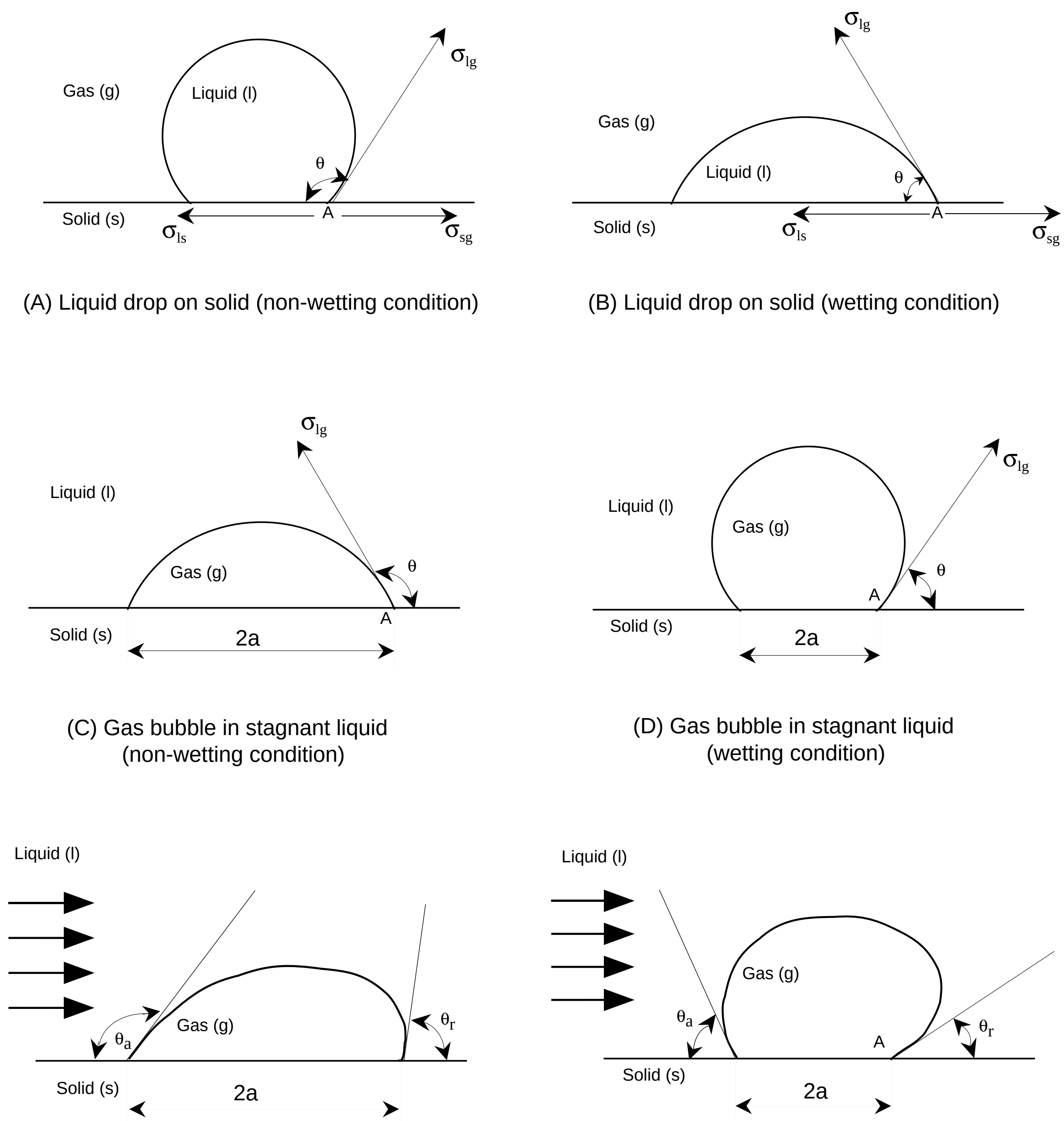

(A) Liquid drop on solid (non-wetting condition)

(B) Liquid drop on solid (wetting condition)

(C) Gas bubble in stagnant liquid (non-wetting condition)

(D) Gas bubble in stagnant liquid (wetting condition)

(E) Gas bubble in transverse flowing liquid (non-wetting condition)

(F) Gas bubble in transverse flowing liquid (wetting condition)

Figure A.1 Surface tension, contact angle and wettability

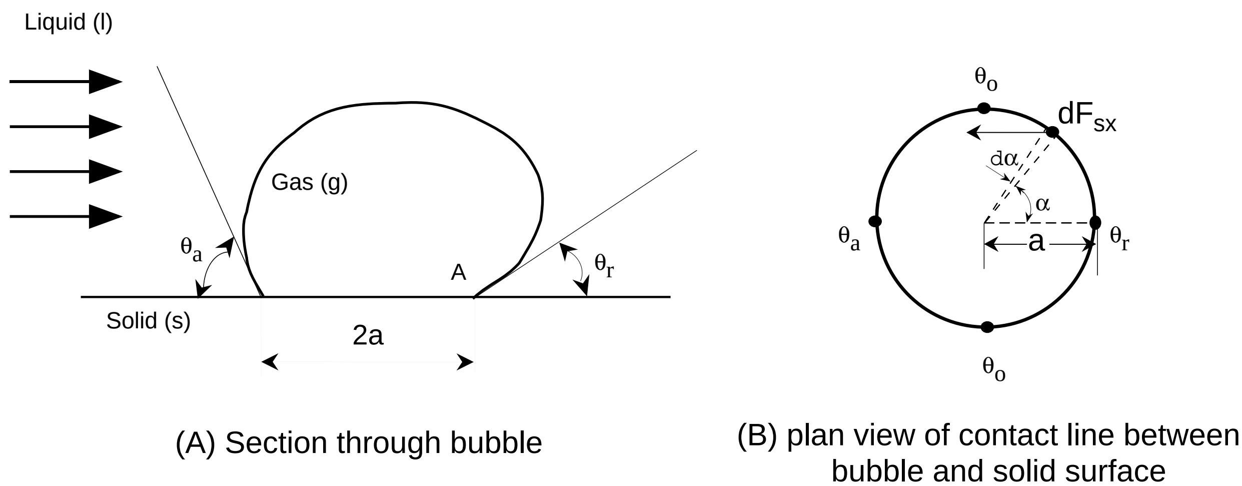

Figure A.2 Contact angles at various points along the contact line between bubble and solid surface for a bubble formed in transverse flowing liquid

APPENDIX B

MATLAB PROGRAM TO CALCULATE THE BUBBLE SIZE USING THE TWO-STAGE MODEL

```
% ***********************************************************************
%
%   This program predict the average bubble size in continuous casting nozzle
%   using the two-stage model
%
%   Model detail may refer to the Chapter 2.4.2 of the Dessertation
%
%   ----- written by Hua Bai on July 14, 1997
%   ----- Modified on April 8, 2000
%
%   ----- in MATLAB
%
%   ***********************************************************************
%
%
%   ----=====   Global constants and variables    ======------
  global a;
  global b;
%
%   ----- 1. Simulation condition and physical properties ----------
%
%
%   Volume flow rate of gas injection per hole      Q          ml/s
%   Diameter of the gas injection hole              d          m
%   Average velocity of liquid in tube              U          m/s
%   Diameter of the nozzle                          Dn         m
%   Density of the liquid                           Rho_liq    kg/m^3
%   Viscosity of the liquid                         MU         kg/m-s(Pa-s)
%   Density of the gas                              Rho_gas    kg/m^3
%   Surface tension coefficient                     Gamma      N/m
%   Contact angle function                          f_theta
%   Elongation factor at bubble detachment
%     from its gas injection hole                   ed
%   Equivalent diameter of the bubble               D          mm
%
        Q = 1;                  % change here for different Q
        Q = 1.E-6*Q;            % convert to SI unit
        d = 0.3E-3;             % change here for different d
        Dn = 0.078;             % change here for different Dn
        Rho_liq = 1000.0;       % =7021.0 for Fe-Ar system
```

```
        MU = 0.001;              % =0.0056 for Fe-Ar system
        Rho_gas = 1.29;          % =0.27   for Fe-Ar system
        Gamma = 0.073;           % =1.192  for Fe-Ar system
%  set initial U, (the program might not ba able to handle smaller U)
        U = 0.4;
%
%   ----- 2. Other constants  ----------------------
        pi=3.1415926;
        g=9.81;
%
%   ----- 3. temp variables ------------------------
%
%   Horizontal radius of the ellipsoidal bubble        r              m
%     rx = ry = r
%   Horizontal radius of the ellipsoidal bubble
%     at the end of the expansion stage                re             m
%   Horizontal radius of the ellipsoidal bubble
%     at the instant of the bubble detachment
%     which is also the final bubble size              rd             m
%
%   Average liquid velocity
%     across the forming bubble                        U_ave          m/s
%   Elongation factor at (re < r < rd)          e
%     e=ar+b
%     where a and b are constant
%       a = (ed-1)/(rd-re)
%       b = (rd-ed*re)/(rd-re)
%
   for j=1:25              % Loop for independent variable
        U = U + 0.1;
        uu(j)=U;
        ed = -0.12793*U^2 + 0.70797*U + 0.78592;
        f_theta = 0.078773*U^2 + 0.33109*U -0.060794;
%
%   -----=====   Stage 1 : expansion stage    =======------
%   Find the bubble radius at the end of the expansion stage
%
        r=d/2;
        Residual = -1;
        while  Residual < 0
                r = r + 0.005E-3;
%
%   ------------------------------------------------------------
%   Calculate the average liquid velocity across the growing bubble
%
                U_ave=1.3173*U*(r/Dn)^(1./7.);
%
%
```

```
%   Calculate the forces acting on the growing bubble
%
%   Find Reynolds # of the bubble-----Re_bub
                Re_bub = 2.*r*U_ave*Rho_liq/MU;
%   Find the drag coeff-----Cd
%   Find the drag coeff-----Cd
                Cd = (1+0.15*Re_bub^0.687)*24./Re_bub + 0.42/(1+4.25E4*Re_bub^(-1.16));
%   Find the drag force--- Fd
                Fd = Cd*0.5*Rho_liq*U_ave^2*pi*r*r;
%   Find the buoyancy force--- Fb
                Fb = (4./3.)*pi*r^3*(Rho_liq-Rho_gas)*g;
%   Find the surface tension force--- Fs
                Fs = 2.*pi*r*Gamma;
                Fs = f_theta * Fs;
%         Fs0= pi*d*Gamma;
%         if Fs < Fs0
%           Fs = Fs0;
%         end
%   Check the force balance
                Residual = Fd - Fb - Fs;
%
        end
        re = r;
%
%   end of ' while  Residual < 0 '
%   ---------- end of stage 1  -------------------------
%
%
%
%   --===== Stage 2 : elongation/detachment stage =======---
%
%        Integrate (U_ave*t) = 2*rd*ed^1.5 + d/2 -re   or
%        Intergrade (fr(r)dr) = 2*rd*ed^1.5 + d/2 -re
%        Using trial and error to solve for rd
%
%   -----------------------------------------------------
%
        rd = re;
        Residual2 = -1;
        while Residual2 < 0.0
                rd = rd + 0.01E-3;
                a  = (ed-1.0)/(rd-re);
                b  = (rd-ed*re)/(rd-re);
%
                uavet = 5.2692*pi*U/Q/Dn^(1/7);
                uavet = uavet*quad('fr',re,rd);
%   'fr' is the name of the function for integrate, and
%    it must be put in the same directory as this file to work
```

```
%
                Residual2 = uavet-(d/2 + 2.0*rd*ed^1.5-re);
        end                     %    end of ' while Residual2 < 0.0 '
%
%   -----------------------------------------------------------
%   Convert the bubble size rd to the equivalent diameter (in mm)
        D(j)=2.0*1000.0*rd*ed^0.5;
   end
% end of the ''for loop'
%
%   plot result
        plot(uu, D)
%   print data : [U, D]
        [uu' D']



%  ************************************************************************
%      function fr=fr(r)
%
%      Refer to Equation 2.27 for the function
%  ************************************************************************
%
      function fr=fr(r)
        global a;
        global b;
        fr=(r.^2.142857).*(a*r+b).^1.5+(r.^3.142857).*0.5*a.*(a*r+b).^0.5;
% end
```

APPENDIX C

CALCULATION OF ARGON GAS HEAT-UP THROUGH THE HOLES IN NOZZLE WALL

Simplified Analytical Model

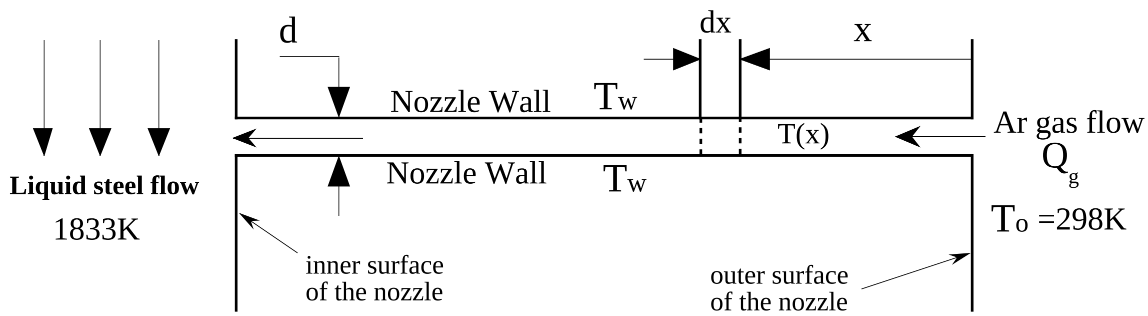

Figure C.1 Schematic of the analytical model of argon gas heat-up through the nozzle wall

Assumptions:

Since the axial dimension of the gas injection hole is 2 order higher than the radius of the hole, the problem can be simplified as 1-D problem, that is, T=T(x)

Constant properties of the gas

Constant wall temperature T_W

Known:

Wall temperature: T_W

Argon gas temperature at outer surface of the nozzle wall: T_O

Argon gas flow rate: Q_g

Physical properties of the argon gas: specific heat: Cp, conductivity: k, density: ρ_g

Heat transfer coefficient : h

Diameter of the hole: d

Find:

Argon gas temperature distribution along the axis of the hole, T(x)

Analysis:

Apply energy balance to the control volume dx. Rate of heat obtained by argon gas is equal to rate of heat transfer from the wall to *gas*, or

$$\rho_g (dV) C_p \frac{dT}{dx} = hA(T_w - T) \tag{C.1}$$

where $Q_g = dV/dt$ *and* $A = \pi d * dx$, thus

$$\rho_g Q_g C_p \frac{dT}{dx} = \pi d h (T_w - T) \tag{C.2}$$

With boundary condition $T = T_O$ at $x = 0$, solution of Equation C.2 is

$$\frac{T_w - T}{T_w - T_0} = \exp\left(-\frac{\pi d h}{\rho_g Q_g C_p} x \right) \tag{C.3}$$

The solution suggests that $(T_w - T)$ decay exponentially with the distance from the outer surface of the nozzle, or the argon gas temperature increases exponentially with the distance.

Calculation for an example case:

Example case: d= 0.4mm, Q_g = 3ml/s for hot argon, T_W = 1833K

The gas volume expansion due to temperature increase will result in smaller ρ_g and larger Q_g, but (ρ_g Q_g) = constant.

The physical properties used in calculation [78]:

ρ_g = 0.319 kg/m^3 for hot argon

Cp = 519 J/kg-K which is relatively independent of temperature for argon.

h is average heat transfer coefficient which can be calculated based on Graete's solution for fully developed flow in pipe [51]:

$$h = NuK/d = 3.66k/d$$

where heat conductivity k is temperature dependent. Take average in the calculation

$$k = \frac{k_{@298K} + k_{@1833K}}{2} = \frac{0.018 + 0.049}{2} = 0.0335 \text{ (W/m-K)}$$

thus, *h*=3.66*0.0335/0.4E-3=306 (W/K-m^2)

When T =99%Tw=1815K, plugging in all of the data yields

$$\frac{1833 - 1815}{1833 - 298} = \exp\left(-\frac{3.14 * 0.4 * 10^{-3} * 306}{0.319 * 3 * 10^{-6} * 519} x \right)$$

or x = 5.7E-3m = 5.7 mm

Conclusion:

Argon gas temperature will rise to 99% of the wall temperature at 5.7 mm from the outer surface of the nozzle. Since the nozzle wall is usually much thicker than 5.7 mm, it is safe to assume that the injected argon gas will be heated up to 99% of the molten steel temperature even before it hits the liquid steel.

Numerical Modeling of the Argon Gas Heat-Up through the Nozzle Wall

In the foregoing analytical calculation, heat transfer in radial direction is not included in the model. The Nusselt number, which represents the ratio of convection heat transfer to conduction in fluid, is 3.66 for fully developed flow in pipe [51], or

$$Nu = \frac{hd}{k} = 3.66 \qquad \text{(C.4)}$$

Equation C.4 shows that the convection and conduction is in the same order. To investigate the effect of heat conduction in radial direction, numerical simulation of argon gas flow and heat transfer in the gas injection hole channel is performed with FLUENT code [79]. Both forced convection and conduction are included and a non-uniformed wall temperature distribution and temperature-dependent physical properties are used in the calculation.

Argon gas heat-up calculation is approximated by modeling the gas through a thin channel (with diameter of 0.4mm) across the nozzle wall (with thickness of 54mm). Two different radial mesh resolutions are used, specifically, 3 and 12 cells respectively. Both cases have 270 cells across the channel or nozzle wall. The wall temperature (boundary condition) is linear distributed, based on previous finding [6] as shown in the Figure C.2.

The temperature-dependent physical properties $\mu=\mu(T)$, $\rho_{gas}=\rho_{gas}(T)$, and $k=k(T)$ are adopted from the "Physical Properties Data for the Chemical and Mechanical Engineer" [78]. The gas injection flow rate Q_g=3ml/s for hot argon and the gas specific heat Cp=519 J/kg-K are used in computation.

The computational solutions for the argon gas temperature at the centerline across the nozzle wall are plotted on Figure C.2, along with the wall temperature boundary condition. It can been seen that the mesh resolution in radial direction has little influence on the results. Both cases give almost same profile, and the finer resolution (12 cells) gives slight lower temperature at the center of the hole than that for 3 cells cases.

Argon gas temperature is heated up to over 98% wall temperature within 6 mm travel, then linearly increases along with the wall temperature as it continues flowing toward the molten steel, and reaches up to 99% of the molten steel temperature even before it hits the liquid steel. This is the similar conclusion as the simplified analytical model.

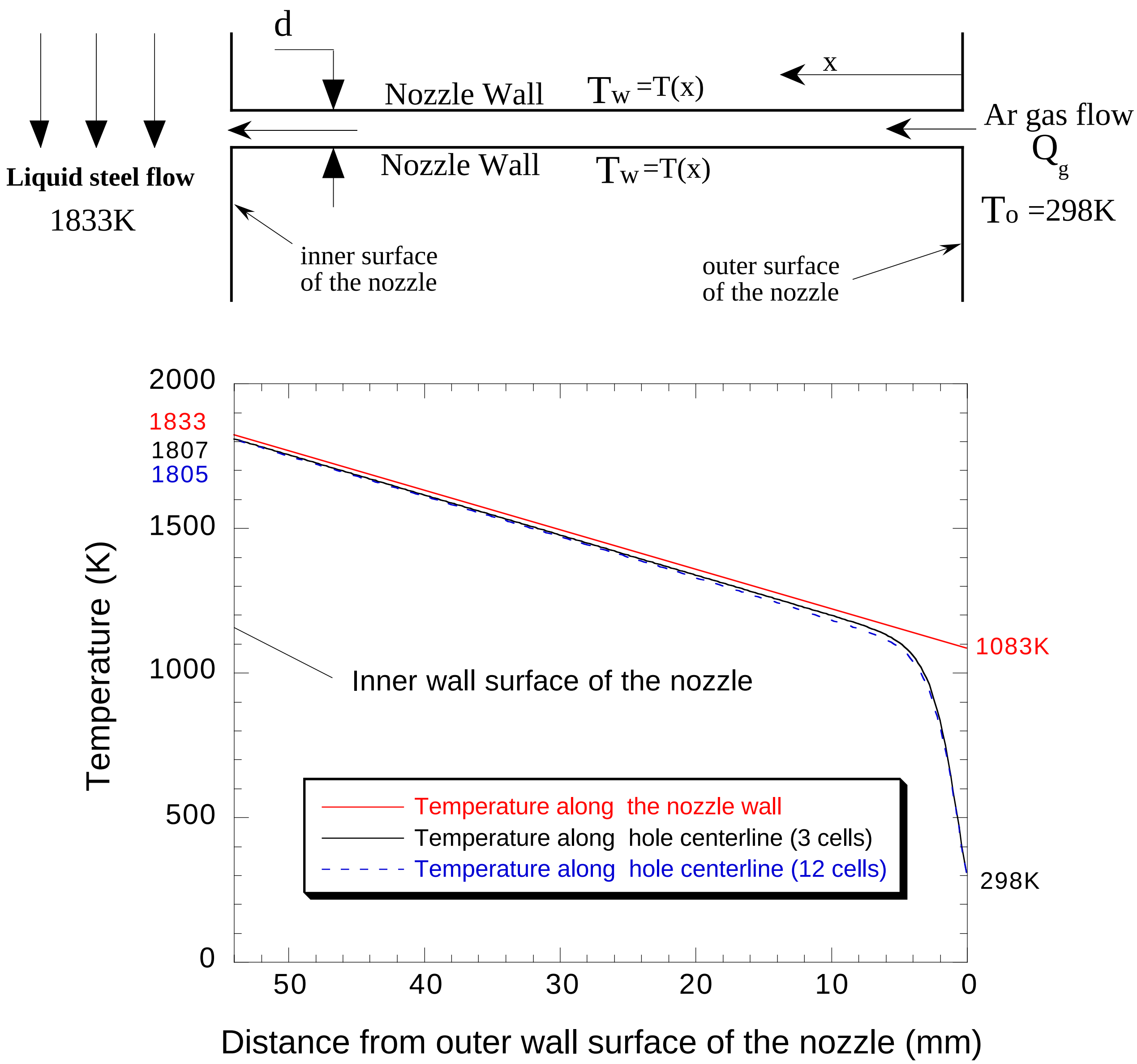

Figure C.2 Numerical simulation of argon gas heat-up through the nozzle wall

APPENDIX D

DERIVATION OF EQUATION 4.1

Apply Bernoulli's Equation on location A and B in the schematic of the continuous casting process given in Figure D.1:

$$p_A + \tfrac{1}{2}\rho_l U_A^2 + \rho_l g z_A = p_B + \tfrac{1}{2}\rho_l U_B^2 + \rho_l g z_B \tag{D.1}$$

where p and U are the pressure and velocity at these locations. Inserting $H_T = z_A - z_B$, $P_A = 0$ and $U_A \approx 0$ yields

$$H_T = \frac{p_B + \tfrac{1}{2}\rho_l U_B^2}{\rho_l g} \tag{D.2}$$

Apply Bernoulli's Equation on location C and D:

$$p_C + \tfrac{1}{2}\rho_l U_C^2 + \rho_l g z_C = p_D + \tfrac{1}{2}\rho_l U_D^2 + \rho_l g z_D \tag{D.3}$$

Since $H_{SEN} = z_D - z_C$, $P_D = 0$ and $U_D \approx 0$, then,

$$p_C = \rho_l g H_{SEN} - \tfrac{1}{2}\rho_l U_C^2 \tag{D.4}$$

and

$$\Delta p = p_B - p_C \tag{D.5}$$

Combining Equations D.2, D.4 and D.5 gives

$$H_T = \frac{\Delta p + \rho_l g H_{SEN} + \tfrac{1}{2}\rho_l (U_B^2 - U_C^2)}{\rho_l g} \tag{D.6}$$

where Δp is the simulated pressure-drop, H_{SEN} is the SEN submerged depth, U_B is the average velocity at the top inlet of the nozzle and U_C is the average jet velocity at the nozzle port.

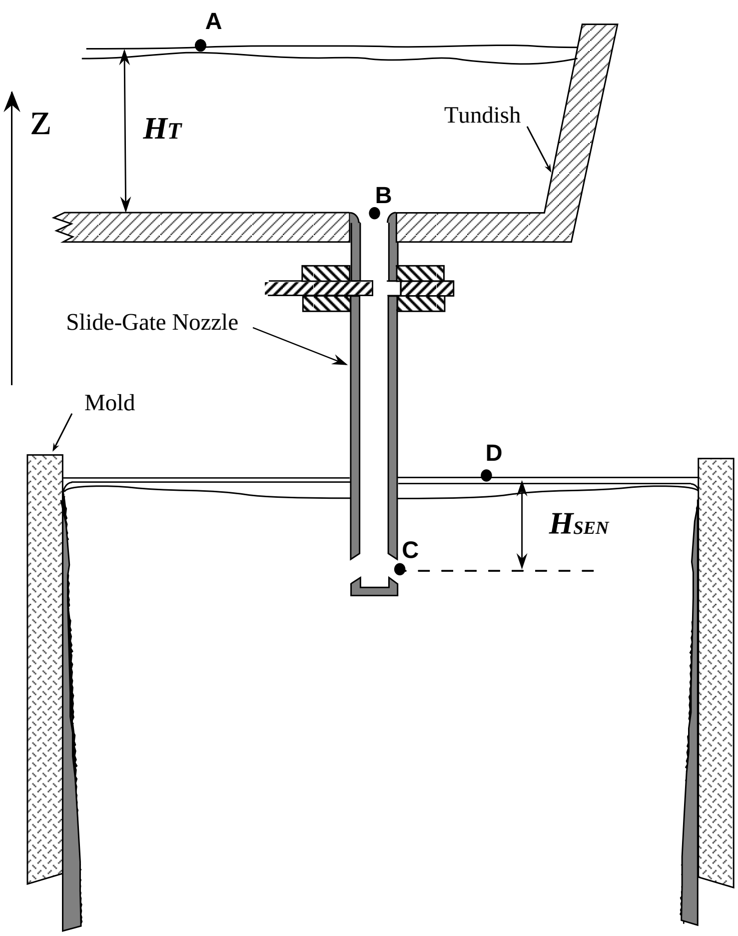

Figure D.1 Schematic of the continuous casting process showing tundish, slide-gate nozzle, mold and Location A, B, C, and D

APPENDIX E

DERIVATION OF THE INVERSE MODELS

Equations for Casting Speed V_C at Gate Openings F_L > 60%

Equation 4.3b can be rewritten as:

$$aV_C^2 + bV_C + c = 0 \tag{E.1}$$

where

$$\begin{aligned} a = {} & c_{81} + c_{82}F_L + c_{83}Q_G + c_{84}F_LQ_G + c_{93}D_N + c_{94}F_LD_N + c_{95}Q_GD_N + c_{96}F_LQ_GD_N \\ & + c_{105}D_N^2 + c_{106}F_LD_N^2 + c_{107}Q_GD_N^2 + c_{108}F_LQ_GD_N^2 \\ & + c_{117}D_N^3 + c_{118}F_LD_N^3 + c_{119}Q_GD_N^3 + c_{120}F_LQ_GD_N^3 \end{aligned} \tag{E.2a}$$

$$\begin{aligned} b = {} & c_{74} + c_{77}F_L + c_{78}Q_G + c_{80}F_LQ_G + c_{86}D_N + c_{89}F_LD_N + c_{90}Q_GD_N + c_{92}F_LQ_GD_N \\ & + c_{98}D_N^2 + c_{101}F_LD_N^2 + c_{102}Q_GD_N^2 + c_{104}F_LQ_GD_N^2 \\ & + c_{110}D_N^3 + c_{113}F_LD_N^3 + c_{114}Q_GD_N^3 + c_{116}F_LQ_GD_N^3 \end{aligned} \tag{E.2b}$$

$$\begin{aligned} c = {} & c_{73} + c_{75}F_L + c_{76}Q_G + c_{79}F_LQ_G - H_T + c_{85}D_N + c_{87}F_LD_N + c_{88}Q_GD_N + c_{91}F_LQ_GD_N \\ & + c_{97}D_N^2 + c_{99}F_LD_N^2 + c_{100}Q_GD_N^2 + c_{103}F_LQ_GD_N^2 \\ & + c_{109}D_N^3 + c_{111}F_LD_N^3 + c_{112}Q_GD_N^3 + c_{115}F_LQ_GD_N^3 \end{aligned} \tag{E.2c}$$

The theoretical casting speed is then obtained from:

$$V_C = \frac{-b + \sqrt{b^2 - 4ac}}{2a} \qquad \text{for} \quad F_L \geq 60\% \tag{E.3}$$

The other root is always negative, which is physically incorrect thus dropped.

Equation for Theoretical Gate Opening F_L

For fixed tundish bath depth (H_T), casting speed (V_C), fixed argon injection flow rate (Q_G), and fixed nozzle bore diameter (D_N), Equation 4.3 can be rewritten as:

$$aF_L^2 + bF_L + c = 0 \qquad \text{for} \quad F_L \le 60\% \tag{E.4a}$$

$$aF_L + b = 0 \qquad \text{for} \quad F_L \ge 60\% \tag{E.4b}$$

Thus, the theoretical gate opening is then obtained from:

$$F_L = \frac{-b - \sqrt{b^2 - 4ac}}{2a} \qquad \text{for} \quad F_L \le 60\% \tag{E.5}$$

where

$$\begin{aligned} a = {} & c_{10} + c_{11}V_C + c_{14}Q_G + c_{15}V_C^2 + c_{16}V_C Q_G + c_{18}V_C^2 Q_G \\ & + c_{28}D_N + c_{29}V_C D_N + c_{32}Q_G D_N + c_{33}V_C^2 D_N + c_{34}V_C Q_G D_N + c_{36}V_C^2 Q_G D_N \\ & + c_{46}D_N^2 + c_{47}V_C D_N^2 + c_{50}Q_G D_N^2 + c_{51}V_C^2 D_N^2 + c_{52}V_C Q_G D_N^2 + c_{54}V_C^2 Q_G D_N^2 \\ & + c_{64}D_N^3 + c_{65}V_C D_N^3 + c_{68}Q_G D_N^3 + c_{69}V_C^2 D_N^3 + c_{70}V_C Q_G D_N^3 + c_{72}V_C^2 Q_G D_N^3 \end{aligned} \tag{E.6a}$$

$$\begin{aligned} b = {} & c_3 + c_5V_C + c_7Q_G + c_8V_C Q_G + c_{12}V_C^2 + c_{17}V_C^2 Q_G \\ & + c_{21}D_N + c_{23}V_C D_N + c_{25}Q_G D_N + c_{26}V_C Q_G D_N + c_{30}V_C^2 D_N + c_{35}V_C^2 Q_G D_N \\ & + c_{39}D_N^2 + c_{41}V_C D_N^2 + c_{43}Q_G D_N^2 + c_{44}V_C Q_G D_N^2 + c_{48}V_C^2 D_N^2 + c_{53}V_C^2 Q_G D_N^2 \\ & + c_{57}D_N^3 + c_{59}V_C D_N^3 + c_{61}Q_G D_N^3 + c_{62}V_C Q_G D_N^3 + c_{66}V_C^2 D_N^3 + c_{71}V_C^2 Q_G D_N^3 \end{aligned} \tag{E.6b}$$

$$\begin{aligned} c = {} & c_1 + c_2V_C + c_4Q_G + c_6V_C Q_G + c_9V_C^2 + c_{13}V_C^2 Q_G - H_T \\ & + c_{19}D_N + c_{20}V_C D_N + c_{22}Q_G D_N + c_{24}V_C Q_G D_N + c_{27}V_C^2 D_N + c_{31}V_C^2 Q_G D_N \\ & + c_{37}D_N^2 + c_{38}V_C D_N^2 + c_{40}Q_G D_N^2 + c_{42}V_C Q_G D_N^2 + c_{45}V_C^2 D_N^2 + c_{49}V_C^2 Q_G D_N^2 \\ & + c_{55}D_N^3 + c_{56}V_C D_N^3 + c_{58}Q_G D_N^3 + c_{60}V_C Q_G D_N^3 + c_{63}V_C^2 D_N^3 + c_{67}V_C^2 Q_G D_N^3 \end{aligned} \tag{E.6c}$$

and

$$F_L = -\frac{b}{a} \qquad \text{for} \quad F_L \geq 60\% \qquad \text{(E.7)}$$

where

$$a = c_{75} + c_{77}V_C + c_{79}Q_G + c_{80}V_CQ_G + c_{82}V_C^2 + c_{84}V_C^2Q_G$$
$$+ c_{87}D_N + c_{89}V_CD_N + c_{91}Q_GD_N + c_{92}V_CQ_GD_N + c_{94}V_C^2D_N + c_{96}V_C^2Q_GD_N$$
$$+ c_{99}D_N^2 + c_{101}V_CD_N^2 + c_{103}Q_GD_N^2 + c_{104}V_CQ_GD_N^2 + c_{106}V_C^2D_N^2 + c_{108}V_C^2Q_GD_N^2$$
$$+ c_{111}D_N^3 + c_{113}V_CD_N^3 + c_{115}Q_GD_N^3 + c_{116}V_CQ_GD_N^3 + c_{118}V_C^2D_N^3 + c_{120}V_C^2Q_GD_N^3 \qquad \text{(E.8a)}$$

$$b = c_{73} + c_{74}V_C + c_{76}Q_G + c_{78}V_CQ_G + c_{81}V_C^2 + c_{83}V_C^2Q_G - H_T$$
$$+ c_{85}D_N + c_{86}V_CD_N + c_{88}Q_GD_N + c_{90}V_CQ_GD_N + c_{93}V_C^2D_N + c_{95}V_C^2Q_GD_N$$
$$+ c_{97}D_N^2 + c_{98}V_CD_N^2 + c_{100}Q_GD_N^2 + c_{102}V_CQ_GD_N^2 + c_{105}V_C^2D_N^2 + c_{107}V_C^2Q_GD_N^2$$
$$+ c_{109}D_N^3 + c_{110}V_CD_N^3 + c_{112}Q_GD_N^3 + c_{114}V_CQ_GD_N^3 + c_{117}V_C^2D_N^3 + c_{119}V_C^2Q_GD_N^3 \qquad \text{(E.8b)}$$

The other root of Equation E.4a is physically incorrect, as reflected in negative value or larger than 100%.

Equation for Theoretical Argon Injection Flow Rate Q_G

For fixed tundish bath depth (H_T), casting speed (V_C), fixed gate opening (F_L), and fixed nozzle bore diameter (D_N), Equation 4.3 can be rewritten as:

$$aQ_G + b = 0 \qquad \text{(E.9)}$$

Thus, the theoretical argon injection flow rate is obtained from:

$$Q_G = -\frac{b}{a} \qquad \text{(E.10)}$$

where for $F_L \leq 60\%$

$$a = c_4 + c_6V_C + c_7F_L + c_8V_CF_L + c_{13}V_C^2 + c_{14}F_L^2 + c_{16}V_CF_L^2 + c_{17}V_C^2F_L + c_{18}V_C^2F_L^2$$

$$+ \; c_{22} D_N + c_{24} V_C D_N + c_{25} F_L D_N + c_{26} V_C F_L D_N + c_{31} V_C^2 D_N$$

$$+ \; c_{32} F_L^2 D_N + c_{34} V_C F_L^2 D_N + c_{35} V_C^2 F_L D_N + c_{36} V_C^2 F_L^2 D_N$$

$$+ \; c_{40} D_N^2 + c_{42} V_C D_N^2 + c_{43} F_L D_N^2 + c_{44} V_C F_L D_N^2 + c_{49} V_C^2 D_N^2$$

$$+ \; c_{50} F_L^2 D_N^2 + c_{52} V_C F_L^2 D_N^2 + c_{53} V_C^2 F_L D_N^2 + c_{54} V_C^2 F_L^2 D_N^2$$

$$+ \; c_{58} D_N^3 + c_{60} V_C D_N^3 + c_{61} F_L D_N^3 + c_{62} V_C F_L D_N^3 + c_{67} V_C^2 D_N^3$$

$$+ \; c_{68} F_L^2 D_N^3 + c_{70} V_C F_L^2 D_N^3 + c_{71} V_C^2 F_L D_N^3 + c_{72} V_C^2 F_L^2 D_N^3 \tag{E.11a}$$

$$b = c_1 + c_2 V_C + c_3 F_L + c_5 V_C F_L + c_9 V_C^2 + c_{10} F_L^2 + c_{11} V_C F_L^2 + c_{12} V_C^2 F_L + c_{15} V_C^2 F_L^2 - H_T$$

$$+ \; c_{19} D_N + c_{20} V_C D_N + c_{21} F_L D_N + c_{23} V_C F_L D_N + c_{27} V_C^2 D_N$$

$$+ \; c_{28} F_L^2 D_N + c_{29} V_C F_L^2 D_N + c_{30} V_C^2 F_L D_N + c_{33} V_C^2 F_L^2 D_N$$

$$+ \; c_{37} D_N^2 + c_{38} V_C D_N^2 + c_{39} F_L D_N^2 + c_{41} V_C F_L D_N^2 + c_{45} V_C^2 D_N^2$$

$$+ \; c_{46} F_L^2 D_N^2 + c_{47} V_C F_L^2 D_N^2 + c_{48} V_C^2 F_L D_N^2 + c_{51} V_C^2 F_L^2 D_N^2$$

$$+ \; c_{55} D_N^3 + c_{56} V_C D_N^3 + c_{57} F_L D_N^3 + c_{59} V_C F_L D_N^3 + c_{63} V_C^2 D_N^3$$

$$+ \; c_{64} F_L^2 D_N^3 + c_{65} V_C F_L^2 D_N^3 + c_{66} V_C^2 F_L D_N^3 + c_{69} V_C^2 F_L^2 D_N^3 \tag{E.11b}$$

and for $F_L \geq 60\%$

$$a = c_{76} + c_{78} V_C + c_{79} F_L + c_{80} V_C F_L + c_{83} V_C^2 + c_{84} V_C^2 F_L$$

$$+ \; c_{88} D_N + c_{90} V_C D_N + c_{91} F_L D_N + c_{92} V_C F_L D_N + c_{95} V_C^2 D_N + c_{96} V_C^2 F_L D_N$$

$$+ \; c_{100} D_N^2 + c_{102} V_C D_N^2 + c_{103} F_L D_N^2 + c_{104} V_C F_L D_N^2 + c_{107} V_C^2 D_N^2 + c_{108} V_C^2 F_L D_N^2$$

$$+ \; c_{112} D_N^3 + c_{114} V_C D_N^3 + c_{115} F_L D_N^3 + c_{116} V_C F_L D_N^3 + c_{119} V_C^2 D_N^3 + c_{120} V_C^2 F_L D_N^3 \tag{E.12a}$$

$$b = c_{73} + c_{74} V_C + c_{75} F_L + c_{77} V_C F_L + c_{81} V_C^2 + c_{82} V_C^2 F_L - H_T$$

$$+ \; c_{85} D_N + c_{86} V_C D_N + c_{87} F_L D_N + c_{89} V_C F_L D_N + c_{93} V_C^2 D_N + c_{94} V_C^2 F_L D_N$$

$$+ \; c_{97} D_N^2 + c_{98} V_C D_N^2 + c_{99} F_L D_N^2 + c_{101} V_C F_L D_N^2 + c_{105} V_C^2 D_N^2 + c_{106} V_C^2 F_L D_N^2$$

$$+ \; c_{109} D_N^3 + c_{110} V_C D_N^3 + c_{111} F_L D_N^3 + c_{113} V_C F_L D_N^3 + c_{117} V_C^2 D_N^3 + c_{118} V_C^2 F_L D_N^3 \tag{E.12b}$$

Equation for Nozzle Bore Diameter D_N

For fixed tundish bath depth (H_T), casting speed (V_C), fixed gate opening (F_L), and argon injection flow rate (Q_G), Equation 4.3 can be rewritten as:

$$aD_N^3 + bD_N^2 + cD_N + d = 0 \tag{E.13}$$

where for $F_L \leq 60\%$

$$\begin{aligned} a = {} & c_{55} + c_{56}V_C + c_{57}F_L + c_{58}Q_G + c_{59}V_CF_L + c_{60}V_CQ_G + c_{61}F_LQ_G + c_{62}V_CF_LQ_G \\ & + c_{63}V_C^2 + c_{64}F_L^2 + c_{65}V_CF_L^2 + c_{66}V_C^2F_L + c_{67}V_C^2Q_G + c_{68}F_L^2Q_G \\ & + c_{69}V_C^2F_L^2 + c_{70}V_CF_L^2Q_G + c_{71}V_C^2F_LQ_G + c_{72}V_C^2F_L^2Q_G \end{aligned} \tag{E.14a}$$

$$\begin{aligned} b = {} & c_{37} + c_{38}V_C + c_{39}F_L + c_{40}Q_G + c_{41}V_CF_L + c_{42}V_CQ_G + c_{43}F_LQ_G + c_{44}V_CF_LQ_G \\ & + c_{45}V_C^2 + c_{46}F_L^2 + c_{47}V_CF_L^2 + c_{48}V_C^2F_L + c_{49}V_C^2Q_G + c_{50}F_L^2Q_G \\ & + c_{51}V_C^2F_L^2 + c_{52}V_CF_L^2Q_G + c_{53}V_C^2F_LQ_G + c_{54}V_C^2F_L^2Q_G \end{aligned} \tag{E.14b}$$

$$\begin{aligned} c = {} & c_{19} + c_{20}V_C + c_{21}F_L + c_{22}Q_G + c_{23}V_CF_L + c_{24}V_CQ_G + c_{25}F_LQ_G + c_{26}V_CF_LQ_G \\ & + c_{27}V_C^2 + c_{28}F_L^2 + c_{29}V_CF_L^2 + c_{30}V_C^2F_L + c_{31}V_C^2Q_G + c_{32}F_L^2Q_G \\ & + c_{33}V_C^2F_L^2 + c_{34}V_CF_L^2Q_G + c_{35}V_C^2F_LQ_G + c_{36}V_C^2F_L^2Q_G \end{aligned} \tag{E.14c}$$

$$\begin{aligned} d = {} & c_1 + c_2V_C + c_3F_L + c_4Q_G + c_5V_CF_L + c_6V_CQ_G + c_7F_LQ_G + c_8V_CF_LQ_G \\ & + c_9V_C^2 + c_{10}F_L^2 + c_{11}V_CF_L^2 + c_{12}V_C^2F_L + c_{13}V_C^2Q_G + c_{14}F_L^2Q_G \\ & + c_{15}V_C^2F_L^2 + c_{16}V_CF_L^2Q_G + c_{17}V_C^2F_LQ_G + c_{18}V_C^2F_L^2Q_G - H_T \end{aligned} \tag{E.14d}$$

and for $F_L \geq 60\%$

$$\begin{aligned} a = {} & c_{109} + c_{110}V_C + c_{111}F_L + c_{112}Q_G + c_{113}V_CF_L + c_{114}V_CQ_G + c_{115}F_LQ_G \\ & + c_{116}V_CF_LQ_G + c_{117}V_C^2 + c_{118}V_C^2F_L + c_{119}V_C^2Q_G + c_{120}V_C^2F_LQ_G \end{aligned} \tag{E.15a}$$

$$\begin{aligned} b = {} & c_{97} + c_{98}V_C + c_{99}F_L + c_{100}Q_G + c_{101}V_CF_L + c_{102}V_CQ_G + c_{103}F_LQ_G \\ & + c_{104}V_CF_LQ_G + c_{105}V_C^2 + c_{106}V_C^2F_L + c_{107}V_C^2Q_G + c_{108}V_C^2F_LQ_G \end{aligned} \tag{E.15b}$$

$$c = c_{85} + c_{86}V_C + c_{87}F_L + c_{88}Q_G + c_{89}V_CF_L + c_{90}V_CQ_G + c_{91}F_LQ_G$$

$$+\ c_{92}V_CF_LQ_G + c_{93}V_C^2 +\ c_{94}V_C^2F_L + c_{95}V_C^2Q_G + c_{96}V_C^2F_LQ_G \tag{E.15c}$$

$$d = c_{73} + c_{74}V_C + c_{75}F_L + c_{76}Q_G + c_{77}V_CF_L + c_{78}V_CQ_G + c_{79}F_LQ_G$$

$$+\ c_{80}V_CF_LQ_G + c_{81}V_C^2 +\ c_{82}V_C^2F_L + c_{83}V_C^2Q_G + c_{84}V_C^2F_LQ_G - H_T \tag{E.15d}$$

Two of the three roots for Equation E.13 are a pair of complex roots, thus dropped. The only real root has a form of

$$D_N = \sqrt[3]{-\frac{q}{2} + \sqrt{\frac{q^2}{4} + \frac{p^3}{27}}} + \sqrt[3]{-\frac{q}{2} - \sqrt{\frac{q^2}{4} + \frac{p^3}{27}}} \tag{E.16}$$

where

$$p = \frac{3ac - b^2}{3a^2} \tag{E.17a}$$

$$q = \frac{2b^3 - 9abc + 27a^2d}{27a^2} \tag{E.17b}$$

and the values for a, b, c, and d are obtained from Equations E.14 or E.15.

APPENDIX F

MULTIVARIABLE CURVE FITTING MODEL FOR MINIMUM PRESSURE IN NOZZLE

Equations 4.7 can be further expanded to yield a new pair of equations with a new group of total of 96 unknowns.

$$
\begin{aligned}
P_L = {} & d_1 + d_2 V_C + d_3 F_L + d_4 Q_G + d_5 V_C F_L + d_6 V_C Q_G + d_7 F_L Q_G \\
& + d_8 V_C F_L Q_G + d_9 V_C^2 + d_{10} V_C^2 F_L + d_{11} V_C^2 Q_G + d_{12} V_C^2 F_L Q_G \\
& + d_{13} D_N + d_{14} V_C D_N + d_{15} F_L D_N + d_{16} Q_G D_N + d_{17} V_C F_L D_N + d_{18} V_C Q_G D_N + d_{19} F_L Q_G D_N \\
& + d_{20} V_C F_L Q_G D_N + d_{21} V_C^2 D_N + d_{22} V_C^2 F_L D_N + d_{23} V_C^2 Q_G D_N + d_{24} V_C^2 F_L Q_G D_N \\
& + d_{25} D_N^2 + d_{26} V_C D_N^2 + d_{27} F_L D_N^2 + d_{28} Q_G D_N^2 + d_{29} V_C F_L D_N^2 + d_{30} V_C Q_G D_N^2 + d_{31} F_L Q_G D_N^2 \\
& + d_{32} V_C F_L Q_G D_N^2 + d_{33} V_C^2 D_N^2 + d_{34} V_C^2 F_L D_N^2 + d_{35} V_C^2 Q_G D_N^2 + d_{36} V_C^2 F_L Q_G D_N^2 \\
& + d_{37} D_N^3 + d_{38} V_C D_N^3 + d_{39} F_L D_N^3 + d_{40} Q_G D_N^3 + d_{41} V_C F_L D_N^3 + d_{42} V_C Q_G D_N^3 + d_{43} F_L Q_G D_N^3 \\
& + d_{44} V_C F_L Q_G D_N^3 + d_{45} V_C^2 D_N^3 + d_{46} V_C^2 F_L D_N^3 + d_{47} V_C^2 Q_G D_N^3 + d_{48} V_C^2 F_L Q_G D_N^3
\end{aligned}
$$

$$\text{for} \quad F_L \le 70\% \qquad \text{(F.1a)}$$

$$
\begin{aligned}
P_L = {} & d_{49} + d_{50} V_C + d_{51} F_L + d_{52} Q_G + d_{53} V_C F_L + d_{54} V_C Q_G + d_{55} F_L Q_G \\
& + d_{56} V_C F_L Q_G + d_{57} V_C^2 + d_{58} V_C^2 F_L + d_{59} V_C^2 Q_G + d_{60} V_C^2 F_L Q_G \\
& + d_{61} D_N + d_{62} V_C D_N + d_{63} F_L D_N + d_{64} Q_G D_N + d_{65} V_C F_L D_N + d_{66} V_C Q_G D_N + d_{67} F_L Q_G D_N \\
& + d_{68} V_C F_L Q_G D_N + d_{69} V_C^2 D_N + d_{70} V_C^2 F_L D_N + d_{71} V_C^2 Q_G D_N + d_{72} V_C^2 F_L Q_G D_N \\
& + d_{73} D_N^2 + d_{74} V_C D_N^2 + d_{75} F_L D_N^2 + d_{76} Q_G D_N^2 + d_{77} V_C F_L D_N^2 + d_{78} V_C Q_G D_N^2 + d_{79} F_L Q_G D_N^2 \\
& + d_{80} V_C F_L Q_G D_N^2 + d_{81} V_C^2 D_N^2 + d_{82} V_C^2 F_L D_N^2 + d_{83} V_C^2 Q_G D_N^2 + d_{84} V_C^2 F_L Q_G D_N^2 \\
& + d_{85} D_N^3 + d_{86} V_C D_N^3 + d_{87} F_L D_N^3 + d_{88} Q_G D_N^3 + d_{89} V_C F_L D_N^3 + d_{90} V_C Q_G D_N^3 + d_{91} F_L Q_G D_N^3
\end{aligned}
$$

$$+d_{92}V_C F_L Q_G D_N^3 + d_{93}V_C^2 D_N^3 + \ d_{94}V_C^2 F_L D_N^3 + d_{95}V_C^2 Q_G D_N^3 + d_{96}V_C^2 F_L Q_G D_N^3$$

$$\text{for} \quad F_L \geq 70\% \qquad \text{(F.1b)}$$

where d_i (i=1,2,…,96) are the new group of unknowns. The least square solution for the linear Equations F.1 are solved using the Normal Equation Method [70].

APPENDIX G

SIMILARITY ANALYSIS FOR LIQUID STEEL-ARGON SYSTEM AND WATER-AIR SYSTEM

In water modeling of the two-phase fluid flow in continuous casting of steel, an often-asked question is how much gas should be injected in order to simulate the liquid steel-argon bubble two-phase flow in a real caster. In water modeling of bubble formation behavior, one also needs to know how those observed gas bubbles are related to the argon bubbles in liquid steel under the same flow condition. This analysis aims to answer these questions and to reveal relationship keeping the similarity between water-air and liquid steel-argon systems.

In the following analysis, all dimensionless groups are derived from the ratios of the forces, which are dependent of the characteristic length. Three different definitions of the dimensionless groups are presented and discussed. Subscripts "*l*" donates for liquid phase, "*g*" for gas phase, "*w*" for water, "*Fe*" for liquid steel, "*Ar-hot*" for hot argon at steel temperature, "*Ar-cold*" for argon at the STP condition, "*air*" for air, and "*mix*" for both gas and liquid.

Heat transfer calculations (Appendix C) reveal that argon gas temperature is already raised to nearly 99% of the liquid steel temperature while in the ceramic nozzle even before it hits the liquid steel. In the study of argon bubble formation and two-phase fluid flow, the physical properties and flow rate of the argon gas such as density and viscosity should be "hot" properties rather than "cold" ones. For convenience, the "hot" argon flow rate used in model is converted to the equivalent "cold" argon flow rate monitored in the real steel casting process. Gas volume expansion coefficient β is taken as 5 and all physical properties used in this similarity analysis are listed in Table G.1.

Table G.1 Physical properties used in the similarity analysis

Physical Properties	Symbol	Unit	Liquid Steel-Argon System	Water-Air System
Liquid density	ρ_l	kg/m^3	7021	1000
Liquid viscosity	μ_l	kg/m-s	0.0056	0.001
Gas density	ρ_g	kg/m^3	0.27	1.29
Gas viscosity	μ_g	kg/m-s	7.42E-5	1.7E-5
Surface tension	σ	N/m	1.192	0.073
Gas volume expansion coefficient	β		5	1

G.1 Review of similarity analysis for single phase flow in real caster and water model

Dimensionless groups:

$$Re = \frac{\rho u L}{\mu} \qquad \text{and} \qquad Fr = \frac{u^2}{gL}$$

where L is the characteristic length associated with the nozzle/mold geometry. For the full scale water model, L is the same as in the real caster, or $L_w = L_{Fe} = L$

Matching Re:

$$\frac{\rho_{Fe} u_{Fe} L_{Fe}}{\mu_{Fe}} = \frac{\rho_w u_w L_w}{\mu_w}$$

results in

$$u_w = \frac{\rho_{Fe}}{\mu_{Fe}} \frac{\mu_w}{\rho_w} \frac{L_{Fe}}{L_w} u_{Fe} = \frac{7021}{0.0056} \frac{0.001}{1000} \frac{L}{L} u_{Fe} = 1.25 u_{Fe}$$

Similarly, matching Fr or $\frac{u_{Fe}^2}{gL_{Fe}} = \frac{u_w^2}{gL_w}$ gives $u_w = u_{Fe}$

<u>*Conclusion:*</u> For a single phase study, the only requirement for keeping similarity between water model and the real caster is using a full scale water model flow pattern as in the real caster, or $u_w \approx u_{Fe}$

G.2 Similarity analysis for two-phase fluid flow in nozzle and mold

For two-phase fluid flow, the characteristic length L is defined as the length associated with the nozzle/mold geometry.

Forces in the two-phase systems:

Inertial force due to liquid momentum (drag force):	$\rho_l L^2 u_l^2$
Inertial force due to gas momentum:	$\rho_g L^2 u_g^2$
Buoyancy force:	$(\rho_l - \rho_g) L^3 g$
Surface tension force:	σL
Viscous force of the liquid:	$\mu_l L u_l$
Viscous force of the gas:	$\mu_g L u_g$

Dimensionless groups:

$$Re_l = \frac{Inertial\ force\ due\ to\ liquid\ momentum}{Viscous\ force\ of\ liquid} = \frac{\rho_l L u_l}{\mu_l}$$

$$Re_g = \frac{Inertial\ force\ due\ to\ gas\ momentum}{Viscous\ force\ of\ gas} = \frac{\rho_g L u_g}{\mu_g}$$

$$Fr_l = \frac{Inertial\ force\ due\ to\ liquid\ momentum}{Buoyancy\ force} = \frac{\rho_l}{\rho_l - \rho_g} \frac{u_l^2}{gL}$$

$$Fr_g = \frac{Inertial\ \ force\ \ due\ \ to\ \ gas\ \ momentum}{Buoyancy\ \ force} = \frac{\rho_g}{\rho_l - \rho_g}\frac{u_g^2}{gL}$$

$$We_l = \frac{Inertial\ \ force\ due\ to\ liquid\ momentum}{Surface\ tension\ \ force} = \frac{\rho_l L u_l^2}{\sigma}$$

$$We_g = \frac{Inertial\ \ force\ due\ to\ gas\ momentum}{Surface\ tension\ \ force} = \frac{\rho_g L u_g^2}{\sigma}$$

$$\frac{Re_l}{Re_g} = \frac{Inertial\ \ force\ due\ to\ liquid\ momentum}{Inertial\ \ force\ due\ to\ gas\ momentum} = \frac{\rho_l u_l^2}{\rho_g u_g^2}$$

Matching calculation:

By matching each of the dimensionless groups between the liquid steel-argon and water-air system, the water velocity u_w, air flow rate Q_{air}, and air volume fraction f_{air} required to keep the similarity can be calculated.

For example, matching Fr_g needs

$$\frac{\rho_{Ar}}{\rho_{Fe} - \rho_{Ar}}\frac{u_{Ar}^2}{gL_{Fe}} = \frac{\rho_{air}}{\rho_w - \rho_{air}}\frac{u_{air}^2}{gL_w}$$

or

$$u_{air} = u_{Ar}\sqrt{\frac{\rho_{Ar}}{\rho_{air}}\frac{\rho_w - \rho_{air}}{\rho_{Fe} - \rho_{Ar}}}\sqrt{\frac{L_w}{L_{Fe}}}$$

$$= u_{Ar}\sqrt{\frac{0.27}{1.29}\frac{(1000-1.29)}{(7021-0.27)}} = 0.17u_{Ar}$$

Due to the same characteristics length for the full scale water model,

$$Q_{air} = 0.17Q_{Ar-hot}$$

Converting to "cold" argon flow rate generates

$$Q_{air} = 0.17 Q_{Ar-hot} \beta = 0.86 Q_{Ar-cold}$$

The calculations for matching other dimensionless groups are similar, and the results are summarized in Table G.2:

Table G.2 Similarity requirements for liquid velocity, gas flow rate, and gas volume fraction for full size water model

To Match	$\frac{u_w}{u_{Fe}}$	$\frac{Q_{air}}{Q_{Ar-hot}}$	$\frac{Q_{air}}{Q_{Ar-cold}}$	$\frac{f_{air}}{f_{Ar-cold}}$
Fr_l	1.00	----	----	----
Re_l	1.25	----	----	----
We_l	0.66	----	----	----
Fr_g	----	0.17	0.86	----
Re_g	----	0.05	0.24	----
We_g	----	0.11	0.57	----
$\frac{Re_l}{Re_g}$	$5.78 \frac{Q_{air}}{Q_{Ar-hot}}$	$0.17 \frac{U_w}{U_{Fe}}$	$0.86 \frac{u_w}{u_{Fe}}$	$\frac{0.86}{1-0.14 f_{Ar-cold}}$

"Mixed" dimensionless groups

Since in two-phase flow, the gas phase mixes up with the liquid phase, it might be more reasonable to account for the mixed effect of gas and liquid in the force evaluation. The "mixed" forces are defined as follows:

Inertial force due to the mixed momentum: $f_g \rho_g L^2 u_g^2 + (1 - f_g) \rho_l L^2 u_l^2$

Mixed buoyancy force: $(\rho_l - \rho_{mix}) L^3 g = f_g (\rho_l - \rho_g) L^3 g$

Mixed surface tension force: $f_g \sigma L$

Mixed viscous force: $f_g \mu_g L u_g + (1 - f_g)\mu_l L u_l$

where $\rho_{mix} = f_g \rho_g + (1 - f_g)\rho_l = \rho_l - f_g(\rho_l - \rho_g)$, and the dimensionless groups are:

$$Fr_{mix} = \frac{Inertial\ force\ due\ to\ mixed\ momentum}{Mixed\ buoyancy\ force} = \frac{f_g \rho_g L^2 u_g^2 + (1 - f_g)\rho_l L^2 u_l^2}{f_g(\rho_l - \rho_g) g L^3}$$

$$\approx \frac{1 - f_g}{f_g} \frac{u_l^2}{gL}$$

$$We_{mix} = \frac{Inertial\ force\ due\ to\ mixed\ momentum}{Mixed\ surface\ tension\ force} = \frac{f_g \rho_g L^2 u_g^2 + (1 - f_g)\rho_l L^2 u_l^2}{f_g \sigma L}$$

$$\approx \left(\frac{1 - f_g}{f_g}\right) \frac{\rho_l u_l^2 L}{\sigma}$$

$$Re_{mix} = \frac{Inertial\ force\ due\ to\ mixed\ momentum}{Mixed\ viscous\ force} = \frac{f_g \rho_g L^2 u_g^2 + (1 - f_g)\rho_l L^2 u_l^2}{f_g \mu_g L\, u_g + (1 - f_g)\mu_l L\, u_l}$$

$$\approx \frac{\rho_l u_l L}{\mu_l}$$

The “mixed” Reynolds number turns out to be same as the non-mixed one. The results of matching calculation for Fr_{mix} and We_{mix} is listed in Table G.3.

Table G.3 Similarity requirement for gas flow rate and gas volume fraction for the “mixed” dimensionless groups

To match	$\frac{Q_{air}}{Q_{Ar-hot}}$	$\frac{Q_{air}}{Q_{Ar-cold}}$	$\frac{f_{air}}{f_{Ar-cold}}$
Fr_{mix}	1.00	5.00	$\frac{5}{1 + 4 f_{Ar-cold}}$
We_{mix}	2.27	11.35	$\frac{5}{5 f_{Ar-cold} + 0.44(1 - f_{Ar-cold})}$

G.3 Similarity analysis for bubble formation study

In bubble formation study, the forces acting on bubble are evaluated, so it is more reasonable to take the average bubble diameter D as the characteristic length for liquid phase and gas injection orifice diameter d as the characteristic length for the gas phase. The bubble size, according to the two-stage model developed in this work, depends on the gas injection flow rate Q_g and the liquid velocity u_l in the nozzle. It is assumed that the gas injection orifice diameter d and the average liquid velocity in water model are the same as those in casting nozzles.

Forces acting on a forming bubble:

Inertial force due to liquid momentum (drag force):	$\rho_l D^2 u_l^2$
Inertial force due to gas momentum:	$\rho_g d^2 u_g^2$
Buoyancy force:	$(\rho_l - \rho_g) D^3 g$
Surface tension force:	σD
Viscous force of the liquid:	$\mu_l D u_l$
Viscous force of the gas:	$\mu_g D u_g$

Dimensionless groups:

$$Re_l = \frac{Inertial\ \ force\ due\ to\ liquid\ momentum}{Viscous\ \ force\ of\ liquid} = \frac{\rho_l D u_l}{\mu_l}$$

$$Re_g = \frac{Inertial\ \ force\ due\ to\ gas\ momentum}{Viscous\ \ force\ of\ gas} = \frac{\rho_g d\ u_g}{\mu_g}$$

$$Fr_l = \frac{Inertial\ \ force\ due\ to\ liquid\ momentum}{Buoyancy\ \ force} = \frac{\rho_l}{\rho_l - \rho_g} \frac{u_l^2}{gD}$$

$$Fr_g = \frac{Inertial\ \ force\ \ due\ \ to\ \ gas\ \ momentum}{Buoyancy\ \ force} = \frac{\rho_g}{\rho_l - \rho_g}\frac{d^2u_g^2}{gD^3}$$

$$We_l = \frac{Inertial\ force\ due\ to\ liquid\ momentum}{Surface\ tension\ force} = \frac{\rho_l D u_l^2}{\sigma}$$

$$We_g = \frac{Inertial\ force\ due\ to\ gas\ momentum}{Surface\ tension\ force} = \frac{\rho_g d^2 u_g^2}{\sigma D}$$

$$\frac{Re_l}{Re_g} = \frac{Inertial\ force\ due\ to\ liquid\ momentum}{Inertial\ force\ due\ to\ gas\ momentum} = \frac{\rho_l D^2 u_l^2}{\rho_g d^2 u_g^2}$$

Matching calculation:

By matching each of the dimensionless groups between the liquid steel-argon and water-air system, the airflow rate Q_{air} required to keep the similarity (or to generate the same size air bubbles) can be found.

For example, matching Fr_l needs

$$\frac{\rho_{Fe}}{\rho_{Fe} - \rho_{Ar}}\frac{u_{Fe}^2}{gD_{Ar}} = \frac{\rho_w}{\rho_w - \rho_{air}}\frac{u_w^2}{gD_{air}}$$

or

$$D_{air} \approx D_{Ar} \tag{G.1}$$

From the two-stage bubble formation model developed in Chapter 2, the bubble size depends on the average liquid velocity in the nozzle and the gas injection flow rate. The requirement for matching Fr_l should also vary with the flow conditions. For instance, with a flowing liquid at the mean velocity of 0.9m/s, 3ml/s hot argon injection rate (per hole) will generate argon bubbles with mean diameter of 3.9mm, as seen from Figure 2.17. To generate the same size air bubbles in a water model, that's is, to satisfy Equation G.1, the required air injection flow rate should be 4.2ml/s. Therefore,

$$\frac{Q_{air}}{Q_{Ar-hot}} = \frac{4.2}{3} = 1.4$$

Converting to "cold" argon flow rate generates

$$\frac{Q_{air}}{Q_{Ar-cold}} = \frac{\beta Q_{air}}{Q_{Ar-hot}} = \frac{5*4.2}{3} = 7.0$$

Similar calculations can be done for matching other dimensionless groups and the results are summarized in Table G.4:

Table G.4 Similarity requirement for gas flow rate in bubble formation study (average liquid velocity 0.9m/s, hot argon injection rate: 3ml/s per hole)

To Match	$\frac{Q_{air}}{Q_{Ar-hot}}$	$\frac{Q_{air}}{Q_{Ar-cold}}$
Fr_l	1.4	7.0
Re_l	2.1	10.5
We_l	0.2	1.0
Fr_g	0.12	0.6
Re_g	0.09	0.45
We_g	0.1	0.5
Re_l/Re_g	0.2	1.0

G.4 Conclusions:

The introduction of the gas phase brings the effects of gas momentum and surface (interface) tension force into the systems, which hence needs some new dimensionless groups to account for those effects. Furthermore, the introduction of the gas phase not only brings a new dimensionless group (*We*), but also makes definitions of the dimensionless groups questionable.

In this appendix, three different similarity analysis methods were presented and discussed, each of which is based on different definitions of force evaluation or length scale.

To keep an ideal similarity between two systems, all of the dimensionless groups should be matched correspondingly. This can be true if the physical properties of the modeling system are the same as those of the real system under the condition of full-scale model.

In single-phase study, the only requirements are same geometry, leading to approximate same Reynolds number and Froude number for the liquid steel and water due to their similar kinematic viscosity. However, there is a big difference between the water-air system and liquid steel-argon system. The similar kinematic viscosity for water and liquid steel is not enough to keep the similarity for the two-phase related studies.

The similarity calculation, shown in Tables G.2, G.3 and G.4, shows very different results, and in each table, matching different dimensionless groups also gave conflicting requirements. Matching all of the dimensionless groups at the same time is impossible. One approximating method is to match only dominant dimensionless groups and ignore others. For example, under high velocity liquid flow, surface tension's contribution to bubble formation is relatively small compared to the dominant liquid momentum even for steel-argon system. By matching the dominant Reynolds number and Froude number for liquid and neglecting the Weber number, the observed air bubble size in water should be close to the argon bubble size in liquid steel under the same flow conditions. Unfortunately, in many practical cases, it is often difficult to tell the dominant or negligible dimensionless groups. This suggests that although water model can be an effective tool for the single-phase steel flow study, water-air system is not suitable for the study of liquid steel-argon system. Using different gas in water modeling could not solve this problem. This also suggests that we should depend more on mathematical models for multi-phase fluid flow and do more physical experiments with flowing steel in the plant in order to understand the continuous casting process. Two-phase water models are most useful only for the validation of the mathematical models.

REFERENCE

1. Hershey, D., Thomas, B.G. and Najjar, F.M., "Turbulent Flow through Bifurcated Nozzles," International Journal for Numerical Methods in Fluids, vol. 17 (1) (1993), pp. 23-47.

2. Nakato, H., Ozawa, M., Kinoshita, K., Habu, Y., Emi, T., "Factors Affecting the Formation of Shell and Longitudinal Cracks in Mold during High Speed Continuous Casting of Slabs," Trans. Iron Steel Inst. Japan, vol. 24 (11) (1984), pp. 957-965.

3. Herbertson, J., He, Q.L., Flint, P.J., Mahapatra, R.B., "Modeling of Metal Delivery to Continuous Casting Moulds" (Paper presented at 74th Steelmaking Conference, Warrendale, PA, 1991, Iron and Steel Society, Inc.), vol. 74, pp. 171-185.

4. Emling, W.H. and Waugaman, T.A., "Subsurface Mold Slag Entrainment in Ultra Low Carbon Steels" (Paper presented at 77th Steelmaking Conference, Washington, D. C., 1994), pp. 371-379.

5. McDavid, R. and Thomas, B.G., "Flow and Thermal Behavior of the Top-Surface Flux/Powder Layer in Continuous Casting Molds," Metallurgical Transactions B, vol. 27B (4) (1996), pp. 672-685.

6. Rackers, K.G. and Thomas, B.G., "Clogging in Continuous Casting Nozzles" (Paper presented at 78th Steelmaking Conference, 1995), pp. 723-734.

7. Sasaka, I. and al., e., "Improvement of Porous Plug and Bubbling Upper Nozzle for Continuous Casting" (Paper presented at 74th ISS Steelmaking Conference, Washington, D. C., 1991),

8. Szekeres, E.S., "Review of Strand Casting Factors Affecting Steel Product Cleanliness" (Paper presented at 4th International Conference on Clean Steel, Balatonszeplak, Hungary, 1992),

9. Knoepke, J. and Hubbard, M., "Pencil Blister Reductions at Inland Steel Company" (Paper presented at 77th Steelmaking Conference, Washington, D. C, 1994), pp. 381-388.

10. Thomas, B.G., Dennisov, A. and Bai, H., "Behavior of Argon Bubbles during Continuous Casting of Steel" (Paper presented at 80th ISS Steelmaking Conference, Chicago, 1997),

11. Buhr, H. and Pirdzun, J., "Development of Refractories for Continuous Casting" (Paper presented at Continuous Casting of Steel, Biarritz, France, 1976),

12. Ozeki, H.H., Yamaguchi, T., Takasu, T., Auki, T., "Prevention of Alumina Clogging in Tundish Shroud" (Paper presented at 2nd International Conference on Refractories, Japan, 1987, Tech Association of Refractories), pp. 398-410.

13. McPherson, N.A. and McIntosh, S.L., "Mould Power Related Defects in Some Continuously Casting Steel Products" (Paper presented at 70th ISS Steelmaking Conference, 1987), vol. 70, pp. 17-25.

14. Nagai, H. and Kuba, Y., "Reduction of Refractory Consumption in Continuous Casting," Taikabuts Overseas, vol. 3 (3) (1984), pp. 22-26.

15. Dawson, S.M., "Blockage of Tundish Nozzles during the Continuous Casting of Aluminum-killed Steel" (PhD Thesis, University of Toronto, 1990).

16. Burty, M., Larrecq, M., Pusse, C., Zbaczyniak, Y., "Experimental and Theoretical Analysis of Gas and Metal Flows in Submerged Entry Nozzles in Continuous Casting" (Paper presented at 13th PTD Conference, Nashville, TN, 1995), vol. 13, pp. 287-292.

17. Najjar, F.M., Thomas, B.G. and Hershey, D., "Numerical Study of Steady Turbulent Flow through Bifurcated Nozzles in Continuous Casting," Metallurgical Transactions B, vol. 26B (4) (1995), pp. 749-765.

18. Wang, Y.H., "3-D Mathematical Model Simulation on the Tundish Gate and Its Effect in the Continuous Casting Mold" (Paper presented at 10th Process Technology Conference, Toronto, Ontario, Canada, 1992, Iron and Steel Society, Inc.), vol. 75, pp. 271-278.

19. Yao, M., "Flow Simulation of Molten Steel for Immersion Nozzle Design in Continuous Casting Process" (Paper presented at Modeling and Control of Casting and Welding Processes IV, 1988, TMS), pp. 893-898.

20. Wang, L., Lee, H.-G. and Hayes, P., "Prediction of the Optimum Bubble Size for Inclusion Removal from Molten Steel by Flotation," ISIJ International, vol. 36 (1) (1996), pp. 7-16.

21. Bessho, N., Yoda, R., Yamasaki, T., FUji, T., Nozaki, T., "Numerical Analysis of Fluid Flow in the Continuous Casting Mold by a Bubble Dispersion Model," Transactions of the ISS (I$SM), (April) (1991), pp. 39-44.

22. Thomas, B.G. and Huang, X., "Effect of Argon Gas on Fluid Flow in a Continuous Slab Casting Mold" (Paper presented at 76th Steelmaking Conference, Dallas, TX, 1993, Iron and Steel Society), vol. 76, pp. 273-289.

23. Thomas, B.G., Huang, X. and Sussman, R.C., "Simulation of Argon Gas Flow Effects in a Continuous Slab Caster," Metallurgical Transactions B, vol. 25B (4) (1994), pp. 527-547.

24. Creech, D., "Computational Modeling of Multiphase Turbulent Fluid Flow and Heat Transfer in the Continuous Slab Casting Mold" (MS Thesis, University of Illinois at Urbana-Champaign, 1999).

25. Tabata, K., Kakehi, T. and Terao, M., "Gas Injection Methods at Tundish Slide Gate Valve for Continuous Casting" (Report No. 31, Shinagawa Technical Report, 1988).

26. Cameron, S.R., "The Reduction of Tundish Nozzle Clogging during Continuous Casting at Dofasco" (Paper presented at 75th ISS Steelmaking Conference, Toronto, Canada, 1992),

27. Tsai, H.T., Sammon, W.J. and Hazelton, D.E., "Characterization and Countermeasures for Sliver Defects in Cold Rolled Products" (Paper presented at 73rd ISS Steelmaking Conference, Detroit, MI, 1990), vol. 73, pp. 49-59.

28. Sano, M. and Mori, K., "Bubble Formation from Single Nozzles in Liquid Metals," Trans. JIM, vol. 17 (1976), pp. 344-352.

29. Thomas, A., Tu, S. and Janke, D., "Frequency of Bubble Formation in Water and Liquid Iron," Steel Research, vol. 68 (5) (1997), pp. 198-200.

30. Sano, M., Fujita, Y. and Mori, K., "Formation of Bubbles at Single Nonwetted Nozzles in Mercury," Metallurgical Transactions B, vol. 7B (June) (1976), pp. 300-301.

31. Iguchi, M., Kawabata, H., Nakajima, K., Morita, Z., Metallurgical Transactions B, vol. 26B (1995), pp. 67.

32. Irons, G.A. and Guthrie, R.I.L., "Bubble Formation at Nozzles in Pig Iron," Metallurgical Transactions B, vol. 9B (March) (1978), pp. 101-110.

33. Davis, K.G., Irons, G.A. and Guthrie, R.I.L., "X-Ray Cinematographic Observations of Gas Injection into Liquid Metals," Metallurgical Transactions B, vol. 9B (December) (1978), pp. 721-722.

34. Iguchi, M., Chihara, T., Takanashi, N., Ogawa, Y., Tokumitsu, N., Morita, Z., "X-ray Fluoroscopic Observation of Bubble Characteristics in a Molten Iron Bath," ISIJ International, vol. 35 (11) (1995), pp. 1354-1361.

35. Wang, Z., Mukai, K. and Izu, D., "Influence of Wettability on the Behavior of Argon Bubbles and Fluid Flow inside the Nozzle and Mold," ISIJ International, vol. 39 (2) (1999), pp. 154-163.

36. Kumar, R. and Kuloor, N.R., "The Formation of Bubbles and Drops," in Advances in Chemical Engineering, vol. 8, (New York, London: Academic Press, 1970), pp. 255-368.

37. Clift, R., Grace, J.R. and Weber, M.E., Bubbles, Drops, and Particles, (Academic Press Inc., 1978).

38. Tsuge, H., "Hydrodynamics of Bubble Formation from Submerged Orifices," in Encyclopedia of Fluid Mechanics, vol. 3, (Houston, TX: Gulf Publishing Co., 1986), pp. 191-232.

39. Rabiger, N. and Vogelpohl, A., "Bubble Formation and its Movement in Newtonian and Non-Newtonian Liquid," in Encyclopedia of Fluid Mechanics, vol. 3, (Houston, TX: Gulf Publishing Co., 1986), pp. 58-88.

40. Davidson, J.F. and Schuler, B.O.G., "Bubble Formation at an Orifice in an Inviscid Liquid," Trans. Instn Chem. Engrs, vol. 38 (1960), pp. 335-342.

41. Kumar, R. and Kuloor, N.R., Chem. Tech., vol. 19 (1967), pp. 733.

42. Pinczewski, W.V., "The Formation and Growth of Bubbles at a Submerged Orifice," Chemical Engineering Science, vol. 36 (1981), pp. 405-411.

43. Terasaka, K. and Tsuge, H., "Bubble Formation at a Single Orifice in Highly Viscous Liquids," Journal of Chemical Engineering of Japan, vol. 23 (2) (1990), pp. 160-165.

44. Terasaka, K. and Tsuge, H., "Bubble Formation under Constant-Flow Conditions," Chemical Engineering Science, vol. 48 (19) (1993), pp. 3417-3422.

45. Tsuge, H., Nakajima, Y. and Terasaka, K., "Behavior of Bubble Formed from a Submerged Orifice under High System Pressure," Chemical Engineering Science, vol. 47 (13/14) (1992), pp. 3273-3280.

46. Hong, T., Zhu, C. and Fan, L.-S., "Numerical Modeling of Formation of Single Bubble Chain and Bubble Breakage due to Collision with Particle in Liquid" (Paper presented at 1996 ASME Fluids Division Conference, 1996), vol. FED 236, pp. 581-588.

47. Hirt, C.W. and Nichols, B.D., "Volume of Fluid (VOF) Method for the Dynamics of Free Boundary," Journal of Computational Physics, vol. 39 (1981), pp. 201-225.

48. Chuang, S.C. and Goldschmidt, V.W., "Bubble Formation due to a Submerged Capillary Tube in Quiescent and Coflowing Streams," Journal of Basic Engineering, vol. 92 (1970), pp. 705-711.

49. Kawase, Y. and Ulbrecht, J.J., "Formation of Drops and Bubbles in Flowing Liquids," Ind. Eng. Chem. Process Des. Dev., vol. 20 (4) (1981), pp. 636-640.

50. Morgenstern, I.B.V. and Mersmann, A., "Aeration of Highly Viscous Liquids," Germany Chemical Engineering, vol. 5 (1982), pp. 374-379.

51. White, F.M., Viscous Fluid Flow, (McGraw-Hill, Inc., 1991).

52. Daugherty, R.L., Franzini, J.B. and Finnemore, E.J., Fluid Mechanics with Engineering Applications, 8th ed., (New York: McGraw-Hill Inc., 1985).

53. Winterton, R.H.S., "Sizes of Bubbles Produced by Dissolved Gas Coming out of Solution on the Walls of Pipes in Flowing Systems," Chemical Engineering Science, vol. 27 (1972), pp. 1223-1230.

54. Jimbo, L., Sharan, A. and Cramb, A.W., "Recent measurements of surface and interfacial tensions in steels" (Paper presented at 76th SteelMaking Conference, Dallas, TX, 1993), pp. 485-494.

55. Thomas, B.G. and Najjar, F.M., "Finite-Element Modeling of Turbulent Fluid Flow and Heat Transfer in Continuous Casting,," Applied Mathematical Modeling, vol. 15 (May) (1991), pp. 226-243.

56. Tsai, H.T., "Water Modeling on Pressure Profile in the Tundish Shroud at Flo-Con", private communication, Inland Steel, 1986.

57. Heaslip, L.J., Sommerville, I.D., A., M., Swartz, G., W.W., "Model Study of Fluid Flow and Pressure Distribution During SEN Injection - Potential for Reactive Metal Additions during Continuous Casting," Transactions of the ISS (I$SM), (August) (1987), pp. 49-64.

58. Sjöström, U., Burty, M., Gaggioli, A., Radot, J., "An Experimental Study of Argon Injection and Aspiration of Air into Stopper Rod in Continuous Casters" (Paper presented at 81st SteelMaking Conference, Toronto, Canada, 1998, Iron and Steel Society, Inc.), vol. 81, pp. 63-71.

59. Mazumdar, D. and Guthrie, R.I.L., "The Physical and Mathematical Modeling of gas Stirred Ladel Systems," ISIJ International, vol. 35 (1) (1995), pp. 1-20.

60. Neifer, M., Rödl, S. and Sucker, D., "Investigations on the Fluid Dynamics and Thermal Process Control in Ladles," Steel Research, vol. 64 (1) (1993), pp. 54-62.

61. Huang, X. and Thomas, B.G., "Modeling of Transient Flow Phenomena in Continuous Casting of Steel," (1998), pp.

62. AEA Technology, "CFX4.2 Users Manual," (1997).

63. Launder, B.E. and Spalding, D.B., Mathematical Models of Turbulence, (London Academic Press, 1972).

64. Launder, B.E. and Spalding, D.B., "Numerical Computation of Turbulent Flows," Computer Methods in Applied Mechanics and Engineering, vol. 13 (1974), pp. 269-289.

65. Lai, K.Y.M. and Salcudean, M., "Computer Analysis of Multi-Dimensional ,Turbulent, Buoyancy-Induced, Two-Phase Flows in Gas-Agitated Liquid Reactors," Computational Fluids, vol. 15 (3) (1987), pp. 281-295.

66. Bai, H. and Thomas, B.G., "Two Phase Flow in Tundish Nozzles during Continuous Casting of Steel" (Paper presented at Materials Processing in the Computer Age III, TMS Annual Meeting, Nashville, TN, 2000),

67. Bai, H. and Thomas, B.G., "Effects of Clogging, Argon Injection and Tundish Depth on Flow Rate and Air Aspiration in Submerged Entry Nozzles" (Paper presented at 83rd Steelmaking Conference, Pittsburgh, PA, 2000, Iron and Steel Society, Warrendale, PA), vol. 83,

68. Sivaramakrishnan, S., Bai, H., Thomas, B., Vanka, P., Dauby, P., Assar, M., "Transient Flow Structures in Continuous Casting of Steels" (Paper presented at 83rd Steelmaking Conference, Pittsburgh, PA, 2000, Iron and Steel Society, Warrendale, PA), vol. 83,

69. Thomas, B.G., Mika, L.M. and Najjar, F.M., "Simulation of fluid flow inside a continuous slab casting machine," Metallurgical Transactions B, vol. 21B (2) (1990), pp. 387-400.

70. Heath, M.T., Scientific Computing, An Introductory Survey, (New York: McGraw-Hill, 1997).

71. Gass, R., private communication, Inland Steel, 1998.

72. Assar, M.B., private communication, LTV Steel, 1998.

73. Dawson, S.M., "Tundish Nozzle Blockage During the Continuous Casting of Aluminum-killed Steel" (Paper presented at 73rd Steelmaking Conference, Detroit, MI, 1990, Iron and Steel Society, Inc.), vol. 73, pp. 15-31.

74. Meadowcroft, T.R. and Milbourne, R.J., "A New Process for Continuously Casting Aluminum Killed Steel," Journal of Metals, (June) (1971), pp. 11-17.

75. Cramb, A.W. and Jimbo, I., "Interfacial Considerations in Continuous Casting," ISS Transactions, vol. 11 (1990), pp. 67-79.

76. Hirt, C.W., "Identification and treatment of stiff bubble problems" (Report No. FSI-92-TN36, Flow Science Inc., 1992).

77. Tai, M.C., Chen, C.H. and Chou, C.L., "Development ans Benifits of Four-Port Submerged Nozzle for Bloom Continuous Casting" (Paper presented at Continuous Casting '85, London, England, 1985), pp. 19.1-19.6.

78. Beaton, C.F. and Hewitt, G.F., Physical Properties Data for the Chemical and Mechanical Engineer, (Hemisphere Publishing Co., 1989).

79. FLUENT Inc., "Computational Fluid Dynamics Software - FLUENT User's Guide," (1995).

VITA

Hua Bai was born on January 12, 1963 in Hubei, China. Upon graduation from high school in 1979, he enrolled in Beijing Institute of Aeronautics and Astronautics in Beijing. He received his Bachelor of Science degree and his Master of Science degree in 1983 and 1986, respectively. He was employed as a research engineer at Nanjing Aeronautical Accessory Factory for next two years, where he was involved in research on the dynamic characteristics of the hydraulic pumps and on the hydraulic pipeline structure vibration. His patented co-invention, Filter-Three-In-One, was awarded a Silver Medal at the 36th Brussel Eureka World Fair for Invention in 1987. In 1988, Hua joined the Yangtze Group of HME Technology as a project engineer, where he engaged in developing hydraulic systems for various mining, building and road construction equipment. He received the Outstanding Achievement Award from China Ministry of Aerospace Industry in 1991.

In the fall of 1995, Hua began pursuing his Ph.D. in the Department of Mechanical and Industrial Engineering at the University of Illinois at Urbana-Champaign. Under the guidance of Professor Brian G. Thomas, he has worked on modeling continuous casting of steel slabs. His research interests are in the area of computational and experimental fluid dynamics, materials processing, and fluid transmission and control. Hua will begin work this summer as a Senior Research Engineer in Engineering Sciences-Fluid Mechanics and Mixing Department at the Dow Chemical Company in Freeport, Texas.

Hua was married to Snow Xue Liu in January of 1990, and they were blessed with their daughter, Carrie, in February of 1997.